Upscaling and testing of a procedure for precipitation of metal oxides and metals from wastewater

Iphigenia Franziska Anagnostopoulos

München, 2024

Upscaling and testing of a procedure for precipitation of metal oxides and metals from wastewater

Dissertation zur Erlangung des Doktorgrades
an der Fakultät für Geowissenschaften
der Ludwig-Maximilians-Universität München

Vorgelegt von
Iphigenia Franziska Anagnostopoulos

München, den 1. Februar 2024

Erstgutachter/in:	Prof. Dr. Soraya Heuss-Aßbichler
Zweitgutachter/in:	Prof. Dr. Wolfgang Schmahl
Tag der mündlichen Prüfung:	24.07.2024

I. Abstract

Water is essential for metal processing. Consequently, significant amounts of heavy metal-loaded wastewater are produced during the processing and manufacturing of metals. These wastewaters are classified as hazardous and toxic to humans and the environment. The collection of these wastewater as mixed wastewater makes their treatment challenging due to their complex composition. The conventional treatment method is a neutralisation process leading to the precipitation of heavy metals as hydroxides. This causes large amounts of voluminous sludge, usually disposed of in hazardous landfills. Recently, waste has received greater attention as a potential metal resource for economic and strategic reasons. Accordingly, research focuses on developing extraction methods of metals from waste. An innovative concept is the so-called Specific Product-Oriented Precipitation (SPOP) process, which aims to purify metal-bearing wastewater and recover the contained metals as a secondary resource.

This thesis focuses on scaling up the SPOP process, which has been carried out as a laboratory process. This includes the installation and optimisation of a pilot facility and its software. Three different wastewater systems (Zn, Au, and Cu) were tested using real and model wastewater. The effect of impurities in real wastewater was also tested using Cu-enriched electroplating wastewater with lower Zn, Pb, Ni, Cr, and Mn concentrations. Applying a one-step process demonstrated the recovery of Zn as ZnO and Cu as ferrite or CuO, depending on the addition of Fe to the system. In a two-step process, Au is obtained as zero-valent Au in the first step and Fe as ferrite in the second step. The treatment with the pilot facility shows good results regarding product-oriented phase formation and water purification. An alteration of the suspension generally leads to reduced metal concentrations, and limit values for discharge are met for Zn, Pb, Ni and Cr. With the upscaling of the process, new parameters became relevant. The stirring speed during precipitation influenced the phase formation and composition. Modifying the SPOP process into a continuous mode enabled the treatment of a larger volume of wastewater in a shorter process time. This variant proved particularly effective for forming specific phases such as delafossite (ABO_2). Overall, it could be shown that the upscaling of the process was successful, as the laboratory and pilot scale results are comparable. The results of this thesis show that the SPOP process is robust and can be operated in an automated batch mode, treating larger wastewater quantities in series, which is a requirement for industrial implementation.

Zusammenfassung

Wasser ist ein wesentlicher Rohstoff für die Metallverarbeitung. Daher fallen bei der Verarbeitung und Herstellung von Metallen erhebliche Mengen an schwermetallhaltigen Abwässern an. Diese werden allgemein als gefährlich eingestuft, da sie für Mensch und Umwelt schädlich sind. Die Sammlung dieser Abwässer als gemischte Abwässer macht ihre Behandlung aufgrund ihrer komplexen Zusammensetzungen zu einer Herausforderung. Die herkömmliche Behandlungsmethode ist ein Neutralisationsfällungsverfahren, bei dem die Schwermetalle in Form von Hydroxiden ausgefällt werden. Dieses Verfahren verursacht jedoch große Mengen an voluminösen Schlämmen, welche in der Regel auf Sondermülldeponien entsorgt werden. In jüngster Zeit findet Abfall aus wirtschaftlichen und strategischen Gründen größere Beachtung, da er eine potenzielle Metallressource darstellt. Dementsprechend konzentriert sich die Forschung auf die Entwicklung von Extraktionsmethoden für Metalle aus Abfällen. Ein innovatives Konzept für die Rückgewinnung von Metallen aus Abwässern ist der sogenannte „Spezifische Produkt-Orientierte Präzipitations“ (SPOP) Prozess, welcher zum Ziel hat Abwasser zu reinigen und die enthaltenen Metalle als Sekundärressource zurückzugewinnen.

Diese Arbeit konzentriert sich auf die Skalierung des SPOP-Prozesses, welches bisher als Laborverfahren angewendet wurde. Dabei wurde eine Technikumsanlage installiert und die automatisierte Behandlung inklusive der Software optimiert. Drei Abwassersysteme (Zn, Au und Cu) wurden mit Industrie- und Modellabwässern getestet. Der Einfluss von Verunreinigungen wurde mit Cu-angereichertem Galvanikabwasser mit niedrigeren Konzentrationen an Zn, Pb, Ni, Cr und Mn getestet. Die Anwendung eines einstufigen Prozesses zeigte die Rückgewinnung von Zn in Form von ZnO und Cu in Form von Ferrit oder CuO, je nach Zugabe oder Ausschluss von Fe zum System. In einem zweistufigen Verfahren wurde erst nullwertiges Au und im zweiten Schritt Fe als Ferrit gewonnen. Eine Alterung der Suspension führt im Allgemeinen zu verringerten Metallkonzentrationen und die Grenzwerte für die Einleitung konnten für Zn, Pb, Ni und Cr eingehalten werden. Damit konnte gezeigt werden, dass sowohl eine produkt-orientierte Phasenbildung als auch eine Wasserreinigung mit der SPOP Technikumsanlage möglich ist. So erwies sich beispielsweise die Rührgeschwindigkeit während der Fällung als ein einflussreicher Prozessparameter für die Phasenbildung und -zusammensetzung. Durch die Modifizierung des SPOP-Verfahrens in einen kontinuierlichen Betrieb konnte eine größere Abwassermenge in einer kürzeren Prozesszeit behandelt werden. Diese Variante erwies sich als besonders geeignet für die Bildung von Delafossit (ABO_2). Insgesamt konnte gezeigt werden, dass das Upscaling des Prozesses erfolgreich war, da die Ergebnisse im Labor- und Pilotmaßstab vergleichbar sind. Die Ergebnisse dieser Arbeit zeigen, dass das SPOP-Verfahren robust ist und in einem automatisierten Batch-Modus betrieben werden kann, um größere Abwassermengen in Serie zu behandeln, was eine Voraussetzung für die industrielle Umsetzung ist.

II. Outline of this thesis

In this PhD thesis, I present the results of upscaling the "Specific Product-Oriented Precipitation" (SPOP) process – a novel treatment technique to purify heavy metal-bearing wastewater and recover the metals as a secondary resource. The thesis is subdivided into three main sections. The first section (Chapters 2-3) gives background information on wastewater treatment and the SPOP process. In the second section (Chapters 4-6), I focus on the experimental results and the pilot facility's technical optimisation. The third section (Chapters 7-8) compiles the thesis' discussion, conclusion, and outlook.

- **Section One: Background information on wastewater treatment (Chapter 2) and technical development (Chapter 3)**

Chapter 2 overviews wastewater treatment methods from the electroplating industry, a typical wastewater stream enriched with heavy metals. I discuss the benefits and current limits of each treatment method. Additionally, the recovery potential of metals from sludges from electroplating wastewater treatment, according to data from the European Waste Catalogue 11 01 09*, is estimated. This chapter contains parts that have been published as a contribution to the article "Residues of industrial wastewater treatment: Hazardous waste or anthropogenic resource?" in Pöllman, H., "*Industrial Waste – Characterization, Modification and Applications of Residues"* (2021) published by De Gruyter.

Chapter 3 focuses on state-of-the-art wastewater treatment with the SPOP process, which aims to purify industrial wastewater and recover metals as a secondary resource. Exemplarily, the phases achieved in the Cu-Fe-O-S-H system are illustrated. The controlling parameters are introduced, and two operational modes, the one-step process and the two-step process, are explained. Furthermore, the functionality of the SPOP pilot facility, which enables a batch treatment procedure and was used for the experimental section of this work, is introduced.

- **Section Two: Experimental setup (Chapter 4), results of experimental work (Chapter 5), and implications of the upscaling experiments (Chapter 6)**

Chapter 4 provides an overview of the materials used for the experimental work (real wastewater from the electroplating industry, chemical catalyst production, and synthetic wastewater) and the applied analytical methods.

The upscaling experiments of the SPOP process with the pilot facility were conducted on three elemental systems: the Zn system, the Au system, and the Cu system. I present the results of these experiments in Chapter 5.

In Chapter 6, I describe technical and process-related influences impacting the output of the upscaling experiments, such as malfunctions and stirring rate. Furthermore, I summarise and discuss the technological changes in the facility, including their effect on the process.

Additionally, I developed a modified process sequence that could enable the continuous execution of the SPOP process. The results of these experiments and a possible technical setup of the continuous mode process are also presented in Chapter 6.

- **Section Three: Discussion (Chapter 7), Conclusion & Outlook (Chapter 8)**

The discussion covers the different main topics of this thesis: Chapter 7.1 covers the testing and upscaling of the precipitation recipes of the Zn- and Au-system compared to the laboratory results and literature. Different modes to recover Cu and the respective reactions are reviewed in Chapter 7.2, and phase formation in the system Cu-S-O-H depending on the stirring rate. An assessment of the robustness of the process is discussed in Chapter 7.3, and in Chapter 7.4, I evaluate the first results on phase formation conducted with a continuous mode process.

I summarise the main findings in Chapter 8 (Conclusion and Outlook) and present my ideas regarding open research questions and future directions

Contents

1. Introduction

The supply of metals and access to clean water have been crucial to humanity since ancient times. The first settlements were trans-regionally close to rivers, providing water and food. Water was also vital to goods production and metal processing. Already in the Third Millennium B.C., Cu-mining and smelting activities caused regional pollution of water bodies *(Nocete et al., 2005; Ong et al., 2018)*.

The industrial revolution caused an exponential increase in the extraction of mineral raw materials. In consequence, industrial wastewater was generated in massive amounts. At that time, all branches of industry discharged their untreated wastewater into rivers, taking advantage of the dissipative dynamics of water. Rivers were considered "self-cleaning", and the strategy for wastewater management was in line with the principle that "the solution to pollution is dilution" *(Lofrano et al., 2015)*.

However, at the beginning of the 20th century, several examples of severe environmental pollution poisoning the population made headlines. One example is the prolonged wastewater discharge from a chemical plant into Minamata Bay (Kyushu, Japan). This catastrophic event triggered the Minamata disease from ingesting toxic methylmercury (MeHg). Inhabitants developed chronic symptoms, and infants were born with congenital Minamata disease. The environmental damage was enormous and irreversible. Meanwhile, Minamata Bay has been covered with plastic and soil to seal millions of tons of mercury sludge.

In Europe, too, industrialisation has caused severe pollution of rivers. Emissions of toxins to the environment reached such a life-threatening dimension that in the second half of the 20th century, extensive efforts were made to revitalise rivers. Consequently, regulations have been established providing limit values for pollutants in industrial wastewater, which must be met before discharge and wastewater purification techniques have been developed. The conventional treatment to purify metal-polluted wastewater is a neutralisation process by which the metals are bound into a highly voluminous hydroxide complex. Nowadays, these sludges are dewatered by, e.g., chamber filter presses, but the remaining water content is still high. Since these sludges contain (toxic) metals, they are disposed of in, e.g., landfills and are lost by dissipation *(Heuss-Aßbichler et al., 2016a)*.

The recovery of metals from wastes is only strived for when the current metal value is high. However, due to the increasing scarcity of metals *(Graedel and Erdmann, 2012)* and increasing prices for raw materials, waste has gained attention as a secondary resource. Furthermore, without retrieving resources from waste, some scarce natural resources will run out of supply *(Friege, 2013)*. Industrial wastewater carries many metals in high concentrations and can be considered a secondary resource material. Yet, efficient recycling technologies must be established in the wastewater treatment sector to make this resource available.

One approach that aims to purify heavy metal-loaded wastewater and recover the metals as a secondary resource is the Specific-Product-Oriented Precipitation (SPOP) process, developed at the LMU Munich since 2014. It is a chemical precipitation process which avoids the formation of metal-hydroxides and instead recovers metals in the form of oxides like ferrites (AB_2O_4) and delafossite (ABO_2), binary oxides (AO and A_2O), and zero-valent metals. The groundwork for this process is the research on the formation mechanism of metal species in aqueous solutions. It was found that each occurring metal has its dynamics and can build different phases depending on the formation conditions. Therefore, formation methods need to be worked out individually and metal-specifically for a recovery process to be effective. The SPOP process was first developed on a laboratory scale and applied to abundant metal systems in wastewater. The most mapped out systems are Cu, Zn, and Au, which have been demonstrated to be recovered as Cu-ferrite, cuprite, and tenorite *(Heuss-Aßbichler et al., 2016b)*, Cu-delafossite *(John et al., 2016a, 2016b, 2016d)*, zinc-oxide *(John, 2016; John et al., 2016c, Tandon et al., 2018; Tandon, 2021)* and metallic Au *(John et al., 2019)*. On a laboratory scale, the results have shown that the phase formation depends on many parameters, such as the initial metal concentration, the reaction temperature, the alkalisation rate, the final pH and the alteration conditions. Additionally, the range of conditions under which a certain phase forms can be very narrow. Therefore, small fluctuations of the parameters can lead to a failure of the synthesis and unwanted phases form instead. For example, the formation of ferrites strongly depends on the pH and redox conditions. Only at a specific pH range around 9, ferrite can form, otherwise Fe-hydroxides are favoured. Hence, synthesising specific metal phases in aqueous solutions is very sensitive and needs to be accurately controlled. Precipitation systems can be well controlled on a small laboratory scale. However, the disturbances grow with increasing reaction volume, which triggers the potential for process failures. Yet, for the SPOP process to be an alternative to established wastewater processes, it must be shown to be feasible on a larger scale.

For this reason, *Knof (2017)* designed an automated SPOP pilot facility to upscale the laboratory process. The reactor within the pilot facility allows the treatment of up to ten times the volume of wastewater (1 l) compared to the laboratory process, plus storage for up to 100 l of treated wastewater.

One outstanding question remains: can the SPOP process be applied to larger than laboratory throughputs? This central question includes questions about the reaction mechanisms: are the reaction mechanisms identified on a laboratory scale also effective on a larger scale? Are there other relevant process parameters that emerge from the upscaling? Upscaling of the SPOP process is connected to the automation of the process. Hence, all process steps conducted manually in the laboratory process are automatically executed in the pilot facility. This, consequently, triggers a series of questions as follows. (1) How does the automation impact the process, and (2) how is the process impacted in case of a partial failure of the automation?

The SPOP process was designed as a batch process; however, for continuously accruing wastewater, a likewise continuous treatment could be favourable. On that account, (3) how can the SPOP process be executed continuously? Are the phases formed in the batch process reproducible in the continuous process? And overall, (4) is the SPOP process robust on a larger scale?

To contextualise the SPOP process to the latest wastewater treatment methods, I review recently published developments in wastewater treatment techniques in Chapter 2. The focus is on the treatment parameters' influences on the resource recovery and purification rates. Chapter 3 comprises the fundamentals for the experimental part of this thesis: the basic SPOP process and the functionality of the pilot facility. To test the reaction mechanisms on a larger scale, the process was performed with the pilot facility using synthetic and real wastewater (Chapter 4). The tested wastewaters were chosen based on the most elaborated elements in the SPOP process: Cu, Zn, and Au. The Zn-containing wastewater is a model system based on sulfate salt. The Cu-containing wastewater stems from a rinsing bath from the electroplating industry and the Au-enriched wastewater from chemical catalyst synthesis. Chapter 5 covers the upscaled experiments, designed based on the laboratory results such that a comparison of the reaction mechanisms is feasible and to test if the laboratory results of the SPOP process are reproducible on a larger scale. Chapter 6 comprises the technical assessment of the pilot facility. In Chapter 6.1, I summarise the technical changes conducted to achieve better performance and suggest future optimisations. During the precipitation process, a homogenisation of the solution is required, which is executed via an overhead stirrer. For the upscaling, a larger volume of wastewater is treated, which required more powerful stirrers to enable a fast homogenisation of the solution. This technical change raised whether the stirring speed influences the process. It could be shown that a stepwise shift in stirring speed affects the products (Chapter 6.2). In Chapter 6.3, the impact of a partial process failure to test for the robustness of the process is demonstrated. Therefore, the interruption of the process is regulated, and its effect on the process products is evaluated. In Chapter 6.4, an attempt is made to convert the batch process into a continuous process. Therefore, the process may not be interrupted, meaning a process sequence change must occur. This alternative was technically designed and tested on a laboratory scale and has shown to be advantageous for delafossite synthesis. In Chapter 7, I discuss the results of the upscaled experiments individually for each elemental system. In Chapter 7.1, I discuss whether the SPOP process can be used as an alternative synthesis route for technically desired phases like ZnO. Furthermore, I discuss which kind of Au-bearing wastewater the SPOP process suits. In Chapter 7.2, I examine the reaction mechanisms in the Cu system. In Chapter 7.2.1, I focus on the reaction mechanisms of ferrite formation in the system Fe^{2+}:Cu^{2+} = 2:1 and the influence of the oxygen fugacity on reaction pathways. In Chapter 7.2.2, I discuss the influence of the process failure mineralogically and propose possible reactions for the formed phases in the system Fe^{total}:Cu^{2+}

= 2:1. In Chapter 7.2.3, I discuss the influence of the reaction temperature and the pH on the formation of delafossite polytypes based on the results of the alternative continuous SPOP process in the system Fe^{2+}:Cu^{2+} = 1:1. In Chapter 7.2.4, the results of the experiments without Fe addition are discussed, which show that a recovery of CuO from electroplating wastewater is possible and the underlying formation reaction is formulated. Furthermore, the results have demonstrated that the stirring speed affects the phase composition. Depending on the stirring speed, Sulphate and Cu are bound together in either one or two separate phases. The mechanism for the different phase compositions is discussed likewise in Chapter 7.2.4. In Chapter 7.3, I evaluate the robustness of the SPOP process by working out the critical process parameters and their influence on the performance of the process. In Chapter 7.4, I discuss the prospect of the tested continuous flow SPOP process and summarise the results achieved in further elemental systems conducted by bachelor theses, which I co-supervised. In the Conclusion and Outlook, Chapter 8, I summarise the main findings of this work and suggest the industrial upscale of the SPOP process and future fields of research. Despite wastewater treatment, the SPOP process can be considered a synthesis method for designed materials.

SECTION ONE

2. Treatment of industrial wastewater – state-of-the-art

Heavy metal-bearing industrial wastewaters are challenging to treat due to their diverse and complex properties. As an example of heavy metal-bearing industrial wastewater, a brief overview of wastewater produced in the electroplating industry is presented in Chapter 2.1. Several treatment methods developed in consequence are presented in Chapter 2.2. Recently, the demand for the recycling of heavy metals from waste has been increasing, as natural mineral deposits are widely consumed, and their mining is getting more extensive. Therefore, the recovery potential of heavy metals from wastewater and the challenges connected with heavy metal recovery from wastewater are discussed in Chapter 2.3.

2.1. Wastewater production in the electroplating industry

A prominent example of heavy metal-containing wastewater is the one generated in the electroplating industry. The finishing of metals and non-metals with metallic coatings was applied after the principles of galvanic cells were found by Luis Galvani in the late 18th century. Therefore, electroplating was one of the first industrial technologies to be developed. By 1840, the electrochemical deposition of various metals on goods was ready *(Neukirchen, 2016)*. Even though electroplating has existed for 200 years, its scope of application is still growing. Branches like the semiconductor industry, which use the latest technologies in metal deposition, like sputtering and evaporation, are lately considering electroplating as an optional process of production, as it provides a very pure material deposition accompanied by a high deposition rate of 4 µm/min *(Witt, 2020)*Nowadays, hardly any industrial branch does not use metal-finished products, such as the automotive, aerospace, military, and medical industries. These sectors' functionality and technological progress would be impossible without electrodeposition and surface treatment.

Metal finishing is a key technology that requires many resources, such as raw materials, metal salts, other chemicals, and vast amounts of water. The trend moves towards the use of critical raw materials in addition to standard metals. Consequently, the advantages of this technology are associated with a massive volume of waste, especially heavy metal-bearing wastewater, which is regularly generated by the exchange of spent process baths and rinsing water. The wastewater reflects the composition of the metals used for electroplating. Prevalent elements are Cu, Ni, Cr, or Zn, but noble metals such as Pd, Au, or Ag may also occur. Depending on the requirements, the volumes of the process and rinsing baths vary from a few litres, e.g., for noble metal coatings up to 500 m^3 for components suppliers.

Over time, different types of coating techniques have been developed. *Figure 2.1* shows a schematic process flow sheet of the electroplating process *(Landesamt für Umwelt Baden-Württemberg, 2017; ABAG-item GmbH 2008)*. The process generally consists of three stages with different metals, each with a sequence of plating and rinsing baths. The wastewater streams are usually combined, treated and disposed of according to the Waste Directive, whereby hazardous materials are indicated with * in the waste code.

The first step is a pre-treatment of the products to remove oily and fatty components, dirt, mechanical residuals and corrosion products on the surface. It is carried out, e.g., with hot cleaning or halogenated hydrocarbons, and the respective waste is listed under the waste codes 11 01 13* and 11 01 14. Next, the surface is activated by pickling with, e.g., (noble metals containing) mineral acids (waste codes 11 01 05*, 11 01 06*, 11 01 07*). The main step is the coating process applied to the cleaned and activated surfaces. The specific metals are electrodeposited as alloys or sequentially in multiple layers. Both acidic or basic metal-containing electrolytes can be used depending on the intended purpose. Basic electrolytes, like cyanide complexes, need additional chelating agents to keep the metals in solution. Typical feed materials are metal-sulfates, -fluoroborates, or -chlorides. Next, solid filtrable materials and adsorbents are partially separated from the process baths (waste code 15 02 02*), and the remaining process solution is reused. In a third step, a post-treatment can be applied to improve corrosion protection or to achieve decorative effects. In most cases, this is done by chromating using chromic acid. In addition, surface treatment processes such as acid dipping can be interposed, involving chemicals such as sulfuric acid, hydrochloric acid or hydrofluoric acid.

The used-up process and rinsing baths are collected and treated in the central wastewater treatment plant, which is commonly a chemical precipitation process initiated by adding a reaction agent. This step generates and collects voluminous hydroxide sludge containing heavy metals, partly disposed of in landfills under the waste code 11 01 09*. The rinsing baths can hold up to 20% of the initial metal salts in the plating baths *(Upadhyay, 2006)*Therefore, they are often purified by ion exchange and reused before being finally treated by chemical precipitation. The accruing heavy metal wastewater and ion exchange eluates are collected and purified in the central wastewater treatment system (waste code 11 01 09*). Finally, the spent ion exchange resins are disposed of or incinerated (waste code 11 01 16*).

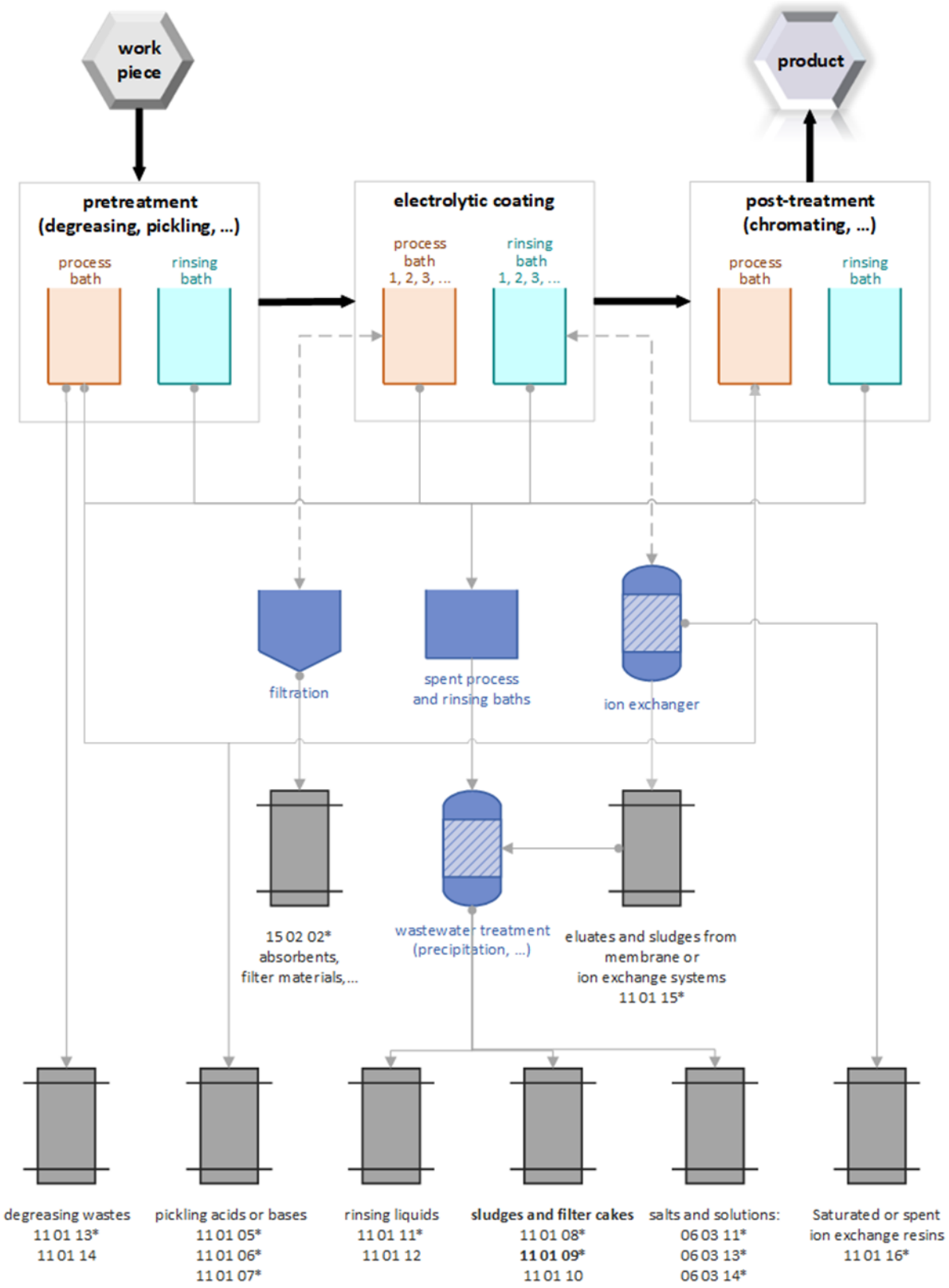

Figure 2.1: *Schematic process flow sheet of the electroplating process with accompanied wastes. Waste codes marked with * indicate hazardous materials. Modified after* ABAG-itm GmbH (2008); Landesamt für Umwelt Baden-Württemberg (2017).

2.1.1. Treatment techniques for heavy metal-bearing wastewater

Heavy metals occur in acidic solutions as dissolved cations. Dissolved heavy metals are inorganic pollutants as they can contaminate the environment and drinking water when discharged into surface waters. Heavy metals are considered persistent environmental toxins because, unlike other contaminants such as pharmaceuticals and most dyes, they cannot be metabolised to carbon dioxide and water or detoxified by chemical or biological remediation processes *(Mohammed et al., 2011)*. For this reason, treated wastewater must meet the strict environmental regulation criteria to prevent pollution of surface waters with heavy metals after direct or indirect discharge.

In practice, the various wastewater streams are collected and mixed into the final wastewater. Accordingly, the wastewater consists of a mixture of different metals with enormous fluctuations in concentration (from mg/l to several g/l) and pH value. Several processes have been developed to treat these complex wastewaters. In addition to the industrially established techniques, various promising alternative methods are being developed. Some have been intensively investigated, and others are still at an early stage of development. An overview of these processes is presented in the following chapter.

2.1.2. Chemical precipitation

Wastewater treatment by chemical precipitation is a robust and technically highly mature process *(Ku and Jung, 2001; Fu and Wang, 2011)* with an implementation rate of 75%, the most widely used treatment process in the electroplating industry *(Karthikeyan et al., 1996)*The principle is based on adjusting the wastewater's pH to a range in which the metal hydroxides ($M^{n+}(OH)_n$) show minimal solubilities and precipitate. Afterwards, sedimentation or filtration separates the generated metal hydroxide sludge from the liquid phase. Hydroxides or sulfides are conventionally used as precipitants.

2.1.2.1 Hydroxide precipitation

Various alkalising agents are used for the hydroxide precipitation of metals from wastewater. Milk of lime ($Ca(OH)_2$) is mainly applied because it is low-priced, can be dosed effortlessly and shows good coagulation of particles *(Baltpurvins et al., 1997)*. On the other hand, caustic soda (NaOH) is less frequently used to form metal hydroxides due to the higher costs. In various studies, soda (Na_2CO_3), sodium bicarbonate ($NaHCO_3$), and magnesia (MgO) have been investigated as alkalisation agents *(Patterson et al., 1977; Lin et al., 2005)*. Other studies showed that soda ash (Na_2CO_3) is an effective alternative for removing Cu, Zn and Pb, as carbonate precipitation occurs at a comparatively lower pH of around 9 *(Chen et al., 2018)*.

The chemical precipitation of metal cations to metal hydroxides follows the reaction:

$$M^{2+} + 2(OH)^{-} \leftrightarrow M(OH)_2 \downarrow \quad (1)$$

where M^{2+} represents the dissolved metal cation, OH^- is the alkaline precipitant and M(OH)2 is the resulting metal hydroxide. Metal hydroxides have their specific minimum solubilities at different pH values; any deviation from the optimal pH for precipitation causes the metals to dissolve. *Table 2.1* gives an overview of the optimum pH values for the precipitation of some metal hydroxides.

Table 2.1: *Overview of the final precipitation pH values for selected metal hydroxides and sulphides.*

	Hydroxide Precipitation		**Sulphide Precipitation**	
Metal	**Precipitation pH**	**Reference**	**Precipitation pH**	**Reference**
Cd	10.4 – 10.9	Patterson et al. (1977)	4	Gharabaghi et al. (2012)
Co(II)	10	Huang et al. (2004)	approx. 3	Jandová et al. (2005)
Cr(III)	8.7	Mirbagheri and Hosseini (2004)	approx. 6	Mudakavi et al. (1995)
Cu(II)	8.1 – 11.1	Pang et al. (2009)	2.5	Gharabaghi et al. (2012)
Fe(III)	6.2 – 7.1	Pang et al. (2009)	3.6 – 5.7	Wei and Osseo-Asare (1996)
Mo	5 – 7	Huang et al. (2004)	-	-
Ni(II)	10.5 – 11	Patterson et al. (1977)	7.5	Gharabaghi et al. (2012)
Pb(II)	7.8 – 8.8	Pang et al.(2009), (Sist and Demopoulos (2003)	7.5 – 8.5	Hien Hoa et al. (2007)
Zn(II)	8,7 – 9,6	Pang et al. (2009)	5,5	Gharabaghi et al. (2012)

Due to the complex mixture of different metals in the final wastewater, it is difficult to determine the best precipitation condition. Therefore, the wastewater is alkalised in the pH range of the main component. As a result, metals with a minimum solubility different from the target metal remain partly in the solution. Due to this limitation caused by the complex composition of the wastewater, other treatment techniques are often applied after the hydroxide precipitation. Additionally, hydroxide precipitation is ineffective for low-concentrated wastewater *(Fu and Wang, 2011)*.

A technical problem is the low sedimentation of the precipitates due to their colloidal properties, which hinders the liquid/solid separation *(Krusenstjern and Axmacher, 1964)*. Techniques like ultracentrifugation or colloid filtration could be applied, but the current

industry standard is the addition of flocculants to initiate coagulation. Using synthetic wastewater consisting of Zn^{2+}, Cd^{2+}, Mn^{2+} and Mg^{2+}, it was shown that adding a coagulant after the precipitation with lime can significantly reduce the residual heavy metal concentration in the solution *(Charerntanyarak, 1999)*. Another approach to improve the separation process is the addition of fly ash as a crystallisation seed, which can enhance the precipitation of heavy metals together with milk of lime. It was found that adding coal fly ash in combination with exposure to CO_2 gas increases the particle size of the precipitate, resulting in better sedimentation of the sludge and increased efficiency of heavy metal removal *(Chen et al., 2009)*.

Another problem poses strongly complexing organic agents like EDTA (ethylenediaminetetraacetic acid). Those agents are often present in wastewater from the electroplating industry and inhibit the removal of heavy metals with hydroxide precipitation *(Lin et al., 1998)*.

Hydroxide precipitation produces large volumes of sludges highly enriched in water and low-concentrated in metals *(Babu et al., 2009)*. Therefore, the sludges are dewatered and disposed of in hazardous landfill sites *(Twidwell and Dahnke, 2001)*. Some research has been done on the use and detoxification of these sludges. The use of dried metal hydroxide sludge from the electroplating industry was studied to solve reactive dye wastewater problems. It was shown that sludge could be used as an adsorbent for azo-reactive dyes *(Netpradit et al., 2003)*. With an enhanced electrokinetic process, it was possible to remove 34 – 69% of Cr, Zn, Ni, Cu and Pb from electroplating sludge by using citric acid as electrolytes in electrode chambers *(Peng and Tian, 2010)*. Experiments with Cr-containing electroplating sludges using HCl achieved an extraction rate of 97.6% *(de Souza E Silva et al., 2006)*. With a combined process of acid-leaching, ammonium jarosite precipitation, and electro-deposition, more than 95% of Cu and Ni were recovered from electroplating sludge *(Li et al., 2011)*. Electroplating sludge enriched with 50 % Sn was treated to recover Sn by leaching with concentrated HCl at room temperature for one month or boiling in 10% HCl solution for two hours. Subsequent electrowinning achieved an Sn recovery of 93% *(Stefanowicz et al., 1991)*.

Recently, upcycling methods for electroplating sludges were investigated. Two specific electroplating sludges containing electroplating wastewater were tested as adsorbents for Zn, Cu, Ni, and Co *(Liu et al., 2020)*The sludges contained significant amounts of Fe, Co, and Cr, respectively. After hydrothermal treatment, particles containing erdite (a sulfide containing Fe, Na, and H_2O) were formed and used as adsorbents.

Implications: Chemical precipitation with hydroxides is the most frequently applied method for heavy metal-bearing wastewater. The process is robust and technically easy, and used chemicals are cheap. However, the removal rates are partly limited due to the re-concentration of metals in wastewater. The liquid/solid separation process is time-consuming and involves

adding further chemicals. The generated sludges contain hazardous materials and pose a burden to the environment. In practice, a recovery of the heavy metals from hydroxide sludge is rarely applied, as it is sumptuous, and the metal content is often too low for recovery. As a result, the sludges must be transported and deposited safely at great expense.

2.1.2.2 Sulphide precipitation

Sulphide precipitation is carried out by adding precipitation agents such as solid (FeS, CaS), aqueous (Na_2S, NaHS) or gaseous sulphides (H_2S). The reaction involved in sulphide precipitation is *(Bhattacharyya et al., 1979)*

$$M^{2+} + S^{2-} \leftrightarrow MS \downarrow \quad (2)$$

where M^{2+} represents the dissolved metal cation, S^{2-} is the sulphide precipitant, and MS is the resulting precipitate.

Treatment with sulphides has the potential for selective precipitation. For example, the treatment of Zn and Cu solution with Na_2S leads to the precipitation of CuS (covellite) and ZnS (sphalerite) *(Sampaio et al., 2009)*. The reaction rate is fast, the settling properties are high due to the high density of the particles, and afterwards, the Me-sulphides can be roasted to oxides. The resulting Me-sulphide sludge is more accessible to concentrate than hydroxide sludge and needs no dewatering process *(Fu and Wang, 2011)*. However, the fine-grained Me-sulphide precipitates make the separation process laborious, and flocculants must be added *(Whang and Young, 1982)*.

An example is a recovery of Cd from electroplating wastewater containing contaminants (Fe, Cu, Ni, Zn) and impurities (Co, Mn) *(Islamoglu et al., 2006)*. At first, the pollutants were removed by acidifying the wastewater with HNO_3 to precipitate the metals as cyano-metal complexes. At this moment, it is critical to control the pH. Next, the wastewater was alkalised with NaOH to precipitate $Cd(OH)_2$. In a final polishing step, sulphide precipitation with Na_2S was conducted to precipitate the remaining Cd in the alkaline pH range. However, due to technical difficulties and criticalities, sulphide precipitation is not a standard method. These involve an insufficiently controlled dosing of sulphide *(Veeken and Rulkens, 2003)*.

Furthermore, the sulphide sludges potentially release H_2S gas, and heavy metals can be redissolved due to the oxidation of metal sulphides to sulfate *(Peters and Ferg, 1987)*. Yet, it shows some conceptual advantages compared to hydroxide precipitation. Contrary to hydroxides, metal-sulphides show no amphoteric properties, and the solubilities of metal-sulphides are lower than those of metal-hydroxides *(Kim and Amodeo, 1983; Peters and Ferg, 1987)*. Therefore, precipitation with sulphides can be applied over a broader pH range. In addition, the acidic wastewater does not need to be highly alkalised to achieve a high degree

of metal removal *(Fu and Wang, 2011)*. Combined sulphide and hydroxide precipitation processes have also been applied for selective metal recovery *(Bhattacharyya et al., 1979)*.

Indications: The sulphide precipitation process has some advantages over the hydroxide precipitation process, e.g., a higher degree of metal removal at lower pH values and selective metal precipitation, but dosing of sulphides and separating the fine precipitate is technically tricky. Therefore, the treatment of electroplating wastewater with sulphides is rarely applied compared to hydroxide precipitation. Instead, hydroxide and sulphide precipitation combinations are used for highly effective metal removal. But metal sulphide sludges pose criticalities to the environment.

2.1.2.3 Heavy metal chelating precipitation

Complexing agents like EDTA hinder the removal of heavy metals from electroplating wastewater by conventional hydroxide or sulphide precipitation. For example, when Ni and Cr form a complex with cyanide, the removal efficiency is impaired *(Naim et al., 2010)*. Therefore, more potent chelating agents are used for precipitation to form complexes with both the metal cations and the metal chelate present. Many commercial chelating agents exist on the market, some for non-selective, some for selective metal removal. For example, nonstoichiometric interbiopolyelectrolyte green complexes (NIBPEGCs) can remove different metals from electroplating wastewater *(López-Maldonado et al., 2017)*. Chitosan and its derivatives proved particularly effective for the selective precipitation of Pd from electroplating wastewater with up to 95% removal efficiency *(Xie et al., 2020)*.

The chemical extraction of chelated metals from the resulting sludges is very costly as it requires strong chemicals and generates other wastes. For noble metals, such as Pd, a recovery process with aqua regia has proven possible *(Xie et al., 2020)*. Therefore, sludges from chelate precipitation are generally disposed of in hazardous waste landfills.

2.1.2.4 Ferrite process

The ferrite process was developed in the 1970s, initially to purify laboratory heavy metal-bearing wastewaters. The idea was to incorporate the heavy metals into the spinel structure of ferrites ($M_xFe_{3-x}O_4$). Ferrites form an (inverse) spinel structure in which many ferrous and non-ferrous metals can be incorporated. The incorporation of cations into the ferrite structure was, e.g., studied for Cu^{2+} *(Inouye et al., 1971; Mandaokar et al., 1994)*, Co^{2+} *(Kiyama Masao, 1978)*, Mo^{3+} *(Kanzaki et al., 1983)*, Ni^{2+} *(Tamaura, 1986; Barrado et al., 2002a)*, Zn^{2+} *(Tamaura et al., 1991; Prieto et al., 2001)*, Cr^{3+} *(Tamaura et al., 1991; Mandaokar et al., 1994; Barrado et al., 2002b; Erdem and Tumen, 2004)*, Pb^{2+}, Fe^{2+} *(Tamaura et al., 1991; Mandaokar et al., 1994)* Cd^{2+}, Mn^{2+} *(Kiyama Masao, 1978; Tamaura et al., 1991)*, and Hg^{2+} *(Zade and Dharmadhikari, 2007)*.

Figure 2.2 depicts the ferrite process as described by *Tamaura et al. (1991)*: $FeSO_4*7H_2O$ is added to the wastewater with a varying molar ratio of M:Fe = 1:10 – 1:20. The reaction pH is adjusted between 9 and 11. Heating is conducted by steam until a reaction temperature of circa 65 °C is achieved. First, the Fe(II) gets oxidised by aeration. Then, the suspension is withdrawn from the reactor via a circulation pump and divided into a ferrite slurry and a largely particle-free solution by a magnetic separator. While part of the ferrite is added as excess sludge for further dewatering, an additional pump conveys the main part of the sludge back into the reactor, which is used as a crystallisation agent *(Franzreb, 2003)*.

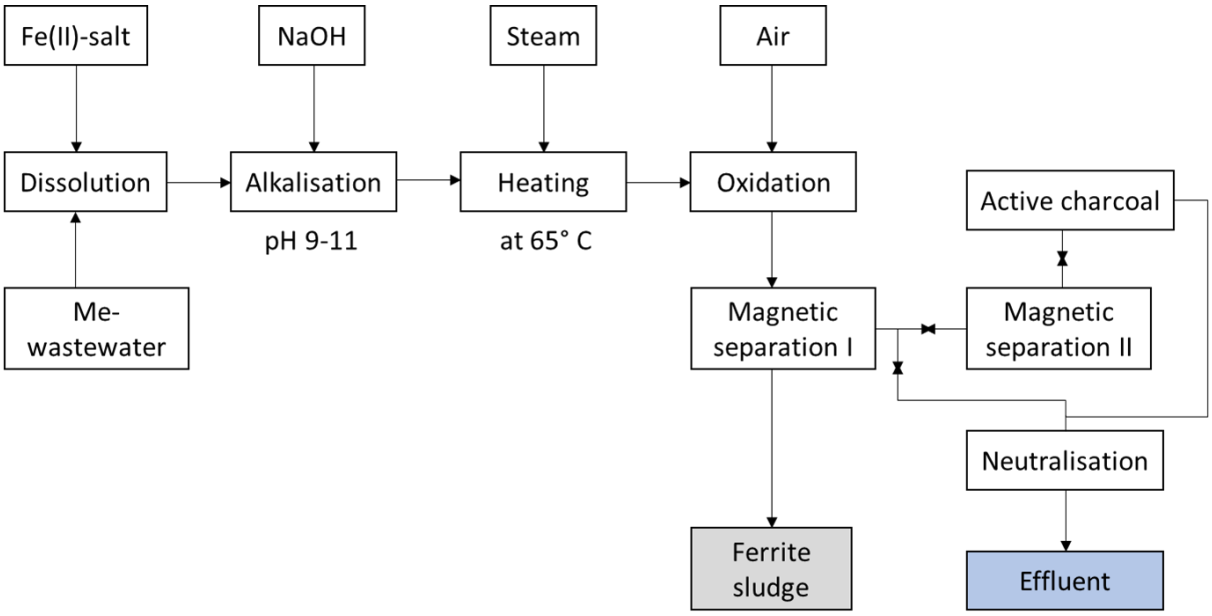

Figure 2.2: *Flowchart of the ferrite process after* Tamaura et al. (1979). *First, the wastewater and the Fe^{2+} salts are combined and alkalised. Next, the solution is heated with steam and oxidised with air. Finally, the ferrite residue is magnetically separated. In the last treatment, active coal reduces the Me-concentration to the minimum. Particles are separated magnetically, and the water pH is adjusted.*

The formation of ferrites is based on the transformation of mixed Me-containing hydroxides. *Mandaokar et al. (1994)* describe the involved mechanisms and reaction equations:

In the first step of the ferrite process, under alkaline conditions, the divalent cations (M^{2+}) in the wastewater and the divalent Fe^{2+} cations form a mixed metal hydroxide

$$x\mathrm{M}^{2+} + \mathrm{Fe}_{3-x}^{2+} + 6\ OH^- \longrightarrow \mathrm{M}_x\mathrm{Fe}_{3-x}(\mathrm{OH})_6 \qquad (3)$$

Subsequent aeration oxidises the mixed metal hydroxides. Mechanisms like redissolution and complex formation take place during the formation of ferrites

$$\mathrm{M}_x\mathrm{Fe}_{3-x}(\mathrm{OH})_6 + \frac{1}{2}\mathrm{O}_2 \rightarrow \mathrm{M}_x\mathrm{Fe}_{3-x}\mathrm{O}_4 + 3\ \mathrm{H}_2\mathrm{O} \qquad (4)$$

Numerous studies investigate the influence of reaction parameters on ferrite formation:

The concentration of required Fe^{2+}

Mandaokar et al. (1994) point out that the minimum amount of Fe^{2+} to be added to the wastewater depends on the target metal incorporated into the ferrite structure and the concentration of the target metal in the solution. For example, for Cu, the required Cu:Fe ratio is 1:2. They also observed that the necessary Fe^{2+} concentration can vary with the concentration of the target metal in the solution. For example, a Cr:Fe ratio of 1:18 must be set to form a Cr ferrite. Hence, a Cr concentration of 50 mg/kg in the solution requires a minimum concentration of 900 mg/kg Fe^{2+}. With increasing Cr concentration, the minimum Fe concentration decreases. For example, for a Cr concentration of 500 mg/kg, the Cr:Fe ratio falls to 1:7.

Effect of pH

The optimum pH depends on the initial heavy metal cation concentration; higher concentrations require a higher pH *(Mandaokar et al., 1994)*. However, *Masao (1978)* found that an excess of NaOH hinders the incorporation of heavy metals into the ferrite structure.

Effect of aeration rate

According to *Mandaokar et al. (1994)*, the aeration rate is a critical parameter for ferrite formation. For Pb^{2+}, the optimum aeration rate increases with increasing Pb^{2+} concentration. In contrast, *Demirel et al. (1999)* observed that the aeration rate has no significant influence on the removal of Ni and Cu.

Effect of temperature

The effect of temperature on the ferrite formation and the metal removal is element-dependent. For Pb, a minimum temperature of 50 °C is required for ferrite formation *(Mandaokar et al., 1994)*. The effect of temperature in the formation of Cu-ferrite and Zn-ferrite was tested between 50 °C and 70 °C *(Demirel et al., 1999)*. The results show no significant effect on the ferrite formation or removal efficiency.

Application of ferritisation: The ferrite process was mainly developed and applied in Japan, e.g., at the Tokyo Institute of Technology. However, this process has not been established in Europe and North America. The reasons are slow reaction kinetics and the high influx of iron salts, which inevitably lead to increased salt loads in the treated water. Another reason is the demand for relatively high amounts of heat and introducing oxygen into the reactor, which causes high costs *(Franzreb, 2003)*.

2.1.3. Ion exchange

Ion exchange has been intensively studied and is a well-established process to remove heavy metals from wastewater. Advantages include high treatment capacities, removal efficiencies, and kinetics *(Kang et al., 2004; Fu and Wang, 2011)*. Generally, both anions and cations can be exchanged, but for SPOP, cation exchangers must be considered for heavy metals. The technique is based on an ion exchange between a cation (B^+) dissolved in a liquid phase and a loaded resin (M^-A^+). The ion transfer between the cation (A^+) bound on the resin M^- and the cations of the wastewater (B^+) can be shown as follows *(Harland, 1994)*

$$\underbrace{M^-A^+}_{\text{Solid}} + \underbrace{B^+}_{\text{Solution}} \leftrightarrow \underbrace{M^-B^+}_{\text{Solid}} + \underbrace{A^+}_{\text{Solution}} \quad (5)$$

According to *Eq. 5*, the number of ions in wastewater remains the same since the desorption of harmless cations like Na^+, Ca^{2+}, or Mg^{2+} compensates for the adsorption of toxic heavy metal cations.

The resin must meet high requirements to guarantee a good cation exchange efficiency, such as a hydrophilic structure with a regular and reproducible shape, a controlled exchange capacity and chemical and thermal stability, to name just a few *(Harland, 1994)*. Natural materials like alumosilicates fulfil these high requirements only to a certain limit. Modern ion exchange materials are synthetically produced organic compounds like, e.g., styrenic or acrylic resins. The exchange-active groups are, e.g., sulpho-groups ($SO_3^-H^+$) or carboxyl groups (COO^-H^+). The exchange of the dissolved cations with hydrogen ions means converting the metal salt solution into free acids, thus acidifying the wastewater. After consuming active hydrogen ions in the resin, the ion exchanger can be treated with caustic soda and regenerated with, e.g., hydrochloric acid. After that, the concentration of cations in the regenerate is higher than in the original wastewater *(Dietrich, 2017)*. Therefore, ion exchange is also a method for concentrating ions in a liquid phase. In the surface coating industry, ion exchangers are used for rinse water recirculation, recovery of materials from rinse water, regeneration of process solutions and subsequent purification of treated wastewater *(Dietrich, 2017)*.

The removal efficiency of the ion exchange resin Dowex HCR S/S was determined to remove Zn and Ni as a function of pH, resin dosage, and contact time *(Alyüz and Veli, 2009)*. The authors concluded that the pH is crucial as it influences the ionisation of surface functional groups, and hydronium ions (H_3O^+) compete for adsorbates, reducing metal cations' exchange rate. The optimum adsorption of Ni^{2+} and Zn^{2+} occurred at pH 4 and 6, respectively; $Ni(OH)_2$ and $Zn(OH)_2$ are formed at higher pH values. The removal efficiency improved with a higher resin dosage as adsorption sites increased. Another critical parameter for the effectiveness of ion exchange is the contact time. For the tested resin, contact times of 90 and 120 min were required for Ni and Zn, respectively *(Alyüz and Veli, 2009)*. The treatment of polymetallic wastewater with an ion exchanger is complex because of the competitive replacement of ions

with the resin. For example, Cr^{3+} can re-mobilise Co^{2+} and Ni^{2+} that had already been removed from wastewater *(Kang et al., 2004)*. Therefore, it is necessary to consider the heavy metal composition in the wastewater before applying ion exchange. Combined processes selectively concentrate metals by ion exchange and precipitate with chemical treatment methods. For example, Cr^{6+} in electroplating wastewater was removed with Cr-selective resins and reduced to Cr^{3+} by hydroxide precipitation using NaOH *(Ye et al., 2019)*.

Natural examples of ion exchange materials are zeolites, which have a good ion exchange capacity due to their crystallographic structure. Clinoptilolite, for example, is a zeolite of the Heulandite group, which is used to remove heavy metals from industrial effluents. Both natural *(Vaca Mier et al., 2001; Rodríguez-Iznaga et al., 2002; Inglezakis et al., 2003)* and synthetic clinoptilolite *(Ćurković et al., 1997; Li et al., 2019a)* were studied for their exchange capabilities. Clinoptilolite consists of SiO_2 and AlO_4 tetrahedra, with Al^{3+} positioned in the centre. By replacement of Al^{3+} with Si^{4+}, one negative charge is created in the lattice. However, other cations in solutions or wastewater can replace the deficiency. Investigations showed that clinoptilolite is particularly useful for the exchange with Pb^{2+} *(Li et al., 2019a)* and thus can selectively bind Pb^{2+} to the structure. In addition, other heavy metal ions (Zn^{2+}, Cd^{2+}, Cu^{2+}) can be removed by ion exchange depending on the pH, the solid/liquid ratio and competitive heavy metal cations *(Li et al., 2019a)*. Tests with natural and synthetic zeolites used in the metal finishing industry to remove heavy metal cations show that the sorption capacity of synthetic zeolites is about ten times higher than that of natural zeolites *(Álvarez-Ayuso et al., 2003)*.

Indications: Ion exchange is an established purification method for heavy metal-bearing wastewater. The exchange resins are partly ion-selective, but treating multi-element wastewater is still challenging due to the remobilisation of metal cations. Parameters like pH, contact time, and dosage must be adjusted to ensure effective purification. Furthermore, prolonged contact time slows down the process. Ion exchange enables the concentration of heavy metal-rich solutions, but the concentrate is often treated with chemical precipitation afterwards. Treatment of large volumes of low-concentration wastewater with ion exchange is not cost-effective and is therefore not applied on a large scale *(Fu and Wang, 2011)*. Another problem is subsequent pollution caused by the regeneration of used ion exchange resins with chemical reagents. After the ion exchange capacity is reached, the resins are either disposed of or incinerated *(Dietrich, 2017)*.

2.1.4. Adsorption

The principle of binding atoms or compounds to a solid phase's surface by adhesion is called adsorption. Physical adsorption processes are mostly reversible because desorption can regenerate the adsorbents. Finding new efficient adsorption materials has recently been the

focus of research, as they offer an effective method for treating heavy metal-bearing wastewater *(Fu and Wang, 2011)*.

One standard adsorbent is activated carbon (AC) because of its large surface area created by large micro- and mesopores *(Fu and Wang, 2011)*. It is, therefore, often used in wastewater treatment. However, commercial coal-based AC is generally expensive, and prices are constantly rising *(Fu and Wang, 2011; Hegazi, 2013)*. Therefore, several materials are proposed as alternatives for AC. Cheap and readily available agricultural wastes, like rice husk *(Hegazi, 2013)*, coconut shell *(Bernard et al., 2013)*, honeydew melon peel *(Yunus et al., 2020)*, groundnut shell, Indian beech and onion skin *(Vinaykumar et al., 2019)* were investigated to remove Ni^{2+} *(Hegazi, 2013)*, Cu^{2+} *(Bernard et al., 2013)*, Fe^{2+}, Pb^{2+} *(Bernard et al., 2013; Hegazi, 2013)*, Zn^{2+} *(Bernard et al., 2013; Yunus et al., 2020)*, Cr^{3+} *(Yunus et al., 2020)*, and Cd^{2+} *(Vinaykumar et al., 2019)* ions from electroplating wastewater. The activation of the alternative carbon sources is achieved either by pre-treatment with chemicals like zinc chloride *(Bernard et al., 2013)* or acids like H_2SO_4 and H_3PO_4 in combination with high-temperature carbonisation *(Yunus et al., 2020)* and final grinding and sieving *(Vinaykumar et al., 2019)*. The adsorption capacity strongly depends on the adsorbent dosage, contact time, pH and stirring rate *(Bernard et al., 2013)*. For example, coconut shell-based activated carbon has the highest removal rates: 93.37% for Fe, 92.22% for Cu, 60.52% for Zn and 100% for Pb *(Bernard et al., 2013)*.

In another approach, electroplating sludge and calcinated electroplating sludge were tested as adsorbents for Ni^{2+} in electroplating wastewater *(Peng et al., 2020)*. The adsorption capacity achieved for the electroplating and calcinated sludge was 135.7 and 118.3 mg/g Ni^{2+}, higher than some commercially available adsorbents *(Peng et al., 2020)*.

Another example of wastewater treatment with materials to be disposed of is the usage of drinking water treatment residual (DWTR) for the adsorption of metals. Coagulants like alum, iron (III) chloride or iron (III) sulfate are used to remove particles and dissolved materials from water. The resulting amorphous sludge consists mainly of Al, Fe oxyhydroxides and organic matter with functional groups on the surface, making them an adsorbent for various metals, including V, Ga, As, Se and B *(Shen et al., 2019)*. However, the application of DWTR has limitations, as industrial waste often contains toxins such as Hg and As, which can be released during the application *(Zhao et al., 2018; Shen et al., 2019)*. In addition, a recovery process for metals from DWTR has yet to be developed *(Shen et al., 2019)*.

Indications: Adsorption processes for removing heavy metals from aqueous solutions are practical but limited to low-concentrated wastewater. Conventional activated carbon is limited due to its high cost *(Fu and Wang, 2011)*. Recently, alternative adsorbents have been studied and shown promising results, but they will still need to be optimised regarding adsorption efficiency. Furthermore, activating alternative carbon adsorbents requires treatment with acids,

other chemicals, or carbonisation at high temperatures. For more information on industrial waste as a low-cost potential adsorbent, see *Ahmaruzzaman (2011)*. Refer to *Xu et al. (2015)* for developing and preparing sludge-based adsorbents.

2.1.5. Membrane filtration

Membrane filtration separates species in a solution by the selective transport of individual atoms or components through a membrane. Different procedures have been developed depending on the particle sizes to be separated. Microfiltration separates particles in the micro range, ultrafiltration for colloids, nanofiltration for macromolecules, and reverse osmosis for molecules and ions.

Since different particle sizes occur in the liquids of the surface coating industry, other membrane separation techniques are applied. In a review paper on membrane technology for the removal of heavy metals from wastewater, *Abdullah et al. (2019)* present the essential methods: (1) polymer-enhanced ultrafiltration (PEUF), (2) micellar-enhanced ultrafiltration (MEUF), (3) adsorptive ultrafiltration mixed matrix membranes (UF MMMs), (4) nanofiltration (NF), (5) reverse osmosis (RO), (6) forward osmosis (FO), (7) liquid membrane (LM), and (8) electrodialysis (ED). Usually, MEUF, PEUF and UF MMMs remove heavy metals from low-concentrated wastewater, while NF, RO and FO can be applied to highly concentrated wastewater.

The heavy metal-rich concentrates generated with membrane technologies, like concentrates from ion exchange, are finally treated with the central wastewater treatment plant of the industrial facility. After that, the spent membranes are disposed of in landfills or incinerated. In 2015, the global mass of spent RO membranes from the desalination industry was estimated to be 12 000 Mg, indicating the potential disposal problem *(Lawler et al., 2012)*.

2.1.5.1 Ultrafiltration

Ultrafiltration (UF) can remove colloids and dissolved materials. Membranes separate based on the membrane pore size and the molecular weight of the solutes *(Wenten et al., 2020)*. Since the pore sizes of UF membranes (ca. 0.01 µm) are 400 – 500 times larger than dissolved metal ions in the form of hydrated ions, these can pass through the membrane *(Abdullah et al., 2019)*. Therefore, improved UF processes such as PEUF, MEUF and UF MMMs have been developed to remove heavy metal ions from wastewater. For this purpose, heavy metals are bound to micelle compounds (MEUF) or charged groups to form large filterable complexes (PEUF, UF MMM).

2.1.5.2 Micellar-enhanced ultrafiltration (MEUF)

MEUF uses charged surfactants that form larger micelle agents by attachment; thus, membranes can retain them. The micelles show electrostatic forces and bind oppositely

charged metal ions or other compounds at the micellar surface *(Yusaf et al., 2019)*. Therefore, MEUF is applied to remove anions or cations from wastewater. The removal efficiency depends on the used surfactant, operating pressure, pH, and solution temperature *(Wenten et al., 2020)*. Micelle formation is only possible within a narrow concentration range of cationic or anionic surfactants, also called critical micelle concentration (CMC) *(Yusaf et al., 2019)*.

One problem is the subsequent contamination by high residual concentrations of non-aggregated surfactant in the permeate *(Abdullah et al., 2019)*. Additionally, the surfactant itself contributes to a large extent to the process costs *(Kim et al., 2006)*. Therefore, it is necessary to develop methods to separate metal ions from micelles and recover the surfactants. Three ways were tested to separate Cu and Cd from the surfactant: (1) acidification to a strongly acidic pH and subsequent UF, (2) complexation with the addition of the chelating agent EDTA followed by UF, and (3) precipitation of Cu and Cd by ferric- and ferrocyanide and surfactant recovery by subsequent centrifugation *(Kim et al., 2006)*. Centrifugation after complexation achieved the highest surfactant recovery with almost 100%.

2.1.5.3 Polymer-enhanced ultrafiltration (PEUF)

Polymer-enhanced ultrafiltration (PEUF), also called CEUF (complexation-enhanced UF), is based on the addition of water-soluble polymers with the chelating capability to the wastewater to form larger heavy metal complexes and thus prevents their passage through a microporous membrane *(Abdullah et al., 2019)*. The metal ions are electrostatically bound to the ligands of the polymers. The most frequently used complexing polymers are poly(acrylic) acids, carboxyl methylcellulose, and polyvinyl ethyleneimine *(Abdullah et al., 2019)*. The polymer adsorption depends on surface wettability, surface charge, and roughness *(Huang and Feng, 2019)*. A suitable polymer and a corresponding membrane are selected depending on the wastewater properties.

Acids or alkalis are needed to regenerate the polymers, making the process less environmentally friendly. A modified technique for electroplating wastewater provides a remedy *(Tang and Qiu, 2019)*. In a shear-induced dissociation coupled with ultrafiltration, the metals (Zn^{2+}, Cu^{2+}, Ni^{2+}, Cr^{3+}, and Fe^{3+}) are selectively bound by a complexing agent and then separated from the complexant by dissociation of metal-polymer complexes.

Even though PEUF has developed since the 1960s, most studies are conducted on a lab- or pilot scale. The main challenges that restrict PEUF from large-scale applications are (1) the regeneration of the polymers for reuse, (2) the low metal concentration recovered from the polymer, and (3) the decline in water flux caused by polymer deposition on the membrane surface or in the pores *(Huang and Feng, 2019)*. Another limitation is the narrow range of critical surfactant concentration for optimal treatment to avoid poor removal rates *(Abdullah et*

al., 2019). Waste ligands, micelles, and other harmful products can accumulate *(Abdullah et al., 2019)*.

2.1.5.4 UF adsorptive mixed matrix membranes (UF MMMs)

In recent years, adsorptive mixed metal membranes (MMM) have been studied primarily for solutions containing low heavy metal concentrations *(Abdullah et al., 2019)*. The great advantage of MMMs is their independence from chemicals to remove heavy metal ions from solutions. Nanoparticles are added to the membrane matrix to improve the physicochemical properties of the membranes for better removal efficiency *(Abdullah et al., 2019)*. However, membrane thickness, pressure and leaching of the nanomaterials in the treated water can limit the process *(Abdullah et al., 2019)*. Effective adsorption depends on the optimal thickness of the membrane. Possible leaching of nanoparticles from MMMs carries the risk of toxic secondary pollutants. Therefore, the number of nanomaterials added to the MMM must be determined to keep leaching processes minimal *(Abdullah et al., 2019)*.

2.1.5.5 Nanofiltration

Membranes for nanofiltration (NF) are thin-film composites of synthetic polymers containing charged groups *(Al-Rashdi et al., 2013)*. The pore sizes are small enough to separate metallic ions. Modified membranes are required to remove metal ions effectively *(Abdullah et al., 2019)*. The separation of metals by nanofiltration is complex and driven by the charged groups, solution diffusion, dielectric exclusion, electromigration, and the Donnan effect *(Al-Rashdi et al., 2013)*, which describes an unequal distribution of permeable ions between two sides of a membrane. The properties of the membranes, i.e., the surface charge and the pore size, are pH dependent, making the pH of the wastewater a controlling parameter for the separation capacity of NF membranes *(Al-Rashdi et al., 2013)*.

For electroplating wastewater treatment, NF membranes were prepared using two different preparation techniques (cast and spray), and cast membranes were found to be less porous, making them more suitable for metal retention *(Boricha and Murthy, 2009)*. As a result, the maximum retention capacity for cast membranes was 94% for Zn and 93% for Fe *(Boricha and Murthy, 2009)*.

2.1.5.6 Reverse osmosis

In a normal osmosis process, a solvent flows from an area with a low solute concentration (high water potential) to an area with a high solute concentration (low water potential). Reverse osmosis (RO) is a diffusion-controlled process which runs in the opposite direction by applying pressure to force water molecules to move against the concentration gradient *(Abdullah et al., 2019)*RO membranes are very dense and semi-permeable, enabling high retention rates for heavy metals. Accordingly, RO can be applied to produce highly purified water.

Indications: In general, the use of energy-intensive membrane technologies in industrial applications is restricted by high costs, process complexity, membrane fouling and low permeate flux *(Fu and Wang, 2011)*.

2.1.6. Coagulation and flocculation

Colloidal particles carry surface charges that repel each other and hinder the particles from settling. The addition of chemicals destabilises colloids in wastewater and promotes the coagulation of compounds to larger aggregates. The added coagulants, e.g., alum, polyaluminium chloride (PAC), ferric chloride, or hydrated lime *(Pang et al., 2011)*, carry the opposite charge to the colloids to neutralise the repulsive effect.

Flocculation is a process which enables the contact and adhesion between colloids to form larger aggregates. As a result, flocculants enhance particles' sedimentation rate and thus accelerate the sludge's sedimentation process. Many different flocculants exist on the market, e.g., PAC, poly ferric sulfate (PFS), or polyacrylamide (PAM) *(Fu and Wang, 2011)*.

The removal efficiency of heavy metals by coagulation-flocculation depends on the type and dosage of the used coagulant, pH, and concentration of metal ions *(Pang et al., 2011)*. Coagulation-flocculation has a reduced separation efficiency for multi-element wastewater compared to single-metal wastewater *(Pang et al., 2011)*. Coagulation-flocculation generally cannot altogether remove heavy metals *(Fu and Wang, 2011; Pang et al., 2011)*. Therefore, coagulation-flocculation is combined with other treatment techniques to obliterate heavy metals. In addition to the high input of chemicals, coagulation-flocculation contributes to an increased sludge volume *(Fu and Wang, 2011)*.

2.1.7. Flotation

Flotation processes separate particles by surface properties *(Al-Zoubi et al., 2015)*. For example, heavy metals are separated from the liquid phase by attaching hydrophobic particles to air bubbles that rise to the surface *(Al-Zoubi et al., 2015)*. The most effective flotation process for heavy metal-bearing wastewater is dissolved air flotation (DAF) because it can separate light and small suspended particles *(Al-Zoubi et al., 2015)*. The DAF process uses collectors to selectively adsorb onto the surface of specific minerals and form a monolayer of non-polar hydrophobic hydrocarbons *(Al-Zoubi et al., 2015; Liu et al., 2017)*. Flotation shows a high removal efficiency and is partly metal selective, but it is rarely applied in industrial applications, as it requires high initial capital costs and high maintenance *(Fu and Wang, 2011)*.

2.1.8. Electrochemical treatment methods

All electrochemical wastewater treatment techniques are based on an electrical current set to the wastewater via electrodes. In principle, it is the same process used in electroplating facilities for surface plating with metal. However, electrochemical techniques for the purification of

heavy metal-bearing wastewater are getting more and more attention because they do not need high temperatures and pressures and use fewer chemicals. In addition, the process is robust and easily controlled *(Tran et al., 2017)*. Electrodeposition is the most frequently applied method among electrochemical treatment techniques and enables the deposition of zero-valent metals onto the cathode *(Fu and Wang, 2011)*. Metal deposition can be achieved on simple plate electrodes for medium (100 mg/l) to highly concentrated wastewater (g/l). However, removal efficiency is reduced with decreasing metal cation concentrations since the current efficiency of simple plate electrodes also decreases. Therefore, residual concentrations of heavy metal cations remain in the electrochemically treated wastewater and have to be removed otherwise, e.g., by ion exchange. Newly developed substrate materials try to solve this process limiting factor. A low-cost and non-toxic material discussed as a substrate is hydrotalcite-like compounds (layered double hydroxides) *(González et al., 2015)*. In a lab-scale study using ZnAl-CO_3 and MgAl-H hydrotalcite as substrate, 75% Cd^{2+} and almost 100% Pb^{2+} were removed from the aqueous solution *(González et al., 2015)*. Pilot-scale experiments combining adsorption and electrodeposition were conducted to remove Ni^{2+} from real electroplating wastewater *(Li et al., 2019b)*. First, the Ni^{2+} ions were concentrated by adsorption with a commercially available cation-exchange resin, and then the regenerate solution (> 30 g/l) was reduced to Ni sheet metals by electrodeposition.

Indications: Due to significant capital investment and expensive electricity supply, electrochemical treatment methods have not been widely installed for water purification *(Fu and Wang, 2011)*.

2.2. Recovery potential of metals in residues from the electroplating industry

In recent years, the recovery of heavy metals from wastes has gained increasing importance, mainly in extracting metals like Co or V, which are classified as critical raw materials. Hydroxide precipitation is the most applied treatment technique for heavy metal-bearing wastewater, and the resulting metal-containing sludges are usually disposed of in hazardous landfills. Therefore, the question arises as to what extent these sludges are a source of metal recovery.

The recovery potential of raw materials in wastes, and in this case, from sludges from electroplating wastewater treatment, can be derived from the amount of waste produced per year and the concentration of specific elements. In Europe, all waste is classified according to the European Waste Catalogue (EWC), which lists the industrial sector and sector-typical processes (EWC codes). However, the recovery potential of raw materials from the waste cannot be calculated directly from the EWC database as this classification does not consider the waste's chemical composition *(Heuss-Aßbichler et al., 2016a)*.

In Germany, 418 700 Mg of waste were treated in 2017, according to EWC 11 01 09* "sludges and filter cakes containing heavy metals" *(Statistisches Bundesamt, 2019)*. *Figure 2.3* shows the quantities of deposited and treated waste: A large proportion of it, 360 400 Mg, underwent physicochemical processes *(Statistisches Bundesamt, 2019)*. In addition, 22 200 Mg of waste went directly to landfills, 34 300 Mg of waste were treated with other methods, and 1 800 Mg of waste was thermally treated. Of the total waste volume, only 5 200 Mg were recycled, corresponding to a recycling rate of 1%. For 2013, a correspondingly low recycling rate of 3% was calculated *(Heuss-Aßbichler et al., 2016a)*.

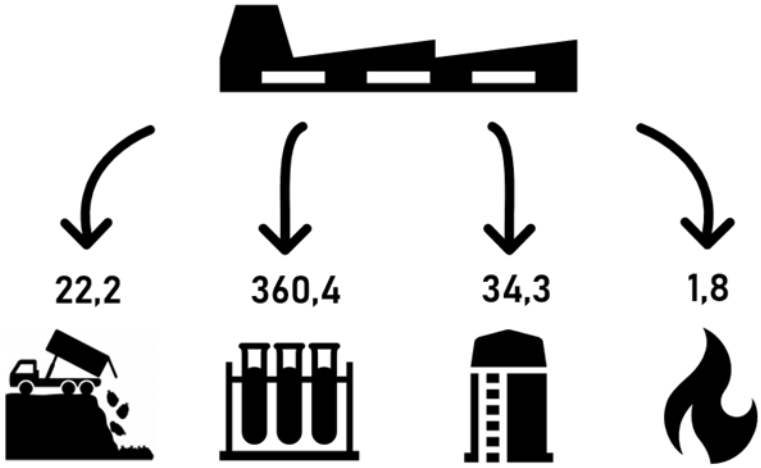

Figure 2.3: *Proportion of sludges deposited and treated in Germany in 2017 according to EWC 11 01 09* in 1 000 Mg, after* Statistisches Bundesamt (2019). *From left to right: 22 200 Mg of waste were directly landfilled, 360 400 Mg were treated with physicochemical processes, 34 300 Mg were treated with other process methods, and 1 800 Mg were thermally treated.*

The German Federal Environmental Agency published the chemical composition of random samples in 2016 based on the Waste Analysis Data Base (ABANDA) results from random samples of industrial companies that participated voluntarily *(Dehoust et al., 2016)*. The average metal concentrations found in waste 11 01 09* for the years 2010 and 2011 were for Fe 58.823 mg/kg, Zn 53.773 mg/kg, Cu 40.458 mg/kg, Ni 35.868 mg/kg, Al 27.855 mg/kg, Cr 27.355 mg/kg, Sn 19.677 mg/kg, Pb 10.000 mg/kg, Mn 1.430 mg/kg and for Pb, Sb, Co, Mo, V and W 1.000 mg/kg each *(Dehoust et al., 2016)*. Due to etching, the amount of Fe found in the sludges arises mainly from the Fe-containing substrate. Compared to all other listed wastes, waste 11 01 09* owns the highest concentration of Sn and the second highest concentration of Cr *(Dehoust et al., 2016)*. It should be emphasised that the values are based on random samples and, therefore, not representative.

Figure 2.4 shows the amount of metals dissipated in 2011, calculated as the product of the mean value of metal concentrations and the landfilled waste (20 200 Mg) according to EWC 11 01 09* *(Statistisches Bundesamt, 2013)*. The values serve only for orientation because the exact quantity behind the analysis is unknown. Accordingly, the following amounts were

removed from the material cycle: Fe (1 188.2 Mg/a), Zn (1 086.2 Mg/a), Cu (817.3 Mg/a), Ni (724.5 Mg/a), Al (562.7 Mg/a), Cr 552.6 Mg/a, Sn 397.5 Mg/a and Mn 28.9 Mg/a *(Statistisches Bundesamt, 2013)*.

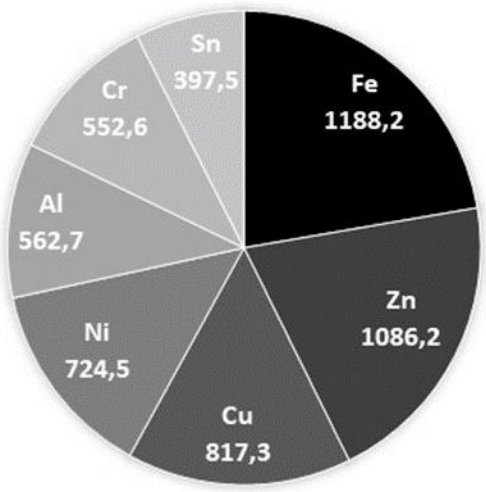

Figure 2.4: *Quantity of metals (Mg/a) determined for waste EWC 11 01 09* based on the proportion of waste going to landfill (20 200 Mg), after* Statistisches Bundesamt (2013); Umweltbundesamt et al. (2016).

Using these values and based on the scrap prices of *Springer & Sohn GmbH (2020)*, a rough estimate of the economic potential of waste 11 01 09* results in a loss of EUR 3.02 million for Cu, EUR 3.98 million for Ni, EUR 1.03 million for Zn, and EUR 1.7 million for Sn. However, the metal concentrations and economic loss for individual companies might be much higher. For example, a survey amongst ten companies in the electroplating or smelting industry resulted in higher concentrations of 2 000 Mg/a for Cu and 5 300 Mg/a for Ni *(Heuss-Aßbichler et al., 2016a)*. It was also observed that wastes from numerous minor surface processing and coating companies are particularly suitable for recycling because they contain more metals *(Dehoust et al., 2016)*. However, the total generated waste per company is relatively small *(Dehoust et al., 2016)*.

It should be noted that companies must pay for the transport of neutralised sludge from the emitter to the waste treatment facilities or landfills. Prices range from 100 to 200 €/t depending on total volume, metal content (recycling capability/toxicity), and transport distance *(Heuss-Aßbichler et al., 2016a)*.

In general, waste recycling becomes interesting when the concentrations of the metals are in the range of concentrations found in ores. *Table 2.2* summarises the lower limit of the typical profitability of a resource in ore for the metals Cr, Cu, Fe, Ni, Pb, Sn, and Zn compared to the concentrations in sludges and filter cakes of waste 11 01 09* *(Dehoust et al., 2016)*. Accordingly, in 2016, the marketability of the waste is fulfilled for the following metals: Cr

(265 469 ppm in sludge), Ni (36 922 ppm in sludge, 6 315 ppm in filter cake) and Zn (114 100 ppm in filter cake).

Table 2.2: *Comparison of metal concentrations determined in waste EWC 11 01 09* and their typical commercial viability based on the data of* Dehoust et al. (2016).

	Cr	**Cu**	**Fe**	**Ni**	**Pb**	**Sn**	**Zn**
				ppm			
profitability of the ore	35 000	4 000	350 000	4 000	40 000	25 000	50 000
11 01 09* sludge	265 469	42	38 742	36 922	25	50	50
11 01 09* filter cake	11 353	87	132 257	6 315	1 646	50	114 100

2.3. Conclusion

In recent years, awareness of the loss of heavy metals as valuable materials with waste has increased, leading to the concept of urban mining and waste as an anthropogenic resource. The recovery of heavy metals from waste is politically demanded. Considering waste as a resource is a key element of a circular economy, which the European Commission addressed in its 7th Environment Action Programme, which was elaborated in 2015. Reuse and recycling are essential to keep metals in the cycle of matter. Landfilling is, therefore, the least favourable option in the waste hierarchy. It was also recognised that obligatory measures are needed to encourage innovation in recycling techniques and to enable efficient metal recovery. To this end, discussions will include whether the limit values for metals in waste going to landfills should be lowered and whether molybdenum (Mo) should be added to the list *(Dehoust et al., 2016)*.

In the case of wastewater, the focus over the last 70 years has been on purifying the water. Accordingly, the treatment processes aimed to bind or discharge the heavy metals and safely dispose of the hazardous sludge. The analysis of waste under the EWC code 11 01 09* showed that most sludges with higher heavy metal content are landfilled *(Dehoust et al., 2016)*. Most of the treatment methods presented in this chapter are designed for wastewater treatment and are generally unsuitable for recycling. Novel treatment methods like SPOP are promising and should be brought to an industrial scale to reuse the heavy metals in the wastewater as raw materials for producing materials. Such a solution requires a conceptual rethink: treatment should not be carried out with centrally collected multi-element wastewater but directly at the source of wastewater production to achieve the highest possible quality of product phases with high purity.

3. The SPOP process and development of a pilot facility

The Specific Product-Oriented Precipitation (SPOP) process was developed as an alternative low-energy concept to purify wastewater and synthesise nanoparticles while recovering the metal ions in the solution. The following chapter presents the principle of SPOP (Chapter 3.1), describes the mineral precipitation products (Chapter 3.2) and explains the laboratory experimental set-up up to 250 ml solution (Chapter 3.3). Chapter 3.4 presents the state of the art of the SPOP results; it represents the basis for the designed pilot facility to treat wastewater with a 1-litre batch reactor in a sequential mode. The pilot facility and its system are summarised in Chapter 3.5.

3.1. Principle of the SPOP process

The SPOP is a new precipitation method with low energy consumption that follows the circular economy principle and a "no-waste" mindset *(Heuss-Aßbichler et al., 2016c; Heuss-Aßbichler and Anagnostopoulos, 2021). Figure 3.1* shows the two goals: (1) An effective wastewater treatment - the water quality should meet the limits for discharge concerning heavy metal concentration; this enables the purified wastewater to be reused or discharged into surface water. (2) Efficient recovery of heavy metals as a secondary raw material such that they are available for new applications.

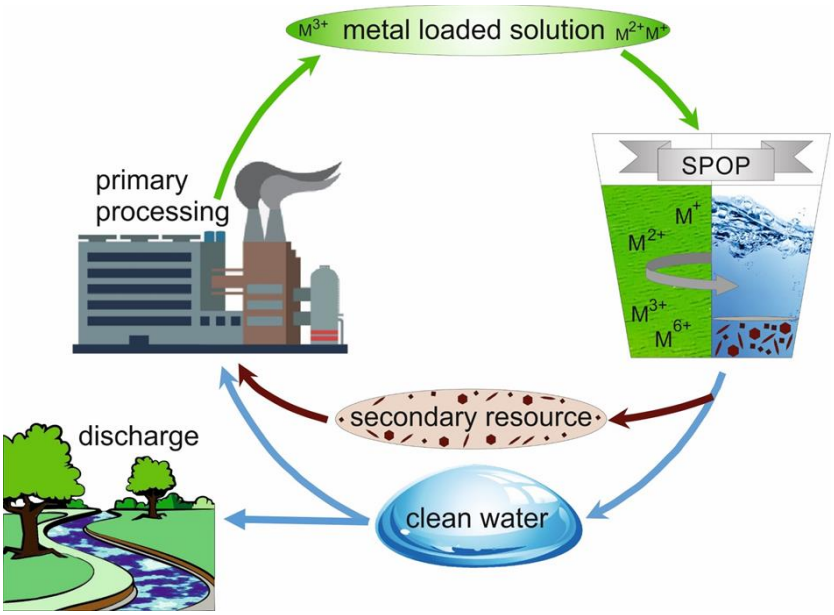

Figure 3.1: *The principle of the SPOP process is designed according to the demands of the circular economy. The aims are to purify the wastewater and recover the heavy metals as secondary raw materials.*

The SPOP process was inspired by the ferrite process, which was developed to treat low-concentrated laboratory wastewaters by binding the heavy metals in ferrites and using their magnetic properties for separation (see Chapter 2.1.2.4). The results showed that the ferrite

process could be modified to relinquish the active introduction of oxygen. Furthermore, Fe-salts' quantity was reduced, and other Fe-bearing phases, e.g., delafossite, can be synthesised *(John et al., 2016a, 2016b, 2019)*. The results of this thesis extend the variability of the process.

Various wastewaters with different non-ferrous target metals have been tested on the laboratory scale with the SPOP process. The results show that every metal requires a specific treatment procedure. Therefore, the SPOP process is no panacea, and the reaction parameters must be controlled and adjusted to the individual wastewater properties. However, once the optimal reaction parameters are worked out, recovering metals from wastewater as a secondary resource, i.e., metal-oxides or zerovalent metals, is feasible.

3.2. Minerals precipitated with SPOP

The recovery of metals from wastewater as either oxides or zero-valent metals by hydrometallurgical processes has many benefits: (I) Compared to pyrometallurgical methods, zerovalent metal or oxide precipitation can be achieved with less energy consumption. (II) The recovered heavy metal-bearing oxides can be used in industry for various applications and can, in the best case, be used directly as a product. (III) No waste is created because compared to heavy-metal hydroxides, oxides are less voluminous; in consequence, the disposal of such sludges as toxic waste can be avoided.

In this thesis, the results obtained with copper-rich wastewater priority were given. Therefore, this chapter presents the structure and application of the oxides in the Cu-Fe-S-O-H system: ferrite, maghemite, delafossite, tenorite and cuprite. In addition, the hydroxides spertiniite and brochantite are presented.

3.2.1. Ferrite and Maghemite

Ferrite and maghemite are spinels. Spinels are minerals with the general formula AB_2O_4, which crystallise in a cubic crystal system, in which 32 oxygen anions form an fcc closed packed cubic lattice and the cations A and B occupy the octahedral and tetrahedral sites in the lattice. One unit cell consists of 8 fcc cells. In the prototypical spinel structure, the A cation is divalent, and the B cation is trivalent ($A^{2+}B_2{}^{3+}O_4$). The spinel structure can incorporate many divalent cations, e.g., Fe^{2+}, Cu^{2+}, Zn^{2+}, Ni^{2+} and trivalent cations, e.g., Fe^{3+}, Al^{3+}, and Cr^{3+} resulting in solid solutions. Spinels which contain Fe are generally called ferrites with the general formula $M^{2+}Fe_2O_4$. The Fe endmember of ferrites is magnetite ($Fe^{2+}Fe^{3+}{}_2O_4$), but, e.g., Cu can be incorporated into the structure, forming cuprospinel ($Cu^{2+}Fe^{3+}O_2$).

Two types of spinel structures have to be distinguished, the normal and the inverse spinel: In a normal spinel ($A^{2+}B^{3+}{}_2O_4$), the cations of the A and B positions are tetrahedrally and octahedrally coordinated. The A-site cations occupy 1/8 of the tetrahedral sites, and the B-site cations occupy ½ of the octahedral sites. On the other hand, in the inverse spinel crystal

structure, the A-site cations occupy ¼ of the octahedral sites, one-half of the B-site cations occupy 1/8 of tetrahedral sites, and the other half occupy ¼ of octahedral sites ($B^{3+}(A^{2+}B^{3+})O_4$).

Figure 3.2a shows an inverse spinel structure, as in the case of magnetite ($Fe^{3+}(Fe^{2+}Fe^{3+})O_4$) or cuprospinel ($Fe^{3+}(Cu^{2+}Fe^{3+})O_4$). The A site cations, Fe^{2+} or Cu^{2+}, occupy ¼ of the octahedral sites, half of the Fe^{3+} cations occupy 1/8 of the tetrahedral sites, and the other half occupies ¼ of the octahedral sites. Maghemite can be considered a Fe^{2+}-deficient magnetite; all Fe is in a trivalent oxidation state. The charge neutrality in the maghemite's spinel structure is kept by vacancies on the octahedrally coordinated cation sites so that the formula of maghemite is summed up to $(Fe^{3+}_{0.67}\square_{0.33})Fe^{3+}_2O_4$, where □ represents a vacancy in the structure. The position of these vacancies can vary; therefore, the structure of maghemite is reported in different space groups *(Andersen et al., 2021)*. *Figure 3.2b* shows one possible structural configuration of maghemite in space group $P4_132$ with two different octahedral sites and vacancies on exclusively one of them.

At ambient conditions, magnetite is stable, while maghemite is metastable and transforms to hematite. Magnetite occurs as a primary mineral in many natural rock assemblages. In comparison, maghemite is a secondary mineral generated by the low-temperature oxidation of magnetite.

In practice, it isn't easy to distinguish between magnetite and maghemite by X-ray diffraction because they have the same spinel structure and almost identical lattice parameters. The only difference is that maghemite shows two additional but weak diffraction maxima at 23.7 °2θ and 26.1 °2θ, which refer to the lattice planes (210) and (211) respectively *(Kim et al., 2012; Andersen et al., 2021)*. The type and distribution of cations at tetrahedral and octahedral sites significantly affect the ferrites' physical and chemical properties. In particular, their magnetic and electronic properties are attractive for industrial applications. For example, ferrite nanoparticles are used in electronic devices, e.g., as humidity/gas sensors *(Srivastava and Yadav, 2012)*, as catalysts in biomedical applications *(Sanpo et al., 2013)*, or in wastewater treatment *(Kefeni et al., 2017a)*. On the other hand, maghemite is primarily used for spin electronic devices, high-density magnetic recording, nanomedicines and biosensors *(Shokrollahi, 2017)*. Consequently, ferrites have gained increasing scientific interest, and new applications are developed hand in hand with new synthesis methods to control these properties. The methods include, e.g., hydrothermal techniques, sol-gel-method, thermal decomposition, and electrochemical synthesis *(Kefeni et al., 2017b)*. One of the most frequently used synthesis methods is co-precipitation.

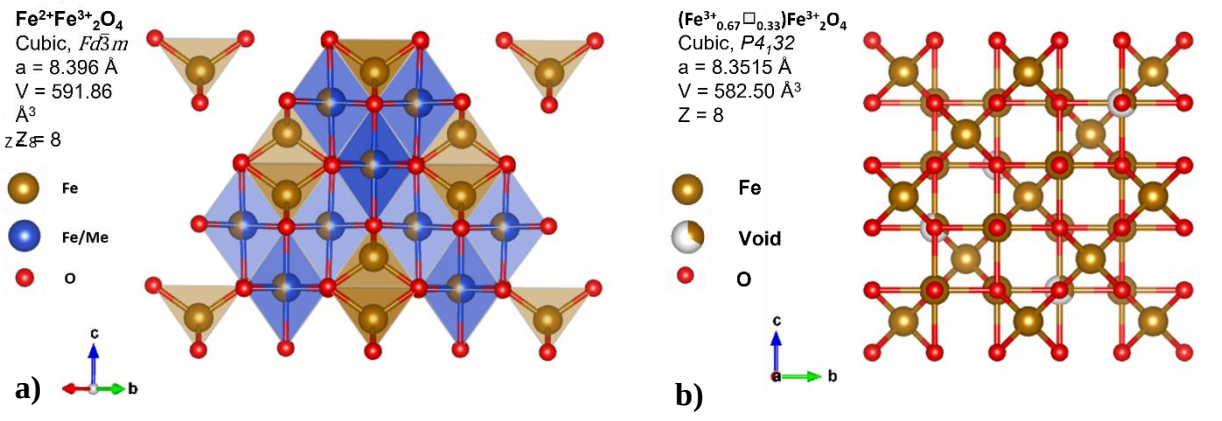

Figure 3.2: *The ferrite structure. Each unit cell consists of 8 fcc cells with 32 oxygen anions and 24 cations, of which eight are four-fold coordinated (tetrahedral sites = brown), and 16 are six-fold coordinated (octahedral sites = blue). In a), the inverse spinel structure of magnetite is shown. The A site cations (blue) occupy ¼ of the octahedral sites, half of the B site cations (brown) occupy 1/8 of the tetrahedral sites, and the other half occupy ¼ of the octahedral sites. Colour intensity corresponds with the relative position along the c-axis perpendicular to the page surface. In b), the structure of maghemite in the space group $P4_132$ is shown with two different octahedral sites and vacancies on exclusively one of them. Plotted with VESTA* (Momma and Izumi, 2011) *after entries a) 9012438* (Verwey and Heilmann, 1947) *and b) 9006317* (Pecharromfin et al., 1995) *of the Crystallography Open Database.*

3.2.2. Delafossite

In nature, delafossite ($Cu^{1+}Fe^{3+}O_2$) is a rare secondary oxide formed from ternary sulfide alteration. Accordingly, it is observed near the base of the oxidised zone of Cu deposits *(Marquardt et al., 2006)*. In Eh-pH diagrams, calculated by the so-called line method approximation, the stability field of delafossite does not appear *(Aquino et al., 2020)*. Recently, point-to-point mass balance diagrams in the Cu-Fe-S-O-H system were computed, showing the system's dependency on the metal-to-sulfur ratio and the temperature *(Aquino et al., 2020)*. In contrast to the previous Eh-pH diagrams for the Cu-Fe-S-O-H system, their results show a large stability field of delafossite under oxidising conditions. This theoretical model gives a new perspective on the formation of delafossite and can be used to synthesise this mineral.

The general formular of delafossite is $A^{1+}B^{3+}O_2$. The A-site cations are monovalent (e.g., Cu^{1+}), and the B-site cations are in a trivalent state (e.g., Fe^{3+}). Like spinel, delafossite forms solid solutions by incorporating different metals at the structure's sites. Typical A-site metals are Cu, Pd, Pt or Ag, while typical B-site metals are *p*-block metals like Fe, Co and Y *(Marquardt et al., 2006)*. As shown in *Figure 3.3*, the delafossite structure comprises two alternating layers with linearly coordinated A-site cations connected with a distorted edge-shared $B^{3+}O_6$ octahedra layer. Delafossite consists of two polytypes, depending on the orientation of the stacking sequence of the layers. The hexagonal 2H type consists of a stacking sequence of B-layers alternating with A-layers aligned at 180° to each other. The rhombohedral

3R type is created when the B-layers and A-layer stacking occur in the same direction, resulting in a three-layer sequence *(Marquardt et al., 2006)*.

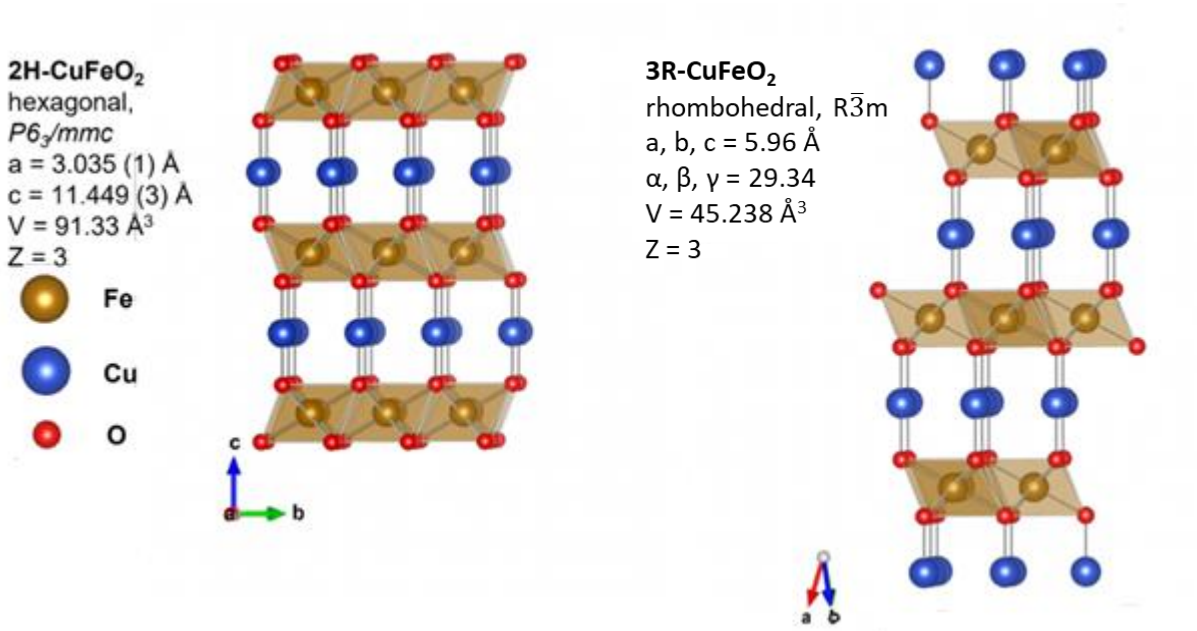

Figure 3.3: *Crystallographic structure of 2H-Cu-delafossite and 3R-Cu-delafossite. Plotted with VESTA* (Momma and Izumi, 2011) *2H-$CuFeO_2$ after entry 2020230* (Effenberger, 1991) *and 3R-$CuFeO_2$ after entry 9000015* (Pabst, 1938) *of the COD.*

Phases with delafossite structures are of technical importance due to their interesting optical and conductive properties. As for ferrites, the delafossites' properties vary with their compositional properties, and different synthesis techniques have been developed. For example, Cu-Cr-O delafossite is investigated as a p-type transparent conductive oxide, which is used in several applications like flat panel displays, smart windows, or functional glasses *(Moreira et al., 2022)*. Solid-state reactions of delafossite at high temperatures (1000 °C) are well-investigated *(Sukeshini et al., 2000; Choi et al., 2009; Amrute et al., 2013)*. Delafossite thin films are synthesised via pulsed laser deposition at high temperatures and pressures *(Sadik et al., 2009; Joshi et al., 2015)* and sol-gel methods at temperatures around 700 °C *(Wang et al., 2011; Prévot et al., 2015)*. Hydrothermal synthesis procedures have been carried out at elevated temperatures and pressures and using mineralisation agents to change the solubility of reactants *(Sheets et al., 2006)*. During the last decade, low-temperature hydrothermal methods at 100 °C were developed to synthesise $CuFeO_2$ within 12 h *(Xiong et al., 2015)* and $CuCoO_2$ within 24 h *(Du et al., 2018)*. Yet, *John et al. (2016b)* synthesised delafossite at temperatures of 70 °C within 24 °C without applying any additional reducing agent using the SPOP methodology. It is the lowest reaction temperature published so far.

3.2.3. Tenorite and cuprite

Cuprite (Cu_2O) and tenorite (CuO) are secondary minerals formed by the oxidation of Cu-sulfide minerals.

The oxygen atoms form a bcc structure in cuprite, as shown in *Figure 3.4*. Each oxygen is tetrahedrally coordinated with 4 Cu atoms, resulting in a linear coordination of Cu with two oxygen atoms. Cuprite is one of the oldest semiconducting materials *(Grondahl and Lsborofory, 1933)*. It is a p-type semiconductor with a direct band gap and has many potential applications, e.g., in solar energy conversion, electrode materials, sensors and catalysis *(Ma et al., 2008)*. It is also used in electrocatalytic applications, e.g., as a catalyst for hydrogen production by water splitting, which is currently being pursued as a promising route for converting renewable energies *(Zhang et al., 2017)*.

In tenorite, the Cu is divalent. Therefore, the oxygen anions are tetrahedrally coordinated, and the Cu cation is square planar coordinated. In this structure, chains of CuO_4 are edge-linked and angled so that two other oxygen atoms are near the Cu cation. One can alternatively describe it as an elongated octahedral coordination. Tenorite is also a semiconductor material and has applications in batteries, supercapacitors, solar cells, gas sensors, biosensors, catalysis, and the removal of arsenic from wastewater *(Zhang et al., 2014)*. Typical synthesis methods are hydrothermal, solid-state thermal conversion of precursors, electrochemical, and thermal oxidation *(Zhang et al., 2014)*.

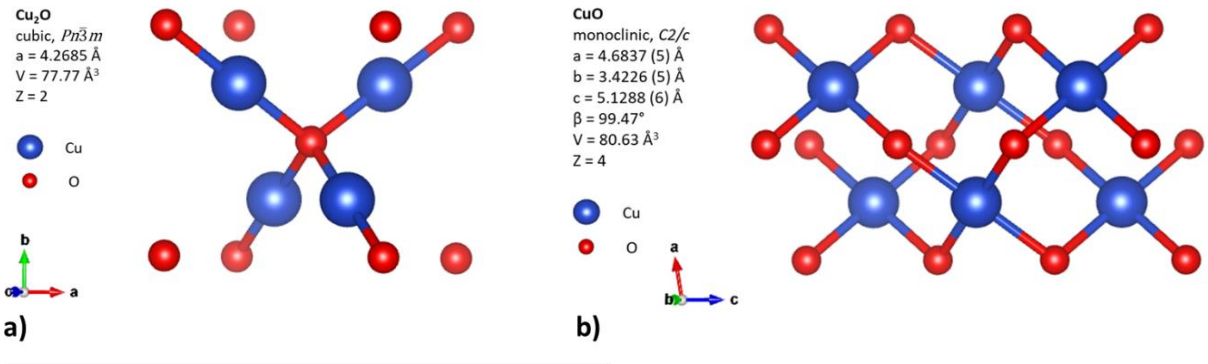

Figure 3.4: *Crystal structures of a) cuprite and b) tenorite. Plotted with VESTA* (Momma and Izumi, 2011) *after entries a) 9007497* (Kirfel and Eichhorn, 1990) *and b) 9008961* (Wyckoff, 1963) *of the COD.*

3.2.4. Spertiniite

Spertiniite ($Cu(OH)_2$) is a metastable hydroxide which quickly transforms into CuO. In spertiniite, Cu is divalent. *Figure 3.5* shows the structure of the spertiniite. It consists of corrugated layers of tetrahedra perpendicular to the b-axis, where Cu is decentred and surrounded by five OH^- ions *(Cudennec and Lecerf, 2003)*.

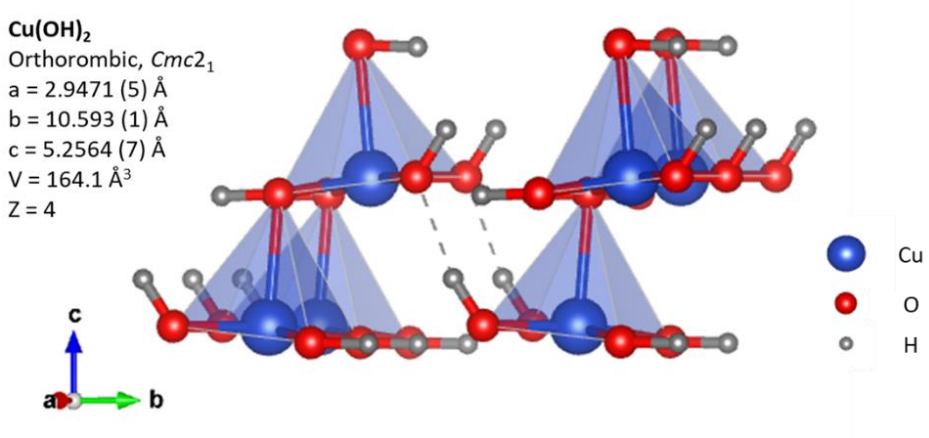

Figure 3.5: *Crystal structure of spertiniite. Corrugated layers of tetrahedra are perpendicular to the b-axis. Plotted with VESTA* (Momma and Izumi, 2011) *after COD entry 9007849* (Oswald et al., 1990).

Spertiniite has few technological applications. However, *Naveenkumar et al. (2018)* have shown that $CuS/Cu(OH)_2$ nanocomposite electrodes are promising for supercapacitor applications. Furthermore, spertiniite has been studied in water treatment as an adsorbent on membranes for reverse osmosis to prevent biofouling of the membranes, which is a significant obstacle to a broader application of this method *(Karkhanechi et al., 2013)*. In the present thesis, spertiniite serves as a metastable precursor for CuO.

3.2.5. Brochantite

Brochantite ($Cu_4(OH)_6SO_4$) is an abundant secondary copper sulfate in the oxidation zone of copper deposits. It is also a corrosion product on manufactured objects like copper alloys *(Zittlau et al., 2013)*.

In brochantite, Cu is divalent. The structure consists of chains of edge-sharing Cu octahedra that build up a 2D network of corrugated planes *(Figure 3.6)*. Each unit cell consists of 4 formula units. The crystal structure of brochantite consists of equivalent layers. The different stacking of neighbouring layers leads to a series of disordered and ordered (polytypes) sequences, collectively called an order-disorder structure *(Merlino et al., 2003)*.

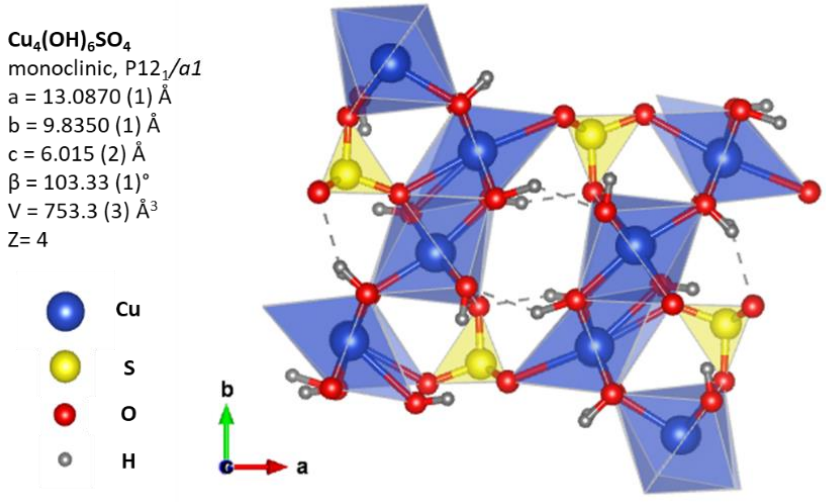

Figure 3.6: *Crystal structure of brochantite. Chains of edge-sharing Cu octahedra build up a 2D network of corrugated planes. Plotted with VESTA* (Momma and Izumi, 2011) *after COD entry 2006544* (Helliwell and Smith, 1997).

Brochantite is a precursor for CuO. It can affect CuO's shape and morphology as a precursor, thereby changing their functional properties. Dendrite-shaped brochantite is used as a precursor for platy CuO nanoparticles; such a shape increases the photocatalytic activity of CuO *(Novikova et al., 2016)*. The thermal treatment of tabular micro spindle brochantite leads to the formation of CuO micro spindles; such a CuO shows good performance as a gas sensor for ethanol and methanol detection *(Liu et al., 2012)*. Brochantite has been investigated as an activator for removing organic pollutants in wastewater with good results *(Dong et al., 2021)*.

3.3. Laboratory process

Figure 3.7 shows the experimental setup of the laboratory experiments. The metal-enriched aqueous solution is filled into a beaker (reaction vessel) and put on a heating plate. A thermocouple connected to the heating plate regulates the reaction temperature. The solution's pH (and later electric potential) is permanently measured during the experiment via electrodes *BlueLine 12 pH* and *BlueLine 31 RX* from *SI Analytics*. The electrodes are connected to an automated titration unit. Two different titrators, *TL 7000* and *TL 7800,* were used, both from *SI Analytics*. The titrator enables a precise addition of a base via a titration needle. It is connected to a computer where the alkalisation condition can be pre-set using the software *TitriSoft* from *SI Analytics.* The solution is continuously stirred during the experiment with an overhead stirrer *(Hei-TORQUE Precision 100, Heidolph Instruments)* and a blade agitator. After the precipitation, a fresh sample was taken by filtering the precipitate from the filtrate with a folded filter.

The suspension was altered at either room or reaction temperature in a closed or open vessel. At the end of the experiment, samples were washed three times with distilled water and dried before analysis. Finally, the residues were taken for mineral characterisation, and the filtrates were analysed regarding their residual metal content.

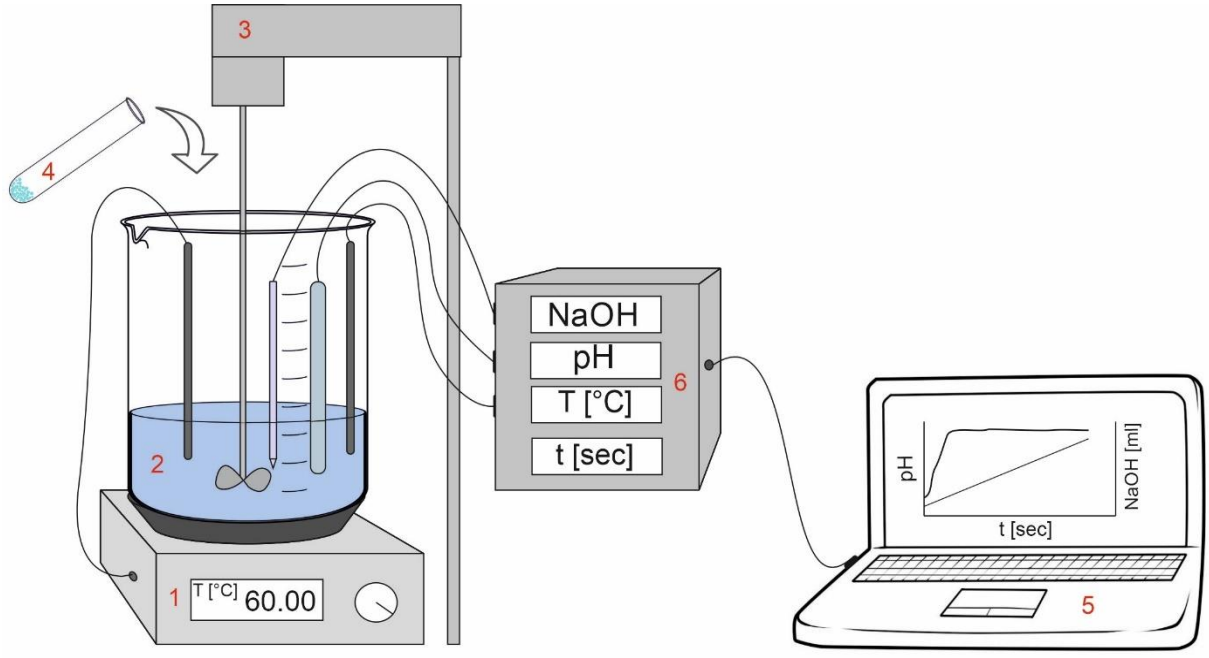

Figure 3.7: *Experimental setup of the lab experiments. On a heating plate (1), the (model or real) wastewater (2) is heated to reaction temperature under continuous stirring by an overhead stirrer (3). Optionally,* $Fe^{2+}SO_4^{2-}$ *as a powder (4) is added to the solution. The reaction parameters (NaOH addition, titration pH, duration of experiment) are controlled by an external PC with the software TitriSoft (5) and executed by an automated titration unit 7600 from SI analytics (6). Figure modified after* Anagnostopoulos (2017).

For the SPOP process, the composition and concentration of metals in wastewater are crucial. Therefore, each wastewater has to be analysed before the treatment to elaborate a precipitation recipe. The experimental conditions are set depending on the target product phase. The reaction parameters are:

- Fe addition and molar ratio Fe:Me
- Reaction temperature (20 – 90 °C)
- Final pH value (4.5 – 11)
- Alkalisation rate
- Type of base (e.g., NaOH, NH_4OH) and its molarity
- Ageing time (none – 24 h)
- Ageing temperature (20 – 110 °C)
- Ageing in an open or closed vessel
- Ageing with or without stirring

Additionally, the composition of the matrix solution (the content of Cl^-, SO_4^{2-}, complexing agents, and organics) must be considered, as it has a decisive influence on the process.

3.4. State of the art of the lab experiments

The scale-up experiments carried out in this thesis build on lab-scale experiments. The main results of the lab-scale experiments are presented below:

- **Cu-system**

The lab-scaled experiments showed that it is possible to precipitate Cu as Cu-ferrite ((Cu, Fe)Fe_2O_4), cuprite (Cu_2O), tenorite (CuO) and zero-valent Cu. The controlling process parameters are the Cu^{2+} concentration (up to 10 g/l), the pH value, the reaction temperature (< 70 °C), and the ageing conditions *(Heuss-Aßbichler et al., 2016b)*. Green rust, a Fe^{2+}-Fe^{3+} containing double-layered hydroxy-sulphate, was observed as the main phase in fresh samples and proved to be a precursor for forming magnetite (Fe_3O_4) in alkaline solutions. Ageing plays an essential role in comprising metal oxides, as it was found that after a minimum ageing time of one hour, the quantity of green rust is low *(Heuss-Aßbichler et al., 2016b)*Cu recovery rates range from 99.98 to almost 100%, and limit values for discharge are partly fulfilled depending on the initial concentration of Cu in the wastewater.

Other stable metal-containing phases were synthesised with the variation of Fe:Me molar ratios. With Fe:Cu = 1:1, delafossite ($CuFeO_2$) was precipitated from Cu^{2+} containing synthetic- and real wastewater; it demonstrated the possibilities of recovering valuable phases from wastewater as a product *(John et al., 2016a, 2016b, 2016d)*.

- **Zn-system**

Zn plays an essential role in fabricating products and materials across several industries. It is mainly used as a corrosion-resistant coating on other metals or alloys, e.g., iron or steel. Furthermore, Zn is the most enriched heavy metal in the fly ash of municipal waste incineration plants *(Tandon, 2021)*. Hitherto, the recovery of Zn with the SPOP process was investigated on a laboratory scale with (I) wastewater from the Zn plating industry *(John, 2016; John et al., 2016c)* and (II) leachates of fly ash from municipal waste incineration *(Tandon et al., 2018)*The main difference between these two systems is the matrix composition: Electroplating wastewater is rich in SO42-, while leachates of municipal waste incineration ashes contain a high concentration of Cl^-.

(I) The wastewater from the electroplating industry contained 1.4 g/l Zn and traces of Ni, Fe, Cu, and Cr. After treatment, they were almost completely removed *(John et al., 2016c)*. The Zn water purification rates ranged between 96.4% and 99.9%. The precipitation product was nanosized doped ZnO, with minor amounts of $ZnCO_3$ and $Zn(OH)_2$.

(II) In the so-called "wet flue gas cleaning" process, the flue gases after waste incineration are first dedusted (fly ash) and then passed through a scrubber to bind the substances in the flue gas, creating acidic wash water. In the FLUWA process, the two waste streams are combined: The acid-containing wash water dissolves the metals, primarily zinc and lead, in the fly ash. Typically, this wastewater is treated with the neutralisation process. Consequently, the sludge is thixotropic and highly corrosive due to the high Cl^- concentrations (> 70 g/l), which makes its technical treatment problematic and hinders the Zn recovery. Accordingly, the influence of high salinity on the recovery of Zn by the SPOP process was investigated *(Tandon et al., 2018)*. Two different multi-stage processes have been developed *(Tandon, 2021)*. In concept 1, at reaction temperatures > 40 °C, the metals are precipitated directly as Zn-oxide and soluble salts. These salts are removed by washing them with water. The recovery rate for zinc was > 99.5%. In concept 2, with a reaction temperature < 40 °C, the metals are precipitated as Cl^- and SO_4^{2-} containing hydroxide (Gordaite). In the following step, ZnO is formed during the ageing of the hydroxides at elevated temperatures.

Treating salt-rich solutions is sophisticated and requires enhanced techniques and materials. This example demonstrates that it was possible to extend the application field of the SPOP process to highly saline wastewater *(Tandon et al., 2018; Tandon, 2021)*. At low salt concentrations, Zn precipitates as ZnO, and with increasing salinity, the stability of various Zn-sulphate-hydroxide phases containing Na^+, Cl^- and SO_4^{2-} is favoured. Fly ash is enriched with Zn and Pb and includes elements such as Cu, Cd and Cr. An acidic extraction of fly ash yields a Cl^-rich solution enriched in Zn. The application of SPOP enabled the concentration of

Zn in the precipitate and simultaneously the wastewater purification *(Tandon and Heuss-Aßbichler, 2021).*

- **Au-system**

For the recovery of Au, a two-step SPOP process was developed by *John et al. (2019)* to treat wastewater from chemical catalyst production. First, $FeSO_4*5H_2O$ was added to the Au-containing wastewater at room temperature with a molar ratio of Fe:Au = 3:1. The addition of Fe^{2+} to the Au^{3+}-containing wastewater caused the reduction to Au°. The precipitated µm-sized Au-rosettes were removed by filtration. In the second step, Fe_3O_4 is precipitated by alkalising the solution to pH 10.5 using NaOH at a reaction temperature of 70 °C. The alkalisation of the Fe-containing solution led to metastable phases like green rust or Fe-hydroxides, which react to magnetite. The two-step process demonstrated that it is possible to extract single-phase products from a mixed solution.

- **Other metal-containing systems**

The applicability of the SPOP process was tested for various metal-containing solutions, e.g., Ni, Pb, Cr, Mn, Sn, Pd, Ag, Co, V, and P. It was found that **Ni** can be incorporated into the ferrite structure ($Ni_xFe_{3-x}O_4$) *(Tandon, 2015; John, 2016; Appel, 2019)*. The concentration of minor elements like **Pb**, **Mn** and **Cr,** which occur in real wastewater, was also reduced, indicating that they are incorporated into the ferrite structure *(John, 2016)*. **Ag** was recovered from synthetic wastewater as either single-phased delafossite ($AgFeO_2$) or composite particles of Ag^0 with delafossite or magnetite *(John et al., 2019)*. The treatment of wastewater from a **Pd**- and **Sn**-containing activator bath from the electroplating industry has shown that Sn could be recovered as jeanbandyite ($FeSnO(OH)_5$) *(John, 2016; Zwerschke, 2019)*. The water analysis also showed that Pd could be removed from the solution, but no crystalline Pd-containing phase was identified. **Co** was recovered as $Co(OH)_2$, CoO and Co-ferrite depending on the experimental conditions *(Engels, 2020)*. In the case of solid VPO-catalyst, **V** and **P** were first leached out and subsequently precipitated using a modified SPOP process. The results show that V and P can be recovered up to 99.6% and 97.3%. The precipitated phases are hydroxides with different compositions *(Weichselgartner, 2020)*.

Conclusion: The lab-scaled experiments demonstrated that it is possible to precipitate different metal-containing phases, such as oxides with ferrite or delafossite structure, doped metal oxides, zero-valent phases, or hydroxides, by adjusting the treatment parameters. The metals are highly enriched in the residues, and the volume of the nano-scaled precipitation products is minimal compared to hydroxide sludge. Therefore, the generated phases from wastewater have the potential to be reused as a product. In the worst case, the precipitation products can be subjected to hydrometallurgical processes for metal recycling.

3.5. Construction of the pilot facility

3.5.1. Tasks of the pilot facility

The SPOP process is a multi-parameter process, and a successful implementation depends on correctly executing the individual tasks. For the upscaling of the SPOP process, the pilot facility was designed to treat a larger volume of wastewater (800 ml – 1000 ml) compared to the laboratory experiments (100 ml – 250 ml) in a serial and automated mode. In addition, the following requirements had to be fulfilled *(Knof, 2017; Anagnostopoulos et al., 2019)*:

- carry out the process steps sequentially,
- monitor the critical parameters online,
- temper the wastewater,
- run the precipitation process by a defined addition of base and Fe solution
- enable ageing of the suspension,
- separate the purified wastewater from the particles
- achieve a suspension with the highest possible product concentration.

3.5.2. Flow diagram

The basic SPOP process is a batch process. The principle is illustrated in *Figure 3.8*. First, the aqueous solution is tempered to the reaction temperature. Next, the Fe-solution is optionally added to the aqueous solution. Then, the mixed solution is alkalised by adding a base with a specific alkalisation rate until the final pH value is reached. The precipitation product produced can be aged before it is separated from the filtrate.

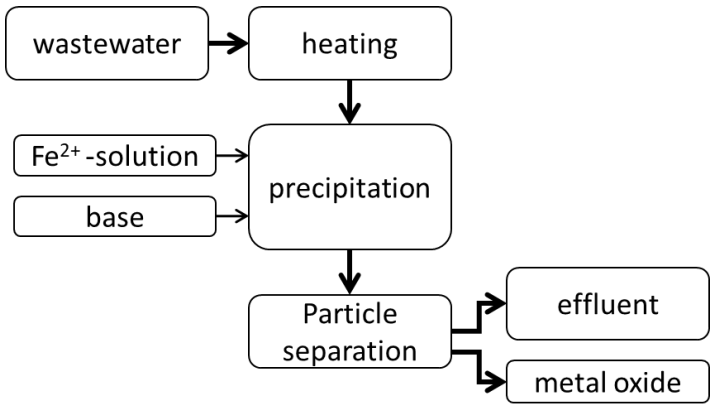

Figure 3.8: *Basic process flow chart of the Specific Product Oriented Precipitation (SPOP) process. The heavy metal-bearing wastewater is heated to reaction temperature (< 70 °C), alkalised with NaOH (≤ pH 11) and optionally treated with Fe^{2+} solution* (after Knof, 2017).

Depending on the composition of the wastewater, two different batch processes were elaborated: a **one-step process** and a **two-step process** *(Figure 3.9)*.

The one-step SPOP process was sequentially executed and used to treat Zn and Cu in this work. The two-step process was developed for the recovery of Au. First, the solution is mixed with Fe-solution, resulting in the spontaneous precipitation of particles immediately filtered. The remaining solution is then alkalised, and the produced particles are optionally altered before filtering.

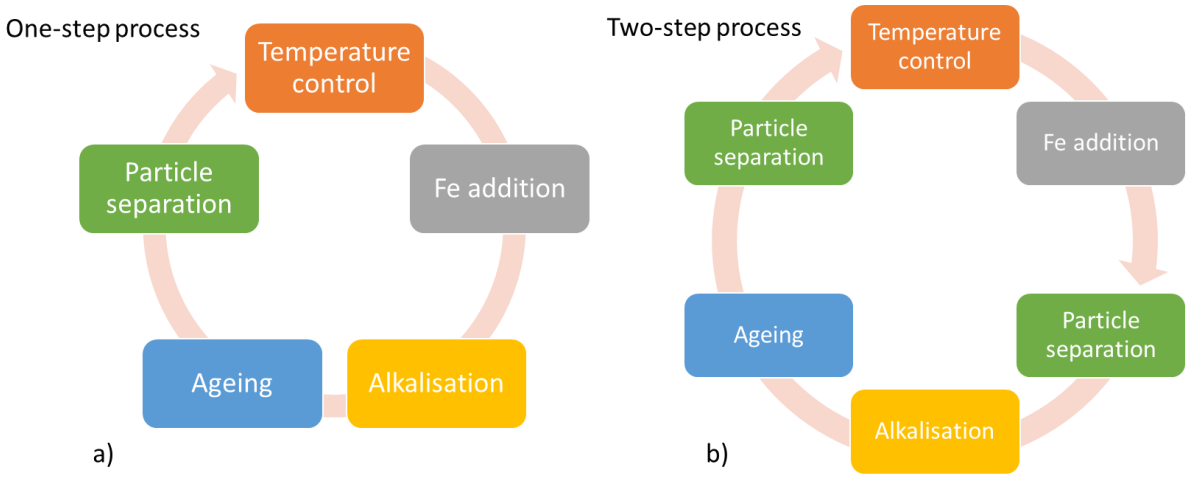

Figure 3.9: *The workflow of the (a) one-step process and the (b) two-step process for the recovery of Au.*

For the technical understanding of the SPOP pilot facility, its workflow is shown in *Figure 3.10*. The process is subdivided into four parts: I) preparation, II) precipitation, III) particle separation, and IV) post-treatment *(Knof, 2017)*.

I) Preparation

During the preparation for the precipitation process, a pump (P1) transfers the wastewater from its storage vessel (V1) to the boiler (B1). After achieving the reaction temperature (T_{max}), the wastewater is pumped (P2) to the reaction vessel (R1), which is equipped with a stirrer, a pH electrode, and a redox electrode. The precipitation process can start when the maximum volume of wastewater in R1 is reached.

II) Precipitation

In the case of treatment with Fe addition, the Fe solution is dosed via a dosing pump to the wastewater in R1. Once the intended volume, including the Fe solution, is achieved, the alkalisation starts.

The precipitation process starts by dosing a base to R1 with a pre-set alkalisation rate and final pH value. During precipitation, the solution is continuously stirred. In general, the suspension consists of nano-scaled particles. After the reaction is completed, the suspension is pumped (P3) to reaction vessel 2 (R2) for storage and alteration. Afterwards, the suspension is transferred to start the particle separation.

III) Particle separation

The suspension is pumped (P4) to the sedimentation tank (S1) for particle separation. For a repetition of the precipitation process, it is also possible to transfer the solution (P5) back to the boiler (B1) or the reactor (R1). If particle separation is not wanted, discharge the suspension from S1 to either collection vessel V2 or V3 via P5 is possible. After the sedimentation of the particles, post-treatment is initiated.

IV) Post-treatment

During the post-treatment, the particles and the treated wastewater are separated in two tanks (V2) and (V3). Both particles and water are manually sampled for analysis.

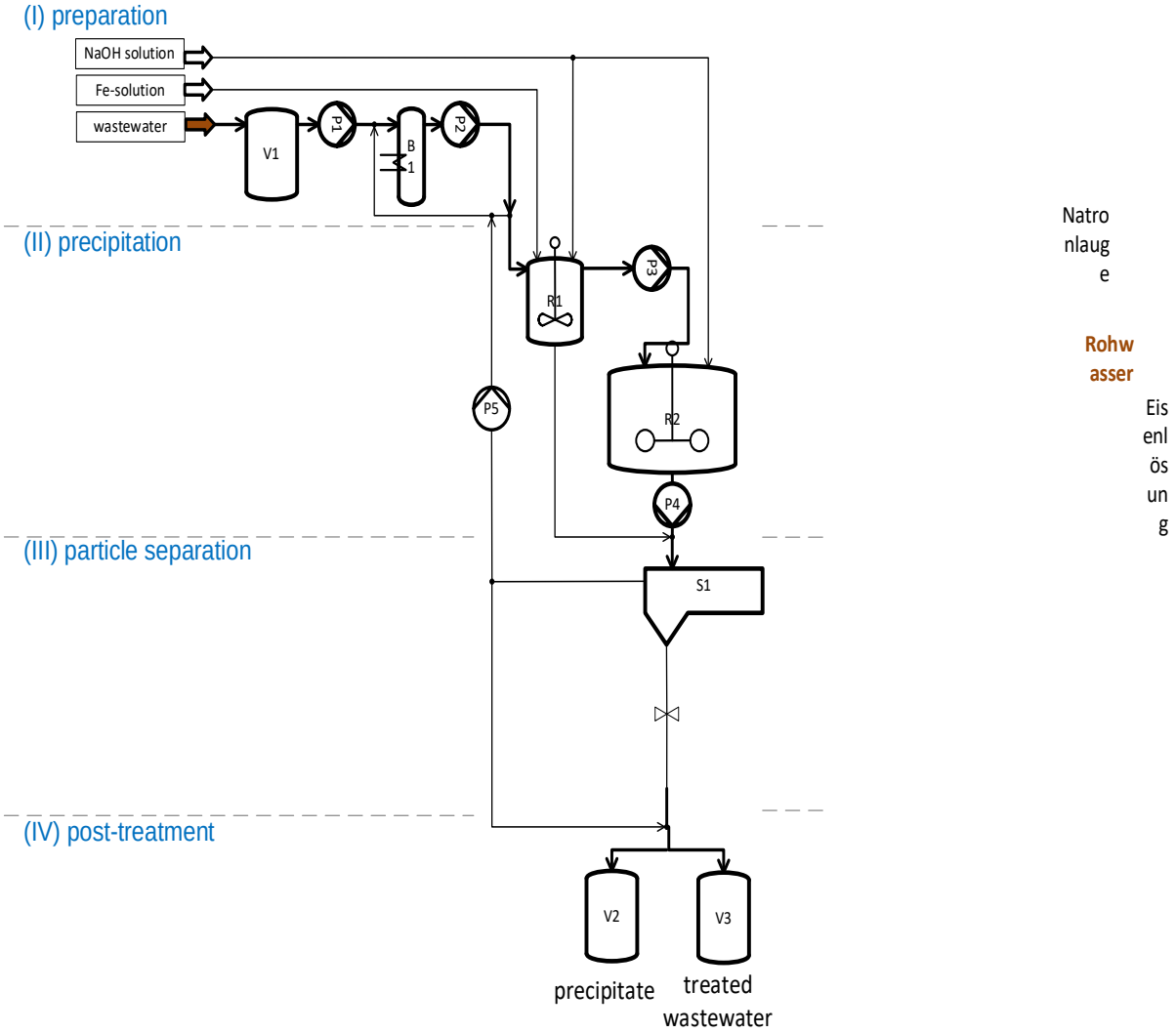

Figure 3.10: *Simplified P&ID diagram of the SPOP process realised in the pilot facility. The process is divided into (I) preparation of the wastewater, (II) precipitation after the addition of optional Fe-solution and NaOH solution, (III) particle separation by sedimentation, and (IV) post-treatment with separation of the particles and the treated water. Scheme modified after* Knof (2017).

3.5.3. Configuration of the SPOP pilot facility

1) Components

The pilot facility was designed for the automatic execution of the process, which influenced the choice of the various components and software. Accordingly, the SPOP pilot facility was first built according to the materials and components selected and proposed by *Knof (2017)*. During this thesis, the SPOP pilot facility was continually tested. Based on the results, operational procedures were adjusted or changed, and individual parts were modified or exchanged.

The materials and components must meet the following properties: They all must be watertight or splash- and condensation water-resistant and temperature-resistant at elevated temperatures (up to 60 °C). In addition, the materials must withstand a wide pH range, from strongly acidic (pH 1 – 2) to strongly alkaline (pH 12 – 14). Finally, they must also be corrosion-resistant, as some effluents can be corrosive. Therefore, polypropylene and Teflon are used mainly. All the components of the pilot facility were built into a rollable frame *(Figure 3.11a)*. The components' arrangement is in three levels *(Figure 3.11b)*; it was chosen to keep the flow paths short and the water dosing as precisely as possible.

First, the tanks and vessels were assembled. Storage tanks with a volume of 30 l for wastewater, suspension, and effluent are located on the bottom level of the pilot facility. On the first level, feed pumps providing the vessels with liquid are installed *(Ecoline VC 380 by Ismatec)*. The boiler (10 l) and the reactor (1.5 l) are placed on the second level. The boiler is one meter long and rises to the pilot facilities' top. The 5 l storage tanks for the Fe-solution and the base solution are placed close to the reactor on the first level with the dosing pump interposed (first *Reglo ICC 4CH*, later replaced by *15QQ by Boxer*). Also, the alteration tank (10 l) and the sedimentation tank (100 l) are placed on the second level. Two stirrers (HEI-TORQUE *Precision 100, Heidolph Instruments*) were installed on the third level for the reactor and the alteration tank. A feed pump *(Masterflex L/S by Cole-Parmer)* was positioned to fill the sedimentation tank with the suspension. The tubing was carried out, and magnetic two-way and three-way valves *(Type 0330, Bürkert)* were integrated *(Figure 3.11c)*. Next, all electrical components, such as pH- and temperature electrodes *(BlueLine pH 18, SI analytics)*, fluid level sensors (first ultrasonic sensors *HC-SR04 by elegoo*, later replaced by capacitive sensors *KQ6003 by ifm*), and a Tyndall-sensor (homemade) for turbidity measurement got installed. The devices were adjusted and calibrated for the pilot facility's first start-up, and the first test runs were executed with water.

2) Hard- and Software

The programmable logic controller, *Controlling MAXI* and *MEGA*, was built into a control box on the third level. It is an industrialised Arduino-compatible board with open-source software.

The pilot facility is connected to the panel computer *Panelmaster 2138* on a movable holder *(Figure 3.11d)*, which carries out the program. All cables are directed in electrical cable cover slats along the frame. The *Controllino* has several inputs and outputs, which are read from a chip on the *Arduino*. *Arduino* boards can be programmed using their software, *Arduino IDE*. However, *Arduino IDE* was not the chosen software for programming the SPOP pilot facility *(Knof, 2017)*. Instead, *LabVIEW* was selected due to its graphical programming style, which makes programming more accessible for unprofessional programmers. *LabVIEW* is typically used for laboratory purposes and small to medium-complex processes in test departments. Since *LabVIEW* is not a standard programming system for Arduino, the add-on *LINX* was used to program the Arduino device with *LabVIEW (Knof, 2017)*.

3) Safety measures

The metal-containing solutions are acidic, toxic to the environment and skin irritating, can damage eyes, and are hazardous to health depending on the metals contained. Hence, contact with these liquids must be strictly avoided. Therefore, the pilot facility had two emergency switches that stopped the system as a safety measure. During this thesis, the emergency system was extended: the pilot facility was equipped with a custom-made canvas cover to prevent splash water from leaking *(Figure 3.11e)*. Another risk is the failure of the water level sensor, which can cause the tank to overflow. Therefore, the pilot facility was equipped with a trough and two capacitive leakage sensors, emitting a loud whistling when in contact with liquid. Another risk is gas formation, which may occur during the heating and precipitation. To safely evacuate possible gases, a PP cover was installed with an air outlet hood connected to the laboratory air exhaust system, equipped with an airflow sensor *(MiniAir6, Schiltknecht)*, and the software constantly monitors the airflow (20 m/s).

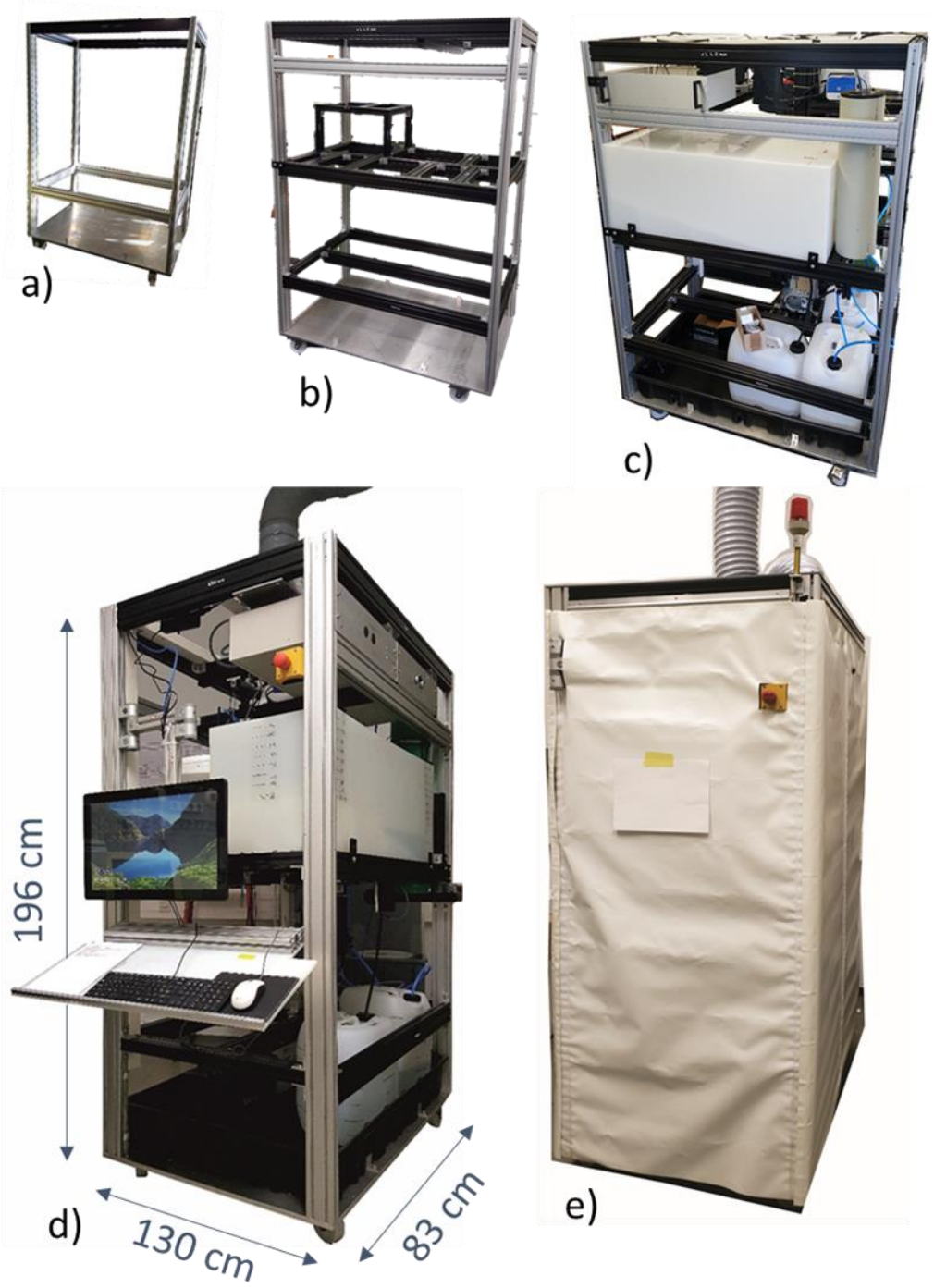

Figure 3.11: *The evolution of the SPOP pilot facility during its construction; a) the pilot facility is built into a metallic frame, which b) consists of three levels into c) & d) the individual components are built-in and e) can be covered by a canvas cover.*

3.5.4. Control Parameters

The SPOP process requires the control of specific parameters. During the experimental work with the pilot facility, these parameters were adjusted for the investigated types of wastewater. This chapter explains the interaction of the control parameters and their function in the process.

The **pH and the alkalisation rate** are crucial process parameters monitored in the reactor and must be worked out individually for every elemental system; this includes a precipitation pH and a final alkalisation pH with a specific alkalisation rate. A pH electrode measures the pH changes caused by alkalisation. The alkalisation rate is controlled using the dosing pumps. After reaching the final pH value, the addition of NaOH is stopped.

The **reaction temperature** is an important process parameter. An optimum reaction temperature must be investigated for each metal system. The reaction temperature is set in the boiler, and then the tempered liquid is transported to the reactor.

Stirring during the precipitation should create a homogeneous composition in the reactor and avoid local chemical differences, particularly during precipitation. As the reaction volume increases, the requirements become more extensive. An optimum stirring speed must be determined since a high stirring speed ensures rapid homogenisation while generating turbulence with uncontrolled oxygen input.

The **fluid level** is a relevant parameter in the vessels, particularly in the reactor. It has to be adjusted because the reactor's wastewater level determines the additives' volumes (Fe-solution and NaOH). The importance of added Fe-solution and NaOH solution depends on the wastewater volume.

The **degree of sedimentation** is an essential parameter in the sedimentation tank. Based on that, precipitate and clear flow separation can be initiated. Solid-liquid separation is critical due to the predominance of nanoparticles in the suspension after treatment. The degree of sedimentation can be determined with a Tyndall sensor with built-in LEDs. The Tyndall effect measures turbidity based on the scattering of light by particles suspended in media such as liquids or gases and whose size is in the range of the optical wavelength. Alternatively, the degree of sedimentation can be derived experimentally by measuring the time needed for sedimentation with a scaled cylinder. When a certain level of turbidity is reached, the solid-liquid separation is initiated with a pinch valve, separating the concentrated suspension and the clear flow into two different vessels.

3.5.5. The programme of the pilot facility

The goal is to operate the SPOP process flow largely automatically with the pilot plant control system, although manual intervention is possible. All process parameters should be set and controlled with the program. Actions had to be put into a logical sequence for the program to work correctly. An initial program was written by *Knof (2017)* proved to be prone to errors in practice due to the large script size. Therefore, a new and compact program was coded during this thesis with the help of Simon Kaphahn, a freelance programmer. The software is executed through a graphical user interface corresponding to LabVIEW's front panel. The interface gives an overview of the process as it is operated in the pilot facility. In the following, the operation of the pilot facility is described based on the various units of the interface. The control panel and the function are explained step by step in their sequence:

1) Loading of precipitation recipes

First, the treatment parameters must be set. The treatment parameters can be saved as recipes ("Rezepte" in *Figure 3.12*) and loaded into the program. The recipes can be adjusted, saved as an external file, and reloaded. The bottom "Manuelle Steuerung" allows switching to manual control; it enables executing each step manually or adjusting the parameters. A time control panel ("Dauer Prozessschritt" in *Figure 3.12*) measures the time for each process step. In case of a failure, the pilot facility can be shut down ("Notaus" in *Figure 3.12*) on the control panel. Furthermore, the outgoing air is surveyed ("Abluftstrom" in *Figure 3.12*), and a sufficient vent is indicated with a green button ("Lüftung OK"). The pilot facility stops operating if the outgoing airflow exceeds the minimum value.

Figure 3.12: *Loading of a precipitation recipe in the control panel.*

2) Process execution

The following sequence shows the flow of a batch reaction. The recipes include the control values for each parameter and are automatically set when loading the recipe. The control values are reaction temperature in °C, Fe-volume in ml, NaOH volume in ml, pH value, stirring speed in revolutions per minute (rpm), and dwell time of the solution in the reactor in minutes. *Figure 3.13* shows the section of the control panel for the preparation and the precipitation process parameters; the control values for each parameter are framed in green, and the real values are

in yellow. The next sequential process step is initiated when the actual values match the control values. First, the wastewater ("Rohwasser" in *Figure 3.13*) is pumped into the boiler. The heating process starts automatically when the maximum water level has been reached. Once the reaction temperature is reached, wastewater is pumped into the reactor, the boiler is refilled, and the temperature is regulated. After reaching the reaction volume in the reactor, the Fe-solution ("Eisenlösung" in *Figure 3.13*) is pumped into the wastewater. Then, the stirrer starts to stir ("Rührer" in *Figure 3.13*). The reaction begins with the dosing of the base solution ("Natronlauge" in *Figure 3.13*) while the pH value is controlled. When the set pH value is reached, the suspension is transported to an alteration tank or, if desired, stays for an alteration time ("Verweilzeit Reaktor" in *Figure 3.13*) in the reactor. After the end of the precipitation process, the stirrer stops, and the reactor is emptied. Subsequently, a new iteration is initiated; the reactor is refilled, and the process is repeated.

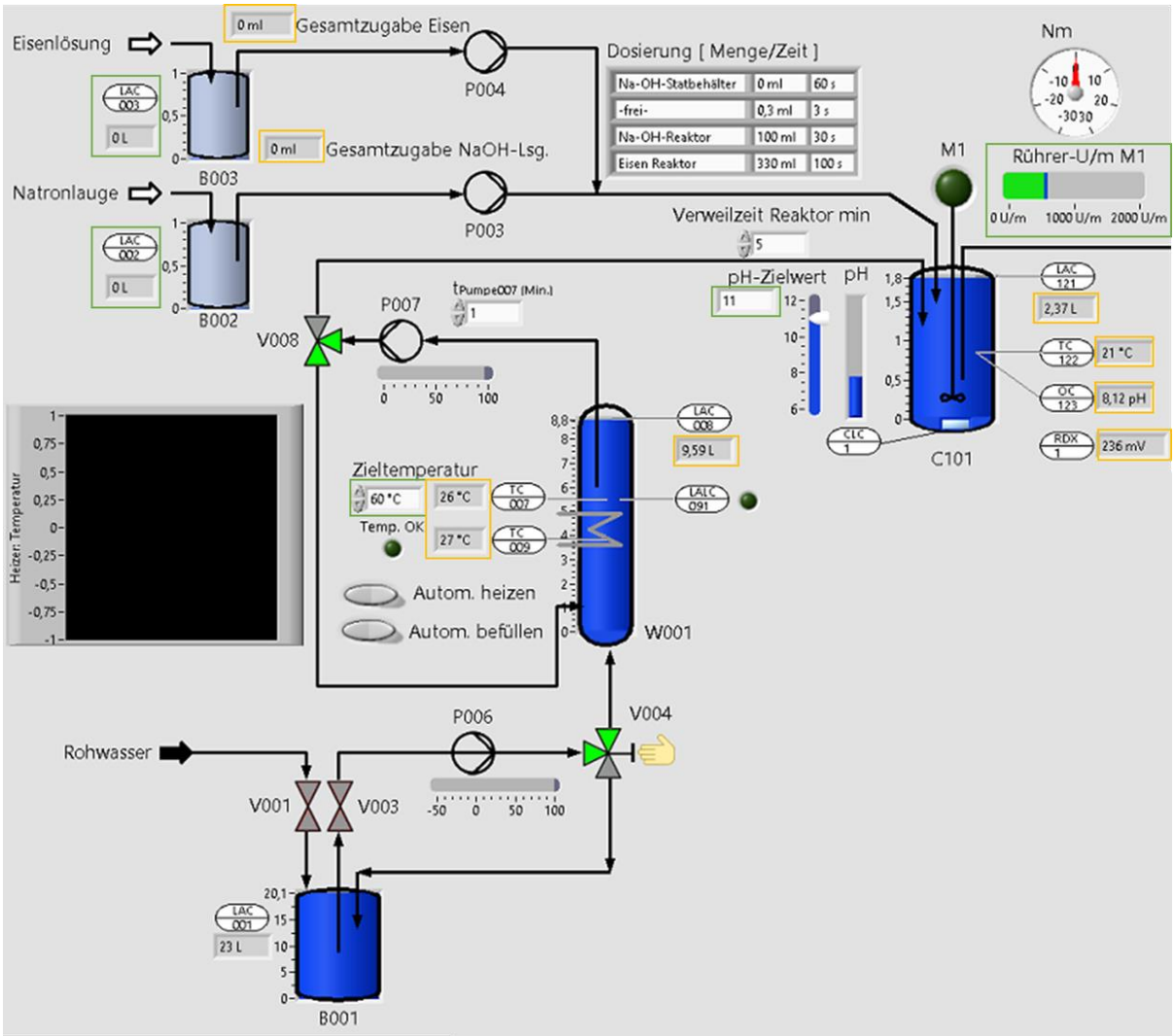

Figure 3.13: *Control panel of the SPOP pilot facility showing the wastewater preparation and precipitation parameters. Control values are framed in green, and real values are in yellow.*

3) Sedimentation

After alteration, the collected suspension is pumped into the sedimentation tank to separate the particles *(Figure 3.14)*. The Tyndall sensor can detect sufficient sedimentation; alternatively, a specific sedimentation time can be set. Then, particle separation via the pinch valve is started, and the residue ("Produkt" in *Figure 3.14*) and the clear flow ("gereinigtes Wasser" in *Figure 3.14*) are separated.

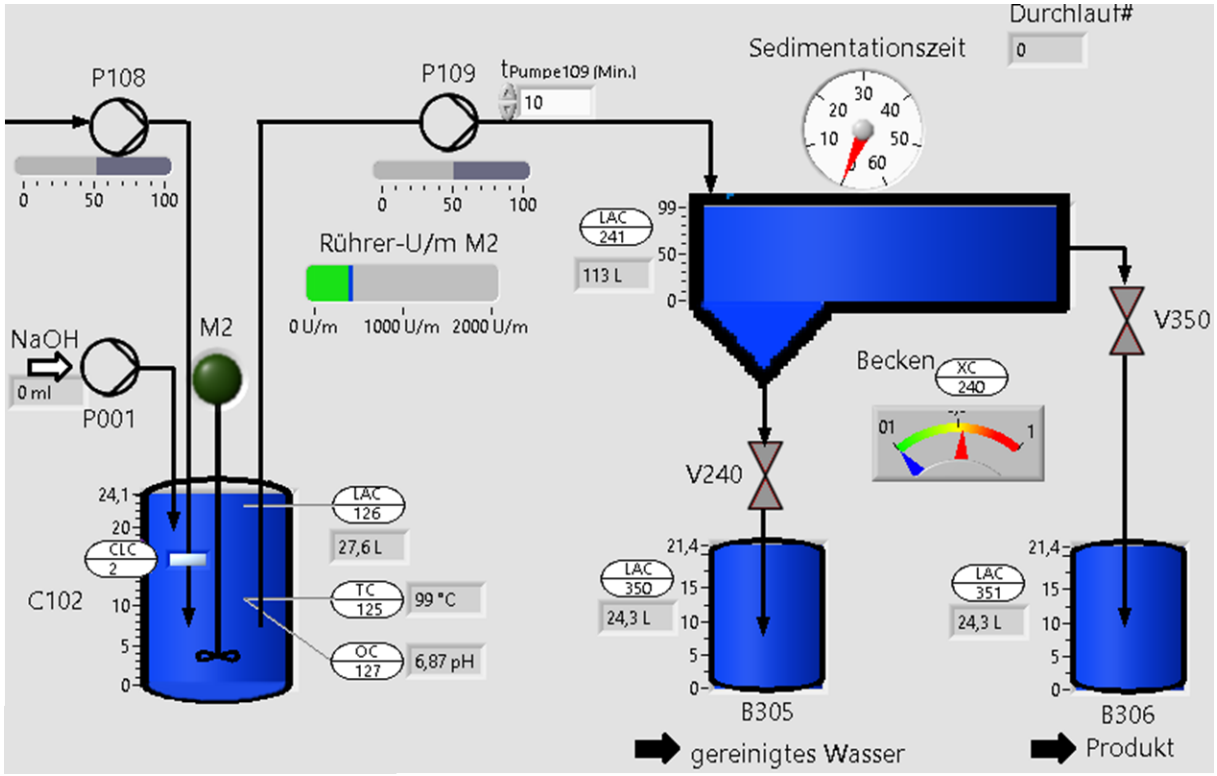

Figure 3.14: *The control panel showing the principle of sedimentation and particle separation.*

The entire control panel can be seen in *Figure VI.1* in the Appendix.

SECTION TWO

4. Material and Methods

4.1. Material

Lab-scale experiments were usually performed with model wastewater and tested with real industrial wastewater. Based on the lab-scale results for the Zn-, Cu-, and Au-system, the performance of the SPOP process with the pilot facility was tested. A base solution of varying molarity was used for all experiments. It was prepared from NaOH pellets dissolved in distilled water. The NaOH pellets were of analytical grade from *Honeywell Chemicals*.

Zn-system

The experiments with Zn were performed with model wastewater representing a model Zn system. Zn(II)-sulphate-heptahydrate from Merck, with a purity of > 99%, was dissolved in distilled water to produce the model wastewater. No other additives were used.

Cu-system

The up-scaling experiments with Cu were performed using a model and real wastewater. In the Cu system, the metal concentration in the model wastewater is defined; for this purpose, Cu(II)-sulphate-pentahydrate was dissolved in distilled water. Fe(II)-sulphate-heptahydrate was used for the experiments with Fe-addition. Both metal salts are from *CHEMSOLUTE®* with a minimum purity of 99.0%. When needed, the pH of the model wastewater was regulated by using concentrated H_2SO_4 (analytical grade).

WAFA Germany, Augsburg, an electroplating facility for galvanising plastic substrates with different metal layers, supplied the real wastewater. The Cu-bearing wastewater was obtained from a rinsing bath. Accordingly, Cu is the main element in the wastewater, accompanied by relatively small amounts of other elements accumulated due to the carryover of the metals. In addition, other minor organic additives like EDTA can occur; their concentration has not been determined and is not explicitly considered in this thesis. For more detailed information about possible substances in electroplating wastewater, see Chapter 2.1.

Au-system

The experiments with Au were carried out with real Au-containing process water used during the production of a special catalyst, which had to be treated afterwards. The chemical catalyst division of *Clariant AG*, Heufeld, provided it. Clariant AG carried out the *water analysis* and made it available to us; it is not published in this thesis for confidentiality reasons.

Sample nomenclature

In general, the composition of each wastewater, real or model, was analysed before the treatment process. This first (initial) water sample is labelled by *(-ini)*. After processing the wastewater with the SPOP pilot facility, the treated water and the precipitation products were sampled. Fresh liquid and solid samples were taken directly after precipitation and labelled with *(-f)*. The effect of washing the precipitates with distilled water or no washing was studied and is indicated with (-*w)* or *(-nw)*. The samples were sometimes altered; the experimental parameters (alteration time and temperature, alteration in closed-c or open-o vessel) are marked in the nomenclature. For example, an alteration for one day at room temperature in an open container is labelled as *(-1dRT-o)* or an alteration for one day at 60 °C in a closed vessel as *(-1d60°C-c)*.

In the case of Au, a 2-step SPOP procedure was applied, and the nomenclature was extended for this purpose. A sample taken after the first or the second treatment step is indicated by *(Au_1)* and *(Au_2)*, respectively.

4.2. Analytical Methods

The initial and treated waters were analysed with ICP-MS, and the residues were analysed with XRD to determine the crystalline phases. FTIR was used to identify low crystalline or amorphous phases. In addition, SEM imaging and EDX measurements were conducted to show the phases' morphology and chemical composition.

Inductively-coupled plasma mass spectroscopy (ICP-MS)

Inductively coupled plasma mass spectroscopy was used to determine the heavy metal concentration of the initial synthetic and real wastewater and all samples after the treatment with the SPOP process. All measurements were carried out by the Stadtwerke München (SWM) with an *MS 7800 by Agilent*. The aqueous solutions were diluted to their measurable concentration and acidified using 1% concentrated HNO_3. The measurement error was calculated for an RSD between 3 and 7%. At a relative standard deviation (RSD) < 3%, no measurement error was calculated due to the high accuracy of the value. The samples with RSD > 7% were re-prepared and measured.

To capture the effectiveness of the treatment, the recovery rates R in (%) of the metals were calculated according to

$$R = 100\left(1 - \frac{C_{treat}}{C_{ini}}\right) \tag{6}$$

where C_{treat} is the metal concentration in the treated, purified wastewater, and C_{ini} is the concentration of the respective metal of the polluted wastewater.

X-ray diffraction (XRD)

The crystalline phase fraction of the precipitate was analysed with X-ray diffraction. All measurements were conducted at the Institute of Crystallography at the LMU Munich using a GE diffractometer *XRD 3003 TT* in Debye-Scherrer geometry with a Cu $K\alpha_1$ anode radiation source and a 1D-detector (Meteor). The samples were hand-ground using an agate mortar and pestle and were either prepared on regular powder XRD brass holders or zero-background quartz holders. Two scans were recorded in step scan mode, starting from 5 ° to 120 ° with a step-width of 0.013 °2θ for an exposure time of 20 sec/count for the brass holders and 100 sec/count for the quartz holders. A threshold of 7.9 keV was set for Fe-containing samples to minimise fluorescence. During the measurements, the samples were rotated to enhance the record of crystal lattice planes.

A qualitative data evaluation was performed with the software *Match!3* and *Match!2*, and the results were compared to the reference database of *the Inorganic Crystal Structure Database (ICSD)* and the *Crystallographic Open Database (COD).*

Fourier Transform Infrared Spectroscopy (FTIR)

Fourier Transform Infrared Spectroscopy (FTIR) was applied to determine the phases with low crystallinity. The analyses were performed with an *EQUINOX55* with Michelson interferometer at the Institute of Mineralogy, Petrology and Geochemistry or a *GladiATR* with monolithic diamond ATR by PIKE Technology at the Institute of Crystallography at the LMU Munich.

For measurements with the *EQUINOX spectrometer*, 1 mg of ground sample material was combined with 200 mg of KBr such that it was homogeneously distributed and pressed into pellets. For the measurements with the *GladiATR*, a spatula tip of the sample material was placed on the monolithic diamond. For both instruments, the samples were measured in 64 scans, from 360 – 4000 cm^{-1}, with a scan time of 4 sec and a resolution of 4 cm^{-1}.

All spectra were corrected for atmospheric effects and baseline corrections. Absorption band fitting was performed using the software *PeakFit,* and bands were assigned using literature values and the *RRUFF* database.

Scanning Electron Microscopy (SEM) and Energy Dispersive X-rays (EDX)

Scanning Electron Microscopy (SEM) and Energy Dispersive X-rays (EDX) measurements were executed with an Analytical Scanning Electron Microscope *SU 5000 Schottky FE-SEM by Hitachi* at the Department of Earth- and Environmental Sciences, LMU Munich.

For sample preparation, the powdered samples were treated with isopropanol in an ultrasonic bath to separate agglomerates and placed on a silicon wafer. For the measurements, the samples were coated with 8 nm of C or Au to reduce the surface's charging and promote the emission of secondary electrons to ensure that the samples conduct evenly. SEM images were taken at an accelerating voltage of 20 kV and a working distance of 8 mm.

5. Upscaling of the SPOP process with the pilot facility

This chapter comprises wastewater treatment results from three different metal systems with the SPOP pilot facility. Experiments developed on a laboratory scale were the basis for the pilot facility's operation. Compared to the laboratory-scale tests, which had a wastewater volume of circa 250 ml, the pilot facility's batch design allows a serial treatment of several litres with up to 1000 ml per batch.

The precipitation with the pilot facility is a batch process in which a given volume of wastewater is treated iteratively. Hence, the reactor was emptied after each precipitation reaction and immediately filled again for a new iteration. For each experiment, this iteration was carried out at least two times. The most successful water purification and phase quality experiments are presented in this chapter. Five experiments were conducted in the Zn-system (Chapter 5.1) by varying the alkalisation rate and the final pH. In the Au-system (Chapter 5.2), sixteen experiments were conducted. The focus was on the variation of the experimental parameters, i.e., the final alkalisation pH and the reaction temperature, in the second treatment step to recover the added Fe. In the Cu system (Chapter 5.3), 35 experiments were conducted with varying reaction temperatures, NaOH solution molarity, and Fe-solution exclusion or addition.

The aim of the treatment is that the metal concentrations are subsequently below the requirements of the *Abwasserverordnung, Anhang 40*. The limit values of the metal ions are summarised in *Table IV.1* in the Appendix.

5.1. Recovery of Zn as divalent oxide

Material & experimental series

Synthetic wastewater with 1.88 g/l Zn was treated with a four-molar NaOH solution at a reaction temperature of 40 °C. The used Zn(II)-sulfate-heptahydrate $ZnSO_4*7H_2O$ shows insignificant quantities of impurities of Li, Fe, K, Cr, Mn, Fe and Ni in the range of a few µg/l. The exact values of those impurities are below the measurement limit and cannot be given. The experimental parameters of this study are based on the findings of *John et al. (2016c)* and are summarised in *Table 5.1*. The precipitation process consisted of 3 batch procedures each, and the products were aged for 21 h at the reaction temperature.

Table 5.1: *Experimental parameters in the Zn-system. The experimental parameters in this work are based on the findings on a laboratory scale* (John et al., 2016c).

	Zn Conc.	**Reaction Volume**	**Reaction Temp.**	**Start pH**	**Final pH**	**Molarity of NaOH**	**Added amount of NaOH**	**Alteration Temperature**
John et al. (2016c)	1.4 g/l	150 ml	40 °C	unknown	9	4 M	unknown	40 °C, 20 °C
This Work	1.88 g/l	3x1000 ml	40 °C	2.5	9	4 M	85 ml	40 °C

The results of the first iteration process are presented below. Four samples were taken after the experiment: two fresh samples and two samples altered for 21 h at 40 °C. The precipitation product was either not washed (-nw) or washed (-w) three times with distilled water.

Result of the water analysis

Table 5.2 shows the initial concentration of Zn in the synthetic wastewater (-ini), the fresh sample (Zn_f-nw), and after 21 hours of ageing at 40 °C (Zn_21h40°C-nw). The washed samples (Zn_f-w) were not determined with ICP-MS. After treatment, the Zn concentration decreased from 1 880 mg/l to 3.04 mg/l, corresponding to a recovery rate of 99.8%. Alteration caused a further decrease in the Zn concentration (1.97 mg/l), reaching a 99.9% recovery rate. It meets the limit value of Zn for discharge (2.0 mg/l).

Table 5.2: *Concentration and recovery rates in brackets of the synthetic Zn-containing wastewater (Zn_ini), the fresh samples taken directly after the treatment and the altered samples. The limit value for discharge is based on the* Abwasserverordnung, Anhang 40.

	Zn_ini	**Zn_f-w**	**Zn_f-nw**	**Zn_21h40°C-w**	**Zn_21h40°C-nw**
Zn limit value for discharge (mg/l)			2.0		
Zn concentration (mg/l)	1 880.00	n.d.	3.04 (99.8%)	n.d.	**1.97 (99.9%)**

Characterisation of the residues

The precipitation product was a fine-grained white powder. *Figure 5.1* shows an SEM image of the aged sample Zn_21h40°C-nw. The residue contains up to 15 µm sized agglomerates consisting of individual spherulites of >20 nm.

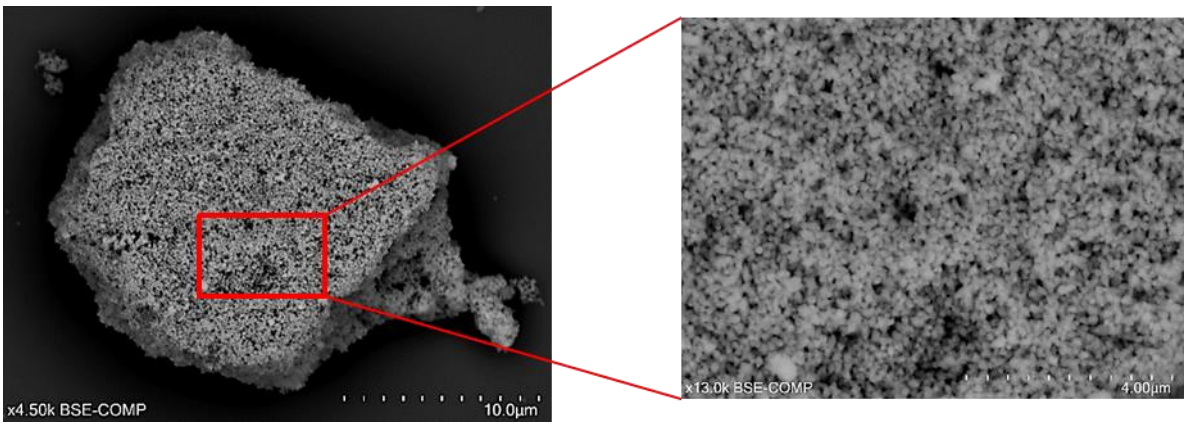

Figure 5.1: *SEM image of sample Zn-21h40°C. The precipitated zincite has a spherical morphology with a grain size < 20 nm. The particles agglomerate to compounds of ca. 15 µm.*

Figure 5.2 shows the X-ray diffractograms of the samples Zn_f-nw and Zn_21h40°C-nw. Both samples show diffraction maxima at the same 2θ positions, with the highest intensities at 81.82, 34.46, and 36.31° 2θ that can be attributed to the (100), (002), and (101) diffraction maxima of ZnO. Peaks with minor intensity are observed at 47.56, 56.58, 62.83, 66.30, 67.30, 67.96, 69.11, 72.48, and 77.14 °2θ. The reference diffractogram of ZnO can be found in *Figure IV.2* in the Appendix. The washed samples show the same results.

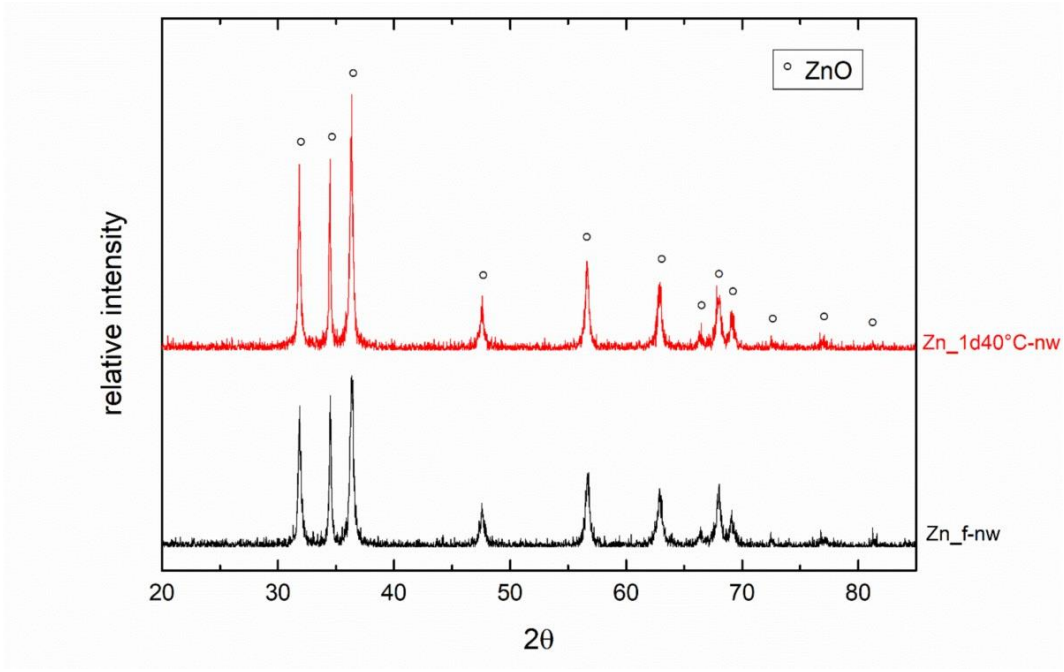

Figure 5.2: *X-ray diffractograms of samples Zn_f-nw and Zn_1d40°C-nw. All diffraction maxima can be assigned to ZnO.*

All samples' FTIR analysis *(Figure 5.3)* shows absorbance at 420, 449, 530, 600, 865, and 1050 $cm^{-1,}$ which can be assigned to ZnO *(Chukanov, 2014)*. An absorption at 1383 cm^{-1} can be assigned to the vibrational mode of S-O and at 1642 cm^{-1} to C-O bands. Two peaks between 3380 and 3560 cm^{-1} can be assigned to the stretching modes of O-H bonds. All samples show the same absorption bands but with more distinct absorbance for the altered samples. Furthermore, no difference was detected between the unwashed and washed samples. The precipitation product is solely ZnO. However, the O-H bonds indicate a small amount of Zn-hydroxide or adsorbed water on the surface of the ZnO particles.

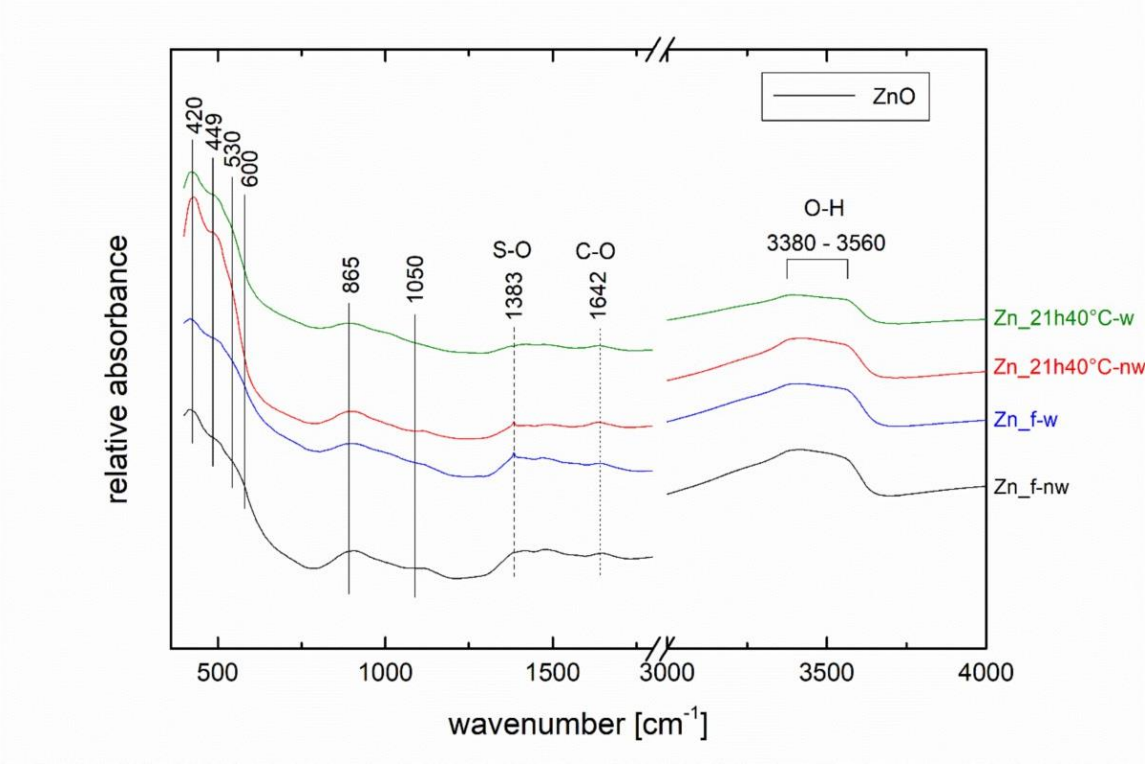

Figure 5.3: *FTIR spectra of the samples Zn_f-nw, Zn_f-w, Zn_21h40°C-nw, and Zn_21h40°C-w. All samples show absorption bands assigned to ZnO.*

5.2. Recovery of Au° as a monovalent metal from Au^{+} -rich wastewater

Experimental conditions of the test series

- **Material**

The wastewater from special catalyst production is intensely yellow; the Au^{+} content was 5.2 g/l, measured by ICP-MS (internal analysis by Clariant, Heufeld) and accordingly higher than the lab-scaled experiments conducted by *John et al. (2019)*.

- **Parameters of the experimental series**

An overview of the parameters of the up-scaled experiment is summarised in *Table 5.3*. They are based on the laboratory parameters published by *John et al. (2019)* in which Au is recovered via two steps (see Chapter 3.5.2. Flow diagram). In the first step, Au° precipitates by adding a Fe^{2+}-rich solution with a molar ratio of Fe:Au of 3:1. Afterwards, the Au^{0} particles are filtered off. The remaining Fe^{2+}-rich wastewater is alkalised in the second step to form magnetite. The particles are likewise filtered out, and the treated wastewater and magnetite remain.

Table 5.3: *Reaction parameters in the Au system of laboratory experiments conducted by* John et al. (2019) *and SPOP pilot facility experiments of this work; RT = room temperature.*

	Au^{+} concentration	**Fe^{2+}:Au^{+} ratio**	**Reaction volume**	**Reaction temperature**	**Final pH**	**Molarity of NaOH**
			STEP ONE			
(John et al., 2019)	1.8 g/l	3:1	200 ml	RT	2.1	-
This work	5.2 g/l	3:1	1000 ml	RT	2.2	-
			STEP TWO			
(John et al., 2019)	-	3:1	200 ml	70 °C	> 9	unknown
This work	-	3:1	1000 ml	60 °C	11.4	8 M

- **Modification of the iron addition**

In the lab experiments, $Fe(II)SO_4*5\ H_2O$ was added as a powder in step one of the two-step SPOP process. However, in the SPOP pilot facility, the Fe addition was modified for technical reasons and was replaced by adding a $Fe(II)SO4*5H_2O$-containing solution. The addition of the Fe-bearing solution took longer compared to the addition of powder for the laboratory experiments. Three effects had to be considered for adding Fe-solution instead of Fe-powder: a longer reaction time, an enhanced reaction volume, and, hence, a dilution of the wastewater.

Results

Figure 5.4 shows five chronological photos depicting the solution's colour change in the reactor during the two-step SPOP process carried out with the pilot facility. *Figures 5.4a-c* illustrate the first treatment step: The initially yellow wastewater *(a)* becomes turbid and brown due to the addition of Fe-solution *(b)*. After completion of Fe addition, the stirrer is paused, and particles settle *(c)*. The suspension was transferred to the sedimentation tank, and the particles were filtered. Next, the second treatment step starts *(Figure 5.4d-e)*: The filtrate is fed back into the reaction tank *(d)*. To recover the Fe, the filtrate is alkalised using a sodium hydroxide solution, which precipitates black particles *(e)*. Finally, the suspension was pumped off, and the filtrate was separated from the precipitate in the sedimentation tank.

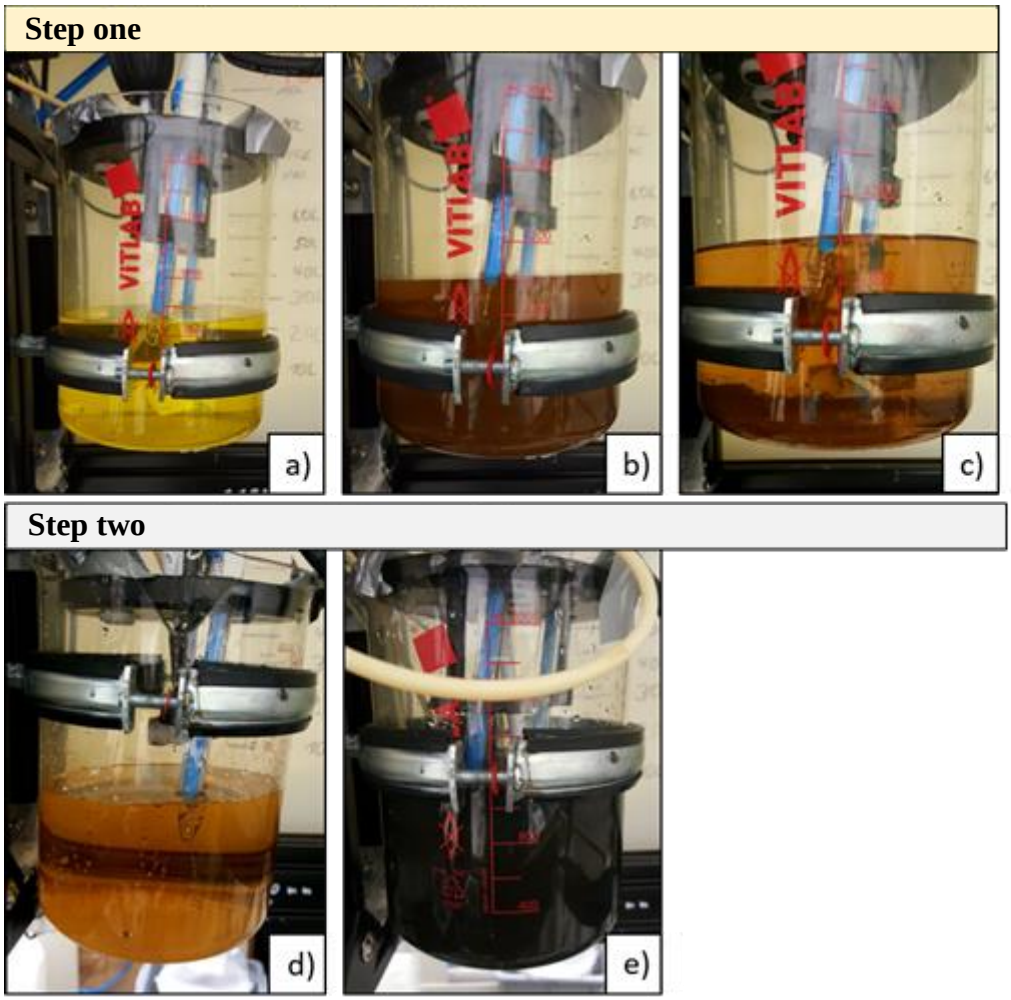

Figure 5.4: *Chronological sequence of the two-step process of Au-containing wastewater with the SPOP pilot facility. Images a-c) show the colour change in step one. (a) the initial Au-wastewater provided by Clariant, (b) the effect of Fe-addition, and (c) the settled Au particles. Images d & e show the colour change in step two; (d) shows the filtrate of step one (Fe-containing solution) before treatment; and (e) the suspension of black particles after alkalisation.*

- **Water purification**

Figure 5.5a-c shows the colours of the liquid samples of the first treatment step: *(a)* the Au-containing wastewater with intense yellow colour, *(b)* the water changed to light brown after precipitation of Au and *(c)* optically transparent filtrate after the second treatment step.

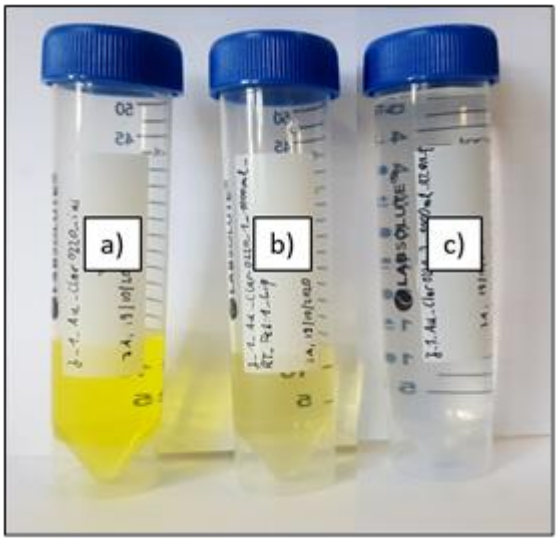

Figure 5.5: *Aqueous solutions of the Au system. a) initial Au-containing wastewater with intense yellow colour, b) filtrate after step-one treatment with the colour changed to light brown; c) clear and colourless filtrate after step two of the SPOP process.*

The Fe and Au concentrations of the initial Au-containing wastewater and the treated wastewater are shown in *Table 5.4*. After the first treatment step, the Au concentration decreased from 5 226 g/l to 6.7 mg/l Au, corresponding to a recovery rate of 99.9%. After the second step, it dropped to 0.04 mg/l (recovery rate of 100%).

7 582 mg/l Fe^{2+} was added in the first step to precipitate Au. After the second treatment step, the fresh sample had 2.05 mg/l Fe, corresponding to a recovery rate of 99.9% immediately after precipitation.

Four samples were taken after one day and two days of ageing at room temperature and 60 °C, respectively, to study the effect of ageing on the residual concentration of Fe in the treated wastewater. After two days of ageing at 60 °C, the lowest concentrations of Au (0.1 mg/l) and Fe (1.06 mg/l) were obtained. Ageing at room temperature resulted in a similar decrease in concentration for both Au and Fe.

Table 5.4: Concentrations of Au and Fe in the aliquots before (Au-ini) and after the treatment. The recovery rates are given in (%) in brackets.

Sample	Au	Fe
	(mg/l)	
Au-ini	5 226.17	44.47
Au_1	6.69 (99.9)	7 582.85
Au_2-f	0.41 (99.9)	2.07 (99.9)
Au_2-1dRT	0.26 (100)	2.05 (99.9)
Au_2-2dRT	0.14 (100)	1.59 (99.9)
Au_2-1d60°C	0.13 (100)	1.47 (99.9)
Au_2-2d60°C	0.1 (100)	1.06 (99.9)

- **Characterisation of the precipitates**

Precipitates of the first step

The precipitate of step one (sample Au-1) is a fine yellow to light brown powder, as shown in *Figure 5.6.*

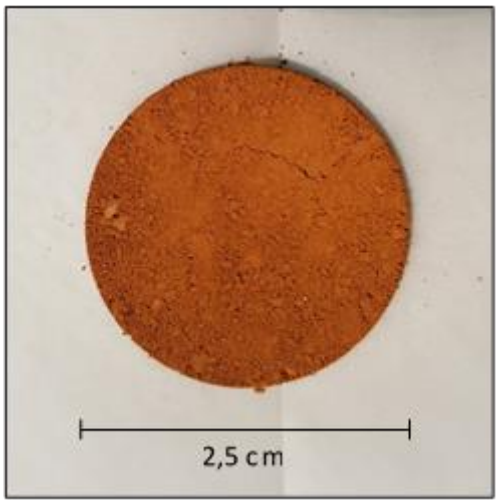

Figure 5.6: *Precipitated Au^0 powder after step one.*

The corresponding SEM images of sample Au-1 are shown in *Figure 5.7*. The agglomerates of Au particles (upper images) consist of spherical rosettes with a grain size of about 4 µm (lower images).

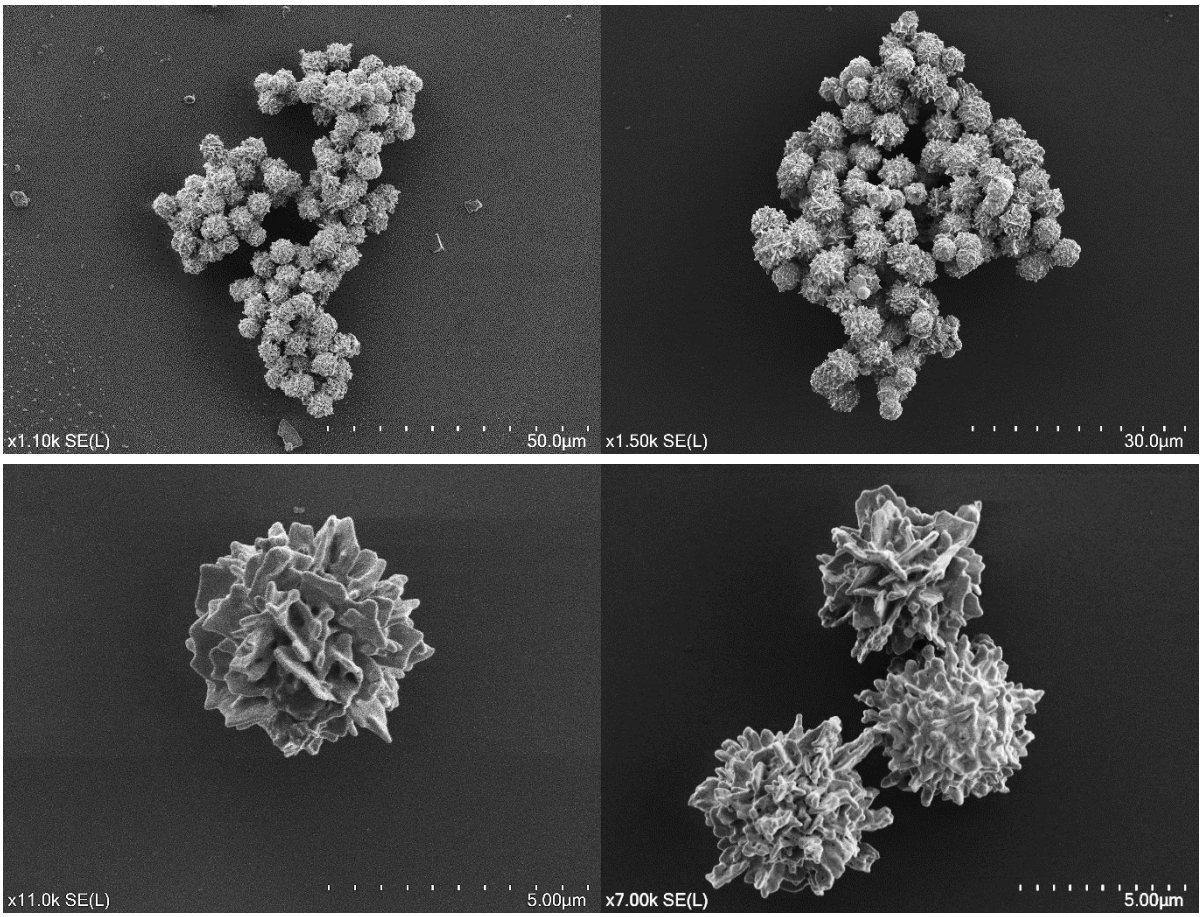

Figure 5.7: *SEM images of sample Au_1. The images show pure metallic Au rosettes with a grain size of about 4 µm. The upper row of images shows that particles agglomerate.*

The X-ray diffractogram in *Figure 5.8* shows precise diffraction maxima without background noise. Therefore, all peaks can be assigned to metallic Au°. The most intense diffraction maxima at 38.20 °2θ corresponds to Au's (111). Other lower-intensity diffraction maxima lie at 44.45, 64.65, 77.68, 81.85, 98.29, 111.04, and 115.49 °2θ. The reference X-ray diffractogram of metallic Au can be found in the Appendix, *Figure IV.3*. Accordingly, > 99.9% of the Au was recovered as metallic Au°.

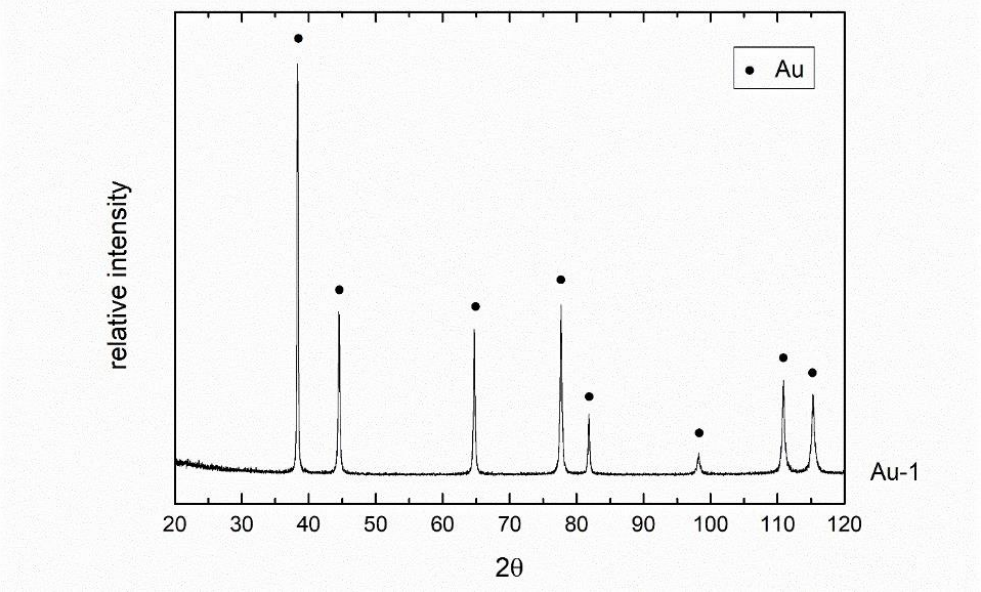

Figure 5.8: *X-ray diffractogram of sample Au-1. All diffraction maxima are assigned to* Au^0.

Precipitates of the second step

The precipitates of step two were analysed with XRD and FTIR. *Figure 5.9* shows the diffractograms of the fresh sample (Au_2-f) and the sample altered for 1d at 60 °C (Au_2-1d60°C) as examples of all samples of this experimental series showing the same diffractogram. The fresh sample shows a higher background noise compared to sample Au_2-1d60°C.

All samples show the same diffraction maxima, which can be assigned to magnetite (see reference diffractogram of magnetite, *Figure IV.4* in the Appendix). No additional peak was observed. Accordingly, magnetite is the only crystalline phase observed.

The FTIR spectra of all samples show an intense absorption band at 580 cm^{-1}, which can be assigned to magnetite. The fresh sample shows minor absorption bands at 623, 1110, 1148, and 1334 cm^{-1} that can be set to green rust. All altered samples show a marked decrease in the intensity of these bands. Moreover, all samples show absorption at 1345 cm^{-1} and 1470 cm^{-1} that can be assigned to atmospheric carbon modes.

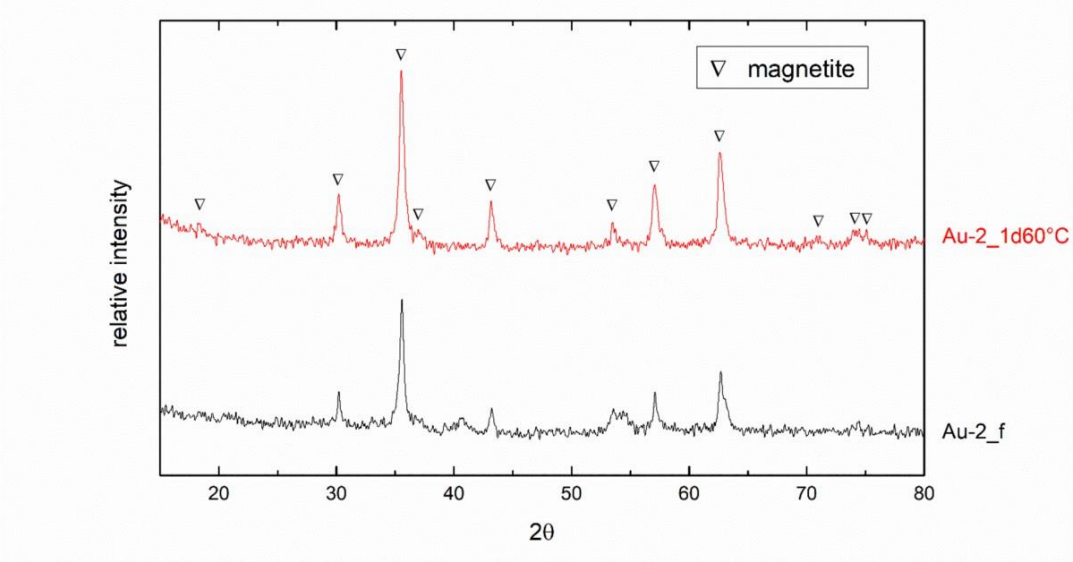

Figure 5.9: *X-ray diffractograms of sample Au-2_f (black) and Au-2_1d60°C (red). All peaks can be assigned to magnetite.*

5.3. Recovery of Cu

This chapter presents the results of two different recipes to recover Cu: (1) the formation of cuprospinel according to the ferritisation procedure and (2) as divalent Cu-oxide. The challenge is treating complex wastewater containing a wide range of elements in concentrations from a few mg/l to several g/l, which implies a robust and efficient treatment process.

The samples were aged in a closed vessel *(-c)* and an open vessel *(-o)*. Since the results of these two approaches were similar, the X-ray diffractograms and FTIR spectra of those samples altered in a closed container *(-c)* are presented.

5.3.1. Recipe A: Recovery of Cu as cuprospinel

Material

The laboratory scale experiments were developed with synthetic wastewater using $CuSO_4*5H_2O$ and $FeSO_4*7H_2O$ *(Heuss-Aßbichler et al., 2016b)*. In this study, the experiments with the pilot facility were performed with real wastewater to demonstrate the applicability of SPOP for larger wastewater volumes. WAFA Germany provided two different types of rinsing baths from electroplating. As the main component, Cu caused an azure-blue colour in the wastewater. *Table 5.5* shows the compositional range of the two wastewater batches, with Cu concentrations between 8 and 10 g/l. Minor elements are Fe, Ni, and Zn, in the range of 20 to 300 mg/l, and traces of Cr, Pb, and Mn being less than 7 mg/l.

Table 5.5: *Composition of the wastewater from the rinse bath after Cu electroplating from WAFA Germany, Augsburg, measured with ICP-MS.*

Element	Batch A Concentration (mg/l)	Batch B Concentration (mg/l)
Cu	7 452.42	8 223.58
Fe	312.48	97.08
Ni	109.96	68.01
Zn	26.66	172.21
Cr	6.47	2.48
Pb	2.14	5.1
Mn	0.96	2.14

Experimental series

The Cu composition of the wastewater from batch A corresponds best with the sample series CH *(Heuss-Aßbichler et al., 2016b)*, with ferrite and cuprite as the main precipitation products. The experimental series R represents an example of the results achieved in this study. Fe was added in a molar ratio of Cu:Fe = 1:2 to produce ferrite. The wastewater was treated with 8 M NaOH at 60 °C. *Table 5.6* summarises the main experimental parameters of sample series R (this study) and CH *(Heuss-Aßbichler et al., 2016b)*.

Table 5.6: *Experimental series developed with Cu-bearing wastewater from an electroplating rinsing bath treated with the SPOP pilot facility compared with the sample series CH published in* Heuss-Aßbichler et al. (2016b).

Sample series	**R-f**	**R-1dRT-c**	**R-1dRT-o**	**R-1d60°C-c**	**R-1d60°C-o**	**CH**
Wastewater	batch A					
Batch wastewater volume	3 x 800 ml					beaker size
Mole ratio Cu:Fe^{2+}	1:2					1:2
Reaction temperature	60 °C					70 °C
NaOH	8 M					unknown
Total volume of NaOH	3x 200 ml					unknown
Ageing temperature	-	RT	RT	60 °C	60 °C	70 °C
Closed ageing	-	yes	no	yes	no	yes

Results

- **Water purification**

Table 5.7 summarises the water analysis results of sample series R before and after the treatment with the SPOP pilot facility. The values are given in mg/l, and the calculated recovery rates (%) are in brackets. All treated wastewater shows a significant decrease in metal concentrations. The samples that meet the discharge limit of wastewater are marked light green. *Table VI.1* in the appendix shows the discharge limit for the metals examined here.

Cu: The Cu content in the wastewater is 7 452.42 mg/l. After treatment, the fresh sample (R-f) shows 3.41 mg/l, the highest Cu concentration remaining in the solution. The lowest Cu concentration, 1.07 mg/l, was found in the sample R-1dRT-c, which was altered for one day at room temperature in a closed vessel. Accordingly, the recovery rates of all samples of the R experimental series are > 99.9%.

Fe: After adding Fe, the Fe concentration in the initial wastewater was 15 408.67 mg/l; this results in a molar ratio Cu:Fe = 1:2.07. After treatment, the highest concentration shows the fresh sample (R-f) with a Fe content of 13.13 mg/l, proving that more than 99.9% of the Fe content was recovered immediately after the test. With alteration, the Fe concentration decreased in all samples. The lowest concentration of 3.63 mg/l was detected in the sample R-1d60°C-o after one-day alteration at 60 °C in an open vessel.

Zn: The initial Zn concentration of 25.07 mg/l was decreased in the fresh sample to 1.77 mg/l. After alteration, the concentrations were in a similar range, with a minimum value of 1.63 mg/l (sample R-1d60°C-c). It corresponds to a recovery rate of around 93%. All samples meet the discharge limit of Zn (2 mg/l).

Ni: The initial wastewater concentration of Ni lies at 84.72 mg/l. After treatment, the concentration of Ni decreased to 0.06 mg/l both in the fresh wastewater R-f and in the samples altered one day at 60 °C. The samples altered at room temperature for one day (R-1dRT-c and R-1dRT-o) show a slightly higher concentration of 0.11 mg/l and 0.17 mg/l, respectively. All samples meet the discharge limit of Ni (0.5 mg/l). The resulting recovery rates were better than 99.8%.

Cr: The initial wastewater concentration of Cr is 2.49 mg/l. After treatment, the Cr concentration was reduced to 0.01 mg/l in the fresh sample R-f. The altered samples show similarly low Cr concentrations between 0.07 mg/l and below the detection limit. All samples meet the discharge limit of Cr (0.5 mg/l). The recovery rates are > 97.8%.

Pb: The Pb concentrations in the initial wastewater were 1.46 mg/l. After the treatment, the concentrations were below the detection limit for all samples, which refers to a recovery rate of 100%. All samples meet the discharge limit of Pb (0.5 mg/l).

Mn: The initial concentration of Mn was 14.57 mg/l. After the treatment, the fresh sample R-f was exposed to 0.05 mg/l, the highest Mn concentration. The recovery rates are generally high, between 99.7% (sample R-f) and 100% (sample R-1d60°C-o).

In sum, after treatment, the concentration of the primary metals Cu and Fe was efficiently decreased with a recovery rate > 99.9%. However, the lowest concentration of Cu and Fe was only achieved by altering the suspension. Alteration at elevated temperatures improved the results. Removing the minor elements Ni, Zn, Cr, Pb, and Mn was generally very high. The results meet the requirements for discharge; note that Mn has no discharge limit *(Abwasserverordnung, Anhang 40)*.

Table 5.7: *Water analysis results with ICP-MS of sample series R and the limit values for discharge for each element according to the* Abwasserverordnung, Anhang 40. *Metal recovery rates are given in (%) in brackets. Fields marked in green fulfil the limit value for discharge.*

	Cu	**Fe**	**Ni**	**Zn**	**Cr**	**Pb**	**Mn**
	(mg/l)						
Limit value for discharge	0.5	3.0	0.5	2.0	0.5	0.5	-
R-ini	7 452.42	15 408.67	84.72	25.07	2.49	1.46	14.57
R-f	3.41 (100)	13.13 (99.9)	0.06 (99.9)	1.77 (92.9)	0.01 (99.7)	<0.0 (100)	0.05 (99.7)
R-1dRT-c	1.07 (100)	11.06 (99.9)	0.11 (99.9)	1.92 (92.3)	0.07 (97.8)	<0.0 (100)	0.02 (99.8)
R-1dRT-o	1.69 (100)	6.64 (99.9)	0.17 (99.8)	1.67 (93.3)	0.01 (99.7)	<0.0 (100)	0.01 (99.9)
R-1d60°C-c	1.17 (100)	4.74 (100)	0.06 (99.9)	1.63 (93.5)	< 0.0 (100)	< 0.0 (100)	< 0.0 (100)
R-1d60°C-o	2.93 (100)	3.63 (100)	0.06 (99.9)	1.64 (93.5)	0.05 (98.4)	<0.0 (100)	0.00 (100)

- **Characterisation of the precipitates**

SEM: The SEM image in *Figure 5.10* shows an agglomeration of platy and angular nanoparticles building porous clusters 1-5 µm in size.

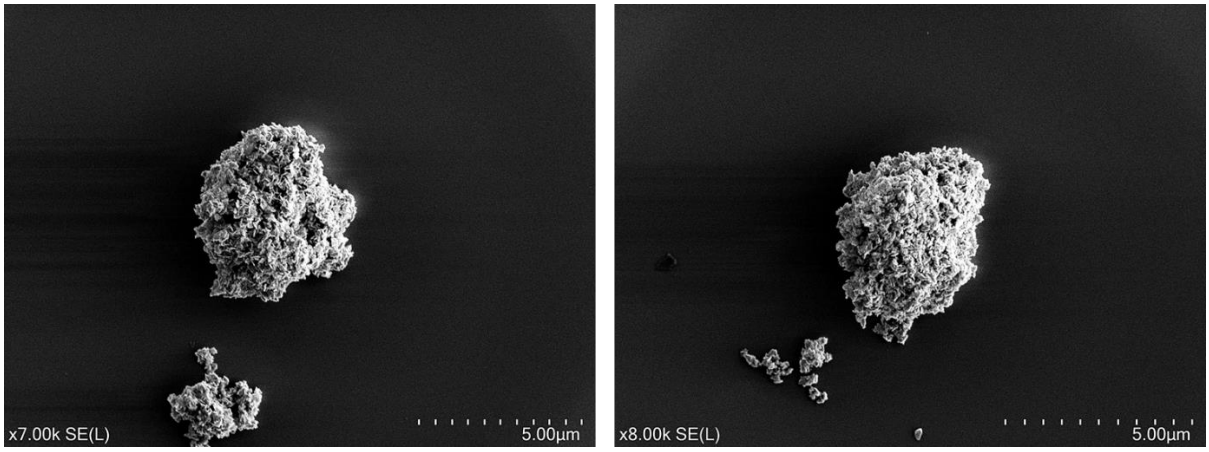

Figure 5.10: *SEM image of sample R-1d60°C-c shows platy and angular particles in aggregation.*

XRD: All samples altered in a closed (-c) and open container (-o) show the same phases. Therefore, only the closed vessel (-c) results are shown in *Figures 5.11* and *5.12*. An overview of the phase analysis with FTIR and XRD is shown in *Table IV.3* in the Appendix. In *Figure 5.11*, the X-ray diffractograms of the fresh sample (R-f) are shown in blue, the sample aged one day at room temperature (R-1dRT-c) in red, and the sample aged one day at 60 °C (R-1d60°C-c) in green. The diffractograms of all samples show sharp diffraction maxima with low background noise. With ageing and increasing temperature, the background noise decreases. All diffraction maxima can be assigned to magnetite (see *Figure IV.4* in the Appendix). The sharp shape and high-intensity diffraction maxima at 18.35 °2θ (111) and 35.55 °2θ (311) correspond to ferrite.

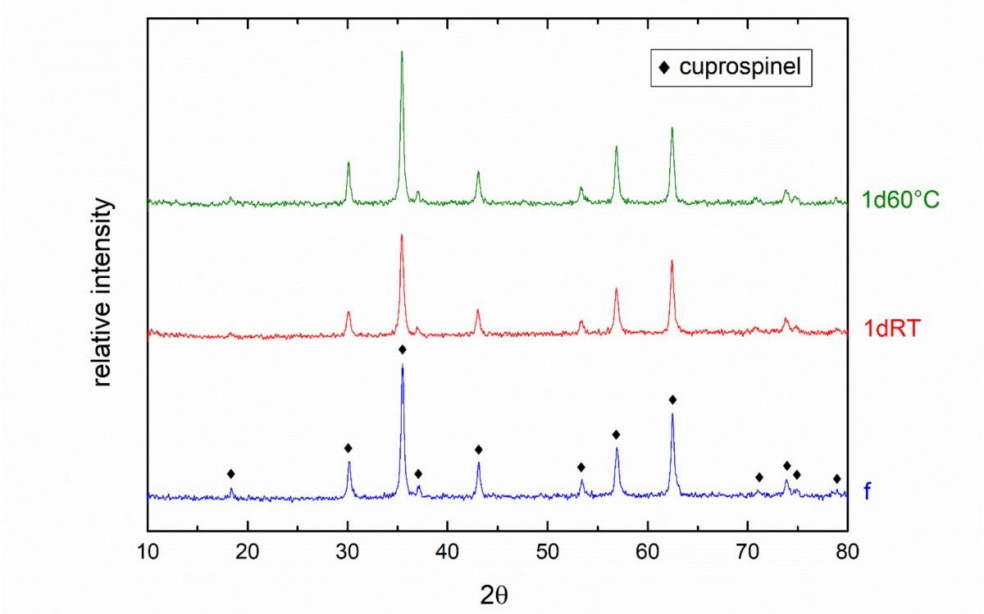

Figure 5.11: *X-ray diffractograms of sample series R. The molar ratio was set to Cu:Fe = 1:2. The fresh samples R (f) and those aged one day at room temperature (1dRT) and 60°C (1d60°C) contain ferrite as the only crystalline phase.*

FTIR: *Figure 5.12* shows the FTIR spectra of sample series R. Based on the bands, three different phases were distinguished. The main absorption band at 565 cm^{-1} and two weaker bands at 530 and 612 cm^{-1} hidden below the shoulders of the main band were assigned to ferrite *(Chukanov, 2014)*. The weakly intense absorption bands at 623, 1330, and 1630 cm^{-1} can be assigned to green rust (GR II), a Fe^{2+}-Fe^{3+} double-layered hydroxide with intercalated tetrahedral anions like SO_4^{2-} *(Feng et al., 2015)*. The weak absorption bands at 835, 1345, and 1470 cm^{-1} can be related to carbonate *(Heuss-Aßbichler et al., 2016b)*.

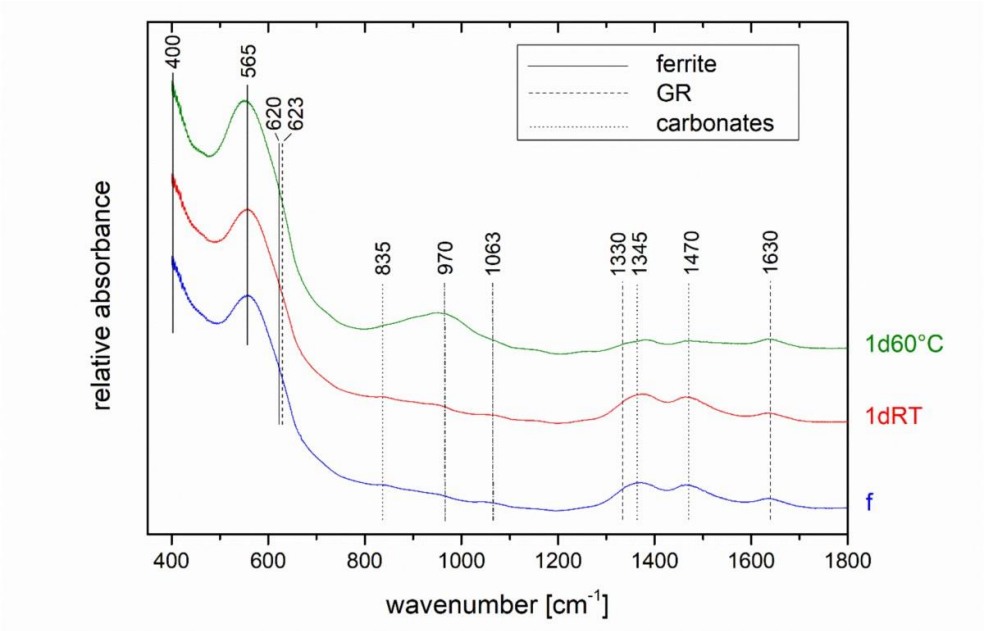

Figure 5.12: *FTIR spectra of sample series R. All samples show absorption bands of ferrite, GR and adsorbed carbonates.*

5.3.2. Recipe B: Recovery of Cu as Cu-oxide

The SPOP process is intended to keep additives low and used only when necessary. Therefore, the recovery of Cu from aqueous solutions was also tested without Fe addition. First, test series in a Fe-free system were carried out on a laboratory scale. Based on these results, the upscaling to the dimension of the pilot facility was performed. The test series Q results are selected and presented as an example. *Table 5.8* gives an overview of the experimental parameters of sample series Q.

Table 5.8: *Experimental parameters of sample series Q.*

Sample Series	**Q-f**	**Q-1dRT-c**	**Q-1dRT-o**	**Q-1d60°C-c**	**Q-1d60°-o**
Wastewater batch	A				
Wastewater volume	3x 800 ml				
Molar ratio Cu:Fe	0				
Reaction temperature	50 – 60 °C				
Molarity of NaOH	8				
Total volume of NaOH	3x 200 ml				
Precipitation pH	ca. 11				
Ageing temperature	-	RT	RT	60 °C	60 °C
Closed ageing	-	yes	No	yes	no

Results

- **Water purification**

Wastewater batch A was used for the experiments. Sample series Q was treated with an eight-molar NaOH solution without adding Fe^{2+}. The water analysis results are given in *Table 5.9*.

Cu: The initial concentration of Cu is 7 452.42 mg/l. After the treatment, recovery rates of Cu ranged between 99.8% and 100%, with the lowest recovery rate in the fresh sample (Q-f); the residual Cu concentration was 12.86 mg/l. Alteration decreased the Cu concentration in the filtrates below 5 mg/L, meaning that during ageing, more than 86.5% of the remaining Cu in the fresh sample was recovered (calculated for sample Q-1d6RT-c). The temperature has an additional effect: by altering at a higher temperature, the concentrations of the two samples Q-1d60°C-c and Q-1d60°C-o were 2.01 mg/l and 1.74 mg/l, respectively. They are thus significantly lower than after ageing at room temperature, with concentrations of 4.27 mg/l (sample Q-1dRT-c) and 3.90 mg/l (sample Q-1dRT-o), respectively.

Fe: The treated wastewater had an initial Fe concentration of 241.52 mg/l; no additional Fe was added. After treatment, the fresh sample (Q-f) and the samples altered at room temperature

showed elevated residual Fe concentrations between 95.08 mg/l and 59.0 mg/l, corresponding with a recovery rate of 60.6 and 75.6%, respectively. Alteration of the samples at 60 °C caused a markedly lower Fe concentration of 4.80 mg/l and 4.21 mg/l for the samples Q-1d60°C-c and Q-1d60°C-o, respectively. Accordingly, 98% of the Fe content can be removed after sample storage at 60 °C for one day.

Ni: With 94.77 mg/l, Ni is the third most abundant metal in the wastewater A. The SPOP process recovered 99.8% to 99.9% of Ni. All samples, including the fresh sample, show a low residual Ni concentration, which meets the discharge limit value (0.5 mg/l). The fresh sample shows a higher residual Ni concentration of 0.19 mg/l, while the samples Q-1d60°C-c and Q-1d60°C-o, altered for 1d at 60 °C, show the lowest Ni concentration of 0.05 mg/l and 0.06 mg/l, respectively.

Zn: The Zn concentration in the wastewater is 26.97 mg/l. After treatment, the residual Zn concentration in the fresh sample and the two samples altered at room temperature were 7.94 mg/l, 5.86 mg/l and 5.18 mg/l, respectively, corresponding to a recovery rate of 70 to 80%. The samples that were altered at 60 °C for one day, Q-1d60°C-c and Q-1d60°C-o, have a lower residual Zn concentration of 1.64 mg/l and 4.66 mg/l, respectively, and thus meet the discharge limit (2 mg/l) according to the *Abwasserverordnung, Anhang 40* (see *Table IV.1* in the Appendix).

Cr: After treatment, the initial Cr concentration of 3.23 mg/l was reduced to 0.23 mg/l in the fresh sample (Q-f), corresponding to a recovery rate of 92.9%. The alteration at room temperature had no marked effect; the samples Q-1dRT-c and Q-1dRT-o show a concentration of 0.20 mg/l and 0.12 mg/l, respectively. However, alteration at 60 °C significantly reduced the residual Cr content to 0.02 mg/l in the samples Q-1d60°C-c and Q-1d60°C-o, corresponding to a total Cr recovery rate of 99.4%. All samples, including the fresh one, meet the discharge limit value (0.5 mg/l).

Pb: The wastewater shows an initial Pb concentration of 1.59 mg/l. After the treatment, the fresh sample Q-f shows a Pb concentration of 0.45 mg/l. The altered samples show slightly lower Pb concentrations between 0.31 mg/l for sample Q-1dRT-o and 0.26 mg/l for sample Q-1d60°C-c. Accordingly, the criteria for the discharge limit (0.5 mg/l) were met. The recovery rates are between 72 and 83%.

Mn: The initial concentration of Mn in the wastewater is 0.78 mg/l. After treatment, the fresh sample shows the highest remaining Mn concentration of 0.27 mg/l. Alteration reduced the Mn concentration: The samples Q-1dRT-c and Q-1dRT-o show a remaining Mn concentration of 0.23 mg/l and 0.14 mg/l, respectively. The alteration at 60 °C resulted in the lowest Mn concentrations of 0.01 mg/l and 0.02 mg/l. Accordingly, the recovery rates of 65.2% (fresh sample) could be improved to 98.4% (1-day alteration at 60°C).

Table 5.9: *The water analysis results with ICP-MS of sample series Q and the limit values for discharge for each metal according to the* Abwasserverordnung, Anhang 40. *Metal recovery rates are given in (%) in brackets. Cells marked in green fulfil the limit value for discharge.*

	Cu	**Fe**	**Ni**	**Zn**	**Cr**	**Pb**	**Mn**
Limit value for discharge	0.5	3.0	0.5	2.0	0.5	0.5	-
Q-ini	8 050.48	241.52	94.77	26.97	3.23		0.78
Q-f	12.86 (99.8)	95.08 (60.6)	0.19 (99.8)	7.94 (70.6)	0.23 (92.9)	0.45 (71.7)	0.27 (65.2)
Q-1dRT-c	4.27 (99.9)	77.70 (67.8)	0.16 (99.8)	5.86 (78.3)	0.20 (93.9)	0.29 (81.8)	0.23 (70.6)
Q-1RT-o	3.90 (100)	59.00 (75,6)	0.12 (99.9)	5.18 (80.8)	0.12 (96.4)	0.31 (80.5)	0.14 (81.6)
Q-1d60°C-c	2.04 (100)	4.80 (98.0)	**0.05** (99.9)	**1.64** (93.9)	**0.02** (99.4)	**0.26** (83.6)	**0.01** (98.4)
Q-1d60°C-o	**1.74** (100)	**4.21** (98.3)	0.06 (99.9)	1.66 (93.8)	**0.02** (99.4)	0.28 (82.4)	0.02 (97.4)

- **Characterisation of the precipitates**

The altered sample Q-1d60°-c was analysed with **SEM**. *Figure 5.13* shows a homogenous precipitation product consisting of only one phase with a hexagonal morphology. The individual particles have a particle size of 50 – 200 nm. The EDX analysis showed a Cu:O ratio of 1:1, corresponding to tenorite (CuO).

.

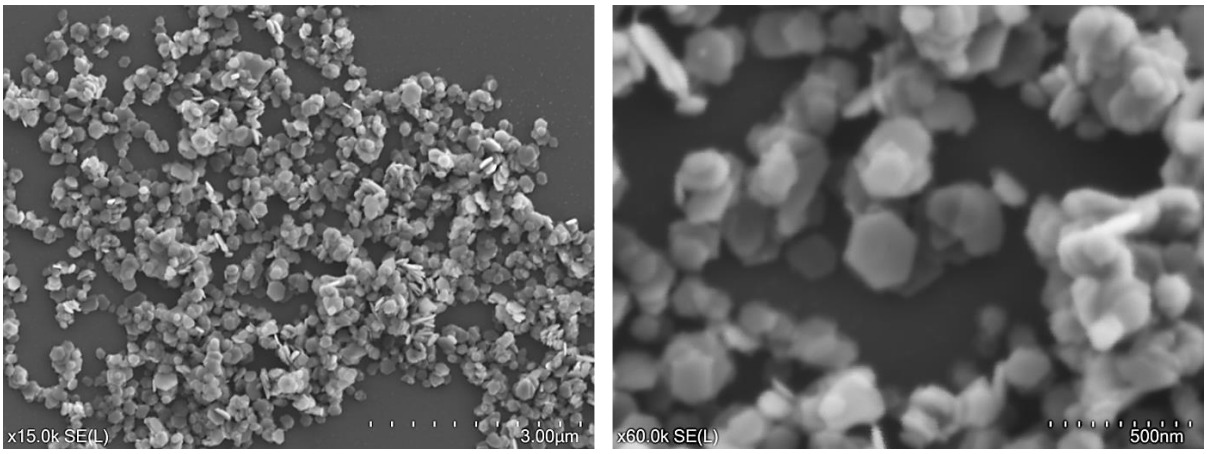

Figure 5.13: *SEM image of sample Q-1d60°C-c shows homogenous tenorite crystals in a hexagonal morphology with particle sizes ranging between 50 – 200 nm.*

The samples aged in a closed vessel (-c) were selected to present the XRD and FTIR results of sample series Q because the samples aged in an open vessel (-o) look similar.

The **X-ray diffractograms** in *Figure 5.14* show sharp diffraction maxima with low background noise. The background noise decreases with ageing. The X-ray diffractogram of the fresh sample Q-f (blue line) shows four diffraction maxima at 16.72, 23.69, 34.09, and 39.81 °2θ that can be assigned to spertiniite ($Cu(OH)_2$). The other diffraction maxima with prominent peaks at 35.49 and 38.56 °2θ, and eight minor peaks at 32.41, 48.82, 53.22, 57.95, 61.50, 66.17, 67.83, and 75.12 °2θ can be allocated to tenorite (CuO). Both altered samples, Q-1dRT-c (red line) and Q-1d60°C-c (green line) show only the presence of tenorite. Reference X-ray diffractograms of CuO and $Cu(OH)_2$ are shown in *Figure IV.5* in the Appendix.

Figure 5.15 presents the **FTIR** spectra of sample series Q. All samples show absorption bands at 432, 497, and 603 cm^{-1}, characteristic of tenorite (CuO). The absorption bands at 603 cm^{-1} and 497 cm^{-1} are assigned to the Cu-O stretching vibration along the direction [101] and [-101] *(Ethiraj and Kang, 2012)*. The absorption bands at 519, 689, and 927 cm^{-1} are only observed in the fresh sample (Q-f) and are assigned to spertiniite ($Cu(OH)_2$) *(Zhu, 2021)*. The characteristic bond at 689 cm^{-1} relates to the Cu-O-H bending mode of the OH group *(Zhu et al., 2021)*. The 839, 1470, and 1630 cm^{-1} bands imply carbonate adsorption (John, 2016), possibly on CuO. Table IV. 3 in the Appendix provides an overview of the phase analysis with XRD and FTIR.

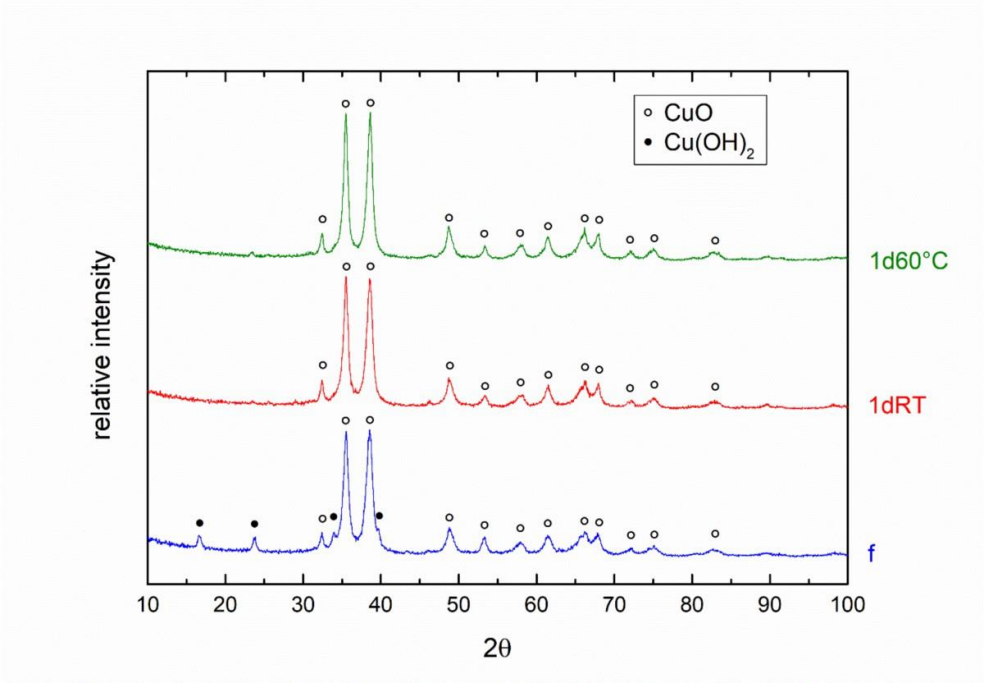

Figure 5.14: *X-ray diffractograms (Cu Kα$_1$) of the sample series Q, after treatment of a Cu-wastewater from the electroplating industry. The fresh sample (blue line) contains CuO and Cu(OH)$_2$. The 1d altered samples at RT (red line) and 60°C (green line) show only CuO.*

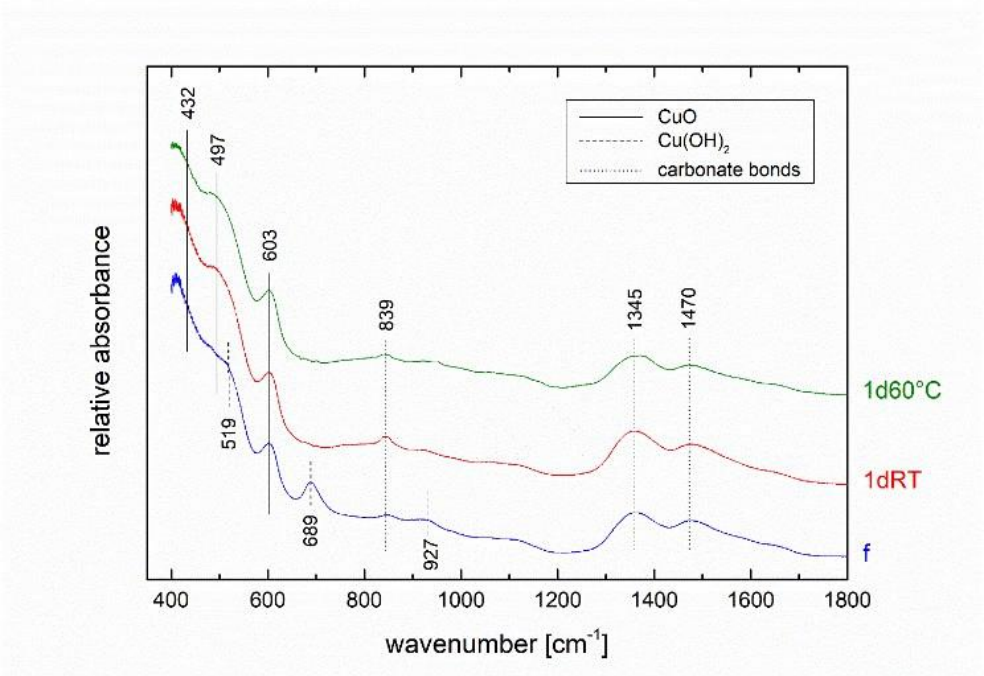

Figure 5.15: *FTIR spectra of the sample series Q. The fresh sample is represented by blue, 1d altered samples at RT in red, and 60°C in green. All samples show the spectral bands of CuO (solid line). Cu(OH)$_2$ (dashed line) was detected in the fresh sample. Additional bands indicate the presence of carbonates (dotted line).*

6. Technical challenges of the SPOP process

The SPOP process is a multi-parameter process and, therefore, has several process steps. Almost all process steps are carried out manually in the laboratory. For the SPOP pilot facility, every process step was transferred for the automatic execution of the process *(Knof, 2017)*The automation included implementing several components, which are introduced in Chapter 3.5.3. Chapter 6.1 presents a technical analysis of these parts, focusing on the components' limitations and influence on the process. It also provides information on the changes that have been made and future recommendations.

With the upscaling, new process parameters became relevant: a more powerful stirrer was used to homogenise the solution, raising the question of whether the stirring speed influences the process products. Therefore, an experimental series was conducted in which the stirring speed was stepwise increased. The results of this investigation are presented in Chapter 6.2.

In case of a technical break-off, the process will likely be interrupted. To test one break-off scenario, adding the Fe-solution was interrupted, leading to oxidation and a wrong Fe^{2+}:Cu^{2+} ratio. The results of this malfunction on the process products are presented in Chapter 6.3.

Another challenge concerns the general procedure of the SPOP process. The process was first designed as a batch process. Hence, it has a defined start and end. Batch process applications are widespread and are favoured for applications with defined and limited output. Conversely, a continuous process is also favourable for continuous production. Therefore, the question of how the SPOP process could be re-arranged to facilitate continuous treatment arose. The experiments performed herein reflected the precipitation conditions of a continuous process and were performed on a laboratory scale. The results of which are presented in Chapter 6.4.

6.1. Technical results and discussion

This study demonstrates that the SPOP process developed on a laboratory scale with 100 – 250 ml reaction volume can be scaled up to 1 litre per sequence, reproducing purification rates and phase quality, as shown in Chapter 5. Nevertheless, there is a need to optimise specific components:

Fluid transport

Fluids are transported via pumps through tubes in the pilot facility, a time-consuming process. In practice, the tubing system was prone to leak at tube connections and valves. Furthermore, the tubes were difficult to clean; they could only be rinsed off, so adhesive particles could only be removed superficially. With a change in the wastewater system, the tubing system had to be exchanged entirely to avoid contamination, which resulted in a high level of piping system

maintenance, including fixing leaks. Therefore, a piping system with membrane pumps is recommended instead of the hose system**.**

Survey of the fluid level

The water level in the reactor is particularly critical because the needed amounts of reagents are calculated using the wastewater volume in the reactor. First, ultrasonic sensors (*HC-SR04, elegoo*) were used to determine the water level. However, in practice, the water level values proved erroneous due to interference signals caused by the various installations in the tanks (electrodes, agitators, float switches, brackets, tubes). Furthermore, condensation and splash water destroyed the electronics of the ultrasonic sensors, resulting in incorrect or no level readings being displayed. The failure of the ultrasonic sensors caused false measurement values and, hence, an uncontrolled addition of Fe solution and base solution, significantly impacting the process in the reactor. In one case, an incorrect addition of Fe-solution caused a wrong Fe/Me ratio in the solution and the precipitation of hydroxide sludge. In another case, a wrong volumetric addition of NaOH solution led to unwanted phases precipitated and low water purification.

Therefore, stable fluid level detection is crucial for successfully executing precipitation. Capacitive sensors (*KQ6003, ifm*) measure the water level by a change of the electrical capacitance; they have the advantage of being precise and robust. Tests delivered good results. Depending on the requirements, the maximum or minimum filling level was set, e.g., to empty or fill the container. The reproducibility of the volume during the iterations of the precipitation process was shown to be higher with the capacitive sensors than with the ultrasonic sensors.

Temperature control

Another challenge is to optimise the heating process. For safety reasons, the boiler with a 10 l capacity must be filled with wastewater before heating can start. Hence, the whole volume must be heated to the reaction temperature, which takes about 20 min. At the end of the treatment, this procedure results in a dead volume of 9 l of wastewater, which must be returned to the raw water tank. Therefore, it is recommended to reduce the volume of the boiler to minimise the heating time and the dead volume or temper the wastewater at its source.

Fe-dosing technique

In scaling up the SPOP process, the Fe-dosing technique was changed from powder form in the laboratory to a liquid solution in the pilot plant. The change had no negative impact on the precipitated product or degree of wastewater purification. Both techniques show comparable and good results, i.e., the dosing technique is not critical.

However, a disadvantage of adding Fe-sulphate as a solution is increased reaction volume and, consequently, treated wastewater. Furthermore, adding Fe-solution took about 10 – 15 min,

extending the process time. In comparison, the addition of salt takes only seconds. Industrial processes require a fast process flow; therefore, I recommend enabling powder dosing.

Alkalisation

The alkalisation rate during the precipitation process is a crucial process parameter. Therefore, high precision and fast alkalisation are required. The dosing pump *(Ismatec Reglo ICC)* was tested using different tubes. However, the minimum alkalisation rate needed for metal oxide formation could not be achieved, resulting in the production of hydroxide sludge. Therefore, it was replaced with peristaltic pumps *9QX and 15QQ (Boxer)*, enabling a faster pump rate and, consequently, a higher alkalisation rate, facilitating the production of metal oxides.

Turbidity and Filtration

Solid-liquid separation is critical after the treatment. The degree of sedimentation determines the initiation of the separation of precipitate and clear flow. Due to the predominance of agglomerated nanoparticles, a sensor must be able to detect minor particles in the range of a few microns and smaller.

A Tyndall sensor was used to measure the turbidity of the suspension in the pilot facility's sedimentation tank. First, the turbidity sensor was placed in the lower third of the sedimentation tank. However, this was disadvantageous as the sensor was easily contaminated by adhering particles, and the actual turbidity value of the suspension could not be recorded. The turbidity sensor was positioned directly below the outflow of the sedimentation tank to reduce particle adherence. In this position, the turbidity of the outflowing suspension is measured. For this setup, the particles were let through a transparent tube where the sensor measured the turbidity. The Tyndall sensor was tested with black and white particles, representing the standard colours of the particles produced in the SPOP process. It was found that the measuring point below the outflow of the sedimentation tank only slightly improved particle separation. Suspensions with approx. 40% of suspended solids were already detected as transparent. Accordingly, the installed sensor was not sensitive enough for this application. Discussions with industry partners revealed that turbidity measurements are generally a challenge and are rarely implemented in practice, and usually, an empirically determined sedimentation time is used.

Sedimentation of particles strongly depends on the particles' size and shape and the density difference between particles and liquid. The larger the particle and the higher the density difference between the particle and liquid, the higher the sedimentation rate. The determined settling velocities vary between 20 and 60 minutes. The separation of the clear flow and the concentrated suspension was carried out with a pinch valve. However, overheating of the pinch valve within 12 minutes of operating time forced an unplanned cooling phase. The technical limitations caused an increase in processing time.

Chamber filter presses are a conventional method of sludge treatment. Aquachem GmbH provided a laboratory chamber filter press with different membranes. The press was tested. However, the suspended nanosized ferrite particles blocked its function within 10 minutes of operation. The fine particles plug the membrane's pores and hinder the clear flow from passing.

For the pilot facility's operation, the solution was to replace the pinch valve with a manual valve and filter the suspension manually through a pleated filter. For larger wastewater volumes generated in industry, a more effective solution for particle separation is needed to achieve a greater throughput.

Hard- and Software

One of the tasks to be mastered was the automation of the process. A stable program is necessary for the fast and correct execution of the SPOP process and the proper interaction of the components. A programmable logic controller (PLC) and a suitable programming language were implemented for the automation.

Controllino is a PLC with open-source software that is fully compatible with Arduino. It is a low-budget alternative to many industrially used and expensive PLCs, e.g., *Siemens SIMATIC*, which is not open-source but has proved to be adequate for the SPOP process.

LabVIEW (Laboratory Virtual Instrument Engineering Workbench) is a system-design platform that is used because of its visual programming language. The first version of the SPOP program with a sequential script style enabled the correct interaction of components *(Knof, 2017)*. However, during the testing of the pilot facility, this program showed to have long looping times due to a large script size. As a result, the execution of the process was delayed, and sometimes it crashed. A second rewritten and compressed version of the script allowed program execution response times to be significantly reduced. All steps were appropriately executed, and monitoring of the process parameters is possible. However, *LabVIEW* software updates caused some sub-programs to stop running. As a result, parts had to be rewritten to get the SPOP program rerunning. As a future recommendation, the program could be re-coded with *Controllino's* standard and open-source software, e.g., *Arduino IDE* or *C++*, to improve the stability of the software.

6.2. Influence of stirring rate on precipitation products

The influence of various process parameters has been tested for the SPOP process. *Heuss-Aßbichler et al. (2016)* investigated the impact of the initial Cu^{2+} concentration, the molar ratio of Fe:Cu, the reaction temperature, the final pH, the ageing temperature and the effect of open or closed ageing on the ferrite formation and the formation of Cu-oxides. *John et al. (2016a)* investigated the influence of the reaction pH, the reaction and ageing temperature, the volume, the concentration of NaOH, and the alkalisation rate on the delafossite formation. *Tandon et al. (2018)* investigated the influence of salinity on the precipitation of Zn. The effect of stirring during alteration on phase formation was also investigated *(Tandon, 2021)*. Yet, the impact of the stirring speed on the precipitation process has not been studied for the SPOP process.

Material & Experimental Procedure

Wastewater batch B, a Cu-rich rinsing bath from *WAFA Germany*, Augsburg, was used for the experiments. First, laboratory-scaled experiments were carried out (see Chapter 3.3), and selected concepts were repeated with the pilot facility. The results using recipe B without the addition of Fe are presented next. The experimental parameters are summarised in *Table 6.1*.

Wastewater was tempered to 40 °C. As soon as the reaction temperature was reached, the alkalisation process was started. The stirring speed was varied between 100 and 500 rpm while all other experimental parameters were kept constant. After each experiment, one fresh sample and one altered for one day at 40 °C were analysed.

The sample nomenclature for the kinetic experimental series is as follows:

- Kin_number of revolutions per minute_alteration.

For example, Kin_100_rpm_1d40°C means that the experiment was carried out with a stirring rate of 100 rpm, and afterwards, the sample was altered for one day at 40 °C.

Table 6.1: *Experimental parameters of the experimental series investigating the influence of the stirring rate on the precipitation process.*

	kin_100rpm	**kin_200rpm**	**kin_300rpm**	**kin_400rpm**	**kin_500rpm**
Wastewater	batch B				
Wastewater volume	380 ml				
Reaction temperature	40 °C				
Revolutions per minute	100	200	300	400	500
NaOH	8 M				
Final pH	11				
Alteration temperature	40 °C				
Alteration time	One day				

Results

- **Water purification**

Table 6.2 gives an overview of the analysed initial and treated wastewater. The initial Cu concentration of the wastewater was 9 256.98 mg/l. After the treatment, the highest and lowest residual Cu concentrations were detected for the experiment performed with the slowest rotation speed (100 rpm), with 26.74 mg/l in the fresh sample and 2.19 mg/l in the altered sample, which corresponds to 99.7% of Cu removal by precipitation and by alteration. The Cu concentration was reduced by factor 12 compared to the fresh material.

A rotation speed of 200 rpm resulted in a similar effect. The fresh sample showed a residual Cu-concentration of 22.85 mg/l, while the altered sample had a significantly lower value of 2.20 mg/l. The increase of the rotation speed to 300 rpm increased the recovery rate of Cu, with a residual Cu concentration of 5.14 mg/l for the fresh sample and 4.36 mg/l for the altered sample. A similar result was obtained for the samples stirred at 400 rpm. Increasing the stirring rate to 500 rpm did not cause any improvement, with 7.70 mg/l Cu for the fresh sample and 4.82 mg/l for the altered sample.

The initial **Fe** concentration was 1 680.44 mg/l. After treatment, all recovery rates of Fe were better than 99.9%. The fresh sample Kin_100rpm_f shows with 0.20 mg/l the highest remaining Fe concentration, and with increasing rotation speed, the Fe concentration decreased to 0.06 mg/l at 400 rpm and below the detection limit (< ppm) for 500 rpm. Alteration showed a decreased Fe concentration only at slow rotation speed (< 200 rpm).

The treatment removed **Ni** with an initial concentration of 57.16 mg/l to values below the limits. In general, the Ni concentration was < 0.06 mg/l, which corresponds to a recovery rate of 100%.

The fresh sample's initial Zn concentration of 56.42 mg/l was reduced to 1.81 mg/l at 100 rpm (recovery rate of 96.8%), and with increasing rotation speed up to 400 rpm, it was further decreased to 0.30 mg/l, which corresponds to a recovery rate of 99.5%. Alteration reduced those values only slightly.

The initial concentration of **Pb** was 2.15 mg/l. The highest remaining concentration was detected in the fresh sample Kin_100rpm_f with 0.27 mg/l, corresponding to a recovery rate of 87.4%. With increasing rotation speed, the Pb concentration dropped below the detection limit at 300 and 400 rpm.

For Fe, Zn, Ni, and Pb, all treated samples fulfil the discharge limit value according to the *Abwasserverordnung, Anhang 40* (see *Table IV.1* in the Appendix). The initial concentrations of Cr and Mn were below the detection limit for all samples and, therefore, not considered in *Table 6.2*.

In summary, the fresh samples stirred with the slowest stirring speed at 100 rpm show the highest remaining metal concentrations but the lowest for the altered samples. As the stirring

speed increases to 300 to 400 rpm, the remaining concentration of the metals in the fresh samples decreases. Alteration generally reduces the concentration.

Table 6.2: *The water analysis results measured with ICP-MS of the initial sample and after treatment with different stirring speeds. The first row shows the limit values for the discharge of each metal according to the* Abwasserverordnung, Anhang 40. *Metal recovery rates in (%) are given in brackets. Green-filled fields indicate compliance with the limit value for discharge.*

Sample	**Cu (mg/l)**	**Fe (mg/l)**	**Ni (mg/l)**	**Zn (mg/l)**	**Pb (mg/l)**
Limit value for discharge	0.5	3.0	0.5	2.0	0.5
kin_ini	9 256.97	1 680.44	57.16	56.42	2.15
kin_100rpm_f	26.74 (99.7)	0.20 (100)	0.06 (99.9)	1.81 (96.8)	0.27 (87.4)
kin_100rpm_1d40°C	**2.19 (99.9)**	0.19 (100)	0.04 (99.9)	1.41 (97.5)	0.11 (94.9)
kin_200rpm_f	22.85 (99.8)	0.15 (100)	0.26 (99.5)	0.76 (98.7)	0.04 (98.1)
kin_200rpm_1d40°C	**2.20 (100)**	0.13 (100)	0.05 (99.9)	1.06 (98.1)	0.07 (96.7)
kin_300rpm_f	5.14 (99.9)	0.09 (100)	0.02 (100)	0.30 (99.5)	b.d.l.
kin_300rpm_1d40°C	4.36 (99.9)	0.10 (100)	0.04 (99.9)	0.31 (99.5)	b.d.l.
kin_400rpm_f	4.95 (99.9)	0.06 (100)	0.02 (100)	0.30 (99.5)	b.d.l.
kin_400rpm_1d40°C	3.46 (99.9)	0.06 (100)	0.03 (99.9)	0.26 (99.5)	b.d.l.
kin_500rpm_f	7.70 (99.9)	b.d.l.	0.03 (99.9)	0.61 (98.9)	0.02 (99.1)
kin_500rpm_1d40°C	4.82 (99.9)	b.d.l.	0.05 (99.9)	0.57 (98.9)	0.02 (99.1)

- **Characterisation of the precipitates with XRD and FTIR**

Table IV.4 in the Appendix gives an overview of all detected phases.

XRD: The X-ray diffractograms of the altered samples are shown in *Figure 6.1*. The highest intensities were observed in the sample stirred at 100 rpm. The two prominent peaks at 35.48 and 38.54 °2θ corresponding with the (-111) and (111) planes identified as tenorite (CuO), the minor diffraction maxima are at 32.40, 48.81, 53.21, 57.93, 61.49, 66.15, 67.81, and 75.10 °2θ. The sample stirred at 200 rpm shows similar diffraction maxima. Additional weak diffraction maxima at 16.71 and 23.68 °2θ were assigned to the (020) and (021) plane of spertiniite ($Cu(OH)_2$). Samples with higher stirring speeds (300 and 400 rpm) lead to the same result but are associated with higher background noise. In addition, the peaks have a lower intensity and a broader shape, indicating a lower crystallinity of the phases. Sample 500rpm_1d40°C, however, shows an entirely different diffractogram. The diffraction maximum with the highest intensity is at 35.75 °2θ. All diffraction maxima are assigned to brochantite ($Cu_4(OH)_6SO_4$). The reference diffractograms for tenorite, spertiniite and brochantite are shown in *Figure IV.5* in the Appendix.

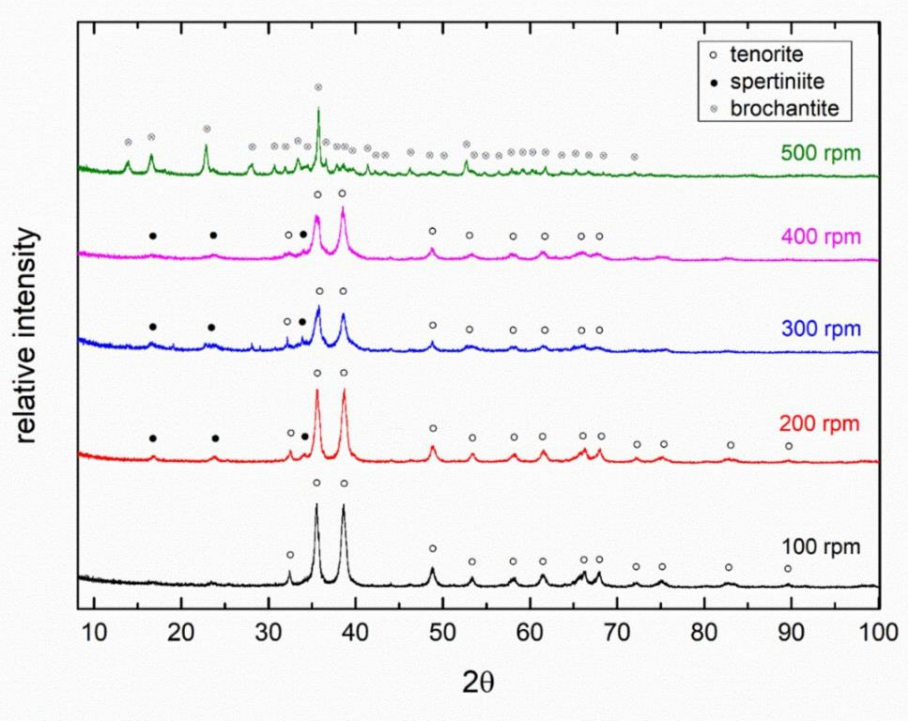

Figure 6.1: *X-ray diffractograms of the altered samples for one day at 40 °C. Stirring at 100 rpm leads to tenorite (CuO) as the only phase. With increasing stirring rate (200 – 400 rpm), spertiniite ($Cu(OH)_2$) emerges additionally to CuO. At 500 rpm all diffraction maxima correspond to brochantite ($Cu_4(OH)_6SO_4$).*

In comparison, the X-ray diffractograms of the fresh samples stirred at 100 up to 200 rpm match with tenorite and spertiniite. The samples stirred at 300 and 400 rpm also show weak diffraction maxima assigned to brochantite. The fresh and altered samples stirred at 500 rpm

show only diffraction maxima attributed to brochantite. *Figure IV.6* in the Appendix shows the fresh samples' X-ray diffractograms. Accordingly, tenorite forms with slower stirring speeds and brochantite forms with increasing stirring speeds.

FTIR: The results of the FTIR analysis are presented in *Figure 6.2*. There is a clear difference between the lower and the highest rotation speed at 500 rpm. The samples stirred at 200 to 400 rpm show the presence of thenardite (Na_2SO_4), tenorite (CuO) and spertiniite ($Cu(OH)_2$). Thenardite was characterised by its band at 1109 cm^{-1}. The band at 603 cm^{-1} refers to CuO caused by the Cu-O stretching vibration along [-101] *(Ethiraj and Kang, 2012)*. All samples stirred at 200 – 400 rpm show a band at 689 cm^{-1} that refers to the bending vibration of hydrogen-bonded OH groups originating from Cu-O-H bending of $Cu(OH)_2$ *(Zhu et al., 2021)*. The samples stirred at 500 rpm show absorption bands, all solely assigned to brochantite. The bands at 3580 cm^{-1}, 3560 cm^{-1}, and 3400 cm^{-1} can be assigned to the ν(OH) vibration of brochantite *(Malvault et al., 1995)*. The bands between 1127 cm^{-1} and 733 cm^{-1} are caused by internal vibrational modes of sulphate ions *(Secco, 1988; Malvault et al., 1995)*. Bands below 509 cm^{-1} are assigned to the ν_2 internal mode of SO_4^{2-} and Cu-O vibrations *(Malvault et al., 1995)*.

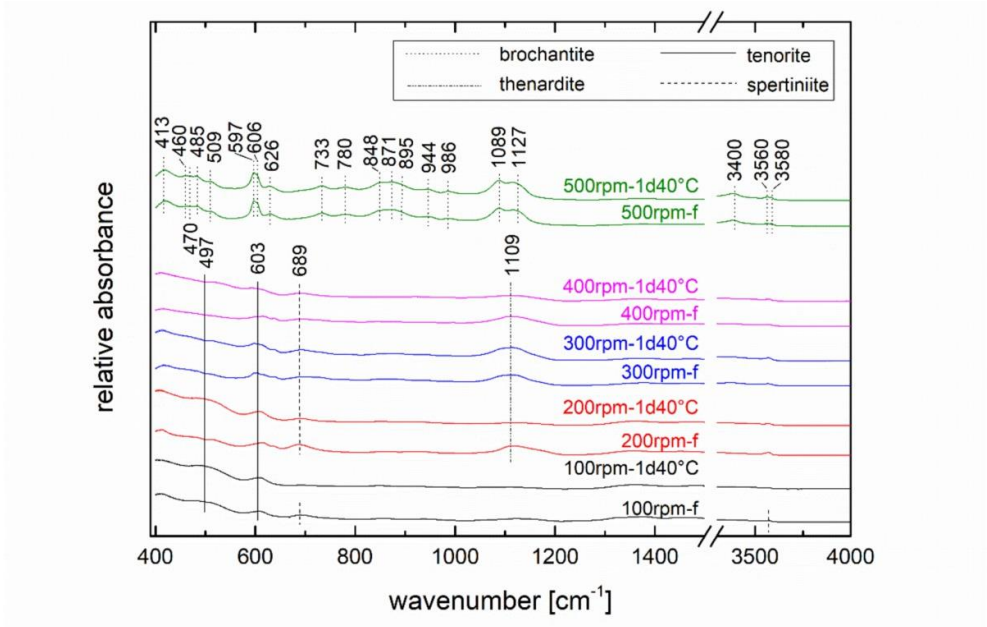

Figure 6.2: *FTIR spectra of all samples synthesised between 100 and 500 rpm.*

- **Phase relationship on stirring rate**

Figure 6.3 graphically shows the occurrence of the phases in fresh and altered samples in dependence on stirring rate. An increase in the intensity of the colour corresponds to a rise in the phase quantity.

Tenorite, spertiniite, and thenardite coexist in the fresh samples stirred at a slow stirring rate of 100 – 200 rpm. The highest amount of spertiniite is observed in the fresh samples. Alteration of the precipitates without stirring for one day at 40 °C promotes the formation of tenorite, pointing to a recrystallisation process. The quantity and crystallinity of spertiniite and cuprite decrease with increasing stirring rate. Brochantite appears first at a stirring speed of 300 – 400 rpm; at 500 rpm, only brochantite occurs.

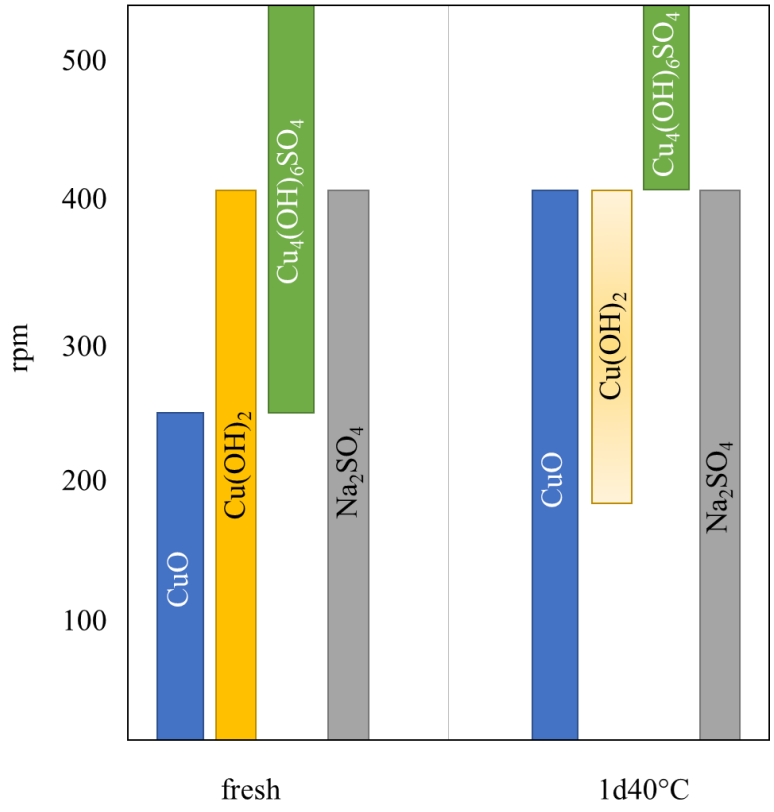

Figure 6.3: *The occurrence of phases depending on the stirring speed (rpm) for the fresh and altered samples. $Cu(OH)_2$ in the altered samples exists only as traces, as light yellow indicates.*

- **Effects of phase formation on water purification**

Figure 6.7 combines the water and solid phase analyses. It shows the dependency of the residual Cu concentration in the filtrate on the formed phases. Three different sections can be distinguished: At low speeds (100 – 200 rpm), the fresh samples expose the highest residual Cu concentration, while the 1-day-aged samples have the lowest Cu concentration. This trend correlates with a high content of spertiniite in the fresh sample, which converts to tenorite with ageing.

At stirring rates > 300 rpm, brochantite, spertiniite, and thenardite precipitated in the fresh samples. Brochantite was not found in the corresponding aged samples; instead, tenorite, thenardite and minor amounts of speriniite were detected. Ageing did not significantly change the residual Cu concentration.

Brochantite is the only Cu-phase formed at high stirring speeds (> 500 rpm). The residual Cu-concentrations for the experiments showing solely brochantite are low, with a slightly decreased concentration of the altered samples. However, the decrease in Cu concentration for the altered brochantite samples is not as significant as for the altered samples in which a phase transformation from spertiniite to tenorite took place.

Consequently, phase formation can be influenced by varying the stirring speed: spertiniite, thenardite, and tenorite precipitate at low rotational speeds and brochantite at high rotational speeds, leading to a final composition in aged samples of tenorite and thenardite (> 400 rpm) and brochantite (500 rpm).

Figure 6.4 clearly shows a high residual Cu concentration for the experiments in which spertiniite formed, indicating a high solubility of spertiniite. In comparison, tenorite and brochantite show lower residual Cu concentrations, with tenorite showing the lowest, marking the lowest solubility. The results of the experiments without Fe-addition (Chapter 5.3.2) likewise show that spertiniite transforms to tenorite during alteration, which is accompanied by a reduction of Cu in the filtrates. Hence, the solubility is highest for spertiniite, intermediate for brochantite, and lowest for tenorite. *Koga et al. (1997)* found that brochantite decomposes to tenorite under thermal dehydration and desulfuration. Therefore, the most stable phase of this system is tenorite. Concerning water purification, the most efficient reaction pathway is precipitation and alteration of spertiniite and tenorite.

Therefore, the most efficient method for water purification is the formation of tenorite at a low stirring speed.

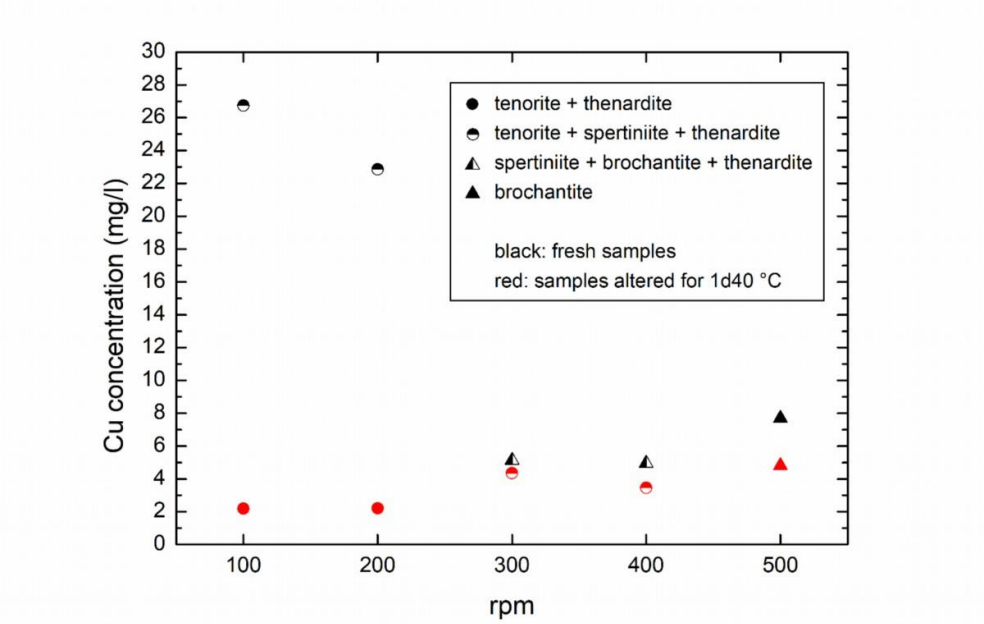

Figure 6.4: *Correlation of Cu concentrations with stirring speed and phase assemblage. The fresh samples are in red, and the samples altered for one day at 40 °C are black.*

- **Effect of stirring rate on the redox state**

Figure 6.5 shows the redox state in dependence on the stirring speed during the stationary titration for each experiment; it also indicates the formed fresh phases. The bars indicate the minimum and maximum redox values measured for each experiment and the data points the average value. The redox state shows a shift towards oxidising conditions with increasing stirring speed. Tenorite, spertiniite, and thenardite formed at the lowest redox states of average –302 mV to –267 mV (100 – 200 rpm). At 300 and 400 rpm, the redox state increases to intermediate values of average –203 to –173 mV; in this regime, brochantite, spertiniite and thenardite formed. Brochantite formed as a single phase at the highest measured redox state (500 rpm) at an average of –146 mV.

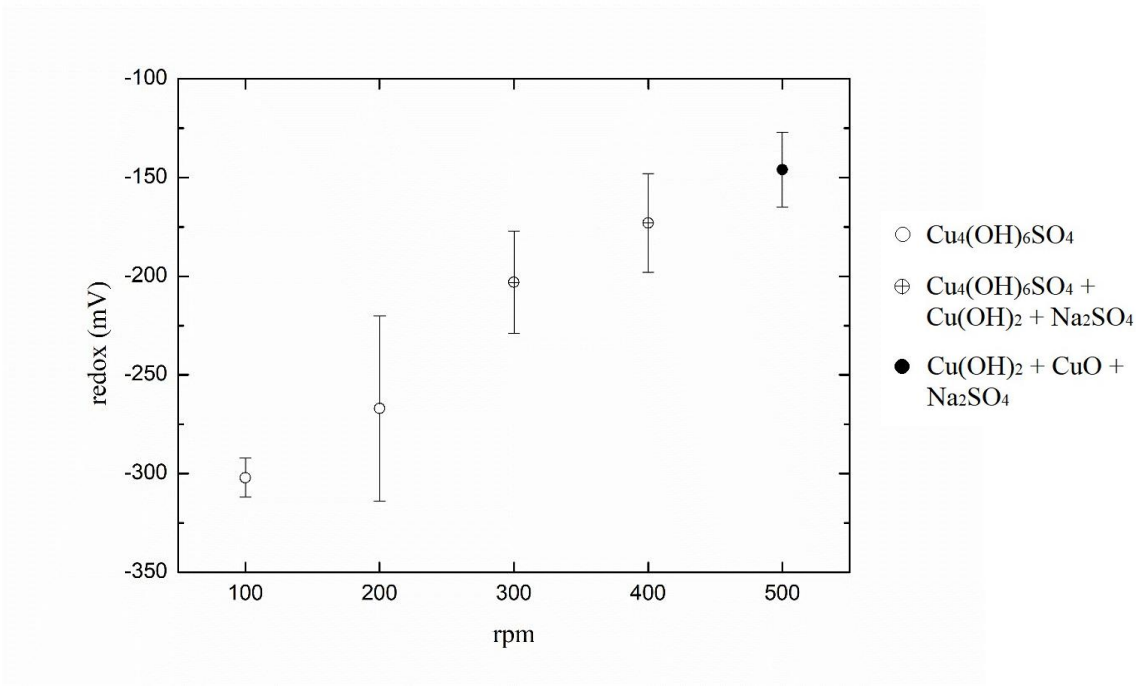

Figure 6.5: *Phase occurrences and redox state during the stationary titration phase depending on the stirring rate. The formed phases change depending on stirring rate/redox conditions. With redox conditions shifting from reducing towards oxidising, the phase assemblage changes from $Cu(OH)_2$, CuO, and Na_2SO_4 to $Cu_4(OH)_6SO_4$.*

- **Effect of the stirring rate on the alkalisation rate**

The final pH was ca. 11 for all experiments (see *Table IV.5* in the Appendix), yet the volume of added NaOH and the alkalisation rate varied. The alkalisation rate AR is based on the linear titration and was calculated with the following equation:

$$AR = \frac{pH_{end} - pH_{start}}{t_{alkalisation}} \quad (7)$$

with pH_{start} being the pH value at the beginning, pH_{end} the pH value at the end of the titration, and $t_{alkalisation}$ the alkalisation duration.

The results show that the volume of added NaOH and the AR vary depending on the stirring rate *(Figure 6.6)*. At the low stirring speed (100 rpm), the AR (0.03 pH/sec) is lowest, although the largest amount of NaOH (53 ml) is consumed. At 200 rpm, the AR increases (0.048 pH/sec), and the consumed NaOH decreases (41.4 ml). At 300 rpm, the AR increases (0.07 pH/sec), and NaOH consumption decreases (24.4 ml NaOH). At 400 rpm, the AR is highest (0.084 pH/sec), but the consumed NaOH stays stable (25 ml). At the highest stirring speed of 500 rpm, the alkalisation rate (0.057 pH/sec) is intermediate, but the least amount of NaOH (22 ml) was consumed. Accordingly, the volume of added NaOH decreases and the alkalisation rate AR increases with increasing stirring rate. The decrease in the alkalisation rate can be considered a technical effect: At low stirring rates, the added NaOH solution is distributed slowly, which leads to local pH differences across the water column. Accordingly, the signal at the pH

electrode is exposed to fluctuations. Before thorough NaOH distribution, the pH at the position of the electrode is higher than the control value (due to the position of the pH electrode in the beaker). Hence, no NaOH is added and so the AR is reduced. After thorough NaOH distribution, the pH measurement value drops below the pH control value. A continuous addition of NaOH is released until the control value is met, resulting in a large volume of added NaOH.

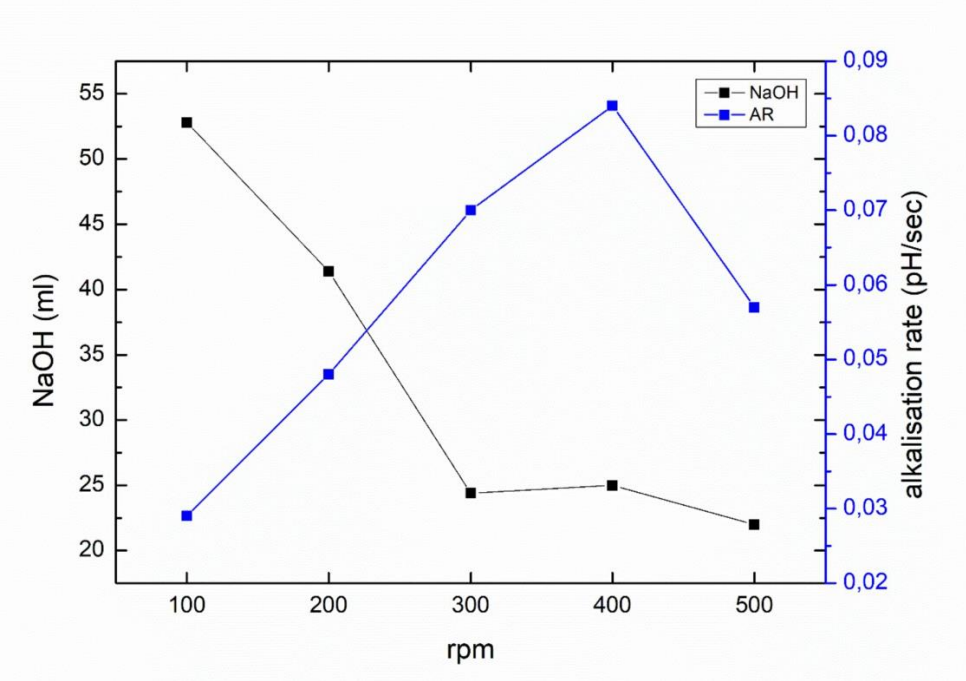

Figure 6.6: *Dependency of the stirring speed on the alkalisation rate. The volume of the NaOH solution depends on the stirring speed (black cubes) and the alkalisation rate (blue cubes). With increasing stirring speed, the AR decreases, and the volume of added NaOH solution rises.*

6.3. Impact of malfunctions

In industrial production, rest periods of the manufacturing process and the wastewater treatment may occur due to, e.g., production-free weekends, staff shortage, reparation, or changes in the production process. The impact of such events on wastewater treatment with the SPOP process must be considered. One aspect is the impact of storing a solution with additives for extended periods. For example, extended exposure to air can cause the oxidation of the Fe solution to Fe^{3+}. Using such an oxidised Fe-solution causes an inaccurate and non-stoichiometric Fe^{2+}/Fe^{3+} ratio in the wastewater. The experimental series P demonstrates the effect of an unknown Fe valence ratio and its consequences on the composition of the precipitation products.

Experimental setting

Wastewater batch A was used for the experimental series P. The experimental parameters are summarised in *Table 6.3;* the process sequence for cuprospinel formation was applied. The

solution was treated with a four-molar NaOH solution under the addition of Fe_{total} with a molar ratio of Cu^{2+}:Fe^{total} = 1:2. The Fe^{2+} solution was prepared with $Fe(II)SO_4*7H_2O$ and then was set aside for two days, open under air. The valence ratio of Fe^{2+}:Fe^{3+} was not determined.

Table 6.3: *Experimental parameters of sample series P.*

Sample series	P-f	P-1d60°C	P-5d60°C
Wastewater batch		A	
Wastewater volume		4 x 800 ml	
Mole ratio Cu:Fe^{total}		1:1.4	
Reaction temperature		60 °C	
Molarity of NaOH		4	
Final pH		8	
Ageing temperature	-	60 °C	60 °C
Closed ageing	-	yes	yes

Results

The following present the results of the experimental series P with the fresh sample (P-f), a sample altered for one day at 60 °C (P-1d60°C), and one sample altered for five days at 60 °C (P-5d60°C).

- **Water purification**

Table 6.4 summarises the water analysis results. Green-filled fields indicate compliance with the discharge limit according to the *Abwasserverordnung, Anhang 40* (see *Table VI.1* in the Appendix).

Cu: The initial Cu concentration in the wastewater is 8 235.95 mg/l. After the treatment, the Cu concentration of the fresh (P-f) and 1-day-aged samples (P-1d60°C) dropped below the detection limit and met the discharge limit (0.5 mg/l). However, the 5-day-aged sample (P-5d60°C) showed a higher residual Cu value of 3.04 mg/l, indicating the instability of the Cu precipitates. In all cases, the recovery rate was better than 99.9%.

Fe: The initial total Fe concentration was 16 684.22 mg/l. After treatment, the Fe content of the fresh sample (P-f) decreased to 140.4 mg/l, corresponding to a recovery rate of 99.1%. The aged samples P-1d60°C and P-5d60°C showed a higher Fe concentration of 1 325.0 mg/l and 1 124.3 mg/l, respectively.

Ni: The initial Ni-concentration in the wastewater was 58.15 mg/l. After treatment, the Ni concentration of the fresh sample was very low (1.18 mg/l), corresponding to a removal rate

of 97.9%. In comparison, the altered samples P-1d60°C and P-5d60°C show higher Ni concentrations of 11.63 mg/l and 11.47 mg/l, respectively.

Zn: The initial Zn concentration was 57.75 mg/l. The concentrations of all treated samples are similar, ranging between 6.0 mg/l for the fresh sample and one-day aged P-1d60°C and 7.28 mg/l for the five-day aged sample P-5d60°C. It corresponds to a recovery rate of about 89%.

Cr: The initial concentration of Cr was 1.53 mg/l. After treatment, the Cr concentration of all samples was below the detection limit (ppb) and accordingly met the discharge limit for Cr (0.5 mg/l).

Pb: The initial Pb concentration was 2.17 mg/l. After treatment, the fresh sample (P-f) had the lowest Pb concentration, 0.13 mg/l, corresponding to a recovery rate of 93.9%. Both altered samples, P-1d60°C and P-5d60°C, showed slightly higher Pb concentrations of 0.17 mg/l and 0.2 mg/l, respectively. All treated samples met the Pb limit values for discharge (0.5 mg/l).

Mn: The initial concentration of Mn in the wastewater was 15.27 mg/l. The fresh sample (P-f) showed 5.90 mg/l Mn, the lowest value corresponding to a recovery rate of 61.4 %. Both altered samples, P-1d60°C and P-5d60°C, showed higher concentrations with 10.55 mg/l and 10.11 mg/l, respectively. In general, Mn shows the lowest recovery rate of all metals.

This example shows that the longer the alteration lasts, the higher the Cu and Fe concentrations are, which indicates that some precipitated phases are unstable. Their decomposition releases Cu and Fe into the solution. The same trend is observable for the minor elements Ni, Zn, Cr and Mn.

Table 6.4: *Water analysis results with ICP-MS of sample series P and the limit values for each metal according to the* Abwasserverordnung, Anhang 40. *Metal recovery rates in (%) are given in brackets. Green-filled fields indicate compliance with the limit value for discharge.*

	Cu	**Fe**	**Ni**	**Zn**	**Cr**	**Pb**	**Mn**
	(mg/l)						
Limit value for discharge	0.5	3.0	0.5	2.0	0.5	0.5	-
P-ini	8 235.95	16 684.22	58.15	57.75	1.53	2.17	15.27
P-f	<0.0 (100)	140.40 (99.1)	1.18 (97.9)	6.0 (89.6)	<0.0 (100)	0.13 (93.9)	5.90 (61.4)
P-1d60°C-c	<0.0 (100)	1 325.00 (92.1)	11.63 (80.0)	6.0. (89.6)	<0.0 (100)	0.17 (92.1)	10.55 (30.9)
P-5d60°C-c	3.04 (100)	1 124.30 (93.3)	11.47 (80.3)	7.28 (87.4)	<0.0 (100)	0.20 (90.8)	10.11 (33.8)

- **Characterisation of the precipitates**

XRD: *Figures 6.7* and *6.8* show the X-ray diffractograms and FTIR spectra of the experimental series P. Only the results of the samples aged in a closed container (-c) are shown, as those aged in an open container (-o) were similar.

All X-ray diffractograms of sample series P in *Figure 6.7* show a high background signal. The diffractogram of the fresh sample P-f (blue line) shows one broad and clear diffraction maximum at 2θ = 35.52 °2θ (Cu $K\alpha_1$), which is attributed to the (311) peak of magnetite/cuprospinel or maghemite. Other diffraction maxima with weak intensity at 2θ = 30.15, 57.07, and 62.79 °2θ correspond to the (202), (511), and (404) lattice planes, respectively. Small diffraction maxima belong to cuprite (Cu_2O), with the most intense peak at 36.38 °2θ corresponding to the lattice plane (111).

The X-ray diffractograms of the sample altered for one day at 60 °C (red line) and five days at 60 °C (green line) look essentially similar to the fresh one. Two other weak diffraction maxima at 2θ = 23.7° and 26.1° are assigned to maghemite, which indicates a phase transformation from cuprospinel/magnetite to maghemite. The diffraction maximas' higher intensities indicate cuprite growth at 2θ = 36.38°, 42.27°, and 61.28°.

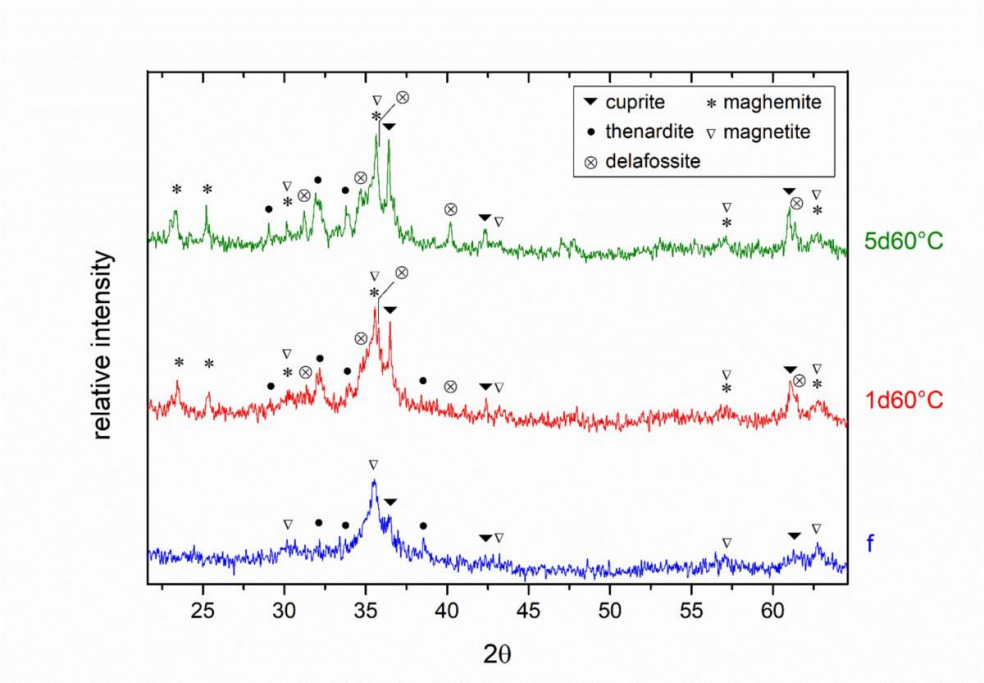

Figure 6.7: *X-ray diffractograms (Cu $K\alpha_1$) of the sample series P. It shows the effect of aeration on the solution. The fresh sample (blue line) contains ferrite and cuprite. Both samples altered for one day (red line) and five days (green line) at 60 °C show a higher proportion of cuprite, additional maghemite, and delafossite. The soluble salt thenardite (Na_2SO_4) is observed in all samples.*

FTIR: The IR spectra of the three samples are shown in *Figure 6.8*. All samples show absorption bands at 1110, 1148, and 1334 cm^{-1}, assigned to green rust (GR). The other bands confirm the results obtained by the X-ray diffractograms. A weak absorption band at 632 cm^{-1} observed in all samples corresponds to the cuprite's Cu–O bond (Zhang et al., 2014). The samples also show an absorption band at 585 cm^{-1}, which is characteristic of ferrites, including maghemite; it refers to the stretching vibration of Fe-O in octahedral and tetrahedral coordination. Both altered samples show five additional bands at 608, 795, 876, 895, and 1064 cm^{-1}, characteristic of maghemite *(Chukanov, 2014)*. Bands at 838, 1345 and 1469 cm^{-1} belong to carbonate modes *(Heuss-Aßbichler et al., 2016b; John, 2016)*. The fresh sample does not show maghemite and delafossite absorption bands compared to both altered samples. Hence, the fresh sample's phase assemblage is composed of fewer phases.

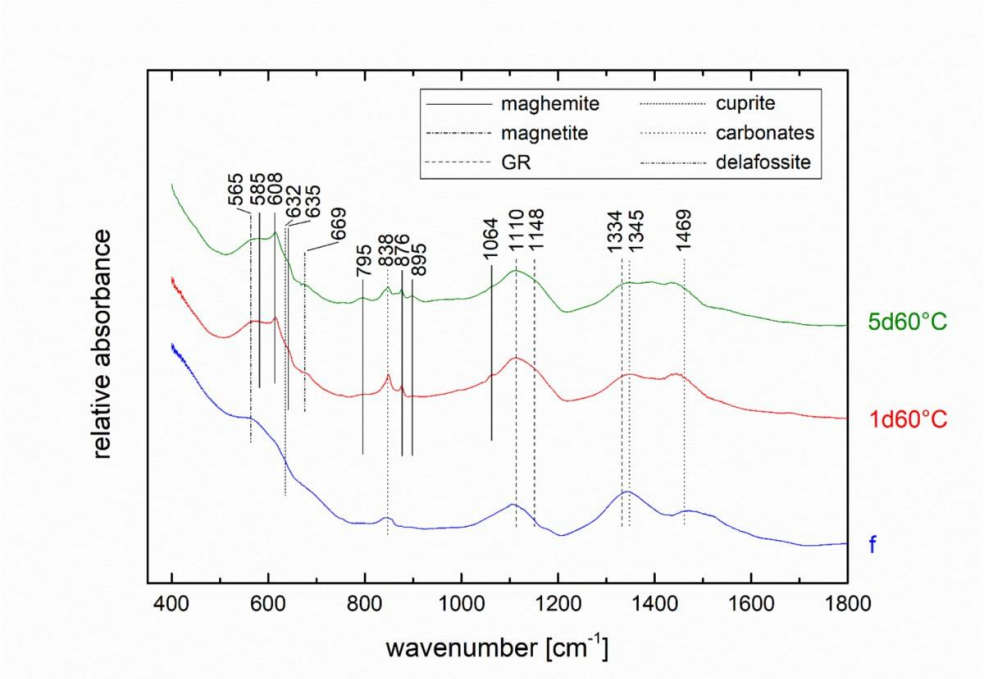

Figure 6.8: *FTIR spectra of the sample series P. The fresh sample (blue line) shows absorption bands of cuprite (narrow dotted line) and green rust GR (dashed line) and weak bands related to magnetite (dash-dot line) or maghemite (solid line) as well as atmospheric carbonate adsorption (dotted line). Both samples, altered at 60 °C for one day at room temperature (1d60°C, red line) and five days (5d60°C, green line), show additional absorption bands related to maghemite.*

SEM: *Figure 6.9* shows two SEM images of the 1-day aged sample P-1d60°C. A summary of the phases found in sample series P is given in *Table IV.3* in the Appendix.

The largest crystals in the phase assemblage are cubes with an edge length of 0.5 nm. EDX analysis identified them as cuprite (Cu_2O) due to a ratio of Cu:O = 2:1. The other dominant phase is needle-like crystals of 10 to 50 nm, identified as green rust GR. The large mass is built by small particles with a partially octahedral shape and 5 – 10 nm size, which clump together into massive clusters. They were identified as ferrite crystals by EDX analysis.

In sum, Fe is bound in the ferrites and the green rust. The Cu is mainly bound in larger cuprite crystals and partly incorporated in ferrites. The increase in Cu concentration in the solution of the aged samples indicates that part of the Cu is adsorbed on green rust GR. The minor metals, Ni, Zn, Cr, Pb and Mn, were detected in ferrite and GR.

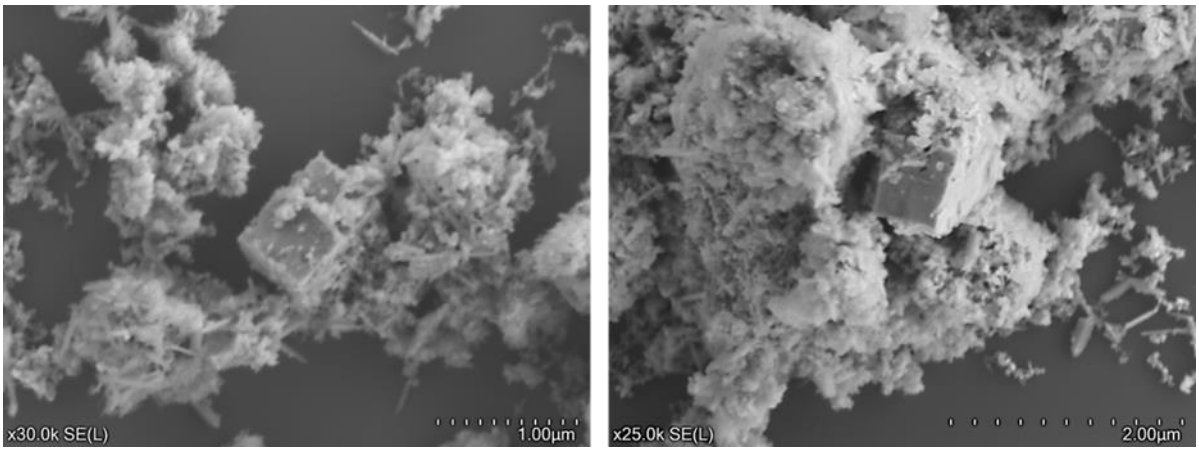

Figure 6.9: *SEM image of the 1-day aged sample P-1d60°C. Cu was detected as cuprite in the large cube-shaped particles with an edge length of 1 µm and clusters of 5 – 10 nm particles identified as ferrite. They dominate the phase assemblage. The needle-like phase with a size of 20 to 80 nm was identified as green rust (GR).*

6.4. Continuous flow SPOP process

Manufacturing processes are carried out as either batch or continuous processes. A batch process treats a specific quantity of wastewater in a single treatment run. It has a defined start- and end-point. Hence, the process is completed once the batch of wastewater has been processed. The SPOP process was first designed and tested as a batch process. Continuous processes are designed so treatments or productions are ongoing without a defined start and endpoint. Therefore, the treatment process is constant without stopping.

Batch processes can be slower than continuous processes because the reaction sequence requires a stop and a start after each batch. Furthermore, the treatment rate is limited because it depends on the capacity of the wastewater tanks. Hence, the production output of a batch

process is generally lower than that of a continuous process, which can treat more significant volumes of wastewater at a constant rate.

Regarding flexibility, batch processes are more flexible than continuous processes because equipment can be exchanged or modified easily. Therefore, batch processes are ideal for first-process developments. On the other side, all materials are continuously induced into the system for continuous treatment processes, which makes it less flexible but also requires stable and sophisticated components.

For wastewater treatment, the choice of treatment process depends on the amount of wastewater and its frequency of occurrence. For example, a batch wastewater treatment process can be more suitable for a defined amount of discontinuously accruing wastewater (e.g., Au-containing wastewater from chemical catalyst production), for whose treatment no fast flow rate is necessary. On the contrary, a continuous treatment process can perform better for wastewater that accrues continuously and where a fast flow rate of wastewater treatment is needed.

For the SPOP process to apply to different wastewater treatment requirements, a continuous flow SPOP process has been tested. Therefore, the experimental setup has been changed. The results of the continuous flow process and a possible technical realisation of it are summarised in this chapter.

Process flow of the SPOP batch and continuous processes

The sequence of material flow had to be changed to enable a continuous flow process. *Figure 6.10* shows the two different process flows of SPOP: batch and continuous flow. For the SPOP batch process, the reactor is filled with wastewater. Optionally, Fe solution is added to the wastewater; then, a base solution is added to initiate the precipitation process. In the end, the whole suspension is removed. Contrarily, the reactor is filled with a base solution and constantly supplied with wastewater (optionally mixed with Fe^{2+} salt) for the continuous process. Likewise, the residue is continuously removed.

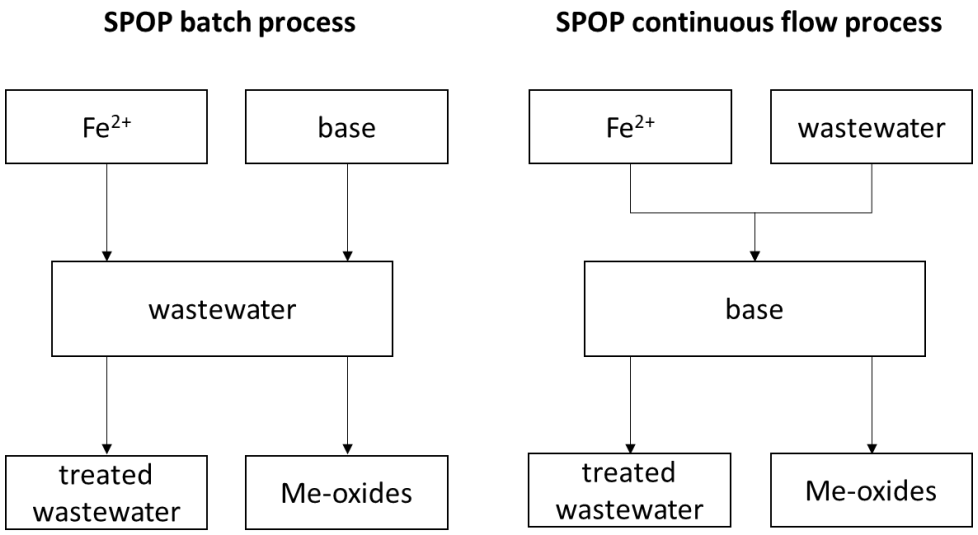

Figure 6.10: *Comparison of material flow in the SPOP batch and continuous flow processes.*

Two different receipts were tested as continuous flow experiments on a lab scale: a) The formation of Cu-ferrite because it is well known and B) the formation of delafossite because its formation mechanism is not yet fully understood.

- **Experimental setup**

The workflow of the continuous experimental setup is shown in *Figure 6.11*; it implies specific changes: In two containers, Fe^{2+} salt mixed with the wastewater and the NaOH solution are heated to reaction temperature. In this case, the (Fe-bearing) wastewater is added to the NaOH solution in the reaction vessel. The pH change is monitored, and additional NaOH solution is added if necessary.

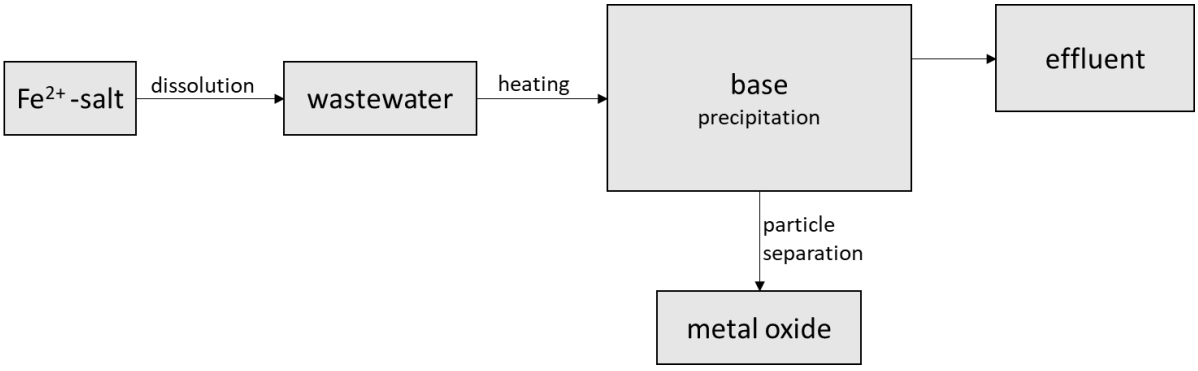

Figure 6.11: *Workflow of the continuous flow SPOP process.*

The precipitation occurred under continuous stirring using an overhead stirrer *(HEITORQUE, Heidolph)*. The pH of the base is continuously surveyed with a pH electrode *(Blue Line 14, SI analytics)*, and the pH value is controlled with an automated titration unit *(Titrator 7800, SI Analytics)*.

- **Materials and experimental parameters**

The continuous process (cp) was tested with Cu-bearing model wastewater based on Cu concentrations found in the rinse bath of electroplating facilities. The synthetic wastewater was produced with $CuSO_4*7H_2O$ (Chemsolute) and $FeSO_4*7H_2O$ (Chemsolute). All chemicals were of analytical grade. The concentration of Cu in the synthetic wastewater was set to 10 g/L (with one exception of 3 g/l). The influence of the following experimental parameters was tested: the molar ratio of Cu:Fe (1:1 and 1:2), the concentration of the NaOH solution (0.4, 16, and 32%), and the reaction temperature (30 and 60 °C). All experimental parameters are summarised in *Table 6.5*.

The sample nomenclature follows the following pattern:

- cp_Cu_Cu:Fe-ratio_concentration of NaOH_reaction temperature_alteration.
- For example, cp_Cu_1-1_16%_30°C_f means the fresh sample of an experiment with a molar ratio of Cu:Fe = 1:1 and a reaction temperature of 30 °C using a four-molar NaOH solution.

After each experiment, XRD, FTIR, and ICP-MS were used to analyse a fresh sample and a sample altered for one day at a reaction temperature in a closed vessel.

Table 6.5: *Experimental parameters of the continuous flow experiments. Each experiment was sampled freshly and after one day at the respective reaction temperature (ww=wastewater).*

	Cp_Cu_1-1_0.4%_RT	**Cp_Cu_1-1_0.4%_60°C**	**Cp_Cu_1-1_16%_30°C**	**Cp_Cu_1-1_32%_30°C**	**Cp_Cu_1-1_32%_60°C**	**Cp_Cu_1-2_16%_60°C**
Element	Cu					
Concentration	10 g/l					3 g/l
Me:Fe ratio	1:1					1:2
Ww volume	50 ml	50 ml	200 ml	100 ml	100 ml	50 ml
pH of ww	3.2	3.2	3.3	3.4	1.3	3.2
Reaction temp.	RT	60 °C	30 °C	30 °C	60 °C	60 °C
Molarity / Conc. of NaOH	0.1 M / 0.4%	0.1 M / 0.4%	4 M / 16%	8 M / 32%	8 M / 32%	4 M / 16%
pH of NaOH solution	11.3	11.3	12.3	12.7	12.3	12.3
NaOH volume	175 ml	175 ml	100 ml	50 ml	50 ml	50 ml
Minimum pH during the experiment	5.5	5.8	10.1	11.4	10.9	10.0
Average reaction pH	6	6	11.9	12.2	11.1	11.9

Results

- **Used buffer solution**

First, a 0.4% concentrated NaOH solution was used (cp_Cu_1-1_0.4%_RT and cp_Cu_1-1_0.4%_60°C). The pH value dropped from pH 11.3 to 5.5 immediately after the first ca. 10 ml of synthetic wastewater was added and could not be adjusted during the experiment – no crystalline phases formed in these experiments. The following experiments were carried out with a 16% concentrated and a 32% concentrated NaOH buffer solution, respectively. In this case, the initial pH of the solutions was 12.3 and 12.7. The reaction was carried out with minor pH fluctuation, and keeping the pH > 9 was possible.

- **Water analysis**

Table 6.6 summarises the water analysis results. In some cases, the composition of the water could not be determined. These samples are marked with "not determined" (n.d.). This experimental series did not sample the initial Cu and Fe solutions.

Cu:Fe ratio of 1:2: For the experiments with a molar ratio of Cu:Fe = 1:2 and an initial Cu concentration of 3 g/l, the Fe and Cu concentrations could be reduced. The remaining **Cu** concentration is lowest for the altered sample cp_Cu_1-2_16%_60°C_1d with 0.54 mg/l compared to 1.24 mg/l for the fresh sample. For **Fe**, the lowest remaining concentration is 3.65 mg/l for the fresh sample (cp_Cu_1-2_16%_60°C_f); however, the altered sample shows a similar remaining concentration of 4.07 mg/l (cp_Cu_1-2_16%_60°C_1d). For the experiments with a Cu:Fe ratio 1:2, the remaining Cu- and Fe-concentrations were higher for the continuous flow process than the batch process.

Cu:Fe ratio of 1:1 For the experiments with a molar ratio of Cu:Fe = 1:1 and an initial Cu concentration of 10 g/l, the results show that Fe and Cu concentrations could be reduced. After the treatment, the highest **Cu** concentration detected is 8.8 mg/l for the experiment performed with a 32% NaOH solution (cp_Cu_1-1_32%_30°C_f), and the lowest is 0.86 mg/l for the experiment conducted with a 16% NaOH solution (cp_Cu_1-1_16%_30°C_f). For **Fe**, after treatment, the highest remaining concentration is 6.66 mg/l for the sample cp_Cu_1-1_32%_30°C_f likewise treated with a 32% NaOH solution, and the lowest is 3.77 mg/l for sample cp_Cu_1-1_16%_30°C_1d treated with a 16% NaOH solution. Hence, a significant difference in remaining Cu and Fe concentrations can be seen for the experiments performed with either a 16% or a 32% NaOH solution. The higher-concentrated NaOH solution (32%) shows higher remaining metal concentrations than those treated with the less concentrated NaOH solution (16%). Hence, the stronger base solution has a negative effect on wastewater purification.

Table 6.6: *Water composition before and after application of the continuous flow SPOP process, analysed by ICP-MS. Samples that were not determined are marked with n.d. The initial composition of the synthetic solutions has not been measured with ICP-MS.*

	Cu (mg/l)	Fe (mg/l)
Initial composition	10 000.00	10 000.00
cp_Cu_1-1_16%_30°C_f	0.86	3.83
cp_Cu_1-1_16%_30°C_1d	6.10	3.77
cp_Cu_1-1_32%_30°C_f	8.83	6.66
cp_Cu_1-1_32%_30°C_1d	n.d.	n.d.
cp_Cu_1-1_32%_60°C_f	n.d.	n.d.
cp_Cu_1-1_32%_60°C_1d	n.d.	n.d.
Initial composition	3 000.00	6 000.00
cp_Cu_1-2_16%_60°C_f	1.24	3.65
cp_Cu_1-2_16%_60°C_1d	0.54	4.07

- **XRD results**

Cu:Fe ratio of 1:2: The X-ray diffractograms of the fresh sample cp_Cu_1-2_16%_60°C_f and the altered sample cp_Cu_1-2_16%_60°C_1d show ferrite as the only crystalline phase. The X-ray diffractogram of the altered sample shows a lower background signal with sharper peaks than the fresh sample, indicating that with alteration, the crystallinity of ferrite increased.

Cu:Fe ratio of 1:1: *Figure 6.12* shows the X-ray diffractograms of the fresh and one-day altered experiments with 16% and 32% concentrated NaOH. The fresh samples show barely any crystalline phase. The two very weak and broad peaks at about 35.50 °2θ and 38.64 °2θ can be assigned to the (-111) and (111) planes of tenorite. The altered samples show distinct and clear diffraction maxima attributed to the two polytypes of delafossite. The 3R delafossite modification was identified based on the following peak positions at 2θ and the corresponding *hkl*s in brackets: 231.37° (222), 34.58° (100), 35.79° (101), 40.32° (211), 55.43° (323), and 61.17° (10-1). 2H delafossite is given based on additional peaks observed at 2θ values and corresponding *hkl*s at 31.22° (004), 35.00° (101), 37.63° (012), 41.36° (013), 53.00° (015), 59.85° (016), and 61.01° (110). The reference diffractogram of 3R and 2H delafossite can be found in the Appendix, *Figure IV. 7.* An overview of the precipitated phases is given in *Table 6.7.*

The experiment with a 16% concentrated NaOH buffer solution shows all diffraction maxima assigned to the 3R polytype. Only two peaks at 31.22 and 37.63 °2θ point to small amounts of the 2H delafossite polytype. Accordingly, the sample shows less 2H delafossite than 3R delafossite. The sample synthesised with a 32% concentrated NaOH buffer solution shows

diffraction maxima of 3R and 2H polytypes with a similar intensity, indicating an equal quantity of the two polytypes.

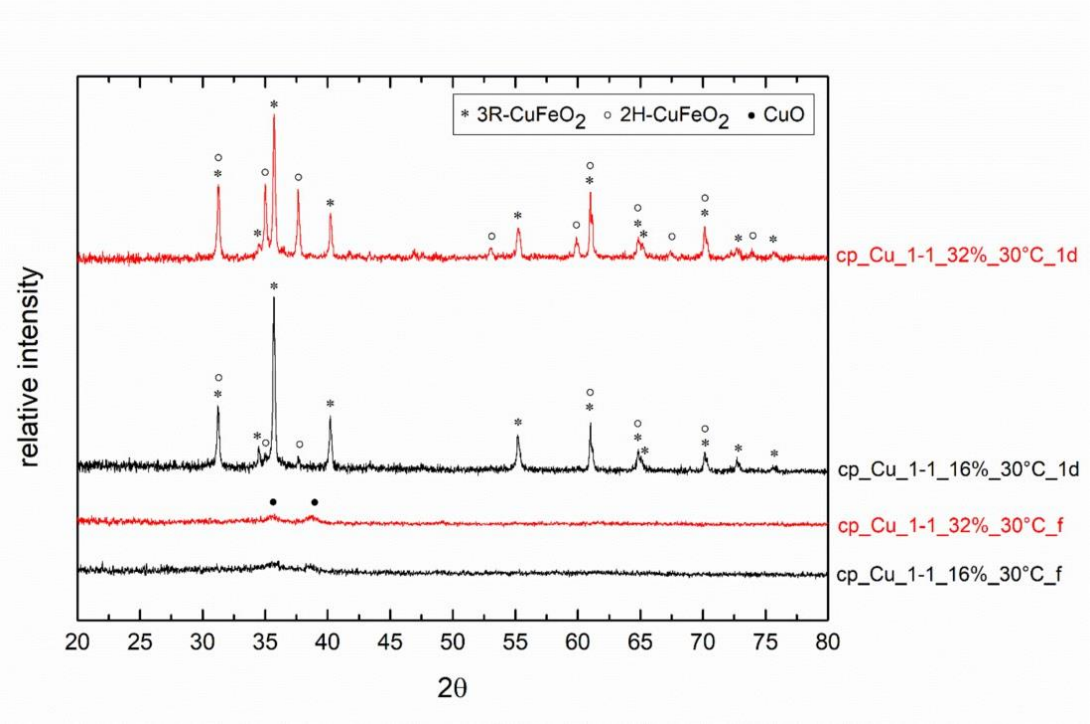

Figure 6.12: *X-ray diffractograms of the continuous flow precipitation experiments cp_Cu_1-1_16%_30°C and cp_Cu_1-1_32%_30°C. The fresh samples show barely any crystalline phase. The two weak and broad diffraction maxima at 35.50 and 38.64 °2θ can be assigned to tenorite's (-111) and (111). Both altered samples show distinct and clear diffraction maxima attributed to delafossite. The sample synthesised with a 32% NaOH shows good signals of both polytypes 3R and 2H, while using a 16% NaOH leads to mainly 3R delafossite.*

The experiments were also carried out at a higher temperature of 60 °C (sample series cp_Cu_1-1_32%_60°C) *(Figure 6.13)*. While the fresh samples contain tenorite at 30 °C, cuprite is present at 60 °C due to the associated reflections (see *Figure IV.4* in the Appendix for the reference X-ray diffractogram of CuO). The corresponding altered sample (cp_Cu_1-1_32%_60°C-1d) shows cuprite and both delafossite polytypes.

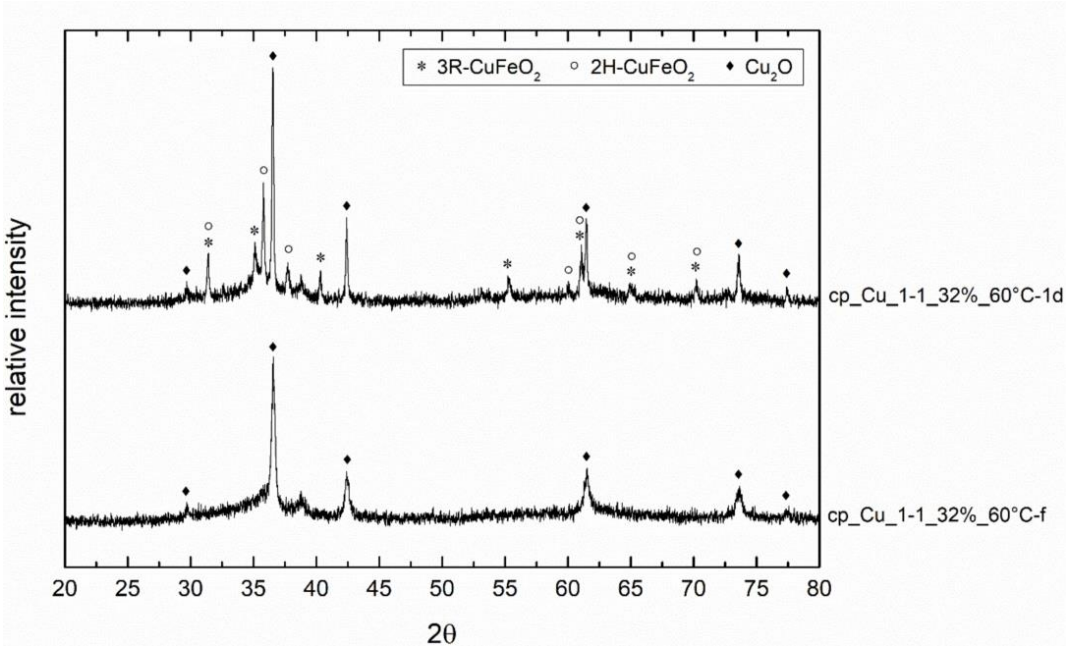

Figure 6.13: *X-ray diffractograms of the continuous flow precipitation experiment cp_Cu_1-1_32%_60°C. The fresh sample shows diffraction maxima assigned to cuprite. The altered sample for 1d at 60° C shows diffraction maxima of cuprite and delafossite polytypes 3R and 2H.*

- **FTIR results**

All sample series' fresh samples show GR-II with bands at 477, 515, 612, 668, 1102, 1144, 1657, 3263, and 3390 cm^{-1}. Hence, GR-II initially forms independently of the molar ratio of Fe:Cu, the reaction temperature, and the concentration of NaOH.

Cu:Fe ratio of 1:2: The sample series cp-Cu-1-2_16%_60°C performed with a molar ratio of Cu:Fe of 1:2 shows bands of GR-II and bands of Cu-ferrite in the fresh sample (cp_Cu_1-2_16%_60°C_f). Only bands related to Cu-ferrite were detected for the one-day altered sample at 60 °C (cp_Cu_1-2_16%_60°C_1d), indicating that the GR-II has fully decomposed.

Cu:Fe ratio of 1:1: The FTIR results of the sample series cp_Cu_1-1_0.4% conducted with the low concentrated NaOH solution of 0.4% and altered for one day at room temperature at 60 °C shows the same phase composition for the fresh and the altered sample without any crystalline phase. The FTIR spectra show GR-II and ferrihydrite ($Fe_{10}O_{14}(OH)_2$) with bands at 450, 600, 1630, and 3430 cm^{-1} for the fresh and the altered sample.

All other experimental series show a differing phase composition between fresh and altered samples, indicating a phase transformation during alteration. The sample series cp_Cu_1-1_16%_30°C was conducted with the intermediate concentrated NaOH solution of 16%. The fresh sample (cp_Cu_1-1_16%_30°C_f) shows GR-II and tenorite with its bands at 432, 496, and 603 cm^{-1}. GR-II is not detected anymore in the one day at 30 °C altered sample (cp_Cu_1-1_16%_30°C_1d) and is replaced by delafossite with its main band at 669 cm^{-1} *(John et al.,*

2016b). The distinction between delafossite polytypes is impossible with the FTIR technique. The sample series cp_Cu_1-1_32%_30°C was conducted with the strong NaOH solution of 32%. The FTIR results show the same phase composition as the experiments conducted with 16% NaOH (cp_Cu_1-1_16%_30°C). Thus, the fresh sample cp_Cu_1-1_32%_30°C_f shows CuO and Gr-II and the altered sample cp_Cu_1-1_32%_30°C_1d is composed of delafossite and tenorite. Hence, at a reaction temperature of 30 °C, the concentration of the base solution does not influence the phase composition.

The sample series cp_Cu_1-1_32%_60°C was conducted with a strong 32% NaOH solution at a 60 °C reaction temperature. The fresh sample cp_Cu_1-1_32%_60°C_f shows bands of GR-II and cuprite, with its main band at 626 cm^{-1}. The altered sample for one day at 60°C shows cuprite and delafossite.

In conclusion, for the experiments with a molar ratio of Cu:Fe of 1:1, the following trends can be seen:

- Delafossite exclusively occurs as an alteration product.
- At a reaction temperature of 30 °C, the concentration of the NaOH solution does not impact the phase composition; the precursor phases are GR-II together with tenorite.
- At a reaction temperature of 60 °C, the precursor phases for delafossite formation are GR-II and cuprite.

The combined results of the phase analysis with FTIR and XRD are summarised in *Table 6.7*.

Table 6.7: *Overview of crystalline and amorphous phases detected with XRD (x) and FTIR (f) conducted with the continuous flow process in the Cu-system. The number of letters corresponds to the quantity of the respective phases in the sample.*

	$CuFeO_2$	**2H-$CuFeO_2$**	**3R-$CuFeO_2$**	**Cu_2O**	**CuO**	**Gr-II**	**FH**	**Fe_3O_4**
cp_Cu_1-1_0.4%_RT						f	ff	
cp_Cu_1-1_0.4%_60°C						f	ff	
cp_Cu_1-1_16%_30°C_f					x,f	fff		
cp_Cu_1-1_16%_30°C_1d	f	x	xxx		x,f			
cp_Cu_1-1_32%_30°C_f					x,f	fff		
cp_Cu_1-1_32%_30°C_1d	f	xx	xxx		x			
cp_Cu_1-1_32%_60°C_f				xx,f		fff		
cp_Cu_1-1_32%_60°C_1d	f	x	xxx	xx,f				
cp_Cu_1-2_16%_60°C_f						fff		xxx,f
cp_Cu_1-2_16%_60°C_1d								xxx,f

Summary: The continuous process requires a new setup with a reaction vessel providing a constant reaction pH. The procedure was tested on a laboratory scale. The results confirmed the formation of ferrite in the system Cu:Fe of 1:2 and delafossite in the system Cu:Fe of 1:1, requiring an alteration of the precipitates. The remaining concentrations of Cu and Fe after the procedure are slightly higher compared to the batch process. The consequences of the design of the SPOP facility are presented in the following chapter.

P&ID diagram of the continuous flow SPOP process

Figure 6.14 shows the P&ID diagram with the piping and process equipment (P) and the instrumentation and control devices (ID) to realise the process. A vessel (V1) stores the NaOH solution to buffer the reaction. This vessel requires a heater and a thermocouple (TC001) to regulate the reaction temperature (T_{max} = 70 °C), a filling level sensor (LC001) and a pH surveyor (pH001). In parallel, the wastewater stored in vessel V2 is pumped via pump (P2) to tank (V4) with a temperature regulator and a monitoring system for the filling level (LC002), the pH (pH002), and the temperature (TC002). In the case of a receipt with Fe-addition, a volumetric auger filler (V3) controls the addition of Fe^{2+} salt as a powder to the wastewater (V4). A stirrer (M1) enables a fast dissolution. The reactor (V5) is filled with the tempered base, and the tempered wastewater is continuously pumped into the heat-able or heat-insulated reactor (V5) with a stirrer (M2) to ensure continuous homogenisation. A monitoring system controls the temperature (TC003), and the pH value (pH003) is kept stable by pumping either base solution (P1) or wastewater (P3) to the reactor (V5).

The reactor design (V5) is a challenge, which must simultaneously enable precipitation and sedimentation. An example of the sedimentation vessel is a separating funnel, where the reaction can occur in the upper third at the cylindrical part and the sedimentation at the lower two-thirds within the cone. Once a highly concentrated suspension has accumulated at the bottom, a valve is opened to discharge the suspension into a collection tank (V6). A post-dewatering process, e.g., filtration or centrifugation, is required to reduce the water content further.

The wastewater must be continuously supplied at one end of the reactor. It is treated while passing through the reactor and flows out opposite as treated wastewater. The treated water has an increased pH, which has to be neutralised. Therefore, it could be put into a collection tank (V7) where acid neutralisation occurs. Alternatively, due to the alkaline pH value, it can be used to regulate the pH in the reactor and pumped back if necessary (P5).

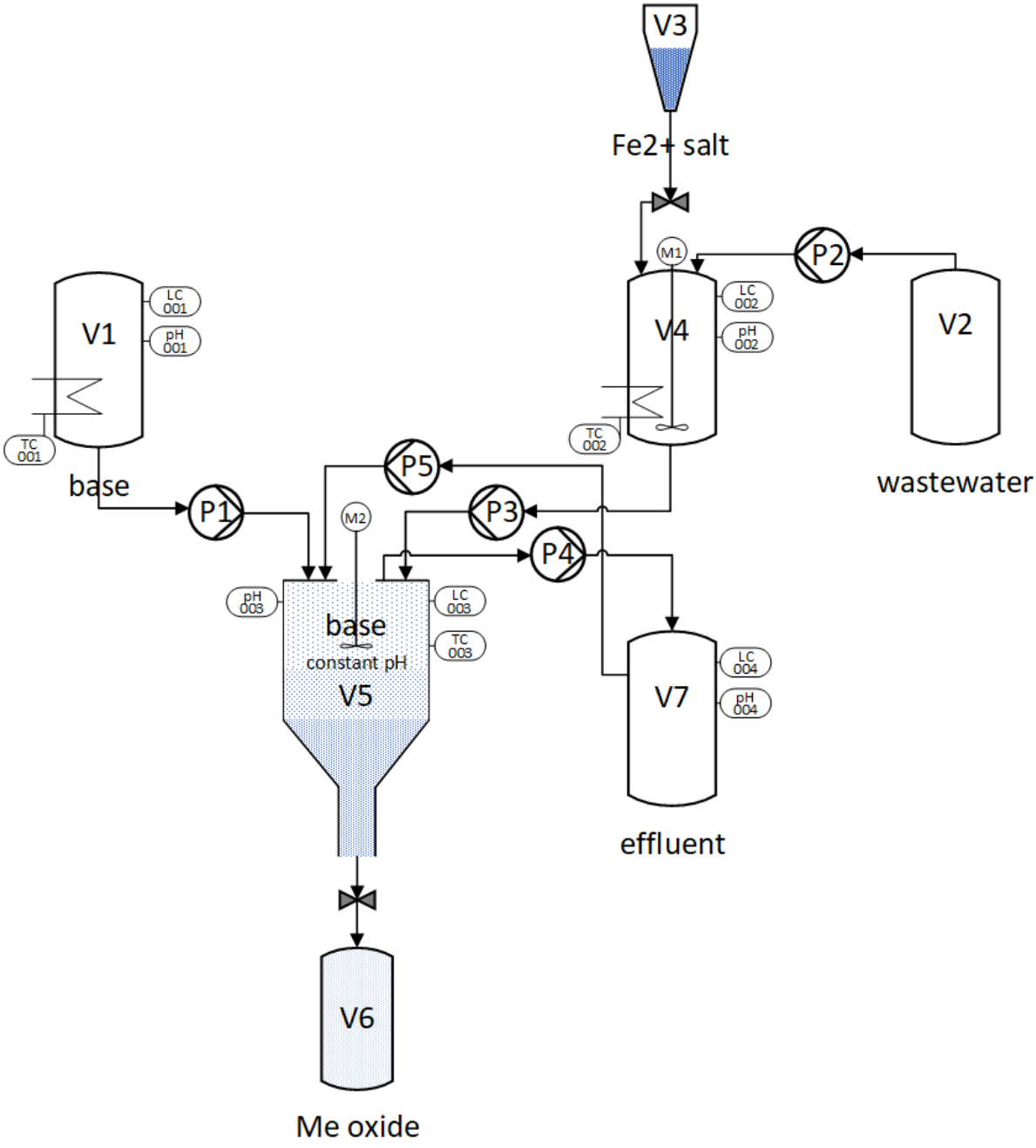

Figure 6.14: *Possible P&ID diagram of the continuous flow SPOP process.*

SECTION THREE

7. Discussion

Wastewater has long been perceived solely as a pollutant, and in general, metals in wastewater are neglected as a source of valuable elements. In general, activities are focused on wastewater treatment and removal of pollutants, sometimes on the return of wastewater to the water cycle of a plant. Correspondingly, as shown in my studies, large quantities of metals are disposed of and thus are lost to the economy due to dissipation. In recent years, due to the geopolitical situation and the growing awareness of the scarcity of critical raw materials, a rethinking of waste as an anthropogenic resource has taken place. Discussing the circular economy's goals and the SDGs' consideration promotes this. Lately, due to the COVID-19 pandemic, the EU's supply of critical raw materials was interrupted, which affected the economy heavily and revealed its dependency on just a few countries. Consequently, in 2023, the European Commission announced the Critical Raw Materials Act to establish secure and sustainable supply chains. It also includes recycling strategies for critical and strategic materials from waste. The following factors make a waste stream attractive as a resource: 1) The quantity of valuable material in the waste – and thus the potential as a business project, and 2) the costs for waste disposal. If the economic value of one of these factors is high, it gives reason for innovations to make materials accessible from waste. Recently, the research on recycling methods has been rising and will presumably increase since the EU is investing in research on critical raw materials.

The question is whether there is an alternative to treating wastewater as hazardous waste in which these metals are accessible as secondary raw material. The literature research showed that most of the new process technologies aiming to recover metals from wastewater are either in an early stage of development (e.g., nanofiltration), use additives (e.g., flocculation), or have other restraints like high process costs (e.g., electrochemical treatment methods). This research on the new technology SPOP shows a novel way to ensure both water purification and recycling are done efficiently and with the lowest possible energy consumption.

The following discussion is structured into two main parts. In the first part, the upscaling of the lab-scaled experiments is discussed: In Chapter 7.1, I focus on the up-scaling of the precipitation recipes of the one-step process in the Zn-system and the two-step process in the Au-system. I discuss the formation mechanism of ZnO depending on the precursors and which parameters influence the particle morphology. In Chapter 7.2, I focus on the Cu-system. I discuss phase formation conditions for Cu-ferrite, delafossite, and Cu-oxides. The second part refers to the technical feasibility of the pilot facility: Chapter 7.3 considers the influence of

crucial parameters on the robustness of the process, and in Chapter 7.4, I discuss the feasibility of the continuous flow SPOP process.

7.1. Upscaling of precipitation recipes

7.1.1. One-step SPOP process (Zn-system)

With the upscaling of the SPOP process, the question arises of how efficient it is compared to other synthesis methods and if environmental issues are connected. In the Zn system, the main product produced with the SPOP process in this thesis is ZnO. In recent years, ZnO-engineered nanoparticles (ZnO-ENPs) have become an essential product due to their many uses, e.g., in consumer products. As a result, many synthesis methods were developed. Therefore, the efficiency of using SPOP as an alternative procedure to produce ZnO is discussed.

ZnO synthesis methods – is SPOP an efficient alternative?

Different synthesis methods have been developed due to ZnO nanoparticles gaining importance due to their interesting physical properties. These synthesis methods can be divided into solution-based and vapour-phase *(Ong et al., 2018)*. In comparison, solution-based techniques are simpler and less energy-consuming *(Ong et al., 2018)* and are those considered in this discussion due to their comparability to the SPOP method. Different reagents and precursors are used for ZnO synthesis, depending on the procedure. One intensively used and studied precursor is zinc acetate ($Zn(CH_3COO)_2$). For example, *Rodríguez-Paéz et al. (2001)* applied a process based on three steps: precipitation, chemical weathering, and thermal treatment. First, intermediate zinc complexes ($Zn(CH_3COO)_2 \cdot (2\text{-}x)H_2O \cdot xCH_3CONH_2$ and $Zn_4(OH)_8(NO_3)_2 \cdot (2\text{-}x)H_2O \cdot xNH_3$) are precipitated as a complex by titration of NH_4OH to a solution of zinc acetate dissolved in HNO_3.

The precipitates are washed with ethanol to transfer the complex to zinc alkoxide during chemical weathering. After one hour of thermal treatment at 320 °C, the zinc alkoxides are converted to zinc oxide. *Musić et al. (2005)* simplified this synthesis procedure in precipitation and autoclaved hydrothermal ageing at 160 °C. They used zinc 2- ethyl hexanoate with 1% ethylene glycol monomethyl ether, and after two hours of hydrothermal ageing at pH 7, the complex is transferred to ZnO by a dissolution/reprecipitation process. They observed that the transformation time can be significantly reduced with increasing pH. At pH 10, the transformation time during autoclaving was only 15 min. *Wong et al. (1998)* studied the growth of ZnO particles in 2-propanol using a suspension of zinc acetate in 2-propanol, which was neutralised with NaOH and stored at room temperature. They concluded that the growth kinetics of ZnO from acetate-based solutions are driven by dissolution/reprecipitation, and growth happens according to the principles of Ostwald ripening. Zinc acetate procedures generally need an intermediate step for forming ZnO and an elevated reaction temperature.

On the other hand, the direct precipitation of ZnO is feasible using zinc nitrate and sulfate solutions (e.g., *Oliveira et al., 2003*). The solutions were alkalised with NaOH (pH 9.5 – 10.5) at room temperature and stirred for two hours. In both cases, ZnO precipitated directly from the solution. Likewise, in my experiments, ZnO precipitated directly from the solution using the same precursor (zinc sulfate) and base solution (NaOH). However, the final alkalisation pH of 9 is lower compared to *Oliveira et al. (2003)*. Their nitrate-based experiments generated starlike ZnO; the sulfate-based experiments, ellipsoids and fibres. In this thesis' experiments, ZnO nanospheres were synthesised.

The morphology of ZnO nanoparticles was found to serve their various purposes. *Tong et al. (2012)* discovered that ZnO nanospheres have great antibacterial activity and an enhanced photocatalytic effect on the decolourisation of methyl orange aqueous solutions. The high surface area associated with their small size generally causes their high reactivity. The ZnO nanoparticles synthesised by *Tong et al. (2012)* have a uniform spherical morphology and a size of about 17 nm. Here, I synthesised similar particles with a very monodisperse size of approximately 20 nm. Hence, the particles are comparable in chemistry, structure, size, and shape to those of Tong et al. (2012), and their results give a prospective application for the particles synthesised within this thesis. However, the synthesis methods differ. While herein I used a chemical precipitation process (SPOP), *Tong et al. (2012)* used solution plasma processing (SPP), for which plasma is injected in a precursor bearing aqueous solution. SPP uses a more involved experimental setup than SPOP in many aspects and needs a higher energetic input.

Furthermore, SPP is still performed on a laboratory scale. Since the SPOP process was scaled up in this thesis, the synthesis output of SPOP is higher than that of SPP because higher volumes and concentrations can be processed. Yet, SPP has recently been considered a possible wastewater treatment process *(Jiang et al., 2014)*. However, a literature search on SPP large-scale reactors for wastewater treatment did not yield anything (August 2023) and *Jiang et al. (2014)* state that such a reactor is considerably complex and challenging.

A difference in the morphology of precipitated ZnO can also be observed using the SPOP process. *Tandon (2021)* adapted the SPOP process to recover Zn from a highly saline solution as this environment corresponds to fly ash leachates from municipal waste incineration. He developed two different ZnO synthesis routes: First, for temperatures below 65 °C, the precursor sulfate mineral gordaite $NaZn_4(SO_4)(OH)_6Cl*6H_2O$ was formed as a result of the alkalisation; the alteration of this precursor at elevated temperatures leads to the formation of ZnO by a dissolution/reprecipitation reaction. As a second path, he describes the direct precipitation of ZnO at a reaction temperature of $T > 60$ °C. In this case, the reaction temperature can be lowered to 35 °C by accelerating the alkalisation process. For both formation cases, ZnO exists as nanosized rods. The initial Zn concentration, the alkalisation

pH, and the reaction temperature are comparable to my experiments. Hence, the treatment parameters are not the critical control factor for shape. However, the matrix composition differs profoundly. While my experiments were carried out at a low content of SO_4^{2-} only, the investigations of *Tandon (2021)* were highly enriched in SO_4^{2-}, Cl^-, Na^+, K^+, and Ca^{2+}. Therefore, the difference in ionic strength seems to impact ZnO particle morphology. Nanospheres are favoured at low ionic strength, and nanorods emerge at high ionic strength.

Compared to the described methods found in the literature, SPOP shows a high efficiency: Compared to acetate-based synthesis routes, the SPOP process is faster because ZnO precipitates directly at comparably lower temperatures. Specifically for the synthesis of ZnO nanospheres, compared to SPP, SPOP needs less energy, shows a higher synthesis output, and has less complex technical implementation.

7.1.2. Two-step SPOP process (Au-system)

In this thesis, the process of recovering Au from wastewater, as *John et al. (2019)* described, was scaled up and applied for the automated and serial treatment of several litres of Au wastewater using the pilot plant. The experiments confirmed the formation of Au°, as in the first step of the two-step SPOP process, a reduction of aqueous Au species to Au° is obtained by adding Fe^{2+} to the wastewater at room temperature. Au precipitated as metallic rosettes. The remaining solution was alkalised via NaOH for the removal of Fe. The results showed that ferrite had already precipitated in the fresh sample but was accompanied by GR II. During alteration for one day, Fe was fully recovered as ferrite. Hence, the results of *John et al. (2019)* could be fully verified in these scale-up experiments. Therefore, the results of this work demonstrate a successful scale-up of the 2-step process for a larger wastewater volume and the suitability of the SPOP process for Au wastewater purification and recovery.

Various techniques have been investigated to recover Au from wastewater. The literature research showed that most approaches for recovering Au from wastewater are applied to very low concentrated wastewater or highly enriched leachates. In the range of microgram per litre, nanoscale zero-valent iron (nZVI) was used to purify Au(III)-containing wastewater from electrochemical refining with a fluctuating concentration between 5.5 – 25 000 µg/l *(Li et al. 2019)*. The nZVI show a core-shell structure ($(Fe_m)_{core}(FeOOH)_{shell}$) and has a high driving force to react with Au(III), which is reduced to Au^0 via a galvanic replacement process to form $(Fe_n)_{core}(FeOOH)_{shell}$ Au(0) + Fe(II). Thereby, the Au^0 nanoparticles form on the micron-sized aggregates of the nZVI, which can be separated. The process shows up to 95% recovery efficiencies and is already used in a continuously operated plant. For slightly higher concentrated wastewater in the range of milligrams/litre, adsorption of Au(III) has been studied with different adsorbents. Adsorbents generally show a short lifecycle, often making them less economically attractive. A superparamagnetic adsorbent ($Ni_{0.6}$ $Fe_{2.4}O_4$-MTD) has been demonstrated to have good adsorption of Au(II) at pH 4 and can be reused for an Au concentration of 150 mg/l *(Zhao et al., 2019)*. Biosorption has lately shown promising results

in Au recovery, too. For example, *Xu et al. (2019)* used *Phomopsis sp. XP-8*, a filamentous endophytic fungus, for selectively recovering gold from electronic wastewater. Under optimum conditions, these techniques delivered a recovery rate of Au of about 80%. However, the adsorption capacities decrease in the case of highly enriched Au wastewater. Highly enriched Au solutions can be found in gold mining and are cyanide-based. The Au concentration can be as high as 10 g/l Au *(Babaei et al., 2020).* Electrodeposition can be used to recover Au from these highly enriched solutions. However, electrodeposition is a costly process with high energy consumption. The electrodeposition rate of Au was higher for pulsed current electrodeposition, as *Babaei et al. (2020)* showed. With the SPOP process, *John et al. (2019)* used wastewater with ca. 2 g/l Au, and in this work, I used wastewater containing about 5 g/l Au. Hence, the wastewater treated with the SPOP process is classified as a medium Au concentration. No other preferable treatment technique could be verified in the literature for those medium-concentrated Au wastewaters. With SPOP, 99.9% of Au was recovered. Consequently, the SPOP process effectively recovers Au for wastewaters with medium concentrations of 2 – 5 g/l. For those wastewaters, SPOP could be used to recover the bulk of Au in wastewater and combined with other techniques to recover the residual micrograms per litre.

7.2. Product-oriented synthesis (Cu-system)

Copper is an excellent example of testing the product-oriented synthesis of phases by upscaling experiments using the SPOP pilot facility. This chapter discusses the variation of Fe addition to Cu-containing wastewater and its effect on phase formation and metal recovery, including the reaction mechanisms during the SPOP process.

7.2.1. Reaction system Fe^{2+}:Cu^{2+} = 2:1

Scale-up experiments using electroplating wastewater and a molar ratio of Fe^{2+}:Cu^{2+} = 2:1 demonstrate the successful synthesis of single-phased cuprospinel. These results are in line with the laboratory studies. Small amounts of other metals in a lower concentration in the solution did not form additional phases. Their low concentrations after the treated solution indicate their incorporation into the spinel structure. The experimental results also show that the real wastewater's partly unknown (organic) components have no adverse effects.

The fresh samples in this work showed green rust (GRII), a Fe^{2+}-Fe^{3+} layered double hydroxy-sulphate, during alkalisation by FTIR measurements. *Heuss-Aßbichler et al. (2016)* performed similar experiments and observed GRII in fresh samples too. The subsequent rapid decomposition of GRII in the alkaline environment was confirmed by several studies indicating that GRII serves as a precursory phase for ferrite *(Tamaura et al., 1984; Tamaura, 1986; Sumoondur et al., 2008; Heuss-Aßbichler et al., 2016b). Garófalo Chaves et al. (2009)* postulated the substitution of Fe^{2+} by divalent heavy metal cation in GR-II. Analogous to this,

John (2016) concluded that Cu is incorporated into GR-II *(Reaction R-I* in *Figure 7.1)* and Cu-ferrite forms as an alteration product *(Reaction R-II* in *Figure 7.1)*. The aged products generated within this thesis and those of *Heuss-Aßbichler et al. (2016)* show a **deviation in the phase assemblages,** which is obviously due to the different oxygen fugacity during the precipitation and ageing of the phases. The applied stirring techniques can cause differing redox conditions. In general, through stirring, oxygen is brought into the solution. *Heuss-Aßbichler et al. (2016)* used a magnetic stirrer, whereas I used an overhead stirrer and applied a high stirring speed. The enhanced power of the overhead stirrer enables a higher oxygen input in the solution, resulting in higher oxidising conditions during the reaction conditions and, therefore, optimal conditions for ferrite formation. In comparison, the lower speed of the magnetic stirrer used by *Heuss-Aßbichler et al. (2016)* led to a lower oxygen supply, keeping the system at a higher reducing environment which enabled the formation of the deviating phases. The oxygen supply during precipitation play a crucial role in the phase assemblage of the final process products. The results of this study and those of *Heuss-Aßbichler et al. (2016)* are combined in *Figure 7.1*: At elevated oxygen fugacity, Fe^{2+} oxidises to Fe^{3+} and is with Cu^{2+} incorporated into the ferrite *(Reaction R-II* in *Figure 7.1)*. At low oxygen fugacity, the Fe^{2+} is oxidised to Fe^{3+} and Cu^{2+} is reduced to Cu^{1+}, so cuprite (Cu_2O) and GR-II formed first *(Reaction R-III* in *Figure 7.1)*. With alteration, ferrite forms at the cost of GR-II while cuprite stays stable *(Reaction R-IV* in *Figure 7.1)*.

The breakdown of GR-II and its transformation to magnetite is indicated by corrosion features on the GR particles *(Sumoondur et al., 2008)*. The change in the morphology of platy GR-II particles to cubic or spherical particles of Fe_3O_4 *(Tamaura et al., 1984)* is evidence of a **dissolution/reprecipitation process**. The change in morphology from GR-II to ferrite observed in this study confirms that a dissolution/reprecipitation process is a possible pathway of recrystallisation. *Tronc et al. (1992)* point out that **topotactic transformation** to spinel may be a specific feature of partly reduced ferric hydroxides in alkaline medium. They observed a short-range ordered mixed-valence state, indicating fast electron mobility. This electron delocalisation causes local structural rearrangements and activates spinel order. Fe^{2+} adsorption induces an electron transfer at the interface, and the extra electrons' mobility within the mixed iron hydroxide drives the transformation *(Jolivet et al., 1992)*. The relative importance of the transformation pathways, i.e., either dissolution/reprecipitation or solid-state reaction, depends on the Fe^{2+} content in the system *(Tronc et al., 1992)*. For topotactic transformations, the surface of a phase serves as a nucleus for new phases to grow. *Usman et al. (2018)* found that the initial phase's particle size and morphology can be preserved during topotactic transformations. The SEM images of the initial phase (GR-II) in this work and *Heuss-Aßbichler et al. (2016)* show that the ferrite grows on the surface of the green rust, which points to a topotactic transformation. Also, the adsorption of Fe^{2+}, which favours the electron transfer, is likely since altered samples partly show elevated Fe concentration. However, in my

experiments, the particle shape changed from a needle-like GR-II to a granularly shaped ferrite. Thus, one can conclude that after initial topotactic nucleation of ferrite on GR-II, these nuclei grow by dissolution/reprecipitation processes.

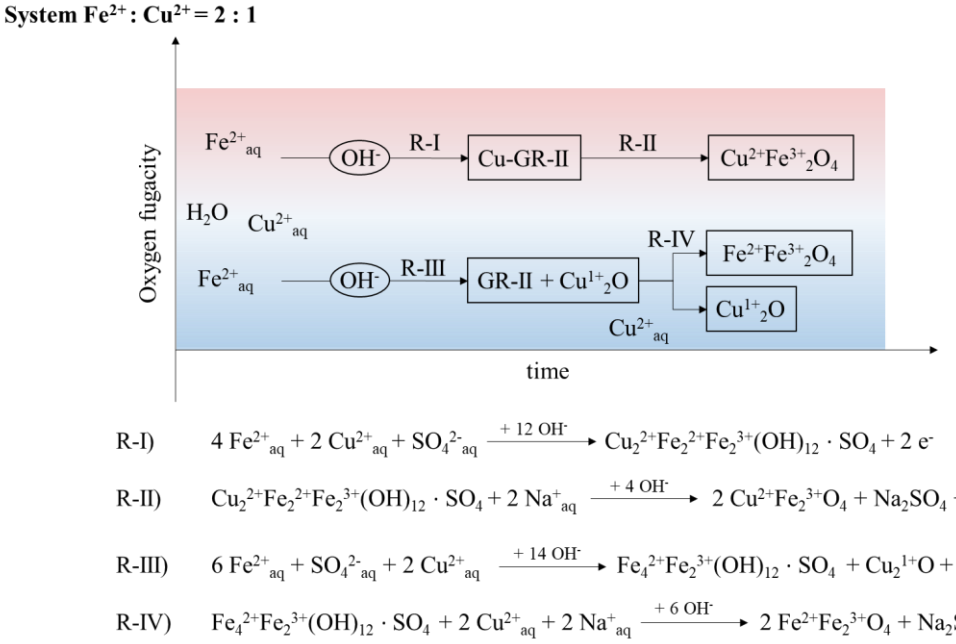

R-I) $4\ Fe^{2+}_{aq} + 2\ Cu^{2+}_{aq} + SO_4^{2-}_{aq} \xrightarrow{+\ 12\ OH^-} Cu_2^{2+}Fe_2^{2+}Fe_2^{3+}(OH)_{12} \cdot SO_4 + 2\ e^-$

R-II) $Cu_2^{2+}Fe_2^{2+}Fe_2^{3+}(OH)_{12} \cdot SO_4 + 2\ Na^+_{aq} \xrightarrow{+\ 4\ OH^-} 2\ Cu^{2+}Fe_2^{3+}O_4 + Na_2SO_4 + 8\ H_2O + 2\ e^-$

R-III) $6\ Fe^{2+}_{aq} + SO_4^{2-}_{aq} + 2\ Cu^{2+}_{aq} \xrightarrow{+\ 14\ OH^-} Fe_4^{2+}Fe_2^{3+}(OH)_{12} \cdot SO_4 + Cu_2^{1+}O + H_2O$

R-IV) $Fe_4^{2+}Fe_2^{3+}(OH)_{12} \cdot SO_4 + 2\ Cu^{2+}_{aq} + 2\ Na^+_{aq} \xrightarrow{+\ 6\ OH^-} 2\ Fe^{2+}Fe_2^{3+}O_4 + Na_2SO_4 + Cu_2^{1+}O + 9\ H_2O$

Figure 7.1: *Illustration of the reactions in system Fe^{2+}:Cu^{2+}=2:1 occurring in an alkaline environment depending on the oxygen fugacity. Cu is incorporated in the intermediate product GR-II (R-I) at a high oxygen fugacity, which recrystallises to Cu-ferrite (R-II). At lower oxygen fugacity, oxidised Fe^{3+} and reduced Cu^{1+} form GR-II and cuprite (R-III). Under subsequent ageing, ferrite forms at GR-II (R-IV) cost.*

7.2.2. Reaction system Fe^{total}:Cu^{2+} = 2:1

The stoichiometric addition of ferrous iron Fe^{2+} to the Cu-bearing solution is crucial for generating a single-phase ferrite. Achieving a single-phase ferrite in a system with ferric iron Fe^{3+} is impossible. Instead, a phase mixture is generated. Experiments with a partially oxidised Fe solution and an unknown ratio of Fe^{2+}:Fe^{3+} and thus Fe^{2+}:Cu^{2+} led to a phase mixture with mainly GR-II, magnetite, and cuprite. After one day alteration, maghemite and delafossite were additionally observed.

The formation of **magnetite** can be explained as follows: (1) Magnetite formed as an alteration product of GR-II (see *Reactions R-III* and *R-IV in Figures 7.1* and *7.2*). (2) The partially oxidised Fe solution promoted the direct formation of magnetite by reacting Fe^{3+} and Fe^{2+} cations in the alkaline environment (*Reaction P-I* in *Figure 7.2)*. This does not exclude an additional formation of ferrite based on the *Reaction R-IV*. The oxidation of Fe^{2+} to Fe^{3+} led to a reduction of Cu^{2+} to Cu^{1+}. As a result, **cuprite** forms in fresh and altered samples *(reactions R-III* and *R-IV)*. In addition, the wastewater is known to exhibit organic acids, which serve as a reducing agent and promote the formation of cuprite.

The magnetite formation shifts the stoichiometry of Fe^{total}:Cu^{2+} to lower Fe content, which can cause the formation conditions for **delafossite** during ageing with a molar ratio of Fe^{2+}:Cu^{2+} = 1:1 *(Reaction P-II* in *Figure 7.2)*.

Maghemite was also observed in the altered samples P-1d60°C-c and P-5d60°C-c (see *Chapter 6.3. Impact of malfunctions*). As a primary phase, maghemite was found to form during co-precipitation at room temperature using ferric and ferrous chlorides *(Nazari et al., 2014)*. Thereby, the primary formation of maghemite could be favoured by a relative excess of Fe^{3+}. In my experiments, maghemite occurs only in the altered samples and has not formed primarily. Maghemite is known to be formed at elevated temperatures by dehydration of ferric hydroxides, e.g., goethite and hematite, at a temperature of 240 °C *(Itoh and Sugimoto, 2003)* or ferrihydrite at temperatures > 300 °C and in the presence of a reductant *(Campbell et al., 1997)*. In my experiments, ferric hydroxides are present in the fresh samples, which could potentially serve as a source for maghemite formation during ageing. However, the experiments were conducted under ambient temperature, precluding the dehydration of ferric hydroxides, making it an unlikely underlying process for the formation of maghemite. Maghemite is thought to be a secondary phase which, at ambient temperatures, forms via slow oxidation of magnetite *(Taylor and Schwertmann, 1974)*. As for the synthesis of maghemite via magnetite, the precipitation pH of the precursory magnetite is known to influence the subsequent oxidation to maghemite *(Correa et al., 2006)*. Magnetite synthesised at pH > 11 is more stable than one synthesised at a lower pH, where it preferentially oxidises to maghemite at pH 8 – 9 *(Correa et al., 2006)*. In my experiments, the precipitation was around pH 8; therefore, the oxidation of magnetite during ageing is the most likely process for maghemite formation *(Reaction P-III* in *Figure 7.2)*. Nevertheless, the direct formation of maghemite could be possible with the SPOP process in a scenario in which ferric ions dominate the system *(Reaction P-I* in *Figure 7.2)*.

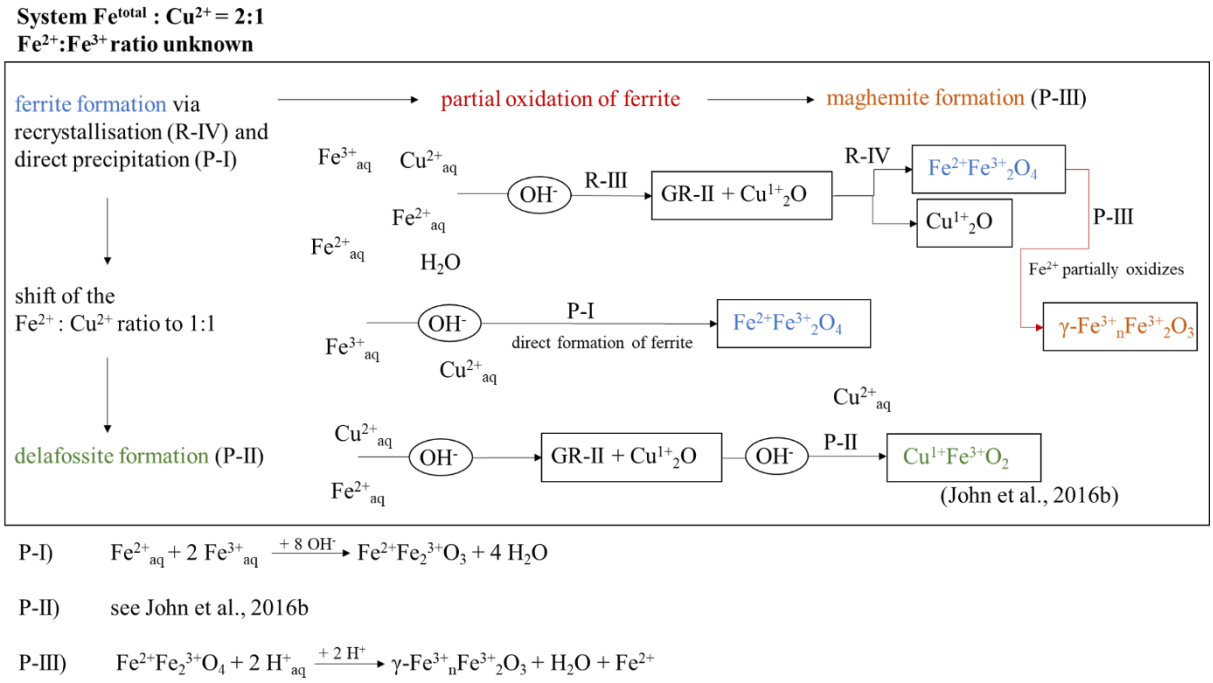

Figure 7.2: *Reactions in the system Fe^{total}:Cu^{2+} = 2:1 with unknown ratio of Fe^{2+}:Fe^{3+}. Ferrite can form via the recrystallisation of GR-II (R-IV) or directly due to the presence of Fe^{3+} (P-I). The formation of ferrite reduces the Fe:Cu ratio and conditions are met for delafossite to form (P-II). Maghemite forms via the partial oxidation of magnetite during alteration (P-III).*

Summary: Different stoichiometries were tested with the pilot facility in the Cu-Fe system. The experiments with an exact molar ratio of Fe^{2+}:Cu^{2+} = 2:1 show that the synthesis of single-phase Cu-ferrite is possible as long as an oxidising state is present in the system. Green rust is the initial phase generated during precipitation. Ferrite is formed by oxidation of the metastable phase green rust during alteration. A system with an overall Fe^{total}:Cu^{2+} = 2:1 but an abundance of ferric Fe and, in consequence, deviating Fe^{2+} to Cu^{2+} ratio leads to a phase mixture of magnetite and cuprite with a minor amount of maghemite and delafossite.

7.2.3. Reaction system Fe^{2+}:Cu^{2+} = 1:1

Delafossite ($CuFeO_2$) occurs in a rhombohedral 3R- and a hexagonal 2H polytype. These polytypes differ in the different relative orientations of the octahedra across the layers. Typically, delafossite consists of a mixture of 2H- and 3R-polytypes.

In various studies, delafossite nanoparticles with the two 3R and 2H polytypes were synthesised at a molar ratio of Cu^{2+}:Fe^{2+} = 1:1 using the SPOP batch method by altering primarily precipitated suspensions of Cu_2O and GR *(John 2016; John et al. 2016a, 2016b, 2016c; John et al. 2019). John et al. (2016a)* concluded that in an alkaline media (pH > 9), the oxidation of GR leads to the intermediate phases ferrihydrite ($Fe_{10}O_{14}(OH)_2$) and cuprite (Cu_2O). Later, after 1 one day of ageing, delafossite crystals grow at the expense of the unstable intermediate phases as the only phase in the suspension. The authors observed that the reaction

rate increases with increasing ageing temperature, reaction pH, and NaOH concentration in the solution.

In this thesis, the reaction process was changed from a batch to a continuous process on a laboratory scale. With this new procedure, it was possible to synthesise delafossite and expand the reaction conditions for delafossite formation in terms of temperature and NaOH concentration:

- **Reaction temperature**

During the last decade, low-temperature hydrothermal procedures at 100 °C were developed to synthesise $CuFeO_2$ within 12 h *(Xiong et al., 2015)* and $CuCoO_2$ within 24 h *(Du et al., 2018)*. The authors claimed that it is the minimum temperature for the synthesis of delafossite. However, *John et al. (2016a)* synthesised delafossite at either a temperature of 70 °C within 10 hours or 50 °C within seven days using the SPOP methodology. It is the lowest reaction temperature published so far.

In this study, with the set-up of the continuous SPOP process, the minimum reaction temperature leading to a successful formation of delafossite was as low as 30 °C within 24 hours.

- **Effect of the alkalisation process**

NaOH solution acts as a mineraliser for delafossite formation as it promotes the solubility of metal hydroxide complexes *(Sheets et al., 2006)*. Several authors studied the effect of NaOH concentration and quantity on delafossite polytype formation in hydrothermal systems. However, the studies do not show a clear trend, and the mechanism of delafossite formation is poorly understood. Using a hydrothermal synthesis technique, *Roble et al. (2019)* found that an increased amount of NaOH promotes the formation of 3R-$CuFeO_2$; they used Cu_2O and FeOOH as reagents mixed with dried NaOH powder at 210 °C for 96 hours, and subsequently, they dried the synthesis product at 70 °C for 16 hours. *Xiong et al. (2014)* found that increasing the excess NaOH can form a uniform crystal phase of 3R-$CuAlO_2$. However, they retracted that result and stated that a reaction temperature above 100 °C could be the critical parameter for delafossite polytype purity *(Xiong et al., 2015)*. *Sheets et al. (2006)* used different concentrations of NaOH between 0.9 and 2.5 M. They consistently synthesised a mixture of 2H- and 3R-$CuFeO_2$ independently of the NaOH concentration using Cu_2O and FeOOH as precursors. They pointed out that the effect of the corresponding hydroxide cations (e.g., Na^+) must be considered. Using the SPOP methodology, *John et al. (2016b)* synthesised 2H-delafossite using a 32% concentrated NaOH solution during the pH-stat time. The results show that the concentration of the NaOH solution influences the polytype formation. All delafossite samples treated with a 16% concentrated NaOH solution show mainly the 3R modification. Increasing the NaOH concentration to 32% increased the amount of 2H polytype,

demonstrating that stronger NaOH solutions enhance the formation of 2H polytype. However, more work must be done to understand how the mineraliser affects the formation of delafossite.

In conclusion, based on the applied continuous precipitation process, the 3R-delafossite is the favoured polytype when a lower 16% concentrated NaOH solution is used, while the stronger concentration of NaOH favours 2H-delafossite formation.

- **Effect of the precursor phases**

The delafossite experiments in this work give insights into the formation of tenorite (CuO) and cuprite (Cu_2O): At **30 °C**, the fresh samples contained mainly **GR-II** with only traces of **tenorite** (CuO) and at **60 °C**, the fresh samples consisted of **GR-II** and well-crystallised **cuprite** (Cu_2O) (see *Chapter 6.4. Continuous flow SPOP process*). After alteration at 30 °C, only single-phased delafossite was observed without traces of GR-II and tenorite. At 60 °C during alteration, cuprite and delafossite exist. The experiments show that the formation of tenorite or cuprite depends on the reaction temperature. Tenorite precipitates at a lower reaction temperature of 30 °C, and it was also observed in the scale-up experiments in the Fe-poor system. In contrast, cuprite formed at 60 °C. Accordingly, at atmospheric pressure, the stability boundary between tenorite and cuprite lies between 30 and 60 °C.

In conclusion, regardless of the reaction temperature, GR-II precipitates first and serves as a precursor phase for delafossite. The formation of single-phase delafossite is possible at 30 °C within 24 hours through the ageing of GR-II with traces of tenorite. At higher temperatures, cuprite can form, which remains stable during alteration.

7.2.4. Cu-system without Fe addition

Reaction Mechanism of $Cu(OH)_2$ and CuO formation

CuO is a highly investigated material because of its manifold technological applications. Therefore, many studies focus on synthesising CuO nanoparticles via hydrothermal synthesis techniques using different precursors. Aqueous solutions with copper acetate ($Cu(CH_3COO)_2$) are highly studied as a precursor. *Zhu et al. (2004)* synthesised CuO at 100 °C or room temperature by adding NaOH to a copper acetate solution to reach pH 6-7. The reaction temperature has been shown to control particle morphology. At 100 °C, the CuO particles show a spherical morphology, while at room temperature, they are needle-like. Other studied precursors are Cu-chloride and Cu-nitrate. *Phiwdang et al. (2013)* precipitated CuO by slowly dropping NaOH to the Cu-chloride or Cu-nitrate solutions until pH 14. Afterwards, calcination at 500 °C of the precipitated CuO nanocrystals was conducted to gain a better crystallisation. *Heuss-Aßbichler et al. (2016)* achieved CuO by the SPOP procedure using copper-sulfate at a ratio of Cu:Fe = 16:1 and a temperature of 40 °C.

The novelty of the present study is that it was possible to get CuO as the only crystalline product using Cu-bearing electroplating wastewater with a Cu concentration of ca. eight g/l and minor concentrations of Fe, Ni, Zn, Cr, Pb, and Mn at pH 11 and 60 °C reaction and alteration temperature. At precipitation pH > 11, all fresh samples show CuO and $Cu(OH)_2$ *(Reaction Q-I* in *Figure 7.3)*, which fully transform to CuO within one day in the alkaline environment, releasing water *(Reaction Q-II* in *Figure 7.3)*. The one-day altered samples solely show CuO as a precipitation product. *Cudennec and Lecerf (2003)* used similar experimental conditions to investigate the transformation of $Cu(OH)_2$ to CuO. The authors conclude that $Cu(OH)_2$, which is metastable in alkaline solution, reacts to CuO very fast at room temperatures. Thereby, $Cu(OH)_2$ dissolves to form tetra-hydroxo-cuprate (II) complex anions $(Cu(OH)_4)^{2-}$, and the loss of two hydroxyl ions and one water molecule leads to the formation of chains of CuO_4 groups, which form the structure of CuO *(Cudennec and Lecerf, 2003)*.

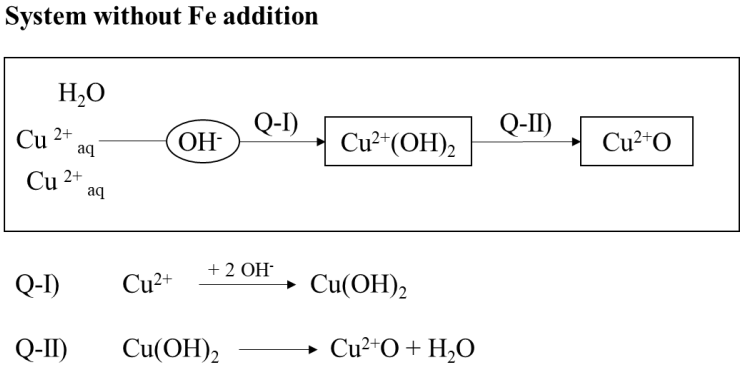

Figure 7.3: *Reactions in the Cu-system without Fe addition, Cu^{2+} precipitates as Cu-Hydroxide (Q-I) in the alkaline environment, which transforms rapidly to tenorite (Q-II) under the release of water.*

Influence of impurities on CuO

Doped CuO is technically relevant because of its interesting physical properties. For example, it is a semiconductor with high capacitance and is used for photocatalysis and antibacterial activity. Therefore, many studies focus on developing chemical precipitation methods to incorporate different metals into the structure of CuO. For example, *Aadil et al. (2021)* partly substituted Cu with Ag and Mn and observed that $Cu_{0.9}Mn_{0.05}Ag_{0.05}O$ can eliminate bacteria and toxic dyes from industrial effluents. Likewise, Zn-doped CuO acts as a photocatalyst to degrade toxic dyes *(Rehman et al., 2021)* and has significant antibacterial activity *(Malka et al., 2013)*, as well as Ni-doped CuO *(Ramya et al., 2016)*.

Several studies focus on removing toxins in wastewater by using CuO nanoparticles as adsorbents. For example, CuO synthesised via precipitation can remove arsenic from the water below the safe limit *(Pal et al., 2017)*. Furthermore, it was found that Hg^0 is strongly adsorbed

on the Cu-terminated CuO (110) surface, and hence, CuO can be used to remove Hg^0 from wastewater *(Xiang et al., 2012)*.

In addition to Cu, the electroplating wastewater in this work showed minor impurities of Fe, Ni, Zn, Cr, Pb, and Mn. After treatment, the water analysis showed a decrease in the concentrations of the minor elements. The alteration of the precipitates at elevated temperatures led to the lowest concentration for all impurities in the solution. The growth of CuO during alteration and the reduction in impurities in the solution indicates that the minor elements are incorporated into the structure of the CuO. An adsorption of the impurities to the surface of CuO cannot be excluded. However, adsorption usually leads to an increased metal concentration in the altered aliquots, which is not the case in my experiments and, hence, is rather unlikely.

Hence, SPOP can be used for doping CuO by using Cu-containing wastewater with accessories of elements like Fe, Ni, Zn, Cr, Pb, and Mn to synthesise designed materials.

Influence of the stirring speed on CuO and brochantite formation

Stirring is needed to reach a homogeneous distribution and a uniform pH value in the reactor. The experiments at pH 11 showed that with increasing stirring speed, the phase paragenesis changed from tenorite (CuO) and the soluble salt thenardite (Na_2SO_4) (< 200 rpm) to Cu-hydroxide, thenardite, and brochantite, a sulfate-containing mineral ($Cu_4(OH)_6(SO_4)$) (> 500 rpm). The formation of brochantite and then the influence of the stirring speed on the phase stabilities are discussed below.

- **Effect of the pH conditions on the brochantite formation**

The applied procedure corresponds with the standard route for brochantite synthesis in which a $CuSO_4$ solution is alkalised with a base. *Table IV.7* in the Appendix overviews the published experimental parameters for brochantite synthesis. It was found that pH conditions affect the formation of brochantite, and most studies show that brochantite is stable at a slightly alkaline pH of 6 to 8. Notably, the pH conditions for brochantite formation vary depending on the concentration of $CuSO_4$ solution. For low-concentrated $CuSO_4$ solutions of 0.001 M, brochantite precipitates at a low pH of 6 *(Zittlau et al., 2013)*. For highly concentrated solutions of 0.1 to 0.5 M, brochantite formation shifted towards a higher pH of approx. pH 8 *(Prasad and Rao, 1985; Koga et al., 1997; Novikova et al., 2016)*. Brochantite formation was found at an even higher pH of 11 by *Rak et al. (2020)* conducted with highly concentrated $CuSO_4$ concentrations of 0.1 to 0.626 M. This corresponds very well with this study, with a 0.15 M $CuSO_4$ solution and a final pH of 11.

- **Effect of the Cu-activity on the brochantite formation**

Zittlau et al. (2013) calculated Eh-pH diagrams in the system Cu-S-O-H for different temperatures and Cu activities. The computed stability fields of brochantite shifted slightly towards higher pH with increasing Cu-activity. At oxidising conditions but with lower Cu- and S-activities than in this study, the stability field of brochantite is between pH 4.9 – 6.8 *(Zittlau et al., 2013)*. For higher Cu activities (1000 ppm $CuSO_4$), *Ding et al. (2019)* calculated a larger stability field for brochantite between pH 4.4 and 10.3. The preconditions and results of *Ding et al. (2019)* and those of *Rak et al. (2020)* are similar to this study, whereby the Cu concentration in my system is even higher, which explains the experimentally determined stability of brochantite at pH 11. These results show that Cu concentration plays a crucial role in brochantite formation; at the same time, it leads to a shift in the stability range of brochantite to higher pH values. In comparison, tenorite has a large stability field between pH 6.8 – 14 under oxidising and reducing conditions *(Zittlau et al., 2013)*. Accordingly, at pH 11, the synthesis of tenorite is expected, and only at pH < 7 brochantite formation.

- **Effect of the stirring speed on the phase formation**

The effects of stirring rate are usually neglected in experimental studies. Most studies state constant stirring without details on the stirring speed (see *Table IV.7* in the Appendix). To investigate this, I conducted experiments using different stirring speeds between 100 and 500 revolutions per minute (rpm). The results clearly show a dependency of the precipitates on the stirring rate: At slow stirring rates, tenorite, spertiniite and thenardite coexist, while at stirring rates higher than 300 rpm brochantite occurs. After one day of ageing, brochantite was only observed in the experiment with 500 rpm. *Rak et al. (2020)* applied a stirring speed of 250 rpm using a magnetic stirrer to obtain brochantite. His reaction condition is within the range of my experiments and shows that brochantite can precipitate as early as 250 rpm. The comparison with my aged experiments, however, indicates that this brochantite is not stable, and over time, it transforms into tenorite.

With increasing stirring speed, a shift towards oxidising conditions was measured. *Figure 7.4* shows the approximate stability fields of the sulfate-bearing phases based on the results shown in *Figure 6.5*. Sulfate is bound into thenardite at low stirring speed (> 200 rpm) and low Eh conditions. Pure brochantite occurs at high stirring speeds (500 rpm) and Eh conditions. Within the range of 250 and 450 rpm, thenardite occurs together with brochantite. The resulting approximate phase stabilities are indicated in *Figure 7.4*. The corresponding reaction K-IV shows no redox reaction; hence, no electron transfer occurs. Therefore, the increase in Eh value seems only caused by oxygen supply due to air intake. However, redox reactions might have occurred for the accessory elements Fe^{2+}, Cr^{3+}, and Mn^{2+} (see wastewater composition in *Table 5.5*). For example, Fe^{2+} might have oxidised to Fe^{3+} to form FeOOH or $Fe_8(OH)_6SO_4$. Yet, none of these phases could be detected using the methods used.

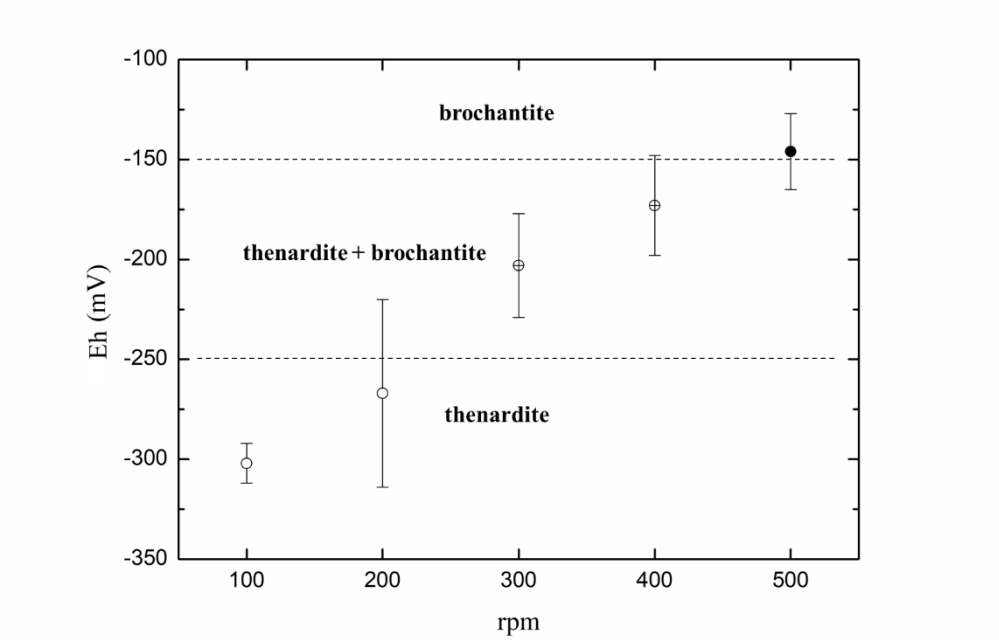

Figure 7.4: *Approximate stability fields of the sulfate-bearing phases thenardite (Na_2SO_4) and brochantite ($Cu_4(OH)_6SO_4$) as a function of electron activity (Eh) and stirring speed. Thenardite occurs at low electron activity (< -250 mV), and pure brochantite is formed at high electron activity (> -150 mV). Within this range, thenardite and brochantite were observed. The corresponding reaction is not driven by electron transfer. Accordingly, the formation of brochantite requires an environment with a high oxygen fugacity, which can only be achieved by rapidly mixing the solution.*

Figure 7.5 shows an overview of the potential reactions as a function of the steering rate. At low stirring speeds (100 and 200 rpm), the phase spertiniite ($Cu(OH)_2$) is formed (*Reaction K-I* in *Figure 7.5)*, and sulfate is bound with Na, forming thenardite (Na_2SO_4). In the alkaline environment (pH > 11) $Cu(OH)_2$ is not stable and is quickly transformed into CuO with loss of water (*Reaction K-II),* indicating that it is the stable phase under the given condition. With increased stirring speed (300 and 400 rpm), brochantite ($Cu_4(OH)_6SO_4$) precipitates spontaneously together with spertiniite and thenardite (*Reaction K-III* in *Figure 7.5*). The fresh, weakly crystalline brochantite (see *Figure IV.6* in the Appendix) decomposes in the alkaline environment to CuO and Na_2SO_4, releasing H_2O and H^+ ions (*reaction K-IV* in *Figure 7.5*).

At high stirring speed (500 rpm), only well crystalline brochantite ($Cu_4(OH)_6(SO_4)$) without other Na-containing phases was formed, which remained stable over the tested alteration time of 24 hours (*reaction K-III*). The *reaction K-IV* confirms that compared to the abovementioned reaction path, less NaOH is needed to maintain a pH of 11 during the experiments (see *Figure 6.6*).

In the Zn-system, *Tandon (2021)* found that stirring during ageing favours the transformation of gordaite with formula $NaZn_4(SO_4)(OH)_6Cl*6H_2O$, to ZnO. This means that stirring favours

the transformation of a Zn-hydroxy-sulfate to an oxide. In contrast, in the Cu-system, fast stirring favours the formation of the Cu-hydroxy-sulfate. However, the concentrations of Cu (> 9 g/l) in this study and Zn (2 g/l) in the study of *Tandon (2021)* are not comparable. As mentioned above, a high Cu concentration is crucial for brochantite formation. For the Zn-system, the influence of the concentration on the phase formation is unknown.

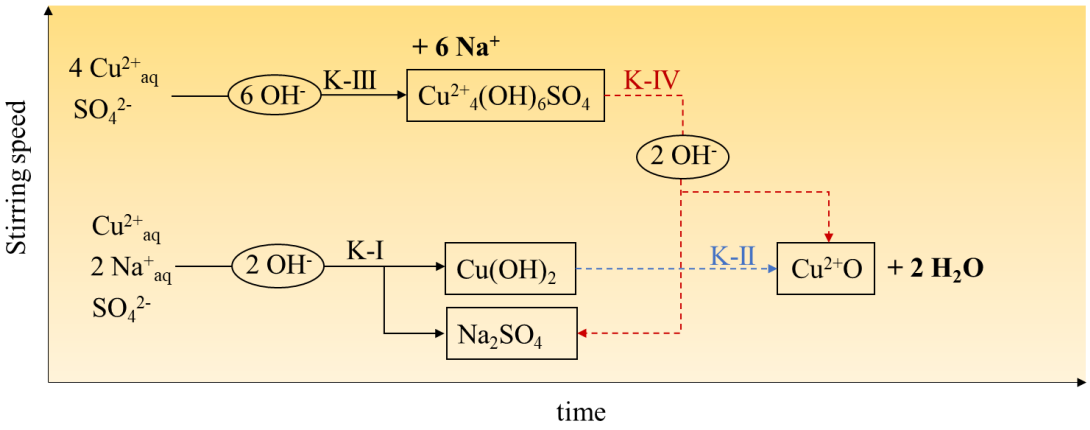

K-I) $Cu^{2+} + SO_4 + 2\ Na^+ \xrightarrow{+\ 2\ OH^-} Cu(OH)_2 + Na_2SO_4$

K-II) $Cu(OH)_2 \longrightarrow Cu^{2+}O + H_2O$

K-III) $4\ Cu^{2+} + SO_4 + 6\ Na^+ \xrightarrow{+\ 6\ OH^-} Cu^{2+}_4(OH)_6SO_4 + 6\ Na^+$

K-IV) $Cu^{2+}_4(OH)_6SO_4 + 2\ Na^+ \xrightarrow{+\ 2\ OH^-} 4\ CuO\ +\ Na_2SO_4\ + 2\ H_2O + 2\ H^+$

Figure 7.5: *Illustration of Cu, SO42- and Na reaction pathways depending on the stirring speed. First precipitation reactions (K-I and K-III) are shown with black continuous arrows. Alteration reactions (K-II and K-IV) are shown with dashed arrows in blue or red, respectively. At low stirring of 100 and 200 rpm, sulfate precipitates as Na_2SO_4 and Cu in the form of $Cu(OH)_2$ (K-I), which rapidly decomposes to CuO (K-II) under the formation of H_2O. With increasing stirring speeds of 300 and 400 rpm, brochantite ($Cu_4(OH)_6SO_4$) forms in the fresh precipitates (K-III). During alteration in the alkaline environment, it decomposes to Na_2SO_4 and CuO (K-IV). At the highest tested stirring speed of 500 rpm, Cu and sulfate precipitate solely as $Cu_4(OH)_6SO_4$ (K-III), which stays stable over 24 hours.*

7.3. Robustness of the process

To be a viable alternative for wastewater treatment regarding water purification and phase synthesis, the SPOP process must be robust in terms of its functions and performance. Generally, a method is robust when insensitive to disturbances and the desired results are achieved even if the reaction conditions deviate from the routine settings. The more parameters must be considered, the harder it is to accomplish such a state. The scale-up experiments show that several parameters can influence the SPOP process. The following outlines some of the critical factors that may deviate from the target value during a routine procedure: reaction

temperature, Fe:Me-ratio, precipitation pH, or, respectively, alkalisation rate, and the composition of the wastewater.

Reaction temperature: The wastewater is tempered in a boiler, the only component in the pilot facility with a regulation system to keep the temperature constant. The other components, e.g., the reactor, are not heated. Consequently, once the tempered wastewater leaves the boiler, it loses heat. Adding reactants, e.g., NaOH and Fe-solution, which are not pre-heated and have room temperature, may intensify the temperature drop.

Even at low temperatures, oxides or native metals can be precipitated without impairing the high purification rates. Hence, the process is robust regarding reaction temperature variations of up to 10 °C for the Zn-, Au-, and Cu-system (see *Table IV. 6* in the Appendix). However, there may be deviations depending on the metal system. In some metal systems, the reaction temperature is a sensitive parameter with only a small window for deviation. For example, in the Ni-system, Ni-ferrite formation requires a minimum temperature of 80 ° C, below the synthesis fails *(Tandon, 2015; Appel, 2019)*.

The results show that temperature is a limiting factor in the process's robustness only for specific systems.

Fe^{2+}/Me-ratio: Another critical factor is the Fe^{2+}/Me ratio. In principle, Me-oxides also precipitate if the Fe/Me-ratio deviates from the target value, affecting the phase composition. An excellent example is the formation of Cu-ferrite as a single-phase. The experiments show that it can only be formed with Fe^{2+}. A solution with ferric Fe^{3+} leads to a mixture of different phases consisting of cuprite, Cu-ferrite, delafossite, and maghemite, accompanied by GR II.

Hence, the SPOP process is robust to a disturbed Fe/Me ratio, as shown in the Cu system. However, the result of the water treatment was comparatively diminished.

Alkalisation rate/precipitation pH: The upscaling experiments showed that the precipitation pH and the alkalisation rates are critical parameters. A decrease in the dosing pump performance and, thus, a deviation from the pH setpoint inevitably leads to hydroxide formation. Hence, the adjustment of the alkalisation process is very sensitive and is a limiting factor for the robustness of the SPOP process; any deviation can contribute to the failure of the process.

Variation of the wastewater composition: The composition of the initial solution and the concentration of the metals are decisive for defining the critical treatment parameters. In practice, highly concentrated wastewater is more suitable for the SPOP process. Evaporation is one way of concentrating metals in wastewater. However, laboratory-scaled experiments have shown that removing metals in the range of a few mg/l is also possible in principle *(Anagnostopoulos, 2017)*.

Real industrial wastewater may contain unknown substances such as EDTA, an additive commonly used in industry. The experiments did not reveal any negative influence on the result. However, some chemical complexes can complicate the application of SPOP due to their chemical properties; in these cases, the treatment must be individually adjusted.

7.4. Modification of the SPOP process

On an industrial scale, batch processes can pose technical or chemical problems, such as long residence times in the reactor, higher energy consumption with lower production efficiencies, and thus higher operating costs *(Gopi et al., 2022)*. For this reason, continuous flow processes are used in many industries, such as petrochemicals, food chemistry, pharmaceuticals and fine chemicals, to achieve higher productivity *(Wiles and Watts, 2012)*. For wastewater treatment, efforts are being made to develop technologies for continuous treatment, too, for example, for rare earth-containing wastewater using a process involving precipitation, adsorption, and oxidation *(Lee et al., 2021)* or wastewater from the textile industry using the degrading abilities of the white rot fungus *Trametes versicolor (Blánquez et al., 2008)*.

The SPOP process involves simultaneous precipitation and sedimentation and requires the removal of a specific volume of wastewater. In this thesis, the implementation of a continuous precipitation process was tested on a laboratory scale based on the known process parameters.

The results of the continuous flow experiments in the **Cu system** show that the formation of ferrite and delafossite is feasible. Therefore, the SPOP process has the potential to be operated in a continuous mode. This has been proven particularly for the formation of delafossite. In contrast, the SPOP batch process is prone to failure regarding delafossite formation because of an intricate alkalisation procedure. However, the water analysis results show that the batch process achieves better purification than the continuous process.

In the **Ni-system,** both procedures, as a batch test or continuous approach, showed that Ni-ferrite formation is feasible *(Appel, 2019)*The quality of the precipitation products is the same when using synthetic wastewater. However, the continuous flow process was more prone to failure when experimental parameters deviated from the optimal precipitation conditions. After treatment, the Ni concentrations in the solutions were low in both precipitation procedures. Most samples met the limit value for discharge of Ni (0.5 mg/l) according to the *Abwasserverordnung, Anhang 40* (see *Table IV.1* in the Appendix).

In the **Sn-system,** wastewater from an activator bath from the electroplating industry was treated *(Zwerschke, 2019)*. In both processes, Sn precipitated as jeanbandyite ($FeSnO(OH)_5$) with traces of hydroromarchite ($Sn_3O_2(OH_2)$).

The precipitation products of the two processes are comparable for all tested Me systems, making the continuous flow process a promising alternative to the batch process. The purification rates may be lower than with the batch process depending on the elemental system.

8. Conclusion and Outlook

This research aimed to scale up the specific product-orientated precipitation process (SPOP) and test its reproducibility with a pilot plant in automated batch operation concerning i) the efficiency of water treatment and ii) the phase composition. Based on a quantitative and qualitative analysis of the initial wastewater and treated process water, it can be concluded that the water purification is efficient in the upscaled system, and the laboratory results can be reproduced for real industrial wastewater. For each tested elemental system, the results show that the quality of water purification depends primarily on the alkalisation rate and the stoichiometric addition of optional Fe. Independently of the addition or abdication of Fe, all tested elements can be removed to > 99% from the wastewater, but Fe has a positive effect on the fast removal of Cu. The alteration time and temperature are crucial for high metal removal for both Fe-rich and Fe-free systems. Generally, the best purification results were achieved after an alteration of 24 hours at elevated temperature (40 – 60 °C). The impurities in the real Cu-containing wastewater were Fe, Ni, Zn, Pb, Cr, and Mn. They have all been removed by the treatment, in many cases below the limit value for discharge.

The precipitation recipes for specific phase formation could be upscaled, and the laboratory results reproduced and extended. The results indicate that ZnO, CuO, (Cu-)ferrite and zero-valent Au can be synthesised with the pilot facility treating several litres of wastewater iteratively. The quality and quantity of oxides increase with the alteration time (< 24 h) and alteration temperature (> 60 °C). Potential hydroxides like green rust (Fe^{2+}-Fe^{3+} double hydroxy sulphate) and spertiniite ($Cu(OH)_2$) are more abundant in the fresh precipitates but were found to be metastable and decrease during alteration until complete dissolution. They are essential precursory phases for the oxides' formation.

The technical analysis has shown that the components used in the pilot facility and the software influence the correct process execution. Consequently, the pilot facility had to undergo several technical and software adjustments to improve the implementation of the SPOP process. Finally, an automated batch mode was realised, proving that the SPOP process can be run autonomously. The application of the SPOP pilot facility revealed insights into the criticality of certain process parameters. For example, it was shown that the precision of the ideal reaction temperature for phase formation is less crucial than the alteration temperature. However, the effectiveness of the SPOP methodology in batch mode depends strongly on the precise performance of the alkalisation rate and the precipitation pH. For the alkalisation rate to be executed correctly, it was found that (1) a strong and precise dosing system is crucial, and (2) the solution needs to be homogenous. Different stirring speeds were tested to ensure a homogeneous solution. By analysing the precipitation products formed at different stirring speeds, this thesis has shown how the stirring speed indirectly governs the structure and

composition of formed phases. This has demonstrated that new process parameters became relevant with the upscaling.

At the users, wastewater may accrue either in intervals or continuously. For each application, either batch or continuous treatment processes are more suitable. Since the SPOP process was initially designed as a batch process, another aim of this thesis was to test for a continuous treatment. Therefore, the process sequence was varied on a laboratory scale, and the results show that ferrite and $CuFeO_2$ (delafossite) can be synthesised, like in the batch mode. For delafossite synthesis, the continuous flow method was less prone to disturbances than the batch method, and the precipitation temperature could be decreased from 70 °C to room temperature. Alteration causes a higher crystallinity of the delafossites but also pushes the remobilisation of Cu from the fresh residues back into the solution. Additionally, the findings of previous studies for delafossite formation could be broadened by showing the influence of the mineraliser concentration on the polytype formation.

In case of a partial process failure, it can be concluded that the water purification rate is reduced, especially for the remaining Fe concentration. The results show that hydroxides occur more abundantly in the fresh precipitates, and the specific phase formation fails. Instead, phase mixtures of different oxides emerge. For sole metal recovery, these precipitation products can still be processed.

This research clearly illustrates that SPOP is robust as all critical process parameters of the multifactor system can be controlled. Still, it also raises the question about its applicability directly at the user. Therefore, the SPOP pilot facility could be operated on-site in the next step. At this stage of development and based on the findings of this thesis, a SPOP pilot plant could be designed for larger industrial applications.

One open challenge is nanoparticle filtration, as nanoparticles are produced with the SPOP process. Due to their small size, the filtration of nanoparticles is a well-known problem. Therefore, many technologies are currently being developed in the field of nanofiltration. One promising technique is the so-called oscillating membrane filtration, in which a filter cake is built up and detached from the membrane to avoid its blockage by the fine particles. An ongoing project tackles the filtration of nanoscale metal-bearing precipitates using oscillating membrane filtration.

Furthermore, the experiments show that the residues are phase mixtures. Still, the metals are bound in distinguishable phases, each with uniform particle sizes (e.g., Cu in large cuprite crystals with cubic morphology). In this case, a selective separation by particle size can be used to sort the contained metals and create processable mono-fractions. Technologies like micro-sieving or oscillating membrane filtration could be explored for this undertaking.

Further research is needed on mono-fractions to investigate whether SPOP can be used to sequentially precipitate metals. As a first step, an extended literature study and modelling of metal stability fields using geochemical software could be conducted, followed by experimental verification. One big challenge is the varying metal concentrations in multi-element wastewater, which range from very low to highly concentrated.

The influence of the agitation rate on the reaction system should be further investigated to understand better the relationship between the agitation rate and the structure of formed phases. The results indicate that the agitation rate directly influences phase formation, and kinetic effects on phase formation should also be further investigated.

SPOP can be used to synthesise nanoscale materials with a specific composition that may be of great interest due to their physical properties. For example, CuO/ZnO nanocomposites show a high photocatalytic effect. They apply to treating textile dye wastewater *(Sakib et al., 2019)*, and doped CuO nanoparticles are interesting due to their various technological applications. To better understand the implications of these results, future studies could address the physical properties of the SPOP synthesis products and start investigating their photocatalytic properties using UV-Vis spectrophotometry.

This research shows that wastewater is a secondary resource material, and recycling technologies can be developed to make it accessible. The upscaling and establishment of efficient recycling technologies can contribute to avoiding the emergence of waste and keeping materials in the cycle of matter. The recycling potential of metals from wastewater with SPOP could be even higher if the wastewater were collected as single-element systems and not mixed with other wastewater. Such a solution requires a conceptual rethink: treatment should not be carried out with centrally collected multi-element wastewater but directly at the source of wastewater production to achieve the highest possible quality and purity of product phases.

III. References

Aadil, M., Rahman, A., Zulfiqar, S., Alsafari, I.A., Shahid, M., Shakir, I., Agboola, P.O., Haider, S., and Warsi, M.F., 2021, Facile synthesis of binary metal substituted copper oxide as a solar light driven photocatalyst and antibacterial substitute. Ad*vanced Powder Technology*, 32, pp. 940–950.

ABAG-itm GmbH, 2008, Abfallsteckbrief 1101 Chemische Oberflächenbearbeitung – Galvanikschlamm. https://abag-itm.de/startseite/.

Abdullah, N., Yusof, N., Lau, W.J., Jaafar, J., and Ismail, A.F., 2019, Recent trends of heavy metal removal from water/wastewater by membrane technologies. *Journal of Industrial and Engineering Chemistry*, 76, pp. 17–38.

Ahmaruzzaman, M., 2011, Industrial wastes as low-cost potential adsorbents for the treatment of wastewater laden with heavy metals. *Advances in Colloid and Interface Science*, 166, pp. 36–59.

Al-Rashdi, B.A.M., Johnson, D.J., and Hilal, N., 2013, Removal of heavy metal ions by nanofiltration. *Desalination*, 315, pp. 2–17.

Álvarez-Ayuso, E., García-Sánchez, A., and Querol, X., 2003, Purification of metal electroplating waste waters using zeolites. *Water Research*, 37, pp. 4855–4862.

Alyüz, B., and Veli, S., 2009, Kinetics and equilibrium studies for the removal of nickel and zinc from aqueous solutions by ion exchange resins. *Journal of Hazardous Materials*, 167, pp. 482–488.

Al-Zoubi, H., Ibrahim, K.A., and Abu-Sbeih, K.A., 2015, Removal of heavy metals from wastewater by economical polymeric collectors using dissolved air flotation process. *Journal of Water Process Engineering*, 8, pp. 19–27.

Amrute, A.P., Łodziana, Z., Mondelli, C., Krumeich, F., and Pérez-Ramírez, J., 2013, Solid-state chemistry of cuprous delafossites: Synthesis and stability aspects. *Chemistry of Materials*, 25, pp. 4423–4435.

Anagnostopoulos, I., 2017, Recovery of heavy metals in low concentrated industry wastewater (Cu-Al-Mn-H_2O, Cu-Zn-Al-H_2O) [Masterthesis]. Ludwig-Maximilians-Universität München.

Anagnostopoulos, I., Knof, J., and Heuss-Aßbichler, S., 2019, Industrieabwasser als Rohstoffquelle für Buntmetalle: Abwassereinigung und Rohstoffrückgewinnung mit einer portablen Technikumsanlage mit Hilfe des SPOP Verfahrens, *in* Deutsche Gesellschaft für Abfallwirtschaft, 9. Wissenschaftskongress, Amberg, pp. 195–199.

Anagnostopoulos I., Heuss-Aßbichler S., 2021, Residues of Industrial Wastewater Treatment: Hazardous Waste or Anthropogenic Resource, in Pöllmann, H., *Industrial wastes – Characterization, Modification and Application of industrial residues*, DeGruyter, pp. 403–432.

Andersen, H.L., Frandsen, B.A., Gunnlaugsson, H.P., Jørgensen, M.R.V., Billinge, S.J.L., Jensen, K.M.O., and Christensen, M., 2021, Local and long-range atomic/magnetic structure of non-stoichiometric spinel iron oxide nanocrystallites. *IUCrJ*, 8, pp. 33–45.

Appel, A., 2019, Precipitation of Nickel from aqueous solutions - comparison of two different processes [Bachelorthesis]. Ludwig-Maximilians-Universität München.

Aquino, A., Lezzerini, M., Giaccherini, A., Montegrossi, G., and di Benedetto, F., 2020, Thermochemical stability of delafossite and other relevant ternary phases in the Cu–Fe–S–O–H system. *Applied Geochemistry*, 123, 104795, pp. 1–7.

Babaei, H., Khosravi, M., Sovizi, M., Khorramie, S., 2020, Investigating the Au-Cu thick layers electrodeposition rate with pulsed current by optimization of the operation conditions. *Journal of Electrochemical Science and Technology*, 11(2), pp. 172–179.

Babu, B.R., Bhanu, S.U., and Meera, K.S., 2009, Waste minimization in Electroplating Industries: A review. *Journal of Environmental Science and Health*, 27(C), pp. 155–177.

Bakhtiari, F., and Darezereshki, E., 2011, One-step synthesis of tenorite (CuO) nano-particles from Cu_4 (SO_4) $(OH)_6$ by direct thermal-decomposition method. *Materials Letters*, 65, pp. 171–174.

Baltpurvins, K.A., Burns, R.C., Lawrance, G.A., and Stuart, A.D., 1997, Effect of electrolyte composition on zinc hydroxide precipitation by lime. *Water Research*, 31, pp. 973–980.

Barrado, E., Prieto, F., Garay, F.J., Medina, J.S., and Vega, M., 2002a, Characterization of nickel-bearing ferrites obtained as by-products of hydrochemical wastewater purification processes. *Electrochimica Acta*, 47, pp. 1959–1965.

Barrado, E., Prieto, F., Medina, J., and Lopez, F.A., 2002b, Characterisation of solid residues obtained on removal of Cr from waste water. *Journal of Alloys and Compounds*, 335, pp. 203–209.

Bernard, E., Jimoh, A., and Odigure, J.O., 2013, Heavy Metals Removal from Industrial Wastewater by Activated Carbon Prepared from Coconut Shell. *Research Journal of Chemical Sciences*, 3, pp. 3–9.

Bhattacharyya, D., Jumawan Jr., A.B., and Grieves, R.B., 1979, Separation of Toxic Heavy Metals by Sulfide Precipitation. *Separation Science and Technology*, 14, pp. 441–452.

Blánquez, P., Sarrà, M., and Vicent, T., 2008, Development of a continuous process to adapt the textile wastewater treatment by fungi to industrial conditions. *Process Biochemistry*, 43, pp. 1–7.

Boricha, A.G., and Murthy, Z.V.P., 2009, Preparation, characterization and performance of nanofiltration membranes for the treatment of electroplating industry effluent. *Separation and Purification Technology*, 65, pp. 282–289.

Campbell, A., Schwertmann, U., Campbell, P., 1997, Formation of cubic phases on ferrihydrite heating. *Clay minerals*, 32, pp. 615–622.

Charerntanyarak, L., 1999, Heavy Metals Removal By Chemical Coagulation And Precipitation. *Water Science Technology*, 39, pp. 135–138.

Chaúque, E.F.C., Zvimba, J.N., Ngila, J.C., and Musee, N., 2016, Fate, behaviour, and implications of ZnO nanoparticles in a simulated wastewater treatment plant. *Water SA*, 42, pp. 72–81.

Chen, Q., Luo, Z., Hills, C., Xue, G., and Tyrer, M., 2009, Precipitation of heavy metals from wastewater using simulated flue gas: Sequent additions of fly ash, lime and carbon dioxide. *Water Research*, 43, pp. 2605–2614.

Chen, Q., Yao, Y., Li, X., Lu, J., Zhou, J., and Huang, Z., 2018, Comparison of heavy metal removals from aqueous solutions by chemical precipitation and characteristics of precipitates. *Journal of Water Process Engineering*, 26, pp. 289–300.

Choi, S., Johnston, M., Wang, G.-S., and Huang, C.P., 2018, A seasonal observation on the distribution of engineered nanoparticles in municipal wastewater treatment systems exemplified by TiO_2 and ZnO. *Science of the Total Environment*, 625, pp. 1321–1329.

Choi, D.H., Moon, S.J., Hong, J.S., An, S.Y., Shim, I.B., and Kim, C.S., 2009, Impurity dependent semiconductor type of epitaxial $CuFeO_2$ (111) thin films deposited by using a pulsed laser deposition. *Thin Solid Films*, 517(4), pp. 3987–3989.

Choi, J.W., Song, M.H., Bediako, J.K., and Yun, Y.S., 2020, Sequential recovery of gold and copper from bioleached wastewater using ion exchange resins. *Environmental Pollution*, 266(3), 115167, pp. 1–7.

Chukanov, N. v, 2014, Infrared spectra of mineral species. *Springer Geochemistry / Mineralogy*, 1.

Correa, J.R., Canetti, D., Castillo, R., Llópiz, J.C., and Dufour, J., 2006, Influence of the precipitation pH of magnetite in the oxidation process to maghemite. *Materials Research Bulletin*, 41(4), pp. 703–713.

Cudennec, Y., and Lecerf, A., 2003, The transformation of $Cu(OH)_2$ into CuO, revisited. *Solid State Sciences*, 5(11-12), pp. 1471–1474.

Ćurković, L., Cerjan-Stefanović, Š., and Filipan, T., 1997, Metal ion exchange by natural and modified zeolites. *Water Research*, 31(6), pp. 1379–1382.

Dehoust, G., Küppers, P., Blepp, M., Jenseit, W., Goldmann, D., and Breitenstein, B., 2016, Überprüfung der Grenzwerte von Metallen in Abfällen, bei deren Überschreitung eine Verwertung mit Metallrückgewinnung der einfachen Abfallverwertung im Versatz oder auf Deponien vorgeht. Umweltbundesamt.

Demirel, B., Yenigün, O., and Bekbölet, M., 1999, Removal of Cu, Ni and Zn from wastewaters by the ferrite process. *Environmental Technology*, 20(9), pp. 963–970.

Dietrich, G., 2017, Hartinger Handbuch Abwasser- und Recyclingtechnik. *Hanser*.

Ding, M., Ariyanti, D., and Gao, W., 2019, Formation of copper hydroxyl sulfates in $CuSO_4$ solution by NaOH titration. *International Journal of Modern Physics B*, 33(1-3) 1940059, pp. 1–6.

Du, Z., Xiong, D., Verma, S.K., Liu, B., Zhao, X., Liu, L., and Li, H., 2018, A low temperature hydrothermal synthesis of delafossite $CuCoO_2$ as an efficient electrocatalyst for the oxygen evolution reaction in alkaline solutions. *Inorganic Chemistry Frontiers*, 5(1), pp. 183–188.

Effenberger, H., 1991, Structure of Hexagonal Copper(I) Ferrite: *Acta Crystallographica*, C(47), pp. 2644–2646.

Engels, K., 2020, Precipitation of Cobalt in the System Co-Cu-Fe-SO_4-H_2O [Bachelorthesis]: Ludwig-Maximilians-Universität.

Erdem, M., and Tumen, F., 2004, Chromium removal from aqueous solution by the ferrite process. *Journal of Hazardous Materials*, 109(1–3), pp. 71–77.

Ethiraj, A.S., and Kang, D.J., 2012, Synthesis and characterization of CuO nanowires by a simple wet chemical method. *Nanoscale Research Letters*, 7(70), pp. 1-5.

Feng, X., Wang, X., Zhu, M., Koopal, L.K., Xu, H., Wang, Y., and Liu, F., 2015, Effects of phosphate and silicate on the transformation of hydroxycarbonate green rust to ferric oxyhydroxides. *Geochimica et Cosmochimica Acta*, 171, pp. 1–14.

Franzreb, M., 2003, Magnettechnologie in der Verfahrenstechnik wässriger Medien. Forschungszentrum Karlsruhe in der Helmholtz-Gemeinschaft, FZKA 6916.

Friege, H., 2013, Waste - valuables - secondary resources - Contaminants - waste again? *Environmental Sciences Europe*, 25(9), pp.1–2.

Fu, F., and Wang, Q., 2011, Removal of heavy metal ions from wastewaters: A review. *Journal of Environmental Management*, 92(3), pp. 407–418.

Garófalo Chaves, H.L., Curry, J.E., Stone, D.A., Carducci, M.D., and Chorover, J., 2009, Nickel Incorporation in Fe(II,II) Hydroxysulfate Green Rust: Effect on Crystal Lattice Spacing and Oxidation Products. *Revista Brasileira de Ciência do Solo*, 33, pp. 1115–1123.

Gharabaghi, M., Irannajad, M., and Azadmehr, A.R., 2012, Selective Sulphide Precipitation of Heavy Metals from Acidic Polymetallic Aqueous Solution by Thioacetamide. *Industrial and Engineering Chemistry Research*, 51(2), pp. 954–963.

Gilbert, F., Refait, P., Lévêque, F., Remazeilles, C., and Conforto, E., 2008, Synthesis of goethite from Fe(OH)2 precipitates: Influence of Fe(II) concentration and stirring speed. *Journal of Physics and Chemistry of Solids*, 69(8), pp. 2124–2130.

González, M.A., Trócoli, R., Pavlovic, I., Barriga, C., and la Mantia, F., 2015, Capturing Cd(II) and Pb(II) from contaminated water sources by electro-deposition on Hydrotalcite-like Compounds. *Physical Chemistry Chemical Physics*, 18(3), p. 1838–1845.

Gopi, R., Thangarasu, V., Vinayakaselvi, A., and Ramanathan, A., 2022, A critical review of recent advancements in continuous flow reactors and prominent integrated microreactors for biodiesel production. *Renewable and Sustainable Energy Reviews*, 154, 111869.

Graedel, T.E., and Erdmann, L., 2012, Will metal scarcity impede routine industrial use?. *MRS Bulletin*, 37(4), p. 325–331.

Grondahl, L.O, 1933, The Copper-Cuprous-Oxide Rectifier and Photoelectric Cell. Reviews of modern physics, 5, pp.141–168.

Harland, C.E., 1994, Discovery and Structure of Solid Inorganic Ion Exchange Materials, *in* Ion Exchange: Theory and Practice, Cambridge, The Royal Society of Chemistry, pp. 1–20.

Hegazi, H.A., 2013, Removal of heavy metals from wastewater using agricultural and industrial wastes as adsorbents. *HBRC Journal*, 9, pp. 276–282.

Helliwell, M., and Smith, J., 1997, Brochantite. *Acta Crystallographica*, C53, pp. 1369–1371.

Heuss-Aßbichler, S., and Anagnostopoulos, I., 2021, Gesamtkonzept zur Umsetzung der hydroxidfreien Fällung von Metallen aus Abwässern verschiedener Branchen: Bau einer mobilen Technikumsanlage. Abschlussbericht.

Heuss-Aßbichler, S., Huber, A.L., and John, M., 2016a, Recovery of Heavy Metals From Industrial Wastewater – Is It Worth It ?, *in* 5th International Conference on Industrial and Hazardous Waste Management, pp. 193–200.

Heuss-Aßbichler, S., John, M., Klapper, D., Bläß, U.W., and Kochetov, G., 2016b, Recovery of copper as zero-valent phase and/or copper oxide nanoparticles from wastewater by ferritization. *Journal of Environmental Management*, 181, pp. 1–7.

Heuss-Aßbichler, S., John-Stadler, M., and Huber, A., 2016c, Abschlussbericht Rückgewinnung von Buntmetallen aus Industrieabwässern.

Hien Hoa, T.T., Liamleam, W., and Annachhatre, A.P., 2007, Lead removal through biological sulfate reduction process. *Bioresource Technology*, 98(13), pp. 2538–2548.

Huang, Y., and Feng, X., 2019, Polymer-enhanced ultrafiltration: Fundamentals, applications and recent developments. *Journal of Membrane Science*, 586(5), pp. 53–83.

Huang, J.H., Kargl-Simard, C., Oliazadeh, M., and Alfantazi, A.M., 2004, pH-Controlled precipitation of cobalt and molybdenum from industrial waste effluents of a cobalt electrodeposition process. *Hydrometallurgy*, 75(1-4), pp. 77–90.

Inglezakis, V.J., Loizidou, M.D., and Grigoropoulou, H.P., 2003, Ion exchange of Pb^{2+}, Cu^{2+}, Fe^{3+}, and Cr^{3+} on natural clinoptilolite: Selectivity determination and influence of acidity on metal uptake. *Journal of Colloid and Interface Science*, 261(1), pp. 49–54.

Inouye, K., Murata, K., and Ishikawa, T., 1971, The Effect of Copper(lI) on the Formation of Magnetite from Colloidal Iron (II) Hydroxide. *Z. anorg. allg. Chem*, 886, pp. 340–344.

Islamoglu, S., Yilmaz, L., and Ozbelge, H.O., 2006, Development of a Precipitation Based Separation Scheme for Selective Removal and Recovery of Heavy Metals from Cadmium Rich Electroplating Industry Effluents. *Separation Science and Technology*, 41(15), pp. 3367–3385.

Itoh, H., Sugimoto, T., 2003, Systematic control of size, shape, structure, and magnetic properties of uniform magnetite and maghemite particles. *Journal of Colloid and Interface Science*, 265(2), pp. 283–295.

Jandová, J., Lisá, K., Vu, H., and Vranka, F., 2005, Separation of copper and cobalt-nickel sulphide concentrates during processing of manganese deep ocean nodules. *Hydrometallurgy*, 77(1-2), pp. 75–79.

Jiang, B., Zheng, J., Qiu, S., Wu, M., Zhang, Q., Yan, Z., and Xue, Q., 2014, Review on electrical discharge plasma technology for wastewater remediation. *Chemical Engineering Journal*, 236, pp. 348–368.

John, M., 2016, Low temperature synthesis of nano crystalline zero-valent phases and (doped) metal oxides as $A_xB_{3-x}O_4$ (ferrite), ABO_2 (delafossite), A_2O and AO. A new process to treat industrial wastewaters? [PhD thesis]: Ludwig-Maximilians-Universität München.

John, M., Heuss-Aßbichler, S., Park, S.H., Ullrich, A., Benka, G., Petersen, N., Rettenwander, D., and Horn, S.R., 2016a, Low-temperature synthesis of $CuFeO_2$ (delafossite) at 70 °C: A new process solely by precipitation and ageing. *Journal of Solid State Chemistry*, 233, pp. 390–396.

John, M., Heuss-Aßbichler, S., and Ullrich, A., 2016b, Conditions and mechanisms for the formation of nano-sized Delafossite ($CuFeO_2$) at temperatures ≤ 90 °C in aqueous solution. *Journal of Solid State Chemistry*, 234, pp. 55–62.

John, M., Heuss-Aßbichler, S., and Ullrich, A., 2016c, Recovery of Zn from wastewater of zinc plating industry by precipitation of doped ZnO nanoparticles. *International Journal of Environmental Science and Technology*, 13, pp. 2127–2134.

John, M., Heuss-Aßbichler, S., Ullrich, A., and Rettenwander, D., 2016d, Purification of heavy metal loaded wastewater from electroplating industry under synthesis of delafossite (ABO_2) by "Lt-delafossite process". *Water Research*, 100, pp. 98–104.

John, M., Heuss-Aßbichler, S., Tandon, K., and Ullrich, A., 2019, Recovery of Ag and Au from synthetic and industrial wastewater by 2-step ferritization and Lt-delafossite process via precipitation. *Journal of Water Process Engineering*, 30, 100532.

Jolivet, J.P., Belleville, P., Tronc, E., and Livage, J., 1992, Influence of Fe(II) on the Formation of the Spinel Iron Oxide in Alkaline Medium. *Clays and Clay Minerals*, 40(5), p. 531–539.

Joshi, T. et al., 2015, Structural and magnetic properties of epitaxial delafossite $CuFeO_2$ thin films grown by pulsed laser deposition. *Journal of Applied Physics*, 117, 013908.

Kang, S.Y., Lee, J.U., Moon, S.H., and Kim, K.W., 2004, Competitive adsorption characteristics of Co^{2+}, Ni^{2+}, and Cr^{3+} by IRN-77 cation exchange resin in synthesized wastewater. *Chemosphere*, 56(2), pp. 141–147.

Kanzaki, T., Furukawa, H., and Katsura, T., 1983, Formation of Molybdenum-bearing Ferrites, $Fe_{3-x}Mo_x$ (x=0.04-0.19), in Aqueous Suspension by Air Oxidation. *J. Chem. Soc. Dalton Trans.*, pp. 1197–1198.

Karkhanechi, H., Takagi, R., Ohmukai, Y., and Matsuyama, H., 2013, Enhancing the antibiofouling performance of RO membranes using $Cu(OH)_2$ as an antibacterial agent. *Desalination*, 325, pp. 40–47.

Karthikeyan, K.G., Elliott, H.A., and Cannon, F.S., 1996, Enhanced metal removal from wastewater by coagulant addition, *in* Proc. 50th Purdue Industrial Waste Conf, 50, pp. 259–267.

Kaş, R., Birer, Özgür, 2012, Sonochemical shape control of copper hydroxysulfates. *Ultrasonics Sonochemistry*, 19, pp. 692-700

Kefeni, K.K., Mamba, B.B., and Msagati, T.A.M., 2017a, Application of spinel ferrite nanoparticles in water and wastewater treatment: A review. *Separation and Purification Technology*, 188, pp. 399–422.

Kefeni, K.K., Msagati, T.A.M., and Mamba, B.B., 2017b, Ferrite nanoparticles: Synthesis, characterisation and applications in electronic device. *Materials Science and Engineering B: Solid-State Materials for Advanced Technology*, 215, pp. 37–55.

Kim, B.M., and Amodeo, P.A., 1983, Calcium sulfide process for treatment of metal-containing wastes. *Environmental Progress*, 2(3), pp. 175–180.

Kim, H., Baek, K., Lee, J., Iqbal, J., and Yang, J.W., 2006, Comparison of separation methods of heavy metal from surfactant micellar solutions for the recovery of surfactant. *Desalination*, 191(1-3), pp. 186–192.

Kim, W., Suh, C.Y., Cho, S.W., Roh, K.M., Kwon, H., Song, K., and Shon, I.J., 2012, A new method for the identification and quantification of magnetite-maghemite mixture using conventional X-ray diffraction technique. *Talanta*, 94, pp. 348–352.

Kirfel, A., and Eichhorn, K., 1990, Accurate Structure Analysis with Synchrotron Radiation. The Electron Density in Al_2O_3 and Cu_2O. *Acta Crystallograhica*, A46, pp. 271–284.

Kiyama Masao, 1978, The Formation of Manganese and Cobalt Ferrites by the Air Oxidation of Aqueous Suspensions and Their Properties. *Bulletin of the Chemical Society of Japan*, 50(1), pp. 134–138.

Knof, J., 2017, Konzeption einer Technikumsanlage zur hydroxidfreien Rückgewinnung von Buntmetallen aus Industrieabwässern [Masterthesis]: Ludwig-Maximilians-Univerität München.

Koga, N., Criado, J.M., and Tanaka, H., 1997, Reaction Pathway and Kinetics of the Thermal Decomposition of Synthetic Brochantite. *Journal of Thermal Analysis*, 49, pp. 1467–1475.

Krusenstjern, A. v., and Axmacher, L., 1964, Zur Neutralisation von Galvanikabwasser mit Kalzium- und Natriumhydroxid. *Metalloberfläche*, 18(3), pp. 65–69.

Ku, Y., and Jung, I.L., 2001, Photocatalytic reduction of Cr(VI) in aqueous solutions by UV irradiation with the presence of titanium dioxide. *Water Research*, 35(1), pp. 135–142.

Landesamt für Umwelt Baden-Württemberg, 2017, Abfallsteckbrief 1101 Chemische Oberflächenbearbeitung Galvanikschlamm: https://www.abfallbewertung.org/repgen.php?report=ipa&char_id=1101_GalS&lang_id=de&avv=&synon=&kapitel=6&gtactive=no.

Lawler, W., Bradford-Hartke, Z., Cran, M.J., Duke, M., Leslie, G., Ladewig, B.P., and Le-Clech, P., 2012, Towards new opportunities for reuse, recycling and disposal of used reverse osmosis membranes. *Desalination*, 299(8), pp. 103–112.

Lee, Y., Ren, Y., Cui, M., Ma, J., Han, Z., Kwon, O., Ko, J., and Khim, J., 2021, Rare earth real wastewater treatment by pilot scale using new concept continuous treatment process. *Chemosphere*, 279, 130523.

Li, S., Li, J., Wang, W., Zhang, W., 2019, Recovery of gold from wastewater using nanoscale zero-valent iron. *Environmental Science: Nano*, 6, pp. 519–527.

Li, Y., Bai, P., Yan, Y., Yan, W., Shi, W., and Xu, R., 2019a, Removal of Zn^{2+}, Pb^{2+}, Cd^{2+}, and Cu^{2+} from aqueous solution by synthetic clinoptilolite. *Microporous and Mesoporous Materials*, 273(5), pp. 203–211.

Li, P.P., Peng, C.S., Li, F.M., Song, S.X., and Juan, A.O., 2011, Copper and nickel recovery from electroplating sludge by the process of acid-leaching and electro-depositing. *International Journal of Environmental Research*, 5(3), pp. 797–804.

Li, T., Xiao, K., Yang, B., Peng, G., Liu, F., Tao, L., Chen, S., Wei, H., Yu, G., and Deng, S., 2019b, Recovery of Ni(II) from real electroplating wastewater using fixed-bed resin adsorption and subsequent electrodeposition. *Frontiers of Environmental Science and Engineering*, 13(6):91.

Lin, X., Burns, R.C., and Lawrance, G.A., 1998, Effect of electrolyte composition, and of added iron(III) in the presence of selected organic complexing agents, on nickel(II) precipitation by lime. *Water Research*, 32(12), pp. 3637–3645.

Lin, X., Burns, R.C., and Lawrance, G.A., 2005, Heavy metals in wastewater: The effect of electrolyte composition on the precipitation of cadmium(II) using lime and magnesia. *Water, Air, and Soil Pollution*, 165(1–4), pp. 131–152.

Liu, Y., Khan, A., Wang, Z., Chen, Y., Zhu, S., Sun, T., Liang, D., and Yu, H., 2020, Upcycling of Electroplating Sludge to Prepare Erdite-Bearing Nanorods for the Adsorption of Heavy Metals from Electroplating Wastewater Effluent. *Water*, 12(1027), pp. 1–16.

Liu, G., Yang, X., and Zhong, H., 2017, Molecular design of flotation collectors: A recent progress. *Advances in Colloid and Interface Science*, 246(8), pp. 181–195.

Liu, X., Zhang, J., Kang, Y., Wu, S., and Wang, S., 2012, Brochantite tabular microspindles and their conversion to wormlike CuO structures for gas sensing. *CrystEngComm*,14, pp. 620–625.

Lofrano, G., Libralato, G., Acanfora, F.G., Pucci, L., and Carotenuto, M., 2015, Which lesson can be learnt from a historical contamination analysis of the most polluted river in Europe? *Science of the Total Environment*, 408, pp. 5254–5264.

López-Maldonado, E.A., Zavala García, O.G., Escobedo, K.C., and Oropeza-Guzman, M.T., 2017, Evaluation of the chelating performance of biopolyelectrolyte green complexes (NIBPEGCs) for wastewater treatment from the metal finishing industry. *Journal of Hazardous Materials*, 335, pp. 18–27.

Ma, L., Lin, Y., Wang, Y., Li, J., Wang, E., Qiu, M., and Yu, Y., 2008, Aligned 2-D nanosheet Cu_2O film: Oriented deposition on Cu foil and its photoelectrochemical property. *Journal of Physical Chemistry C*, 112(48), pp. 18916–18922.

Malka, E. et al., 2013, Eradication of multi-drug resistant bacteria by a novel Zn-doped CuO nanocomposite. *Small*, 9(23), pp. 4069–4076.

Malvault, J.Y., Lopitaux, J., Delahaye, D., and Lenglet, M., 1995, Cathodic reduction and infrared reflectance spectroscopy of basic copper(II) salts on copper substrate. *Journal of Applied Electrochemistry*, 25, pp. 841–845.

Mandaokar, S.S., Dharmadhikari, D.M., and Dara, S.S., 1994, Retrieval Of Heavy Metal Ions From Solution Via Ferritisation. *Environmental Pollution*, 83, pp. 277–282.

Marani, D., Patterson, J.W., and Anderson, P.R., 1995, Alkaline Precipitation and Aging of Cu(II) in the Presence of Sulfate. *Water Research*, 29(5), pp. 1317–1326.

Marquardt, M.A., Ashmore, N.A., and Cann, D.P., 2006, Crystal chemistry and electrical properties of the delafossite structure. *Thin Solid Films*, 496(1), pp. 146–156.

Merlino, S., Perchiazzi, N., and Franco, D., 2003, Brochantite, $Cu_4SO_4(OH)_6$: OD character, polytypism and crystal structures. *European Journal of Mineralogy*, 15(2), pp. 267–275.

Mirbagheri, S.A., and Hosseini, S.N., 2004, Pilot plant investigation on petrochemical wastewater treatment for the removal of copper and chromium with the objective of reuse. *Desalination*, 171(1), pp. 85–93.

Mohammed, A.S., and Al., E., 2011, Heavy Metal Pollution: Source, Impact, and Remedies, *in* Khan, M.S., Zaidi, A., Goel, R., and Musarrat, J. eds., Biomanagement of Metal-Contaminated Soils, *Environmental Pollution*, Springer Netherlands, 20, pp. 1–28.

Momma, K., and Izumi, F., 2011, VESTA 3 for three-dimensional visualization of crystal, volumetric and morphology data. *Journal of Applied Crystallography*, 44(6), pp. 1272–1276.

Moreira, M., Afonso, J., Crepelliere, J., Lenoble, D., and Lunca-Popa, P., 2022, A review on the p-type transparent Cu–Cr–O delafossite materials. *Journal of Materials Science*, 57(5), pp. 3114–3142.

Mudakavi, J.R., Venkateshwar, G., and Ravindram, M., 1995, Removal of chromium from electroplating effluents by the sulphide process. *Indian Journal of Chemical Technology*, 2(2), p. 53–58.

Musee, N., Zvimba, J.N., Schaefer, L.M., Nota, N., Sikhwivhilu, L.M., and Thwala, M., 2014, Fate and behavior of ZnO- and Ag-engineered nanoparticles and a bacterial viability assessment in

a simulated wastewater treatment plant. *Journal of Environmental Science and Health - Part A Toxic/Hazardous Substances and Environmental Engineering*, 49(1), pp. 59–66.

Musić, S., Dragčević, D., Popović, S., and Ivanda, M., 2005, Precipitation of ZnO particles and their properties. *Materials Letters*, 59(12-20), pp. 2388–2393.

Naim, R., Kisay, L., Park, J., Qaisar, M., Zulfiqar, A.B., Noshin, M., and Jamil, K., 2010, Precipitation Chelation of Cyanide Complexes in Electroplating Industry Wastewater. *International Journal of Environmental Research*, 4(4), pp. 735–740.

Naveenkumar, P., Paruthimal Kalaignan, G., Arulmani, S., and Anandan, S., 2018, Solvothermal synthesis of CuS/$Cu(OH)_2$ nanocomposite electrode materials for supercapacitor applications: Journal of Materials Science. *Materials in Electronics*, 29(19), pp. 16853–16863.

Nazari, M., Ghasemi, N., Maddah, H., Motlagh, M., 2014, Synthesis and characterization of maghemite nanopowders by chemical precipitation method. *Journal of Nanostructure in Chemistry*, 4(99), pp. 1–5.

Netpradit, S., Thiravetyan, P., and Towprayoon, S., 2003, Application of "waste" metal hydroxide sludge for adsorption of azo reactive dyes. Water Research, 37(4), pp. 763–772.

Neukirchen, F., 2016, Industrielle Revolution und Hightech, *in* Von der Kupfersteinzeit zu den Seltenen Erden, Springer-Verlag Berlin Heidelberg, pp. 113–152.

Nocete, F., Álex, E., Nieto, J.M., Sáez, R., and Bayona, M.R., 2005, An archaeological approach to regional environmental pollution in the south-western Iberian Peninsula related to Third millennium BC mining and metallurgy. *Journal of Archaeological Science*, 32(10), pp. 1566–1576.

Novikova, A.A., Moiseeva, D.Y., Karyukov, E. v., and Kalinichenko, A.A., 2016, Facile preparation photocatalytically active CuO plate-like nanoparticles from brochantite. *Materials Letters*, 167, pp. 165–169.

Oliveira, A.P.A., Hochepied, J.-F., Grillon, F., and Berger, M.-H., 2003, Controlled precipitation of zinc oxide particles at room temperature. *Chemistry of Materials*, 15(16), pp. 3202–3207.

Ong, C.B., Ng, L.Y., and Mohammad, A.W., 2018, A review of ZnO nanoparticles as solar photocatalysts: Synthesis, mechanisms and applications. *Renewable and Sustainable Energy Reviews*, 81, pp. 536–551.

Oswald, H.R., Reller, A., Schmalle, H.W., and Dubler, E., 1990, Structure of Copper(II) Hydroxide, $Cu(OH)_2$. *Acta Crystallographica*, C46, pp. 2279–2284.

Pabst, A., 1938, Crystal structure and density of delafossite. *American Mineralogist*, 23, p. p175–176.

Pal, D.B., Giri, D.D., Singh, P., Pal., S., and Mishra, P.K., 2017, Arsenic removal of synthetic waste water by CuO nano-flakes synthesized by aqueous precipitation method. *Desalination and Water Treatment*, 62, pp. 355–359.

Pang, F.M., Kumar, P., Teng, T.T., Mohd Omar, A.K., and Wasewar, K.L., 2011, Removal of lead, zinc and iron by coagulation-flocculation. *Journal of the Taiwan Institute of Chemical Engineers*, 4285), pp. 809–815.

Pang, F.M., Teng, S.P., Teng, T.T., and Mohd Omar, A.K., 2009, Heavy Metals Removal by Hydroxide Precipitation and Coagulation-Flocculation Methods from Aqueous Solutions. *Water Quality Research Journal of Canada*, 44(2), pp. 174–182.

Patterson, J.W., Allen, H.E., and Scala, J.J., 1977, Carbonate Precipitation for Heavy Metals Pollutants. *Journal Water Pollution Control Federation*, 49(12), pp. 2397–2410.

Pecharromfin, C., Gonzfilez-Carrefio, T., and Iglesias, J.E., 1995, The Infrared Dielectric Properties of Maghemite, beta-Fe_2O_3, from Reflectance Measurement on Pressed Powders. *Physics Chemistry Minerals*, 22, pp.21-29.

Peng, G., Deng, S., Liu, F., Li, T., and Yu, G., 2020, Superhigh adsorption of nickel from electroplating wastewater by raw and calcined electroplating sludge waste. *Journal of Cleaner Production*, 246(2), 118948.

Peng, G., and Tian, G., 2010, Using electrode electrolytes to enhance electrokinetic removal of heavy metals from electroplating sludge. *Chemical Engineering Journal*, 165(2), pp. 388–394.

Peng, Y.-H., Tsai, Y.-C., Shiung, C., Lin, Y.-H., and Shih, Y., 2017, Influence of water chemistry on the environmental behaviors of commercial ZnO nanoparticles in various water and wastewater samples. *Journal of Hazardous Materials*, 322, pp. 348–356.

Peters, R.W., and Ferg, J., 1987, The Dissolution/Leaching Behavior of Metal Hydroxide/Metal Sulfide Sludges from Plating Wastewaters. *Hazardous Waste and Hazardous Materials*, 4(4), pp. 325–355.

Phiwdang, K., Suphankij, S., Mekprasart, W., and Pecharapa, W., 2013, Synthesis of CuO Nanoparticles by Precipitation Method Using Different Precursors. *Energy Procedia*, 34, p. 740–745.

Prasad, S.V.S., and Rao, V.S., 1985, Thermal Analysis, X-ray Diffraction And Infrared Spectroscopic Study Of Synthetic Brochantite. *Journal of Thermal Analysis*, 30, pp. 603–609.

Prévot, M.S., Guijarro, N., and Sivula, K., 2015, Enhancing the Performance of a Robust Sol-Gel-Processed p-Type Delafossite $CuFeO_2$ Photocathode for Solar Water Reduction. *ChemSusChem*, 8(8), pp. 1359–1367.

Prieto, F., Barrado, E., Medina, J., and Lopez-Gomez, F.A., 2001, Characterisation of zinc bearing-ferrites obtained as by-products of hydrochemical waste-water purification processes. *Journal of Alloys and Compounds*, 325, pp. 269–275.

Rak, P., Fink, D., Bureš, R., and Stoulil, J., 2020, Novel procedure for brochantite based pigment production and its immobilization for restoration of historical copper objects. *Coatings*, 10(10), pp. 1–11.

Ramya, S., Viruthagiri, G., Gobi, R., Shanmugam, N., and Kannadasan, N., 2016, Synthesis and characterization of Ni^{2+} ions incorporated CuO nanoparticles and its application in antibacterial activity. *Journal of Materials Science: Materials in Electronics*, 27(3), pp. 2701–2711.

Rao, S., and Shekhawat, G.S., 2014, Toxicity of ZnO engineered nanoparticles and evaluation of their effect on growth, metabolism and tissue specific accumulation in Brassica juncea. *Journal of Environmental Chemical Engineering*, 2(1), pp. 105–114.

Rao, M.D., Singh, K.K., Morrison, C.A., and Love, J.B., 2021, Recycling copper and gold from e-waste by a two-stage leaching and solvent extraction process. *Separation and Purification Technology*, 263, 11840.

Rehman, A., Aadil, M., Zulfiqar, S., Agboola, P.O., Shakir, I., Aly Aboud, M.F., Haider, S., and Warsi, M.F., 2021, Fabrication of Binary Metal Doped CuO Nanocatalyst and Their Application for the Industrial Effluents Treatment. *Ceramics International*, 47(5), pp. 5929–5937.

Rezaei, H., Abdollahi, H., and Ghassa, S., 2023, Recovery of gold ions from wastewater using a three-compartment electrodialysis separation system. *International Journal of Environmental Science and Technology*, 20(5), pp. 4827–4838.

Roble, M., Rojas, S.D., Wheatley, R., Wallentowitz, S., Cabrera, A.L., and Diaz-Droguett, D.E., 2019, Hydrothermal improvement for 3R-CuFeO 2 delafossite growth by control of mineralizer and reaction atmosphere. *Journal of Solid State Chemistry*, 271, pp. 314–325.

Rodríguez-Iznaga, I., Gómez, A., Rodríguez-Fuentes, G., Benítez-Aguilar, A., and Serrano-Ballan, J., 2002, Natural clinoptilolite as an exchanger of Ni^{2+} and NH^{4+} ions under hydrothermal conditions and high ammonia concentration. *Microporous and Mesoporous Materials*, 53(1-3), pp. 71–80.

Rodríguez-Paéz, J.E., Caballero, A.C., Villegas, M., Moure, C., Duran, P., and Fernández, J.F., 2001, Controlled precipitation methods: formation mechanism of ZnO nanoparticles. *Journal of the European Ceramic Society*, 21, pp. 925–930.

Sadik, P.W., Ivill, M., Craciun, V., and Norton, D.P., 2009, Electrical transport and structural study of $CuCr_{1-x}Mg_xO_2$ delafossite thin films grown by pulsed laser deposition. *Thin Solid Films*, 518, 3439.

Sakib, A.A.M., Masum, S.M., Hoinkis, J., Islam, R., and Molla, M.A.I., 2019, Synthesis of CuO/ZnO nanocomposites and their application in photodegradation of toxic textile dye. *Journal of Composites Science*, 3(91), pp. 1–13.

Sampaio, R.M.M., Timmers, R.A., Xu, Y., Keesman, K.J., and Lens, P.N.L., 2009, Selective precipitation of Cu from Zn in a pS controlled continuously stirred tank reactor. *Journal of Hazardous Materials*, 165(1–3), pp. 256–265.

Sanpo, N., Berndt, C.C., Wen, C., and Wang, J., 2013, Transition metal-substituted cobalt ferrite nanoparticles for biomedical applications. *Acta Biomaterialia*, 9(3), pp. 5830–5837.

Schmelzer, J.W.P., and Abyzov, A.S., 2017, How Do Crystals Nucleate and Grow: Ostwald's Rule of Stages and Beyond, *in* Šesták, J., Hubík, P., and Mareš, J. eds., Thermal Physics and Thermal Analysis. Hot Topics in Thermal Analysis and Calorimetry, Springer , v. 11, p. 195–211.

Schmidt, M., and Lutz, H.D., 1993, Hydrogen Bonding in Basic Copper Salts: A Spectroscopic Study of Malachite, $Cu_2(OH)_2CO_3$, and Brochantite, $Cu_4(OH)_6SO_4$. *Phys Chem Minerals*, 20, pp. 27–32.

Secco, E.A., 1988, Spectroscopic properties of SO_4 (and OH) in different molecular and crystalline environments. I. Infrared spectra of $Cu_4(OH)_6SO_4$, $Cu_4(OH)_4OSO_4$, and $Cu_3(OH)_4SO_4$. *Can. J. Chem.*, 66, p. 329–336.

Sheets, W.C., Mugnier, E., Barnabé, A., Marks, T.J., and Poeppelmeier, K.R., 2006, Hydrothermal synthesis of delafossite-type oxides. *Chemistry of Materials*, 18, pp. 7–20.

Shen, C., Zhao, Y., Li, W., Yang, Y., Liu, R., and Morgen, D., 2019, Global profile of heavy metals and semimetals adsorption using drinking water treatment residual. *Chemical Engineering Journal*, 372(2), pp. 1019–1027.

Shokrollahi, H., 2017, A review of the magnetic properties, synthesis methods and applications of maghemite. *Journal of Magnetism and Magnetic Materials*, 426, pp. 74–81.

Sist, C., and Demopoulos, G.P., 2003, Nickel Hydroxide Precipitation from Aqueous Sulfate Media. *JOM*, 55(8), p. 42–46.

de Souza E Silva, P.T., de Mello, N.T., Menezes Duarte, M.M., Montenegro, M.C.B.S.M., Araújo, A.N., de Barros Neto, B., and da Silva, V.L., 2006, Extraction and recovery of chromium from electroplating sludge. *Journal of Hazardous Materials*, B128, pp. 39–43.

Springer & Sohn GmbH, 2020, Metallabrechnung, 2020,

https://www.springer-und-sohn.de/uploads/springer-und-sohn_rv-preise.pdf.

Srivastava, R., and Yadav, B.C., 2012, Ferrite materials: Introduction, synthesis techniques, and applications as sensors. *International Journal of Green Nanotechnology: Biomedicine,* 4(2), pp. 141–154.

Statistisches Bundesamt, 2013, Umwelt Abfallentsorgung 2011.

Statistisches Bundesamt, 2019, Umwelt Abfallentsorgung 2017.

Stefanowicz, T., Golik, T., Napieralska-Zagozda, S., and Osińska, M., 1991, Tin recovery from an electroplating sludge. *Resources, Conservation and Recycling*, 6(1), p. 61–69.

Sukeshini, A.M., Kobayashi, H., Tabuchi, M., and Kageyama, H., 2000, Physicochemical characterization of $CuFeO_2$ and lithium intercalation. *Solid State Ionics*, 128, pp. 33–41.

Sumoondur, A., Shaw, S., Ahmed, I., and Benning, L.G., 2008, Green rust as a precursor for magnetite: an in situ synchrotron based study. *Mineralogical Magazine*, 72(1), pp. 201–204.

Tamaura, Y., 1986, Ni(II)-Bearing Green Rust II and Its Spontaneous Transformation into Ni(II)-Bearing Ferrites. *Bulletin of the Chemical Society of Japan*, 59, pp. 1829–1832.

Tamaura, Y., Katsura, T., Rojarayanont, S., Yoshida, T., and Abe, H., 1991, Ferrite Process; Heavy Metal Ions Treatment System. *Water Science and Technology*, 23, pp. 1893–1900.

Tamaura, Y., Sun Chyo, G., and Katsura, T., 1979, The Fe_3O_4-Formation By The "Ferrite Process": Oxidation Of The Reactive $Fe(OH)_2$ Suspension Induced By Sucrose. *Water Research*, 13, pp. 21–31.

Tamaura, Y., Yoshida, T., and Katsura, T., 1984, The Synthesis of Green Rust II ($FeIII_1$-$FeIII_2$) and Its Spontaneous Transformation into Fe_3O_4. *Bulletin of the Chemical Society of Japan*, 57(9), pp. 2411–2416.

Tandon, K., 2015, The Ferrite Process in the Nickel-Iron Model System: Characterization of Nanocrystalline Residues [Masterthesis]. Ludwig-Maximilians-Universität München.

Tandon, K., 2021, Wet chemical precipitation of ZnO from Cl-rich solutions - an innovative method for the recovery of Zn from municipal solid waste incineration fly ash [PhD thesis]. Ludwig-Maximilians-Universität München.

Tandon, K., and Heuss-Aßbichler, S., 2021, Fly Ash from Municipal solid waste Incineration - from industrial residue to resource for zinc, *in* Pöllmann ed., Industrial wastes - Characterization, Modification and Application of industrial residues, DeGruyter.

Tandon, K., John, M., Heuss-Aßbichler, S., and Schaller, V., 2018, Influence of salinity and Pb on the precipitation of Zn in a model system. *Minerals*, v. 8(2), pp. 1–16.

Tang, S.Y., and Qiu, Y.R., 2019, Selective separation and recovery of heavy metals from electroplating effluent using shear-induced dissociation coupling with ultrafiltration. *Chemosphere*, 236(12), 124330.

Taylor, R.M., Schwertmann, U., 1974, Maghemite in soils and ist origin II. Maghemite synthesis at ambient temperature and pH 7. *Clay Minerals*, 10, pp. 299–310.

Tong, D.G., Wu, P., Su, P.K., Wang, D.Q., and Tian, H.Y., 2012, Preparation of zinc oxide nanospheres by solution plasma process and their optical property, photocatalytic and antibacterial activities. *Materials Letters*, 70, pp. 94–97.

Tran, T.K., Chiu, K.F., Lin, C.Y., and Leu, H.J., 2017, Electrochemical treatment of wastewater: Selectivity of the heavy metals removal process. *International Journal of Hydrogen Energy*, 42(45), pp. 27741–27748.

Tronc, E., Belleville, P., Jolivet, J.-P., and Livage, J., 1992, Transformation of Ferric Hydroxide into Spinel by Fe^{II} Adsorption. *Langmuir*, 8, pp. 313–319.

Twidwell, L.G., and Dahnke, D.R., 2001, Treatment of metal finishing sludge for detoxification and metal value. *The European Journal of Mineral Processing and Environmental Protection*, 1(2), pp. 76–88.

Upadhyay, K., 2006, Solution for wastewater problem related to electroplating industry: An overview. *Journal of Industrial Pollution Control*, 22(1), pp. 59–66.

Usman, M., Byrne, J.M., Chaudhary, A., Orsetti, S., Hanna, K., Ruby, C., Kappler, A., and Haderlein, S.B., 2018, Magnetite and Green Rust: Synthesis, Properties, and Environmental Applications of Mixed-Valent Iron Minerals. *Chemical Reviews*, 118(7), pp. 3251–3304.

Vaca Mier, M., López Callejas, R., Gehr, R., Jiménez Cisneros, B.E., and Alvarez, P.J.J., 2001, Heavy metal removal with mexican clinoptilolite: Multi-component ionic exchange. *Water Research*, 35(2), pp. 373–378.

Veeken, A.H.M., and Rulkens, W.H., 2003, Innovative developments in the selective removal and reuse of heavy metals from wastewaters. *Water Science and Technology*, 47(10), pp. 9–16.

Verwey, E.J.W., and Heilmann, E.L., 1947, Physical properties and cation arrangement of oxides with spinel structures I. Cation arrangement in spinels. *The Journal of Chemical Physics*, 15(4), pp. 174–180.

Vilminot, S., Richard-Plouet, M., André, G., Swierczynski, D., Bourée-Vigneron, F., Marino, E., and Guillot, M., 2002, Synthesis, structure and magnetic properties of copper hydroxysulfates. *Crystal Engineering*, 5(3–4), pp. 177–186.

Vinaykumar, S.N., Reddy, B.C., and Sah, A.B.P., 2019, Removal of Cadmium from Electroplating Industrial Waste Water using Natural Adsorbents. *International Research Journal of Engineering and Technology*, 6(5), pp. 86–92.

Wang, J., Zheng, P., Li, D., Deng, Z., Dong, W., Tao, R., and Fang, X., 2011, Preparation of delafossite-type $CuCrO_2$ films by sol-gel method. *Journal of Alloys and Compounds*, 509(18), pp. 5715–5719.

Wei, D., and Osseo-Asare, K., 1996, Particulate pyrite formation by the Fe^{3+} /HS^- reaction in aqueous solutions: effects of solution composition. *Colloids and Surfaces A: Physicochemical and Engineering Aspects*, 118(1–2), pp. 51–61.

Weichselgartner, N., 2020, Preliminary study on the recovery of vanadium and phosphorus from spent industrial vanadyl pyrophosphate catalyst by Specific Product-Oriented Precipitation (SPOP) [Masterthesis]: Maximilians-Universität München.

Wenten, I.G., Khoiruddin, K., Wardani, A.K., and Widiasa, I.N., 2020, Synthetic polymer-based membranes for heavy metal removal, *in* Ismail, A.F., Wan Norharyati Wan, S., and Norhaniza, Y. eds., Synthetic Polymeric Membranes for Advanced Water Treatment, Gas Separation, and Energy Sustainability, Elsevier Inc., p. 71–101.

Whang, J.S., and Young, D., 1982, Soluble-Sulfide Precipitation for Heavy Metals Removal from Wastewaters. *Environmental Progress*, 1(2), pp. 110–113.

Wiles, C., and Watts, P., 2012, Continuous flow reactors: A perspective. *Green Chemistry*, 14(1), pp. 38–54.

Witt, K., 2020, Electroplating: An Old Technology For The Future. *Silicon Semiconductor*, p. 1–5, https://siliconsemiconductor.net/article/97266/Electroplating_An_old_technology_for_the_future/feature (accessed July 2020).

Wong, E.M., Bonevich, J.E., and Searson, P.C., 1998, Growth Kinetics of Nanocrystalline ZnO Particles from Colloidal Suspensions. *J. Phys. Chem. B*, 102, pp. 7770–7775.

Wyckoff, R.W.G., 1963, Crystal Structures. New York, Interscience Publishers, 1, pp.85–237.

Xiang, W., Liu, J., Chang, M., and Zheng, C., 2012, The adsorption mechanism of elemental mercury on CuO (110) surface. *Chemical Engineering Journal*, 200–202, pp. 91–96.

Xie, Q., Liang, G., Lin, T., Chen, F., Wang, D., and Yang, B., 2020, Selective chelating precipitation of palladium metal from electroplating wastewater using chitosan and its derivative. *Adsorption Science and Technology*, 38(3–4), pp. 113–126.

Xiong, D., Qi, Y., Li, X., Liu, X., Tao, H., Chen, W., and Zhao, X., 2015, Hydrothermal synthesis of delafossite $CuFeO_2$ crystals at 100 °C. *RSC Advances*, 5(61), pp. 49280–49286.

Xiong, D., Zeng, X., Zhang, W., Wang, H., Zhao, X., Chen, W., and Cheng, Y.B., 2014, Synthesis and characterization of CuAlO2 and $AgAlO_2$ delafossite oxides through low-temperature hydrothermal methods. *Inorganic Chemistry*, 53(8), p. 4106–4116.

Xu, X., Yang, Y., Zhao, X., Zhao, H., Lu, Y., Jiang, C., Shao, D., and Shi, J., 2019, Recovery of gold from electronic wastewater by Phomopsis sp. XP-8 and its potential application in the degradation of toxic dyes. *Bioresource Technology*, 288, 121610, pp. 1–8.

Ye, Z., Yin, X., Chen, L., He, X., Lin, Z., Liu, C., Ning, S., Wang, X., and Wei, Y., 2019, An integrated process for removal and recovery of Cr(VI) from electroplating wastewater by ion exchange and reduction–precipitation based on a silica-supported pyridine resin. *Journal of Cleaner Production*, 236, 117631.

Yoder, C.H., Agee, T.M., Ginion, K.E., Hofmann, A.E., Ewanichak, J.E., Schaeffer, C.D., Carroll, M.J., Schaeffer, R.W., and McCaffrey, P.F., 2007, The relative stabilities of the copper hydroxyl sulphates. *Mineralogical Magazine*, 71(5), pp. 571–577.

Yunus, Z.M., Al-Gheethi, A., Othman, N., Hamdan, R., and Ruslan, N.N., 2020, Removal of heavy metals from mining effluents in tile and electroplating industries using honeydew peel activated carbon: A microstructure and techno-economic analysis. *Journal of Cleaner Production*, 251(4), 119738.

Yusaf, A., Adeel, S., Usman, M., Mansha, A., and Ahmad, M., 2019, Removal of Heavy Metal Ions from Wastewater Using Micellar- Enhanced Ultrafiltration Technique (MEUF): A Brief Review, *in* Shabbir, M. ed., Textiles and Clothing. *Environmental Concerns and Solutions*, Wiley, New Jersey, p. 289–315

Zade, P.D., and Dharmadhikari, D.M., 2007, Retrieval of Mercury from Wastewater as Stable Mercury Ferrite. *Water Qual. Res. J. Canada*, 42(4), pp. 311–318.

Zhang, H., Zhang, Z., Li, N., Yan, W., and Zhu, Z., 2017, Cu_2O@C core/shell nanoparticle as an electrocatalyst for oxygen evolution reaction. *Journal of Catalysis*, 352, pp. 239–245.

Zhang, Q., Zhang, K., Xu, D., Yang, G., Huang, H., Nie, F., Liu, C., and Yang, S., 2014, CuO nanostructures: Synthesis, characterization, growth mechanisms, fundamental properties, and applications. *Progress in Materials Science*, 60(1), pp. 208–337.

Zhao, J., Wang, C., Wang, S., Zhang, L., Zhang, B., 2019, Selective recovery of Au(III) from wastewater by a recyclable magnetic $Ni_{0.6}Fe_{2.4}O_4$ nanoparticles with mercaptothiadiazole: Interaction models and adsorption mechanisms. *Journal of Cleaner Production*. 236, 117605.

Zhao, Y., Liu, R., Awe, O.W., Yang, Y., and Shen, C., 2018, Acceptability of land application of alum-based water treatment residuals – An explicit and comprehensive review. *Chemical Engineering Journal*, 353(5), pp. 717–726.

Zhu, X., Chen, Y., Xie, R., Zhong, H., Zhao, W., Liu, Y., and Yang, H., 2021, Rapid Gelling of Guar Gum Hydrogel Stabilized by Copper Hydroxide Nanoclusters for Efficient Removal of Heavy Metal and Supercapacitors. *Frontiers in Chemistry*, 9, 794755.

Zhu, J., Li, D., Chen, H., Yang, X., Lu, L., and Wang, X., 2004, Highly dispersed CuO nanoparticles prepared by a novel quick-precipitation method. *Materials Letters*, 58(26), pp. 3324–3327.

Zittlau, A.H., Shi, Q., Boerio-Goates, J., Woodfield, B.F., and Majzlan, J., 2013, Thermodynamics of the basic copper sulfates antlerite, posnjakite, and brochantite. *Chemie der Erde*, 73(1), pp. 39–50.

Zwerschke, E., 2019, Recovery of tin from aqueous solution - a comparative study of two different precipitation processes [Bachelorthesis]: Ludwig-Maximilians-Universität München.

IV. Appendix

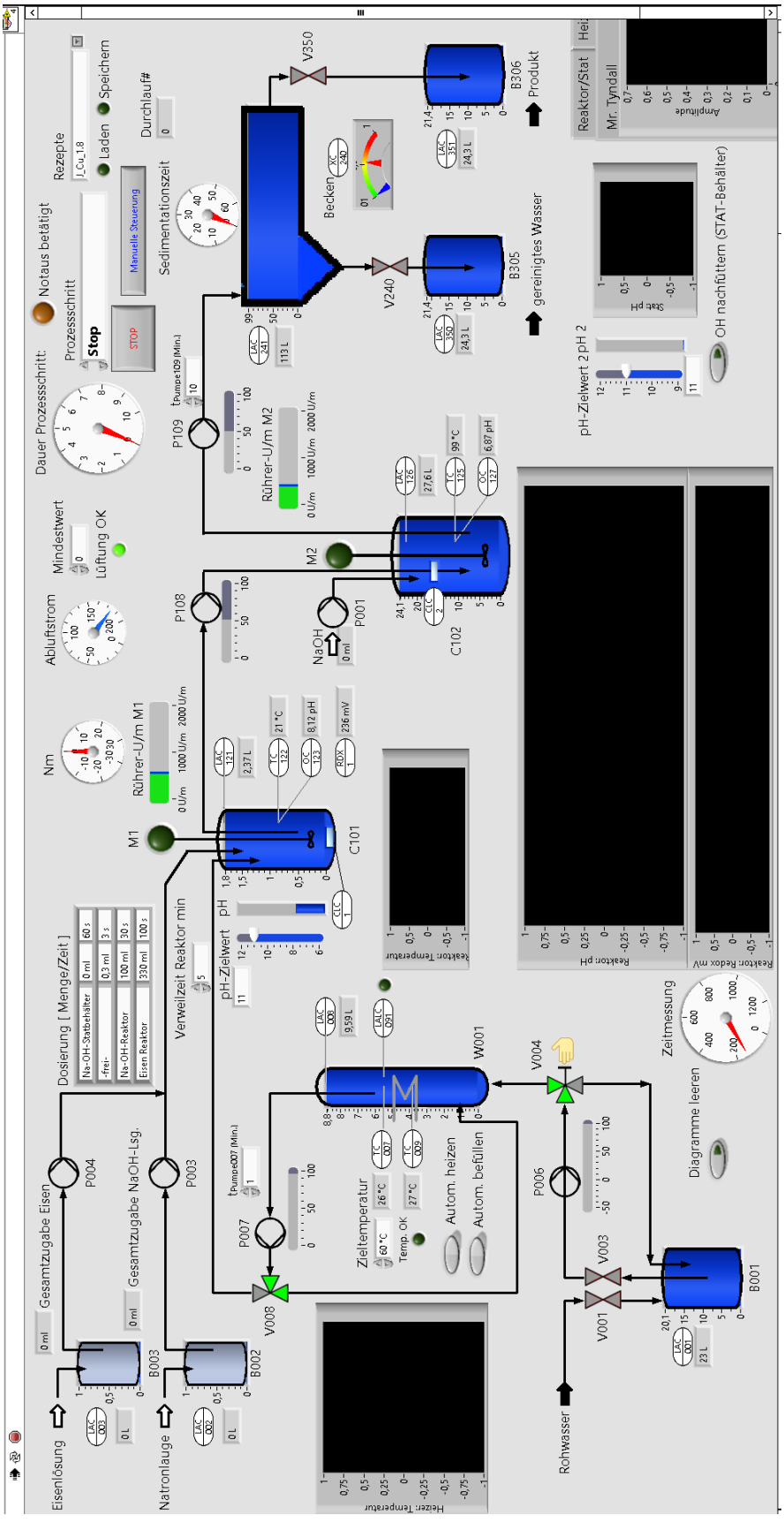

Figure IV.1: *Control panel of the SPOP pilot facility.*

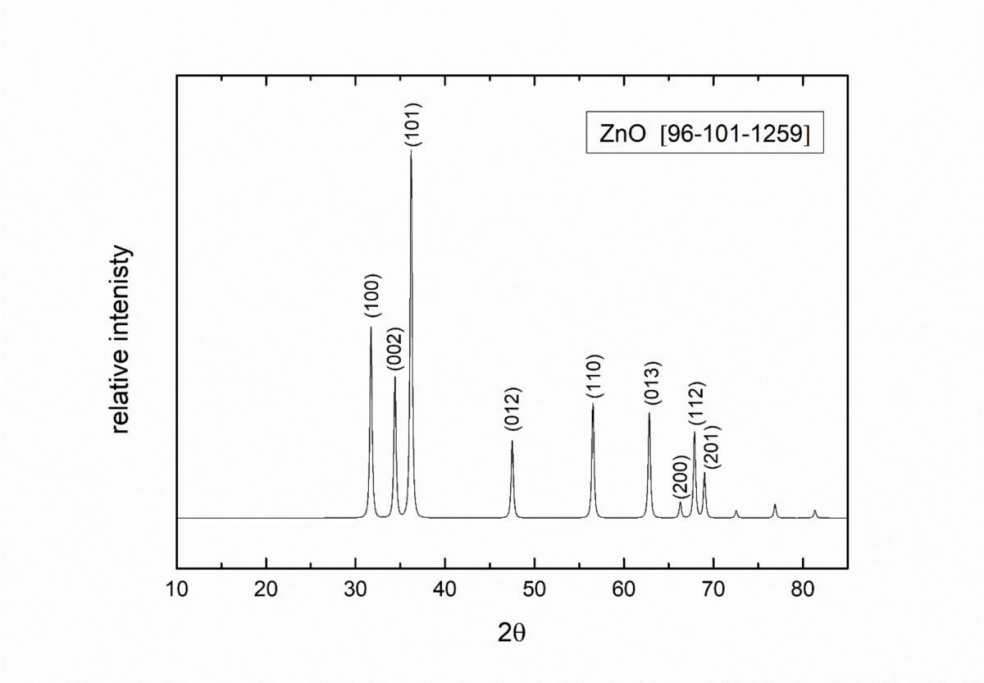

Figure IV.2: *Reference X-ray diffractogram of zincite (ZnO). Reference file [96-101-1259] with miller indices (hkl). Source of entry: COD.*

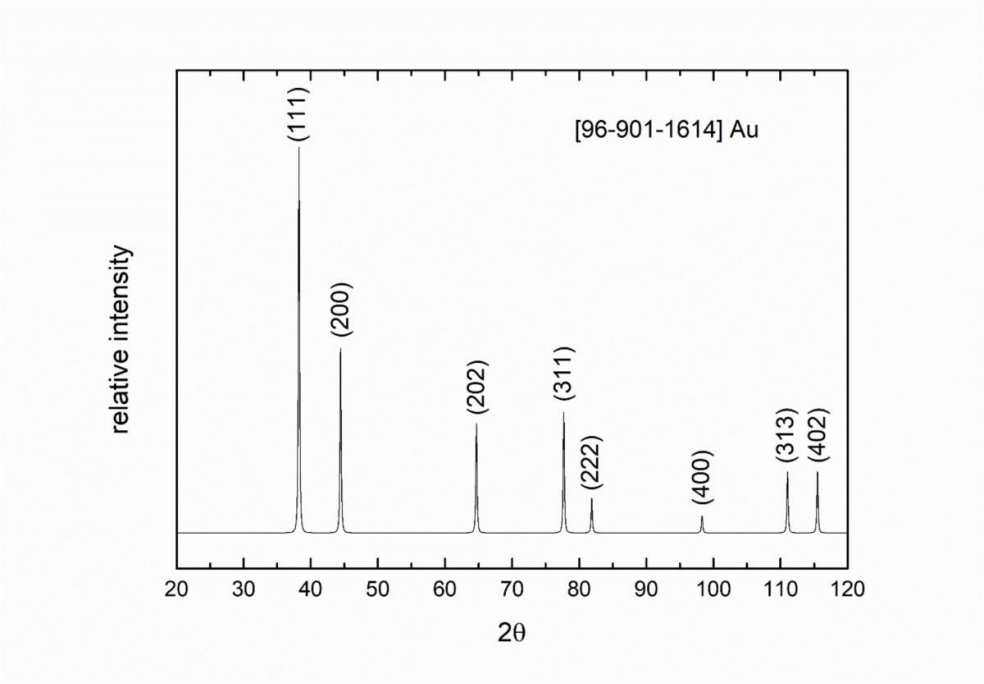

Figure IV.3: *Reference X-ray diffractogram of Au. Reference file [96-901-1614] with miller indices (hkl). Source of entry: COD.*

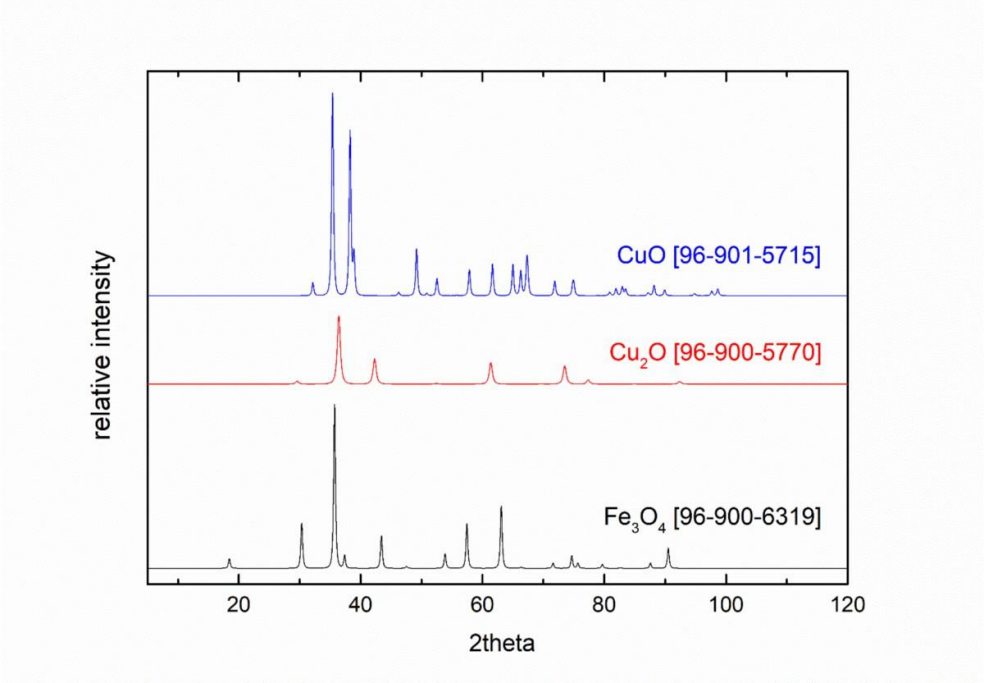

Figure IV.4: *Reference X-ray diffractograms of magnetite Fe_3O_4 (black), cuprite Cu_2O (red), and tenorite CuO (blue). Source of entry: COD.*

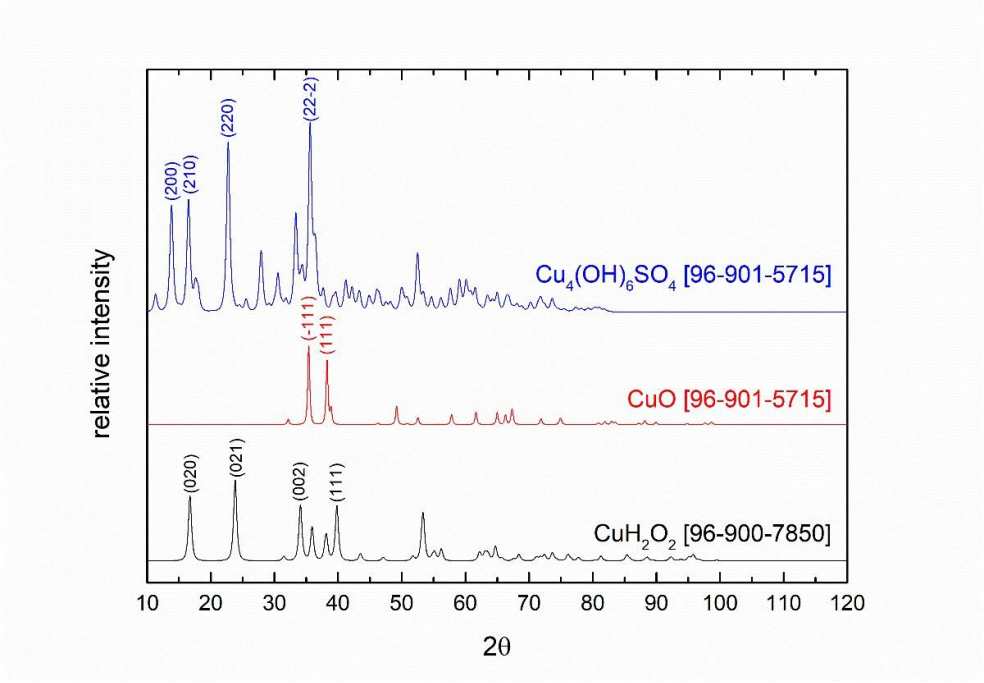

Figure IV.5: *Reference X-ray diffractograms of spertiniite CuH_2O_2 (black), tenorite CuO (red), and brochantite ($Cu_4(OH)_6SO_4$. Source of entry: COD.*

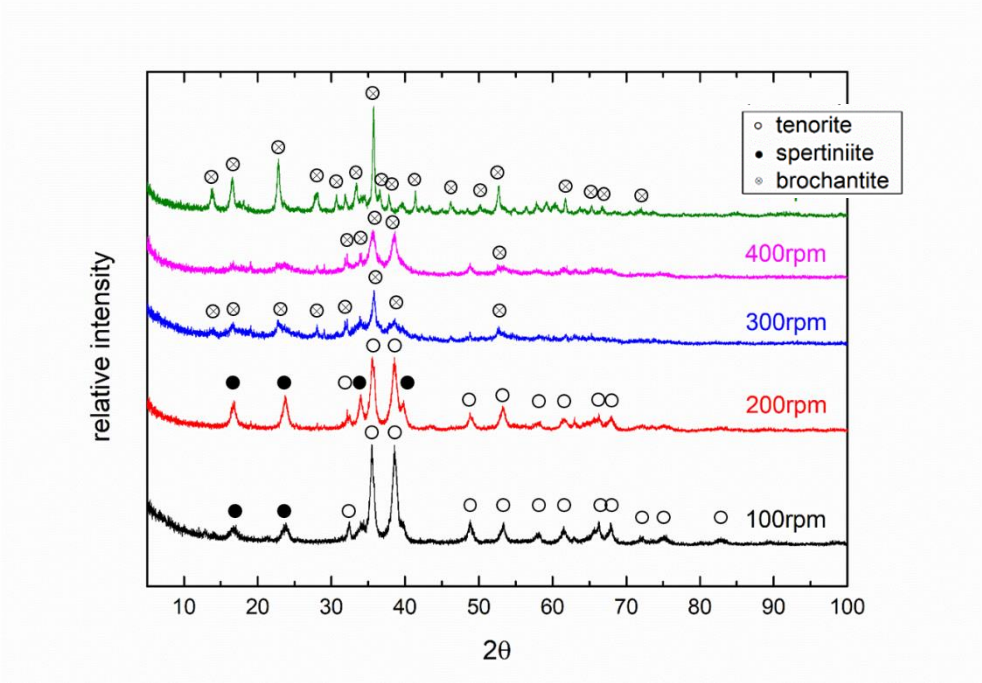

Figure IV.6: *X-ray diffractograms of fresh samples in the kinetics study. Samples 100rpm_f, 200rpm_f, 300rpm_f, and 400rpm_f show diffraction maxima assigned to spertiniite and tenorite. Samples 300rpm_f and 400rpm_f show traces of brochantite. The diffraction maxima in sample 500_rpm_f can be solely assigned to brochantite.*

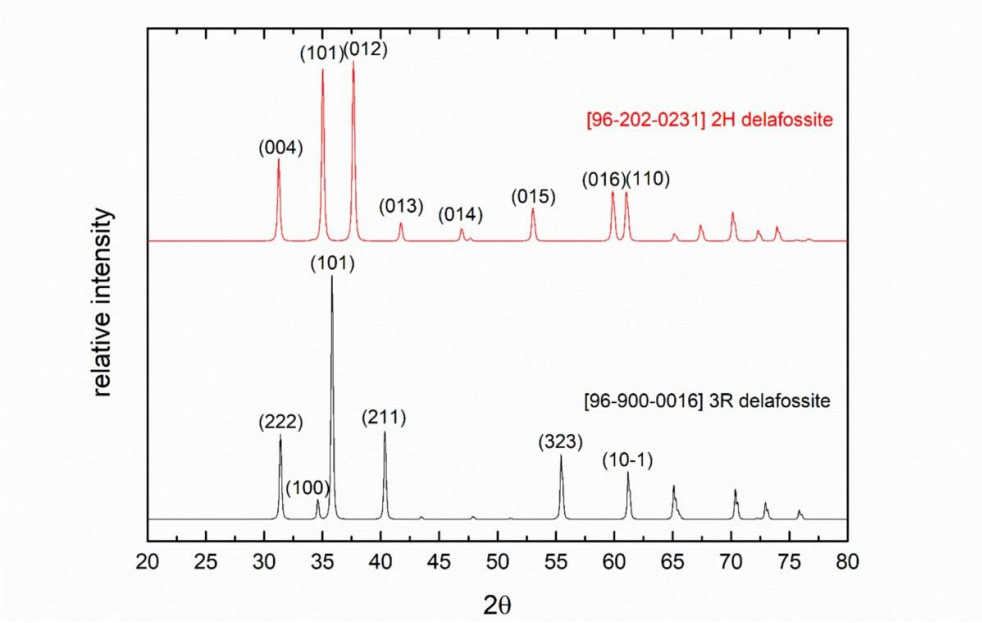

Figure IV.7: *Reference files for 2H delafossite and 3R delafossite of the COD. Source of entry: COD.*

Table IV.1: *Excerpt of limit values for discharge according to the* Verordnung über Anforderungen an das Einleiten von Abwasser in Gewässer (Abwasserverordnung – AbwV), Anhang 40 Metallbearbeitung, Metallverarbeitung.

Metal	**Fe**	**Pb**	**Cr (total)**	**Cu**	**Ni**	**Zn**
Limit Value	3 mg/l	0.5 mg/l	0.5 mg/l	0.5 mg/l	0.5 mg/l	2 mg/l

Table IV.2: *Water analysis results with ICP-MS of sample series P, R, and Q. Metal recovery rates are given in brackets (%). Fields marked with green fulfil the limit value for discharge according to the* Abwasserverordnung, Anhang 40.

	Cu	**Fe**	**Ni**	**Zn**	**Cr**	**Pb**	**Mn**
				[mg/l]			
Q-ini	8 050.48	241.52	94.77	26.97	3.23	1.59	0.78
Q-f	12.86 (99.8)	95.08 (60.6)	0.19 (99.8)	7.94 (70.6)	0.23 (92.9)	0.45 (71.7)	0.27 (65.2)
Q-1drt-c	4.27 (99.9)	77.70 (67.8)	0.16 (99.8)	5.86 (78.3)	0.20 (93.9)	0.29 (81.8)	0.23 (70.6)
Q-1drt-o	3.90 (100)	59.00 (75.6)	0.12 (99.9)	5.18 (80.8)	0.12 (96.4)	0.31 (80.5)	0.14 (81.6)
Q-1d60°C-c	2.04 (100)	4.80 (98.0)	0.05 (99.9)	1.64 (93.9)	0.02 (99.4)	0.26 (83.6)	0.01 (98.4)
Q-1d60°C-o	1.74 (100)	4.21 (98.3)	0.06 (99.9)	1.66 (93.8)	0.02 (99.4)	0.28 (82.4)	0.02 (97.4)
R-ini	7 452.42	15 408.67	84.72	25.07	2.49	1.46	14.57
R-f	3.41 (100)	13.13 (99.9)	0.06 (99.9)	1.77 (92.9)	0.01 (99.7)	<0.0 (100)	0.05 (99.7)
R-1dRT-c	1.07 (100)	11.06 (99.9)	0.11 (99.9)	1.92 (92.3)	0.07 (97.8)	<0.0 (100)	0.02 (99.8)
R-1dRT-o	1.69 (100)	6.64 (99.9)	0.17 (99.8)	1.67 (93.3)	0.01 (99.7)	<0,0 (100)	0.01 (99.9)
R-1d60°C-c	1.17 (100)	4.74 (100)	0.06 (99.9)	1.63 (93.5)	< 0.0 (100)	< 0.0 (100)	< 0.0 (100)
R-1d60°C-o	2.93 (100)	3.63 (100)	0.06 (99.9)	1.64 (93.5)	0.05 (98.4)	<0.0 (100)	0.00 (100)
P-ini	8 235.95	11 684.22	58.15	57.75	1.53	2.17	15.27
P-f	<0.0 (100)	140.4 (98.8)	1.18 (97.9)	6.0 (89.6)	<0.0 (100)	0.13 (93.9)	5.90 (61.4)
P-1d60°C-c	<0.0 (100)	1,325.0 (88.7)	11.63 (80.0)	6.0 (89.6)	<0.0 (100)	0.17 (92.1)	10.55 (30.9)
P-5d60°C-c	3.04 (100)	1,124.3 (90.4)	11.47 (80.3)	7.28 (87.4)	<0.0 (100)	0.2 (90.8)	10.11 (33.8)

Table IV.3: *Overview of phase assemblages in the sample series P, R, and Q. X stands for detected with XRD, and f stands for detected with FTIR.*

Sample	**Phases**						
	ferrite	**cuprospinel**	**maghemite**	**CuO**	**Cu_2O**	**GR**	**$Cu(OH)_2$**
P-f	x, f				x, f	f	
P-1d60°C-c			x, f		x, f	f	
P-5d60°C-c			x, f		x, f	f	
R-f		x, f				f	
R-1dRT-c		x, f				f	
R-1dRT-o		x, f				f	
R-1d60°C-c		x, f				f	
R-1d60°C-o		x, f				f	
Q-f				x, f			x, f
Q-1drt-c				x, f			
Q-1drt-o				x, f			
Q-1d60°C-c				x, f			
Q-1d60°C-o				x, f			

Table IV.4: *Overview of phases found in all samples in the kinetics study. X stands for detected with XRD, and f stands for detected with FTIR.*

	CuO	**$Cu(OH)_2$**	**$Cu_4(OH)_6SO_4$**	**Na_2SO_4**
kin_100rpm_f	x, f	x, f		
kin_100rpm_1d40°c	x, f			
kin_200rpm_f	x, f	x, f		f
kin_200rpm_1d40°c	x, f	x, f		f
kin_300rpm_f	x, f	x, f	x	f
kin_300rpm_1d40°c	x, f	x, f	x	f
kin_400rpm_f	x, f	x, f	x	f
kin_400rpm_1d40°c	x, f	x, f	x	f
kin_500rpm_f			x, f	
kin_500rpm_1d40°c			x, f	

Table IV.5: *Experimental results of the kinetics study.*

	rpm	NaOH (ml)	Start pH	End pH	Start redox stat	End redox stat	Alkalisation time (sec)	Alkalisation rate	time (sec)
kin_100rpm	100	52.8	1.13	11.70	-292.2	-312.3	337.80	0.029	923.9
kin_200rpm	200	41.4	1.10	12.10	-220.6	-315	208.62	0.048	804.62
kin_300rpm	300	24.4	1.10	11.04	-177.9	-230.7	124.37	0.07	725.44
kin_400rpm	400	25.00	1.14	11.26	-148.0	-198.1	124.00	0.084	726.80
kin_500rpm	500	22.00	1.09	11.65	-127.1	-165.6	388.90	0.057	983.85

Table IV.6: *Temperature decrease in the reactor during the precipitation process exemplarily shown for some experimental series. The set temperature is the controlled temperature in the boiler, the start temperature is the temperature of the wastewater in the reactor after filling, and the end temperature is the temperature after adding the NaOH and the Fe-solution when the precipitation is completed.*

Experiment	Set temperature (° C)	T_{Start} (° C)	T_{End} (° C)	Delta T (° C)
N_Cu-1	30	31.68	23.56	8.12
N_Cu-2		31.5	23.70	8.25
N_Cu-3		32.05	23.14	8.91
N_Cu-4		31.98	23.45	8.53
D_Cu-1	40	42.80	29.08	13.72
D_Cu-2		42.53	30.80	11.73
D_Cu-3		43.26	31.20	12.06
D_Cu-4		42.44	29.71	12.73
D_Cu-5		42.51	30.02	12.49
D_Cu-6		42.41	29.88	12.53
K_Cu-1	60	61.59	50.33	11.26
K_Cu-2		61.87	51.41	10.46
K_Cu-3		61.74	52.05	9.69
K_Cu-4		61.75	52.48	9.27
L_Cu-1		62.07	51.97	10.10
L_Cu-2		61.98	50.75	11.23

Table IV.7: *Synthesis parameters found in the literature for the hydrothermal synthesis of brochantite.*

	Reactant	**Base**	**Temperature**	**Stirring**	**Final pH**	**Volume**	**Duration**
Prasad and Rao, 1985	0.5 M $CuSO_4$ solution	NaOH solution	60° C	yes	8.0	-	-
Schmidt and Lutz, 1993	0.5 M $CuSO_4$ solution	0.25 M $CO(NH_2)_2$ solution	70° C	-	-	-	2 days
Koga et al., 1997	0.1 M $CuSO_4$ solution	Dropwise addition of 0.1 M NaOH solution	298 K	yes	8.0	100 ml	-
Vilminot et al., 2002	$CuSO_4$ solution	NaOH	170° C	-	-	-	6 days
Yoder et al., 2007	0.05 – 1.0 M $CuSO_4$ solution	Dropwise addition 0.05 – 1.0 M NaOH or Na_2CO_3	-	Yes, magnetic stirrer	-	-	Up to 1 month
Bakhtiari and darezereshki, 2011	0.5 M $CuSO_4$ solution	0.5 M Na_2CO_3 solution	55° C	1200 rpm	-	-	1 h
Kaş & Birer, 2012	3.7 mmol Cu acetate monohydrate	1.8 mmol sodium peroxydisulfate	5, 25, 60, 80 °C	Ultrasound irradiation	6.5, 7.5, 8.5	50 ml	1 h
Zittlau et al., 2013	0.001 M CuSO4 solution	Dropwise addition of 0.1 M NaOH	55° C	Continuous stirring for 20 min	6.23		
Novikova et al., 2016)	0.5 M $CuSO_4$ solution	0.5 M Na_2CO_3 solution	60° C	yes	8	75 ml	-
Ding et al., 2019	1000 ppm (=0.006 M)	0.1 M NaOH	-		5 6 10		
Rak et al., 2020	0.01 M $CuSO_4$ solution	0.1 M NaOH	-	250 rpm Magnetic stirrer	11	100 ml	-
	0.1, 0.4, 0.626 M	1 M		250 rpm Magnetic stirrer		100 ml	

V. Acknowledgements

This thesis was written as part of the project BAFOISoFo-71263 “Gesamtkonzept zur Umsetzung der hydroxidfreien Fällung von Metallen aus Abwässern verschiedener Branchen: Bau einer mobilen Technikumsanlage”, funded by the Bavarian State Ministry of the Environment and Consumer Protection.

Many people have contributed significantly to this work – to them, I want to express my sincere thanks.

First, I would like to thank my supervisor, Prof. Soraya Heuss-Aßbichler. She enabled me to carry out this work and apply mineralogy to an environmentally relevant topic. She always accompanied me with high commitment and great care and gave me constructive and valuable advice. Also, I want to thank my second examiner, Prof. Wolfgang Schmahl, for evaluating this work, being part of the committee and helping with the FTIR.

I want to thank the whole workgroup for creating the most pleasant atmosphere:

My special thanks go to Kai Tandon for your kindness and friendship. The many discussions and laboratory work we shared helped me improve my research. I profited greatly from your goal-oriented mindset and helpfulness. I want to thank Johannes Knof for his excellent work on the pilot facility and the fun and challenging times during its construction. Many thanks go to my friend Simon Kaphahn for his support with the software and his creative and unconventional ideas. I am very grateful to Dr. Werner Ertl-Ingrisch for helping me with analytical questions, creating a safe workspace, and helping me. A big thank you to Adriana Gerz for your support and garden parties. Your organisational talent and profound and reliable work created a highly functional laboratory where I enjoyed working. I want to thank Katharina Engels, Sebastian Gölitz, Natalie Weichselgartner, Andreas Appel, and Elena Zwerschke for their committed work and essential contributions. Also, I would like to thank Alexandra Huber for her helpful advice and support. I sincerely thank Markus Sieber, Günter Hesberg, and Max Häberle, who contributed to building the pilot facility. Thanks to Prof. Sohyun Park and Moritz Zenkert for the advice on analytical questions and the help in the lab.

I want to thank my industry partners, the WAFA Kunststofftechnik GmbH, especially Dr. Harald Prestel, and Clariant AG, especially PD Dr. Gerhard Mestl, for the numerous talks and the supply of sample material whenever needed.

Thanks a lot to all my colleagues for all the good times: Ana, Baha, Caron, Chris, Christina, Daniel, Diana, Eleonora, Joana, Lukas, Luiz, Marize, Markus, Mathieu, Michi, Natasha, Omar, Simon, Sidd, Steffi, Pancho, and Zeynep. Thank you, Jérémie, for supporting and accompanying me. You always had open ears for questions, and knowing you would be there strengthens me. Last, I want to thank my family for their support and patience. Special thanks to my brother Alex and Christian, whose continuous encouragement finally drove me to get my first draft of this thesis and made me finish it. You both know best how to motivate or annoy me to get me off the ground.